



Guevara Jelid, Hassam Israel (2024) *Plasma-based micro-propulsion system for nanosatellites: design, nanofabrication, and characterisation of plasma-based micro-thruster chip*. PhD thesis

<https://theses.gla.ac.uk/84724/>

Copyright and moral rights for this work are retained by the author

A copy can be downloaded for personal non-commercial research or study, without prior permission or charge

This work cannot be reproduced or quoted extensively from without first obtaining permission in writing from the author

The content must not be changed in any way or sold commercially in any format or medium without the formal permission of the author

When referring to this work, full bibliographic details including the author, title, awarding institution and date of the thesis must be given

Enlighten: Theses

<https://theses.gla.ac.uk/>
research-enlighten@glasgow.ac.uk

**Plasma-based micro-propulsion system for nanosatellites:
design, nanofabrication, and characterisation of plasma-
based micro-thruster chip**

Hassam Israel Guevara Jelid

Submitted in fulfilment of the requirements for the
Degree of Doctor of Philosophy
in
Aerospace Engineering

James Watt School of Engineering
College of Science and Engineering
University of Glasgow



University
of Glasgow

September 2022

Author's Declaration

"I declare that, except where explicit reference is made to the contribution of others, that this dissertation is the result of my own work and has not been submitted for any other degree at the University of Glasgow or any other institution."

Printed Name: Hassam Israel Guevara Jelid

Signature: Hassam Israel Guevara Jelid

Date: 18.08.2024

Acknowledgements

This thesis represents the culmination of four years of research and development, which would not have been possible without the help of countless others. It does not show that it allowed me to do what I love for a living, connect with interesting people, learn new things, and travel the world. Though challenging at times, beginning this project has been one of the best decisions of my life, and I want to make sure that everyone who has helped me along the way, whether professionally or personally, knows how much I appreciate their assistance. Before anything else, I'd like to express my appreciation to Professor Konstantinos Kontis, who served as my advisor throughout this research, and Dr Craig White, who has shown enthusiasm for this endeavour.

I would also like to thank my parents, Dr Lourdes Jelid Lopez and Dr Cecilio Guevara de Jesus, for their unwavering love and encouragement and for serving as a model of tenacity and determination that inspired me to keep pushing forward no matter what obstacles I've had to overcome. I would also like to thank my parents, Dr. Lourdes Jelid Lopez and Dr. Cecilio Guevara de Jesus, for their unwavering love and encouragement and for serving as a model of tenacity and determination that inspired me to keep pushing forward no matter what obstacles I've had to overcome. I am also deeply grateful to my dogs, Lasser and Shelby. Their presence, love, and loyalty have meant the world to me.

In addition, I would like to thank the Espinosa Rugarcia Foundation (ESRU) and the Mexican government's National Council of Science and Technology (CONACYT) for helping me fund this project and earn my doctorate in aerospace engineering. I extend my deepest gratitude to Dr Pedro Aspe Armella, Mr Rafael Posada Cueto, and Mrs Paulina Sastrias Massieu, whose encouragement has been invaluable to me.

I would also like to thank the James Watt Nanofabrication Centre staff for assisting with my research. In particular, I would like to thank Donald Nicholson for his help in fabricating the microdevice chip, which would not have been possible under the stricter conditions imposed by the COVID pandemic's lockdown. Furthermore, I appreciate the guidance of James Grant, Corrie Farmer, and Linda Pollock with my nanofabrication efforts. Additionally, thanks to my friend and future doctor, Eve McGlynn, for providing me with the resources I needed to streamline a nanofabrication process that would have otherwise taken months.

I want to express my gratitude to everyone who helped me during my time at the College of Science and Engineering, particularly Professor Marc Sorel, Julia Deans, Peter Miller, Jim Greene, Johnnie Sloan, James Blunn, and Ian Scouller.

Above all else, I owe a tremendous debt of gratitude to my dear friend Dr Thomas Andreou for his invaluable assistance during the PhD programme, especially during the experimental phase of the study. Moreover, I would like to express my appreciation to Miguel Angel Martinez Vazquez and Jose Armando Rivera Tello, two of my closest friends. They have encouraged me since this trip was only a thought.

Finally, I'd like to extend my gratitude to my close friends; Abdoalbaset Ali Yusef Abohmra, Alfonso Martnez Carmena, Burak Agir, Clément Civrais, Fan Jiang, Gaargi Jain, Goushuai Lee, Handika Sandra Dewi, Karuppasamy Pandian Soundarapandian, Laura Cariño Aguirre, Roksana Grzelak, and Senthilkumar Subramanian. Thank you for being a continual source of inspiration and happiness in my life and lighting a fire within me that has allowed me to get where I am now.

Abstract

Micro-electromechanical systems have experienced a major expansion in their use as flow control devices and CubeSats' onboard attitude and orbit determination systems (AOCS) in recent years, where plasma thrusters have a potential application in this field. As a result, further understanding of plasma micro-thrusters and plasma processes at micrometer scale sizes is required. Consequently, the propulsion system under development in this project, aims to integrate electrostatic and cold gas thruster in a two-mode operation. Being in specific, a plasma-based micro-thruster chip was fabricated for the micro-propulsion system used in nano and picosatellites, enabling accurate manoeuvre operations in space and producing thrust in the range of nanonewtons (nN) to millinewtons (mN).

The micro-thruster chip, is conceived as a breakthrough hybrid design chip combining the two-mode operation systems (electrostatic and cold-gas) into a hybrid propulsion system, increasing the flexibility to adapt the thrust control and power consumption according to the mission requirements by switching on or off the current through the electrodes.

Computational simulations were used to evaluate geometric possibilities in defining the shape and location of the electrode of the micro-thruster chip. A significant problem was presented on the inclusion of plasma in simulations due to the method's limitations and the high processing power requirements, which are numerically expensive. Therefore, a novel code was developed to simulate micro-discharge interaction with the flow as a slim alternative based on the dsmcFOAM+ solver from the OpenFOAM platform. The code reduces the computational burden by simulating ionisation without introducing new electrons as particles, increasing the velocity of an existing number of equivalent gas particles in the mesh and finding a numerical solution to the Fowler-Nordheim equation.

As a result, an in-house 5 mm x 7.4 mm x 0.75 mm plasma based micro-thruster chip was designed to connect to the microSD card's electrical connection. A comprehensive method for the nanofabrication of the micro-thruster was established based on fifty cleanroom processes, including photolithography, wet etching, dry etching, metal deposition, and bonding procedures inside the James Watt Nanofabrication Centre (JWNC). The neutraliser designing and manufacture are no cover in this project.

After the micro-thruster was manufactured, a bespoke experimental setup to characterise the performance of the chip as a cold gas thruster was built based on a prior PIV configuration from the TSI time-resolved particle image velocimetry (PIV) system. The experimental setup was constrained

when magnification lenses were used to see the micro-size jet, which reduced the field of view for capturing exhaust particles from the micro-thruster traveling at higher velocities (8 m/s), encouraging the design and fabrication of a calibration sheet with micrometre dots for camera alignment to be used for higher magnification lenses. In the attempt to obtain the characterisation of the velocities on the jet, it was able to capture velocities up to 12 m/s, being a significant increase but not sufficient for the full jet velocities profile that allows a further reliable thrust calculation. Therefore, no electrostatic performance features were investigated given by the restrictions on equipment capabilities for the detection and readiness of high voltage (200 V - 1.2 KV) with low current (1 μ A – 100 μ A). Therefore, the most significant contributions or findings of this current project are:

- The creation of a micro-discharge algorithm for the dsmcFOAM+ solver on OpenFOAM that can simulate DC discharge at the micro-scale while taking the enhancement factor for micro-gaps into account.
- Design and nanofabrication of a novel plasma-based micro-thruster chip prototype.
- Feasibility of using SPR220-7 positive photoresist and physical vapour deposition were used to deposit 500nm-thick Au (gold) through a 100 m trench (PVD).
- Identification of the particle image velocimetry (PIV) system limitations in the development of an experimental testing rig for micro-thrusters based on cold gas tests.

Table of Contents

1. Author's Declaration	i
2. Acknowledgements	ii
3. Abstract	iv
5. List of Figures	xi
6. List of Tables	xv
7. Nomenclature	xvi
8. Abbreviation	xix
9. Publication List	xx
1. Chapter 1 Introduction	1
1.1. Motivation.....	1
1.2. Aim	3
1.3. Project goals.....	4
1.4. Micro-thruster chip operational description	5
1.5. Contributions / objectives.....	6
1.6. Thesis outline	7
2. Chapter 2 Literature survey	9
2.1. Plasma.....	9
2.1.1. Breakdown current considerations.....	12
2.1.2. Electron impact reactions	13
2.2. Technological overview of the micro-thruster chip.....	13
2.2.1. Discharge characteristics	14
2.2.2. Ionization processes.....	14
2.2.3. Relevance to plasma processes	14
2.2. Micro-propulsion system for CubeSats.....	15
2.1.1. Electrothermal thrusters.....	16
2.1.1. Electromagnetic thrusters.....	21
2.2.4. Electrostatic thrusters.....	22
2.3. Calculation of the thrust force	26
2.3.1. For electrostatic thrusters.....	26
2.3.2. For cold gas thrusters.....	27
2.3.3. Specific impulse.....	27
2.4. Propellants analysis.....	27
2.4.1. Inert gases	29
2.4.2. Ionization energy	29

2.4.3.	Propellant selection and relevance to micro-thruster operation.....	31
2.4.4.	Selection for cold gas mode.....	31
2.4.5.	Selection for electrostatic mode.....	32
2.5.	Physics of gases.....	33
2.5.1.	Particle density.....	33
2.5.2.	Mean free path	33
2.5.3.	Kinetic diameter.....	34
2.5.4.	Scattering cross-section	34
2.5.5.	Knudsen number.....	35
2.6.	Summary	38
3.	Chapter 3 Micro-plasma discharge algorithm development	39
3.1.	Theory and Background	41
3.1.1.	Direct Simulation Monte Carlo (DSMC)	43
3.1.2.	The DSMC algorithm	43
3.1.	Micro-plasma discharge algorithm	47
3.1.1.	How does the micro-plasma discharge algorithm (MPDA) works?	48
3.1.2.	Micro-plasma algorithm (MPDA) restrictions	51
3.1.3.	Time Step selection (Δt)	51
3.1.4.	Electric field calculations.....	53
3.1.3.	Townsend's first ionization coefficient (α)	56
3.1.4.	Townsend's second ionization coefficient (γ_{SEE})	57
3.1.5.	Field emission coefficient (γ_{FE})	57
3.1.6.	Ion density n_+	58
3.1.7.	Corrective functions t_y and v_y	58
3.1.5.	Applied current density.....	59
3.1.6.	Ionic density distribution	59
3.1.7.	Particle acceleration.....	63
3.1.8.	Leapfrog method.....	65
3.1.9.	Wall-particle temperature exchange	65
3.2.	Algorithm validation.....	66
3.2.1.	Validation case 1	66
3.2.2.	Validation case 2	68
3.2.3.	Electron temperature validation.....	69
3.2.4.	Ion temperature validation.....	71
3.3.	Simulation cases.....	75

3.3.1.	Results and discussions	76
i.	Flow temperature analysis during discharge	79
ii.	Electric field simulation results	80
iii.	Simulations results analysis	81
iv.	Key factors behind temperatures results.....	84
3.4.	Summary	86
4.	Chapter 4 Designing the micro-thruster chip.....	87
4.1.	Electrical current for plasma generation	91
4.1.1.	Breakdown current considerations.....	92
4.2.	Breakdown voltage for plasma generation.....	92
4.3.	Breakdown voltage in function of A and B gas constants definition	94
4.4.	Heat transfer	99
4.4.1.	Heat transfer considerations in space	100
4.5.	Heat transfer calculation.....	101
4.5.1.	Radiation heat transfer	102
4.5.4.	Thermal conductivity	104
i.	Thermal conductivity k	105
4.5.5.	Convection	106
4.6.	Electrode geometry shape analysis	107
4.7.	Electrodes heat over time.....	110
4.8.	Considerations on design.....	112
4.8.1.	Electrode location	113
4.8.2.	Electrode size	115
4.8.3.	Flow acceleration caused by nozzle expansion	115
4.8.4.	Microtubing definition	116
4.8.5.	Handleable chip design	127
4.9.	Quantitative Operating Regime of the Device.....	133
4.10.	Summary	134
5.	Chapter 5 Nanofabrication of the micro-thruster chip.....	135
5.1.	Photolithography	136
5.1.1.	Photomask	137
5.1.2.	Alignment markers.....	139
5.1.3.	Photoresist	141
5.1.5.	Photoresist: profile.....	145
5.1.6.	Shadow printing resolution.....	147

5.1.7.	Photoresist: processing	149
5.2.	Baking.....	152
5.3.	Development.....	154
5.4.	Etching.....	154
5.4.1.	Bosch deep silicon etching (DSIE)	157
5.4.2.	Silicon (Si) mixed etching	161
5.4.3.	Carrier wafer procedure	162
5.5.	Electrical Breakdown within the device.....	163
5.6.	Insulator layer deposition	164
5.7.	Metal deposition.....	164
5.7.1.	Conformal deposition	166
5.7.2.	Covering issues.....	169
5.7.3.	Lift-off.....	169
5.8.	Glass cover fabrication.....	170
5.9.	Bonding	170
5.10.	Process traveller for the plasma-based micro-thruster chip nanofabrication	172
5.11.	Characterisation.....	173
5.11.1.	Depth analysis in microchannels.....	173
5.11.2.	Symmetry of the shapes/borders analysis.....	176
5.12.	Summary	179
6.	Chapter 6 Experimental testing of the micro-thruster chip.....	181
6.1.	PIV system.....	182
6.2.	Hardware	185
6.2.1.	Pneumatic setup	185
6.2.2.	Laser	187
6.2.3.	Tracer	188
6.2.4.	Cameras and Lenses.....	189
6.2.5.	Calibration plate.....	189
6.3.	Software - measurement settings.....	191
6.3.1.	Interrogation window	191
6.3.2.	Inter-frame time Δt	192
6.4.	PIV experimental results.....	193
6.4.1.	The field of view (FoV)	193
6.4.2.	Challenges in PIV for micro-thruster jet characterisation	198
6.4.3.	Jet characterisation.....	199

6.4.4.	Uncertainty calculation	205
6.4.5.	Thrust and Specific Impulse calculation challenges and future improvements	208
6.5.	Summary	209
7.	Chapter 7 Conclusions.....	211
7.1.	Chapter 2: Literature survey achievements.....	211
7.2.	Chapter 3: Micro-plasma discharge algorithm development achievements	212
7.3.	Chapter 4: Designing the micro-thruster chip achievements.....	212
7.4.	Chapter 5: Nanofabrication of the micro-thruster chip achievements	212
7.1.	Chapter 6: Experimental testing of the micro-thruster chip achievements.....	213
7.2.	Future work.....	213
8.	Bibliography.....	215
9.	Appendices.....	231
A.	Geometrical dimensions of the micro-thruster chip	231
B.	Micro-thruster performance as a cold gas thruster based on dsmcFoam+.	236
C.	Performance of plasma thrust based on dsmcFoam+.	238
D.	Traveller procedure for the nanofabrication of the plasma-based micro-thruster chip	242
E.	jet half width velocities results from PIV experimental results	246

List of Figures

Figure 1-1. Prototype concept of the DC plasma-based micro-thruster chip.....	4
Figure 1-2. Sections that compose the micro-thruster chip	5
Figure 1-3. Micro-thruster chip size comparison.....	7
Figure 2-1. Main parameters for breakdown voltage on parallel electrode plates.....	10
Figure 2-2. Gas discharge regimes characterised by their current density-voltage curves.....	11
Figure 2-3. Micro-propulsion classification.....	16
Figure 2-4. Schematic of the microwave electrothermal thrusters (MET) device.....	17
Figure 2-5. Schematic of an arcjet thruster	17
Figure 2-6. Schematic of a planar solid propellant micro-thruster (SPM)	19
Figure 2-7. 7x1 silicon array micromachined planar SPM	19
Figure 2-8. Electrolytic micro-thruster design	20
Figure 2-9. The Resistojet diagram.	20
Figure 2-10. AIS-gPPT3-1C Single-Channel Gridded Pulsed Plasma Thruster	21
Figure 2-11. Schematic of a liquid propellant pulsed plasma thruster(LP-PPT)	22
Figure 2-12. Left side shows the 31.1 μ N electro spray micro-thruster	22
Figure 2-13. ion electro spray thrusters	23
Figure 2-14. Left side shows the IRIT4 thruster	24
Figure 2-15. Schematic view of a micro ion thruster	25
Figure 2-16. Inert gases performance for micro-satellite propulsion.....	29
Figure 2-17. Ionization energy of inert gases.....	30
Figure 2-18. Mean free path and kinetic diameter representations for a gaseous propellant.	34
Figure 2-19. Flow regimen according to the Knudsen number on a duct	37
Figure 2-20. Knudsen number range for MEMS and nanotechnology applications	37
Figure 3-1. Flowchart of the DSMC algorithm.	44
Figure 3-2. Flowchart of the micro-plasma discharge algorithm in dsmcFoam+.	48
Figure 3-3. Time plot diagram contrasting the integration time step and characteristic time scale in plasma phenomena	52
Figure 3-4. MPDA electric field lines from two parallel electrode plates.....	53
Figure 3-5. MPDA electric field lines from an anode and two cathodes	55
Figure 3-6. MPDA electric field lines from two parallel pairs of anodes and cathodes.....	56
Figure 3-7. Elementary discharge behaviour diagram.....	60

Figure 3-8. Micro-plasma discharge algorithm, representation of the ion density distribution per cell column in a mesh between parallel electrode plates.....	61
Figure 3-9. Ion and electron density results from 1D PIC-DSMC simulation	67
Figure 3-10. Ar + density distribution in a 50 μm gap.....	68
Figure 3-11. Geometry for a double inlet microchannel with a single outlet orifice..	76
Figure 3-12. Time-evolution intervals of N2 flow velocities in a 50 μm gap microchannel.	78
Figure 3-13. Steady DC micro-discharge simulation results	79
Figure 3-14. Electric field intensity results from the steady DC micro-discharge simulations	80
Figure 3-15. Highest temperatures and thrusts results at steady state from the simulations.....	83
Figure 3-16. Velocity flow profiles at steady state on 50 μm gap at 800 V	85
Figure 4-1. Design of a plasma-based micro-thruster chip procedure flowchart.....	88
Figure 4-2. Schematic illustrating the mathematical modelling of heat transfer during plasma generation between two micro-electrode plates.....	89
Figure 4-3. Surface area representation of an electrode	89
Figure 4-4. Paschen curve vs Fowler-Nordheim equation.....	93
Figure 4-5. Fitted curves for the breakdown voltage of N2 at varying pressures	96
Figure 4-6. Redefined values of A and B gas constants for N2	98
Figure 4-7. Breakdown voltages at different pressures based on the gap distance.....	99
Figure 4-8. Dependence of melting temperature, sublimation and saturation temperature on pressure	100
Figure 4-9. Vapor pressure of materials	101
Figure 4-10. Diagram of the heat conduction between an electrode and the substrate.....	105
Figure 4-11. Thermal conductivity formula for each material for micro-thruster chip electrodes. ...	106
Figure 4-12. Electrical net power flow rate on electrodes modelling based on their shape.....	108
Figure 4-13. Electrical net power flow rate on electrodes modelling based on their thickness.	109
Figure 4-14. Size and location of the smallest electrode on the micro-thruster chip.	110
Figure 4-15. Temperature increase on electrodes subjected to electrical power	111
Figure 4-16. Alternatives for electrode placement.....	114
Figure 4-17. Degradation on walls caused by plasma according to the outlet geometry.	115
Figure 4-18. Layout of the micronozzle.	116
Figure 4-19. Layout of the micro-tubing channel.	117
Figure 4-20. N2 dsmcFOAM+ simulation results for the velocity magnitude on the micronozzle	118
Figure 4-21. Thrust performance based on the geometric parameters of the micronozzle	120
Figure 4-22. The main effect plot for thrust based on the geometric parameters	121
Figure 4-23. Pareto chart of the standardised effects	122

Figure 4-24. Comparison between simulations results and $T_{\mu Nozzle}$ equation	123
Figure 4-25. Diagram illustrating the number of computational.....	123
Figure 4-26. Normalized thrust performance based on the plasma effect on microgaps.....	125
Figure 4-27. Comparison between simulations results based on $T_{\mu Plasma}$ and Eq. 115	127
Figure 4-28. Design of a plasma-based micro-thruster chip and its components.....	128
Figure 4-29. A microSD connector connection diagram for the micro-thruster chip.....	129
Figure 4-30. Electrodes design on the chip's micronozzle.....	129
Figure 4-31. Layout of the plasma-based micro-thruster chip.	130
Figure 4-32. Voltage breakdown characteristics of SiO ₂ , SiN and Silicon wafer	131
Figure 5-1. The configuration of 63 micro-thruster chips on a 4-inch Si wafer	136
Figure 5-2. Representation of the photolithography technique for the micro-thruster nozzle.....	137
Figure 5-3. Masks alignment representation on L-edit.....	138
Figure 5-4. Allocation of photomask alignment markers	139
Figure 5-5. Deterioration of the overlap on alignment markers after a deep dry etch.....	140
Figure 5-6. Comparison of the "original design" and the "extended mode design"	141
Figure 5-7. Comparison of exposure times for micronozzle patterning in the photoresist	145
Figure 5-8. Photoresist profiles of the cross-sectional area of the nozzle exhaust.....	145
Figure 5-9. Photoresist profile overview.....	146
Figure 5-10. Shadow printing (Contact and Proximity) diagram	147
Figure 5-11. Shadow printing based on the thickness of the photoresist.	148
Figure 5-12. SPR220-7 and SPR220-4 thicknesses based on the spin speed ω for 4" wafer.	149
Figure 5-13. RCD8 spinner at the JWNC.....	150
Figure 5-14. Trenches flooding representation by photoresist on the microthruster chip.....	153
Figure 5-15. Anisotropic, partially anisotropic, and isotropic etching of silicon	154
Figure 5-16. Variations in depth on a single Si substrate test for a deep etching process.....	156
Figure 5-17. Diagram of the Bosch etching process applied to the deep etching	157
Figure 5-18. Normalized average depth factor for DSIE based on the open area width.....	160
Figure 5-19. Metal deposition process	165
Figure 5-20. Schematic of the position relative to a flat sample for thin film deposition.....	166
Figure 5-21. Sample's directionality and rotation during vapour deposition.....	167
Figure 5-22. Schematic of the conformal Au-coat routing for electrodes.....	168
Figure 5-23. General scheme of the nanofabrication processes for the micro-thruster chip.....	172
Figure 5-24. SEM image of the micro-thruster chip from top view.	173
Figure 5-25. Diagram for depth etching analysis	174

Figure 5-26. Frontal SEM image of the outlet of a medium-sized (M) micro-thruster.....	177
Figure 5-27. Top-lateral SEM image displaying conformal deposition	178
Figure 5-28. Top-lateral SEM image of the plenum microchamber	179
Figure 6-1. Lateral perspective of the experimental PIV setup.	184
Figure 6-2. Frontal perspective of the experimental PIV setup.....	184
Figure 6-3. Pneumatic schematic of the micro-thruster chip testing PIV experimental setup.	185
Figure 6-4. Potential setup methods to improve atomisation of particles.....	187
Figure 6-5. Micro-scale PIV calibration instrument	190
Figure 6-6. Calibration of the camera on INSIGHT 4G software	190
Figure 6-7. Visualisation of the micro-thruster jet at various interrogation window sizes	191
Figure 6-8. Visualisation of the micro-thruster jet at various inter-frame times Δt	192
Figure 6-9. Effects of laser sheet proximity to the microdevice on image capture.....	194
Figure 6-10. PIV results of the velocity profiles of the jet on the L50E3 micro-thruster chip	195
Figure 6-11. Polar diagram illustrating the maximum velocity of a jet vs inlet pressure	196
Figure 6-12. Schematic of the structure of the jet flows exhaust from the micro-nozzle outlet	199
Figure 6-13. Half-width jet velocities from PIV experimental results based on pressures.....	201
Figure 6-14. Jet spread rate according to inlet and outlet pressures on the L50E3 micro-thruster. .	202
Figure 6-15. Virtual origin according to inlet and outlet pressures on the L50E3 micro-thruster.	202
Figure 6-16. Jet contour tracing from the centerline	203
Figure 6-17. Jet angles of L50E3 micro-thruster according to inlet and outlet pressures.....	204

List of Tables

Table 1. Comparison of thermal and cold plasmas.....	10
Table 2. Gas phase reactions involving electrons	13
Table 3. performance for micro-satellite propulsion.....	28
Table 4. Cold gas propellant performances	30
Table 5. Propellants with their respective kinetic diameters.	34
Table 6. Comparison between corrected electron temperature and reference values.....	69
Table 7. Comparison of mean absolute differences in electron temperature T_e calculations.....	70
Table 8. Comparison between corrected ion temperature and reference values	73
Table 9. Comparison of mean absolute differences in ion temperature calculations.....	73
Table 10. Electrode Types and Materials.....	97
Table 11. Alignment tolerance on the electrode photomask (mask #3)	140
Table 12. Comparative analysis of conventional positive and negative photoresists	142
Table 13. MA6 input parameters for UV exposure on SPR220-7	143
Table 14. Shadow printing resolution on every micro-thruster chip nanofabrication stage.	148
Table 15. RCD8 process description recipe for SPR220-7 deposition.....	150
Table 16. Spinning parameters for each nanofabrication stage of the micro-thruster chip	151
Table 17. Soft baking conditions for thicker SPR220-7 resist layers($>1\mu\text{m}$)	152
Table 18. Practical soft baking parameters based on resist thickness in micro-thruster trenches. ...	153
Table 19. Estrelas DSIE parameters for an A/R of 1:1 etch along $320\mu\text{m}$ -width	158
Table 20. Etching rates for Bosch Deep Silicone Etching (DSIE) from JWNC	159
Table 21. DSIE normalized average depth	159
Table 22. Normalized depth difference between different micro-trench widths	161
Table 23. Parameters for the Si Mixed Etching procedure.....	162
Table 24. Dry etching process on the microtubing channel	174
Table 25. Variations in depth after the dry etching process on the micronozzle.....	175
Table 26. Variations in depth after the dry etching process on the metal routing path.....	176
Table 27. Olive oil tracing parameters.....	189

Nomenclature

Latin		Units
A	Gas constant, area	$cm*Torr, m^2$
A_e	Exhaust nozzle area	m^2
A_h	Area of the hot object	m^2
A/R	Aspect Ratio	
$\vec{a}_{i,j}$	Ion's acceleration in a cell	m/s^2
B	Gas constant	$V/[cm*Torr]$
C	Confidence interval	
C_{e-n}, C_m	Correction factor of the transferred energy	
C_p	Correction factor in function of the pressure	
C_{PDSMC}	Energy transfer factor	
c	Heat capacity	J/K
c_e	Exhaust velocity	m/s
c_m	Centre of mass velocity	m/s
c_r, c_i, c_j	Relative speed	m/s
D	Gas dependent constant, length of the nozzle outlet	$V/cm, m$
d	Gap distance	m
d_k	Kinetic diameter	m
d_p	Particle diameter	m
\vec{E}	Electric field	V/m
E	Exposure dose	mJ/cm^2
E_{el}	Supplied electrical energy	J
\vec{E}_x	Electric field component on the x-axis	V/m
\vec{E}_y	Electric field component on the y-axis	V/m
\vec{E}_{ij}	Electric field of a cell in the mesh	V/m
E_{ave}	Average etch rate	$\mu m/min$
E_{max}	Maximum etch rate	$\mu m/min$
E_{min}	Minimum etch rate	$\mu m/min$
E_{th}	Thermal energy	J
$E(k)$	Elliptic integral of the second kind	
F	Force, thrust	N
F_{ij}, F_{12}	View factor	
F_N	Equivalent number of particles	
f_k	Thermal conductivity factor	
$f(\vec{E})$	Correction factor of the electric field	
$f(v)$	Velocity probability density	
$f(v_{ij})$	Velocity probability density on a cell mesh	
$f(v_{e,i,ave})$	Probability distribution function of $v_{e,i,ave}$	
$f(\sigma)$	Correction factor by collision cross-section	
$\overline{f(v)}_{ij}$	Distribution factor	
g	Gap distance	m
g_0	Gravitational acceleration	m/s^2
H	Depth	μm
H_{Norm}	Normalized average depth	
I	Applied electrical current, light intensity	$A, mW/cm^2$
I_{sp}	Specific impulse	s
i	Final current between the gap	A
i_0	Initial current between the gap	A

J_{TF}	Current density	A/m^2
K	Field emission coefficient constant, conformity	
$K_E, K_{E,+}$	Kinetic energy	J
$K(k)$	Elliptic integral of the first kind	
Kn	Knudsen number	
K_u	Jet spread rate	
k	Thermal conductivity	$W/[m*K]$
k_B	Boltzmann's constant	J/K
L	Characteristic length	m
L_1, L_2	Material's thickness	n
M_{mass}	Molar mass	Kg/mol
m_{gas}	Mass of gas	Kg
\dot{m}	Mass flow rate	Kg/s
m_t, m_j	Gas molecule's total mass	Kg
m_e	Electron mass	Kg
m_+	Ion mass	
NU	Etch factor	
\bar{N}	Instantaneous number of particles in a cell	
N_A	Number of atoms	
n	Particle density	m^{-3}
\bar{n}	Rate of ion-electron pair production	
n_e	Electron number density	m^{-3}
n_{e_0}	Initial electron number density	m^{-3}
$n_{e_0,ij}$	Electron density in a specific cell at (i, j)	m^{-3}
n_{gas}	Gas particle density	m^{-3}
n_+	Ion number density	m^{-3}
$n_{+,ij}$	Ion density in a specific cell at (i, j)	m^{-3}
n_j	Cell in the column	
$n_{j,total}$	Total number of cells in the column	
P	Electric power	W
P_e	Exhaust pressure	Pa
p	Pressure	Pa
Q	Total charge	C
$Q_{cathode_1}, Q_{cathode_2}$	Cathodes charge	C
q	Amount of charge	C
q_{cond}	Conduction flow rate	W
q_{Jh}	Joule Heating flow rate	W
q_{net}	Net heat transfer	W
q_{rad}	Radiation flow rate	W
R	Gas constant, resolution	$J/[mol*K], m$
R_{dep}	Deposition rate	nm/s
R_f	Random fraction uniformly	
r	Radius, distance between the charges	m
$r_{k,1}, r_{k,2}$	Kinetic radius of a particle specie	
\hat{r}	Unit vector of the distance between the charges	
\hat{r}_{ij}	Unit vector components x and y	
S	Specific heat	$J/[Kg*K]$
St	Stokes number	
T	Thermodynamic temperature, thrust, spin resist thickness	K, N, m
T_c	Absolute temperature of the cold surroundings	K
T_e	Electron temperature	K, eV
T_{eref}	Reference value of the electron temperature	eV
T_{gas}	Gas temperature	K
T_h	Hot body absolute temperature	

T_+	Ion temperature	K, eV
T_p	Particle temperature	K
T_0	Initial temperature	K
T_1	Temperature at end	K
$T_{\mu Thrusterchip}$	Micro-thruster's thrust with plasma contribution	F
$T_{\mu Nozzle}$	Micro-thruster's thrust as cold gas propulsion system	F
$\hat{T}_{\mu Plasma}$	Normalised factor of plasma thrust	
t	Time	s
$t(y)$	Corrective functions for Fowler-Nordheim equation	
t_c	Mean collision time	s
t_{res}	Cell residence time	s
U	Uncertainty	
U_E	Electric potential energy	J
U_m	Mean velocity	m/s
U_{peak}	Maximum velocity of the particles	m/s
u_e	Exit velocity	m/s
u_m	Maximum velocity profile	m/s
$\vec{v}_{o,ij}$	Particle's initial velocity vector in a cell	m/s
\vec{v}_{ij}	Particle's velocity vector in a cell	m/s
$\vec{v}_{p,ij}$	Particle's total velocity vector after acceleration in a cell	m/s
$\vec{v}_{p,ij}^t$	Half of the velocity before particle's movement	m/s
$\vec{v}_{p,ij}^{t+\Delta t}$	Particle's velocity at the end of the timestep	m/s
$\vec{v}_{p,ij}^{t+\Delta t/2}$	Half of the velocity after particle's collisions	m/s
\bar{v}_{∞}	Average cell stream velocity of the gas	m/s
\vec{v}	Particle's velocity	m/s
V	Voltage, volume	V, m^3
V_b	Breakdown voltage	V
V_C	Cell volume	m^3
V_e	Exhaust velocity	m/s
$v(y)$	Corrective functions for Fowler-Nordheim equation	
\vec{v}_e	Electron velocity	m/s
$v_{e,ave}$	Average thermal speed of the electron in i -position	m/s
$v_{e,max}$	Maximum thermal speed	m/s
$v_{e,prob}$	Most probable speed of the electron in i -position	m/s
$v_{+,j}$	Average thermal speed of the ion in j -position	m/s
v_{seg}	Segment speed	m/s
$v_{+,ave}$	Ion's average thermal speed	m/s
$v_{\infty,prob}$	Most probable molecular speed	m/s
x_{A-B}	number of pixel between point A and B	$pixel$
x_0	Virtual origin	m
y_i	Jet half-width	m
Greek		Units
α	Townsend's first ionization coefficient, jet angle	
$\bar{\alpha}$	Mean angular width	Degree, rad
β	Field enhancement factor	
γ_{FE}	Field emission coefficient	
γ_{SEE}	Townsend's second ionization coefficient	
Δd	Distance between pixels	$pixel$
ΔH	Transition heat	J
$\Delta P/t_{min}$	pressure per minute	Pa/min
$\Delta P/t_{sec}$	pressure per second	Pa/s
Δt	Time step size, inter-frame time	s

Δt_{char}	Characteristic time	<i>s</i>
Δx	Cell size, pixel displacement distance	<i>m, pixel</i>
ε	Emissivity coefficient	
ε_0	Vacuum permittivity	<i>F/m</i>
η	Viscosity	<i>N·s/m²</i>
ϑ	Scattering angle	
$\theta, \theta_1, \theta_2$	Angle	
λ	Wavelength of the light	<i>m</i>
λ_e	Electrons' mean free path	<i>m</i>
λ_m	Mean free path	<i>m</i>
μ_f	Fluid's viscosity	<i>Pa·s</i>
v	Drift velocity	<i>m/s</i>
ξ_T	Total collision cross-section	
ρ	Density	<i>Kg/m³</i>
σ	Cross-section, Stefan-Boltzmann constant	<i>m²</i>
σ_α	Standard deviation	
τ_p	Relaxation time	<i>s</i>
ϕ	Work function	<i>eV</i>
φ	Azimuthal angle	
ω	spin speed	<i>RPM</i>

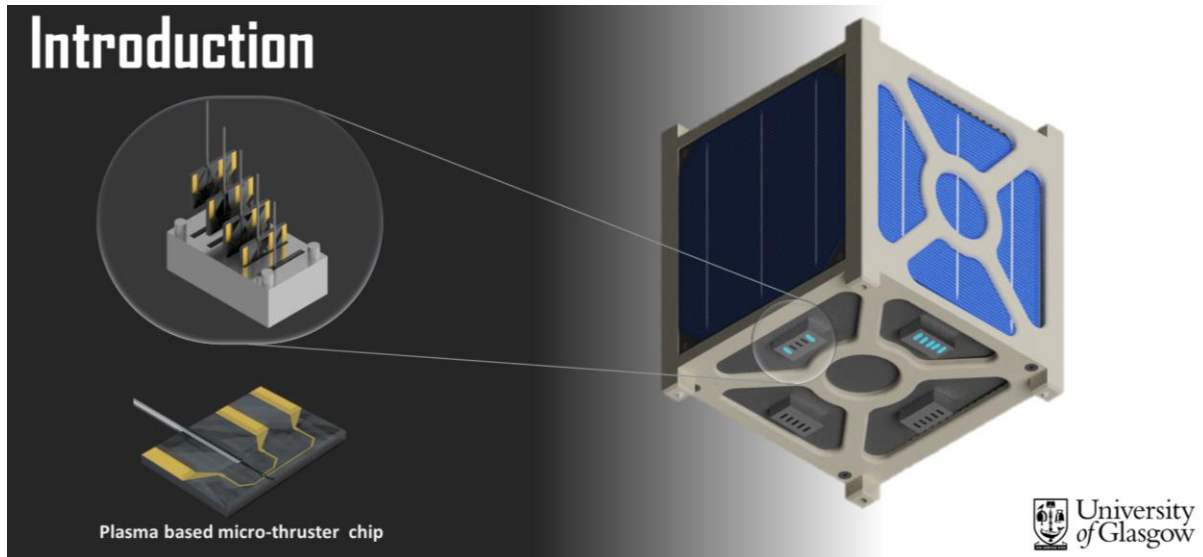
Abbreviation

ALD	Atomic layer deposition
C4F8	Octafluorocyclobutane, perfluorocyclobutane
CEFR	Conformal-evaporated-film-by-rotation
DNQ	Diazonaphthoquinone
DRIE	Deep reactive ion etching
DSIE	Bosch Deep Silicone Etching
DSMC	Direct Simulation Monte Carlo
EBL	Electron beam lithography
FEED	Field-emission electric propulsion
JWNC	James Watt Nanofabrication Centre
LEO	Low earth orbit
MEMS	Micro-electromechanical system
MPDA	Micro-plasma Discharge Algorithm
OAD	Oblique-angle deposition
PPT	Pulsed plasma thruster
PR	Photoresist
PTFE	Polytetrafluoroethylene
PVD	Deposition methods as physical vapor deposition
RIE	Reactive ion etching
SF6	Sulfur hexafluoride, sulphur hexafluoride
Si	Silicon
SIO	Silicon-on-insulator
SPM	Solid propellant micro-thruster

Publication List

- Guevara Jelid, H. I. White, C. and Kontis, K. "Development of a novel DC micro-discharge controller on dsmcFOAM+ for plasma effect in DSMC flow profile simulations." *Advances in Space Research*. (accepted - Manuscript number AISR-D-22-00343R1.)

Chapter 1



1.1. Motivation

The increased interest in reducing the size of satellites as a result of the introduction of micromachining and micro-electromechanical systems (MEMS) fabrication techniques have allowed the space community to find new ways to significantly decrease the overall life-cycle cost by reducing manufacturing resources [1] [2]. It falls within the purview of government agencies and commercial sectors [2] due to its fewer components and mass production processes. Compared to larger spacecraft, the small satellite community has low costs and average power requirements of less than 150 watts in low earth orbit (LEO) and a cost of less than £4 million. In addition, using non-toxic propellants reduces the technical risk associated with the logistics of transfer and handling at the launch site.

The classification of the next generation of small satellites is based on their masses: 0.1 to 1.0 kg for picosatellites and 1.0 to 10.0 kg for nanosatellites [3]. Where the weight and size of each component is critical for the mission, including the propulsion system, where thrust ranges becomes in proportion of the size (between nN to mN). Therefore, according to the nanosatellite mission specifications, the small propulsion systems currently use are implemented for orbital manoeuvres to counteract the effects of trajectory deviations and fine attitude control [4]. Consequently, there are several possibilities for supplying propulsion. Cold-gas thrusters offer a lower approach of the efficiency consumption of the propellant by the thrust generated, also known as specific impulse [5]. In

Chapter 1. Introduction

comparison to electric propulsion systems, also known as plasma propulsion systems, which have the capacity to have up to a hundred times the specific impulse of a cold gas thruster. Enabling the continuation of deep space exploration with a new generation of spacecraft and propulsion technologies [6] to provide thrust with a more efficient propellant consumption that allows us to travel further.

In order to discover a more reliable thruster solution, this research attempts to create a plasma-based micro-thruster chip device [7]. Due to their capacity to be downsized to produce MEMS that generate thrust, chips are an ideal option for the development of a micro-propulsion system. Combining electrostatic and cold-gas operation into one hybrid propulsion system, increases the adaptability of the thrust control and power consumption in accordance with the needs of the mission by turning on or off the current via the electrodes. It was thought that when the current was turned on, the electrodes would likewise get a high voltage between 200 and 1200 volts, which would ionize the gas passing between them. As a result, the ions will be accelerated toward the nozzle's exit, increasing the thrust, due to the electric field created by the location of the electrodes. As a result, the ions will be accelerated toward the nozzle's outlet, increasing the thrust, due to the electric field generated by the location of the electrodes. The capacity to control the propulsion should be possible if the ion density increases or decreases in accordance with changes in the electric power being provided. It is expected that while switching from cold gas to electrostatic mode, ionization would boost thrust while using the same quantity of propellant, and as a result, the specific impulse performance will be greater than the cold gas performance. Furthermore, this project focuses on the development of the thruster component of the propulsion system, whereas the neutraliser for the electrostatic mode, the power processing unit (PPU), the propellant tank, and the feeding system are not covered in this study.

Since the James Watt Nanofabrication Center (JWNC) and the Aero-science facilities will be used to fabricate and characterise the thruster, this will be the first time in the history of the Aero-science Division that a micrometer-scale thruster will be developed. The initial challenges of the project involved understanding the micro-plasma effect through computational simulations in order to comprehend how it interacts with gas flow on the macroscale (velocity, temperature, and pressure) as well as how the location of electrodes affects the speed at which ions and neutral gas particles move towards the micronozzle's outlet. The quantum concerns, such as the field emission and enhancement factor of the electric field provided by the micrometer distance between the electrodes, were thus not taken into account by the codes that were available. Where a modification of the dsmcFOAM+ solver's algorithm that replicates the acceleration of flow caused by the micro-plasma phenomenon described in Chapter 3 was developed. The positioning of the electrodes was chosen to provide a balance between the highest thrust and the lowest rise in temperature in order to avoid its

Chapter 1. Introduction

over increase, which could result in the sublimation of the electrodes material, once the computational results had provided more information about the theoretical performance of the effects of the suggested electrodes configuration.

The design of the micro-thruster chip was idealized with dimensions of 5 mm x 7.4 mm x 0.75 mm, as specified in Chapter 4. This was done after the position of the electrodes was determined in Chapter 3. For a better understanding of the theoretical performance in temperature and thrust of the micro-thruster chip, additional simulations were run to determine the geometry and size of the micro-nozzle for the cold gas mode as well as in electrostatic mode when the electric power is applied through the electrodes from 0.001W to 1W. Taking into account the electrodes' electric routing's shape, route, and size in order to connect them to a microSD card connector.

Once the design was acquired, the nanofabrication process for the development of the micro-thruster chip was specified based on the availability and capabilities of the equipment inside the JWNC detailed in Chapter 5. where an innovative method was used to fabricate a 100 μm trench pattern with SPR-220 photoresist for the deposition of gold for the electrical routing of the micro-thruster.

During this work, the characterisation of the micro-jet velocities emerging from the chip in the cold gas mode was attempted utilizing the particle image velocimetry technique. Even with the development of a micro-calibration sheet to calibrate the camera to increase the capabilities of the current setup, it was impossible to fully characterise the micro-jet particle velocities due to equipment limitations. More information about the test and the results obtained are shown in Chapter 6. For the short time left after the cold gas test to present this work, the characterisation of the electrostatic mode is planned to be for future work.

More details of this general overview are commented through the present document.

1.2. Aim

This project aims to develop a DC plasma-based micro-thruster chip for the micro-propulsion systems used in nano and pico-satellites, enabling high precision manoeuvring operations in low Earth orbit (LEO) or in the space environment, with thrust ranging from nN to mN. In addition, contribute to understanding plasma processes in microgaps as a source of thrust generation under vacuum conditions. . It is important to emphasize that the present project focus on the micro-thruster development, where the neutraliser designing, manufacture and testing will be assigned for a future work.

1.3. Project goals

Consequently, the following goals were set:

- Create a novel hybrid design plasma-based micro-thruster chip , as it shown in Figure 1-1, which can work in two modes: as a electrostatic thruster and as a cold-gas thruster.
- Standardise a portable chip size and shape to have interchangeable micro-thruster configurations to produce thrust for the micro-propulsion system based on mission requirements.
- Maintain a 2-dimensional geometry for the shape of the micro-thruster chips.
- Easy-to-handle design, allowing for electrical and pneumatic connectors to commercial off-the-shelf (COTS) components.
- Provide a controlled thrust range of nN to mN.
- Nanofabrication of an in-house micro-thrusters chip at James Watt Nanofabrication Centre (JWNC).
- Design, built and commission rig for testing the micro-thruster chip.
- Characterisation and testing of microdevice using particle image velocimetry(PIV).

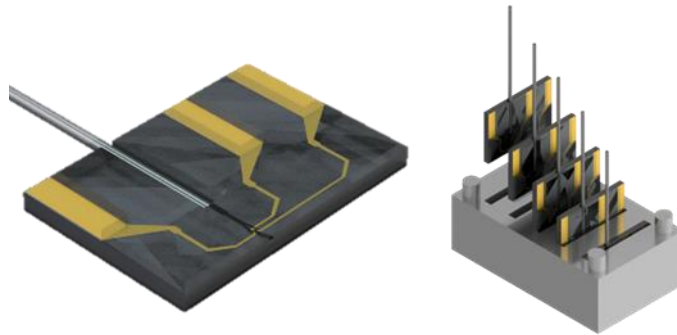


Figure 1-1. Prototype concept of the DC plasma-based micro-thruster chip.

1.4. Micro-thruster chip operational description

The micro-thruster chip is a rectangular chip with dimensions of 5 mm x 7.4 mm x 0.75 mm. A microtubing channel (Figure 1-2) is etched into the chip, where a needle is placed to supply/inject the gas propellant into the device. The propellant then flows into a micro-plenum to increase the gas volume, thereby providing a continuous flow in the subsequent sections. The gas flow is divided by an inverted triangular structure, with an anode electrode situated at the base of the triangle. On the opposite side, there are two cathode electrodes with a neck channel in the middle. The neck wall's thickness reduces the likelihood of altering the outlet dimensions due to plasma degradation, which could otherwise change the micro-thruster's performance. The neck channel then connects to a divergent nozzle, which expands and accelerates the gas flow.

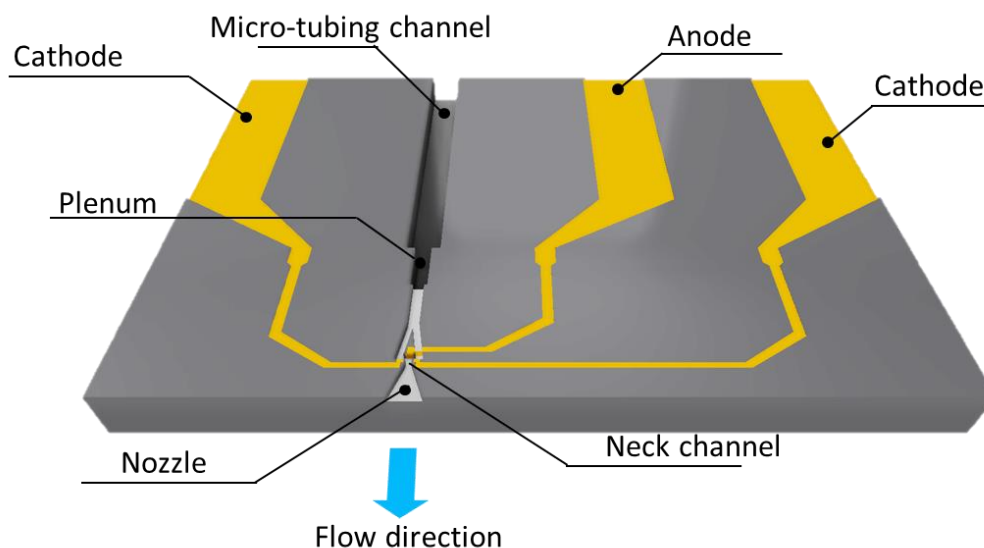


Figure 1-2. Sections that compose the micro-thruster chip

The electrode pins are connected to a microSD pin connector to a power source. Therefore, the micro-thruster chip can operate in two modes: 1) cold gas mode and 2) electrostatic mode.

Cold gas mode: In this mode, the flow passes from the needle through to the nozzle without powering the electrodes, so the thrust generated comes solely from the expansion of the pressurized gas in the nozzle.

Electrostatic mode: In this mode, the propellant/gas follows the same path toward the electrode region. The electrodes are powered to create a discharge, ionizing the gas and increasing the flow's temperature. The cathodes, located closer to the neck channel, accelerate the ions toward the nozzle, imparting more energy to the flow. This additional energy increases the thrust as the gas expands in the nozzle.

1.5. Contributions / objectives

The plasma-based micro-thruster chip is the first microdevice manufactured in the JWNC by Aerospace Division. As a result, no prior work or experience with tangible microfluidic devices has been conducted within the department. Several publications on plasma interaction on flow are based on macro-scale effects [8] [9] [10], but not on micro-plasma interactions, such as the field emission effect, that require quantum considerations [11]. Additionally, this project is based on the thruster component without the designing and manufacture of a neutraliser, where will be set for a future work. Consequently, the following are the most significant contributions of this work:

- Creation of a micro-discharge algorithm using the dsmcFOAM+ solver from the OpenFOAM platform. To obtain a design for the micro-thruster chip prototype, it was necessary to first model the micro-plasma interaction with the flow to establish the location of the electrodes and comprehend how the thrust varies as the micronozzle geometry is altered. Few solvers, including pdFoam [12], PICLas [13] [14], and DRACO [15], can simulate the interaction between ions and gas flow. These options are, unfortunately, computationally expensive, necessitating the development of new code.
- Design and nanofabrication of a novel plasma-based micro-thruster chip prototype with a size of 5 mm x 7.4 mm x 0.75 mm (Figure 1-3) which can be easily connected to a microSD card's electrical connector.
- Maintain as few bonding or assembly elements as possible throughout the microfabrication process to reduce the risk of gas leakage from non-contact locations (delamination, kissing bond, disband). Incorporating nonmagnetic components prevents the accumulation of contaminants (space dust) that can compromise the integrity and performance of the micro-propulsion system and nanosatellite.
- Conformal deposition of 500 nm-thick Au (gold) through a 100 μm trench using SPR220-7 positive photoresist and physical vapour deposition (PVD).
- Design of rig for testing micro-thrusters using a series of experimental techniques.
- Identification of the TSI time-resolved particle image velocimetry (PIV) system limitations and even that their capabilities were expanded to be utilized for microfluidics characterisation by creating and fabricating a calibration sheet for camera alignment. In order to provide the system with the ability to characterise the velocity profile of the flow ejected from the outlet of the micro-thruster in cold gas mode. It was able to capture particles with velocities of up to 12 m/s, which was a significant advancement but not enough for the whole jet velocities profile of the micro-thruster.

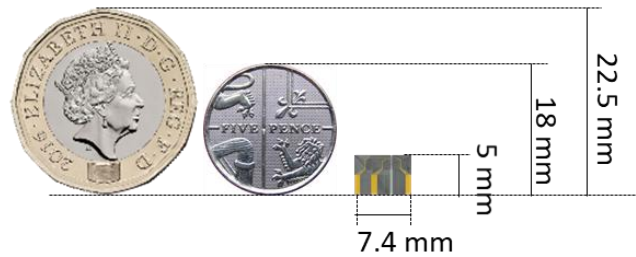


Figure 1-3. Micro-thruster chip size comparison.

1.6. Thesis outline

In Chapter 2, a short introduction to plasma phenomena is provided, along with the current state of the art on micro-thrusters for CubeSats, including an analysis of the propellants and how the thrust is determined.

In Chapter 3, the direct simulation Monte Carlo (DSMC) method is utilised to develop an algorithm for simulating the impact of DC micro-plasma on a flow. To investigate the micro-plasma contribution to thrust in simulations of micro-fluidic channels exposed to space/vacuum environments, a novel micro-discharge controller based on OpenFOAM's dsmcFOAM+ solver was developed. During the vacuum field emissions effect for the micro-plasma simulation, the rarefied gas flow was solved with the DSMC method, and the Fowler-Nordheim equation was utilised to calculate the ionic current density, avoiding the need for a significant increase in computational power during a DSMC simulation.

In Chapter 4, an analysis of electrical current and high voltage is performed for plasma formation. Then, a heat transfer analysis is performed based on the electrodes' size, shape, and location within the proposed micronozzle design. As a result, a 5mm x 7.4mm x 0.75mm plasma-based micro-thruster chip prototype that can be easily coupled to a high voltage source via a microSD card connector was developed.

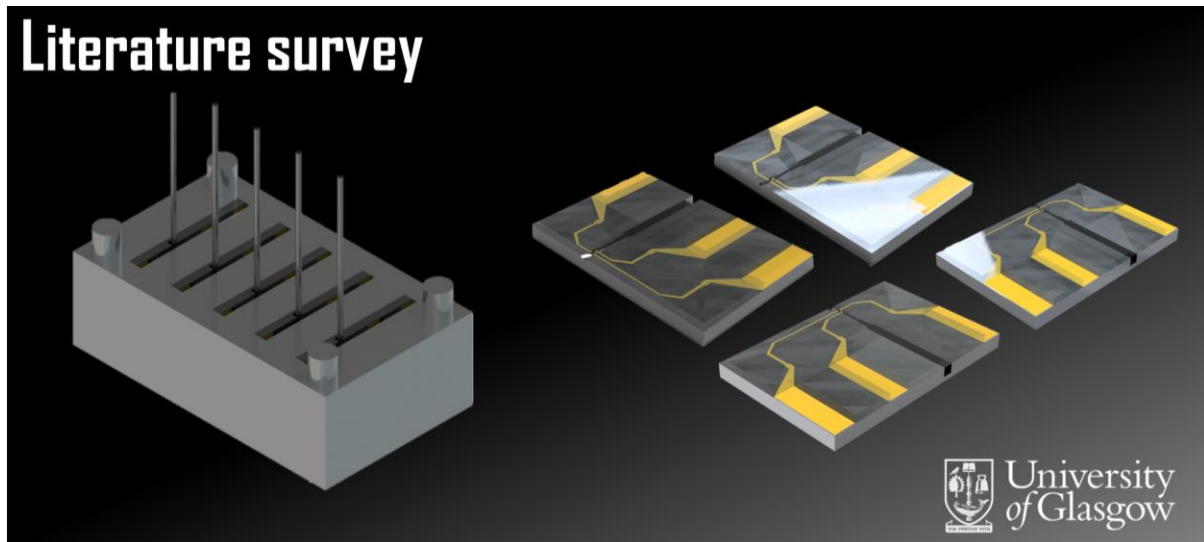
In Chapter 5, the nanofabrication process of the plasma-based micro-thruster chip prototype is described using photolithography, wet etching, dry etching, plasma-enhanced chemical vapour deposition (PECVD), and physical vapour deposition (PVD) processes at the James Watt Nanofabrication Centre (JWNC).

In Chapter 6, the velocity profile of the flow jet exiting the outlet of the micro-thruster chip was intended to be characterised on cold gas mode by using particle image velocimetry (PIV) and a mass flow rate analysis to intent to calculate the thrust of the device. Including equipment limitations, and their analysis of the outcomes.

Chapter 1. Introduction

Chapter 7 concludes with a discussion of the significant achievements of the research presented in this thesis and future work based on these findings.

Chapter 2



This chapter provides a high-level introduction to the topic of plasma, which is central to the idea behind the micro-thruster chip's design and development. Topics covered include the current state of the art of electric micro-propulsion systems (to which the chip is a part) and the effect of propellants on plasma performance. Before discussing plasma-based micro-thrusters, it is essential to comprehend that there are two types of plasma: 1) Thermal plasma is a hot, highly ionised gas with an equal number of free positive and negative charge carriers (quasi-neutral). 2) Non-thermal or cold plasma, on the other hand, is a less ionised gas with an unequal number of free positive and negative charge carriers. In both cases, thermal energy in excess of a certain number of electron volts is required to ionise these particles in a gas [16].

2.1. Plasma

Cold plasma refers to plasma in which most of the coupled electrical energy is predominantly routed to the plasma's electron portion, producing energetic electrons rather than heating the entire gas stream. In the meantime, the plasma ions and neutral components are at or near ambient temperature. Energetic electrons drive cold plasma chemistry with no visible rise in gas enthalpy. The temperature of the electrons can be several orders of magnitude higher than the temperature of the heavier particles. Because the ions and neutrals are relatively cold, these plasmas do not cause thermal harm to the surfaces with which they come into contact.

Table 1. Comparison of thermal and cold plasmas [17].

Parameter	Thermal (LTE)	Non-Thermal (non-LTE)
Thermodynamic equilibrium	Reaches local thermodynamic equilibrium	Does not reach local thermodynamic equilibrium
Pressure (atm)	Low pressure to several atmospheric	Typically, low pressure or close to atmospheric
Electron density (cm ⁻³)	High electron density of the order of (10 ¹² -10 ¹⁹)	Low electron density (10 ⁸ -10 ¹³)
Electron Temp. (eV)	≈ 1 – 2	≈ 1 – 10
Electron, ion and gas temperature	$T_e \approx T_i \approx T_p \leq 2 \times 10^4 K$	$T_e \gg T_i \approx T_p = 300 \dots 10^3 K$ $T_e \leq 10^5 K$
Typical sources	Arc plasmas, plasma torches, RF inductively coupled	Glow, corona, DBD, MHCD
Energy source	Electrical, nuclear	Electromagnetic radiations

Four main factors (Figure 2-1) must be considered for gas ionisation: 1)current, 2)voltage, 3)gap distance, and 4)pressure.

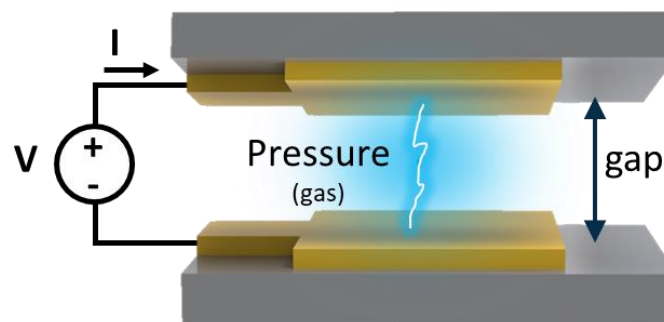


Figure 2-1. Main parameters for breakdown voltage on parallel electrode plates

1) As depicted in Figure 2-2, depending on the applied voltage V , multiple electrical discharge regimes are available for plasma formation over a broad range of electrical current I values. According to the literature [18] and [19], the current range for detecting plasma formation on micro-devices is between 10^{-6} and 10^{-2} amperes. The ionisation must be within the visible spectrum (plasma luminescence), and the electron energy and number density are sufficient to emit visible light via excitation collisions,

enabling the camera to identify the breakdown voltage and plasma events during the characterisation step.

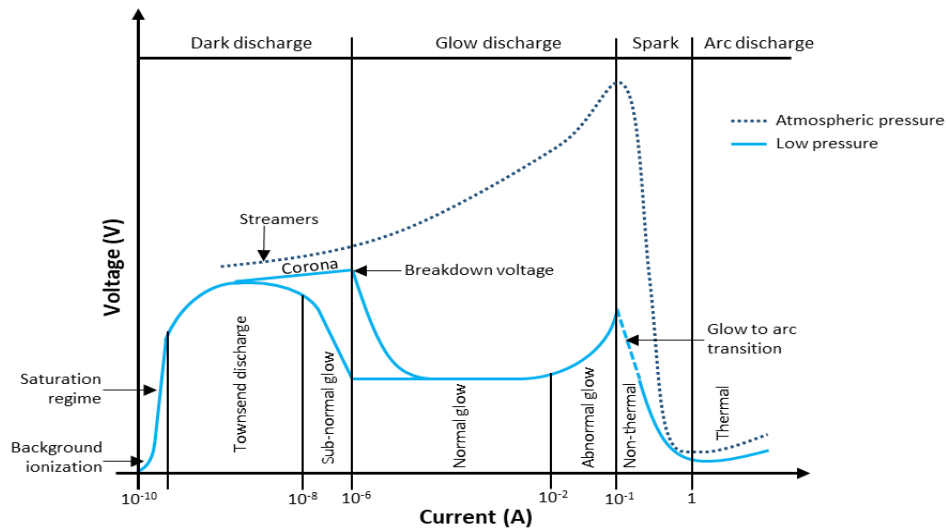


Figure 2-2. Gas discharge regimes characterised by their current density-voltage curves, adapted from [18] [19].

It is proposed that the device operates in the range of 10^{-6} to 10^{-2} A. This assumption seems to be based on gas breakdown detection rather than intended thrust of the system. These operational parameters need to be supported by a deep understanding about basic technical principles and physics governing the performance of micro-thrusters.

Firstly, this current range selection ensures efficient ionization of the propellant gas. Propulsion depends on ionisation for both cold gas and plasma thrusters. Since the amount of charged particles available for acceleration is determined by the efficacy of ionization, it directly affects the thrust produced. Therefore, current ranges between 10^{-6} to 10^{-2} A allows the control and sustain of the ionization process, which is essential for maintaining a steady thrust output.

Secondly, gas breakdown within this current range serves as a consistent measure of thrust. Gas breakdown is an important step in plasma formation because it shows the propellant transition from neutral to an ionized state. By monitoring this parameter, the thruster can be able to maintain uniformity in terms of thrust performance during ignition.

Additionally, power limitations and thermal constraints needed on the micro-thrusters are defined by these ranges of currents used. If operating current exceeds 10^{-2} A then there might occur too much heating up (heat transfer) which may eventually damage thrusters. While anything less than or equal to 10^{-6} A will not sustain enough ions thereby resulting into low thrust performances. Therefore, this

current range involves a trade-off between the ionization efficiency, the thermal stability, and the power consumption.

In conclusion, the assumption that the micro-device operates between 10^{-6} to 10^{-2} A comes by considering the need to achieve efficient ionization of the propellant, ensuring a reliable detection of gas breakdown, and the consideration of the thermal restrictions and power constraints. This current range parameter is very critical in achieving desired thrust performance as well as ensuring long-term reliability of micro-thrusters. Further experimental validation and theoretical analysis will be undertaken to confirm the suitability of this current range for the specific thrust requirements of the system.

2.1.1. Breakdown current considerations

The relationship between current and micro-gap size is a critical area of study in various technological fields. Researchers have explored the electrical breakdown behaviours in microgaps, which can provide valuable insights into this phenomenon. One key finding is that the current is 1.6 times greater in micro-gap environments compared to larger gaps [20]. Several causes leading to increased breakdown currents in microgaps have been investigated by researchers [21].

Firstly, electron field emission from cathode surface is one major cause for breakdown at microscale. As the size of the gap decreases the becomes electric field stronger at cathodes, resulting into very high levels of electron emissions. This enhanced electron emission can then initiate and sustain the breakdown process, resulting in the observed higher breakdown currents[150].

Additionally, the dynamics of ion generation and movement within the microgap also contribute to the increased breakdown current. The high electric fields in the microgap can lead to efficient ionization of the gas molecules, and the resulting positive ions can further enhance the field emission at the cathode, creating a positive feedback loop that sustains the breakdown.

Moreover, the unique geometry and surface characteristics possessed by electrodes in microgap can also influence the breakdown phenomenon. The surface roughness, material properties, and local field enhancements at the electrode edges or protrusions can all play a role in the breakdown process and contribute to the increased current observed [22][150].

The research community has made significant progress in understanding the mechanisms behind the 1.6 times current on microgap breakdown. By combining experimental, computational, and analytical

approaches, researchers have gained valuable insights into the complex interplay of electron field emission, ion dynamics, and microscale electrode effects that underlie this intriguing phenomenon [22] [20] [21].

2.1.2. Electron impact reactions

The tables below illustrate the effects of the interaction between electrons and gas molecules/particles during ionisation. Hence, plasma species A , B represent atoms; e represents an electron; M represents a transient collision partner; + or - represent ions; R represents a simple radical (an unpaired valence electron), and P represents a polymer (many repeating subunits). An asterisk (*) indicates an excited species, and $h\nu$ indicates the release of radiation energy; $S - A$ indicates an atom adsorbed to a surface. The subscripts g and s , respectively, represent a species in the gas or solid phases.

Table 2. Gas phase reactions involving electrons [17] [23].

Name	Reaction	Description
Elastic collision	$e + A \rightarrow e + A$	Impact with no kinetic energy loss
Excitation of molecules	$e + A_2 \rightarrow A_2^* + e$	Impact of electrons of sufficient energy with heavy targets
Excitation of atoms	$e + A \rightarrow A^* + e$	lead to electronically excited states of atoms/molecules.
Ionization	$e + A_2 \rightarrow A_2^+ + 2e$	Energetic electrons can ionize atoms/molecules through
	$e + A_2 \rightarrow A^+ + A + 2e$	electron detachment and form positively charged species
	$e + A \rightarrow A^+ + 2e$	
Dissociation	$e + A_2 \rightarrow 2A + e$	Inelastic electron impact causes dissociation of molecules
	$e + AB \rightarrow A + B + e$	without the formation of ions
Dissociative ionization	$e + AB \rightarrow A^+ + B^- + e$	Negative ions can also be produced by dissociative
	$e + AB \rightarrow A^+ + B + 2e$	ionization reactions

2.2. Technological overview of the micro-thruster chip

Chapter 1 describes a thruster prototype that relies on a specific discharge. The process of such discharge involves a low-temperature plasma, where electrodes are subjected to potential difference causing breakdown of the neutral gas which creates plasma. This discharge is classified as glow discharge which is typical in many micro-propulsion systems because it ionizes the working gas at low pressures effectively.

2.2.1. Discharge characteristics

The voltage-current relationship across the plasma indicates different phases of discharges known as Townsend at low currents and then transition into glow mode with increased current. In order not to destroy micron sized parts due to high heat levels produced when an arc discharge occurs instead of sustaining glow discharges within this region should apply only those voltages which lie between them.

2.2.2. Ionization processes

Within cascade collisions and electron impact ionizations are main processes through which ions get formed in the micro-thruster chip prototype. On entering into discharge space neutral gases collide with electrons accelerated by electric fields but this knocks off other atoms' or molecules' electrons thereby creating more positive ions together with extra free electrons.

Due to collisional multiplication effect whereby charged particles multiply exponentially leading to sustainable plasmas; majority step being mostly affected during these events is primary ionisation or else called electron-impact-ionisation where very high speed moving electrons give away some energy required for overcoming ionization energy thus forming additional negative charges (electrons) plus positive charges (Ions).

With respect of the efficiency of ionization in the micro-thruster chip, it directly influences the thrust performance. If more atoms are positively charged then there will be more particles with charge in them which can be effectively accelerated by electric field in electrostatic mode thus creating thrust.

On the other hand if such levels are not achieved, interaction between neutrals and ions becomes important where neutral species acceleration becomes less efficient resulting into lower overall thrust. Large number of uncharged atoms might also have an effect on directed energy loss through charge exchange collisions between neutrals and ions leading to decrease in efficiency of thrust production.

2.2.3. Relevance to plasma processes

Table 1 and Table 2 given within this chapter talk about various plasma processing steps applicable for micro-thrusters like ionization or charge exchange.

These processes are key for determining how well a cold gas or electrostatic mode thruster works. Knowledge about this kind of plasma and finding ways of making it function better are important steps towards improving the performance of different types of thrusters in various environments, mainly for chapter 3 during the developments of a micro-plasma discharge algorithm.

2.2. Micro-propulsion system for CubeSats

It is very important to talk about plasma micro-thrusters because it is the centre of technology in this study. The investigation aims at developing new plasma technologies for micro-thrusters design and efficiency improvement where these systems have been given prominence. By looking into what already exists in terms of technology, we can find out points that need to be filled or improved thus guiding us on how best we can come up with a different chip for micro-thruster. Literature review has great relevance in any research work and in this case it cannot be ignored since what is being done is creating a propulsion system that is compact enough for small satellites. There are two things which must be taken into account here; firstly current trends should be understood alongside challenges facing miniaturization of such devices so as to know why our proposed study matters most thereby underscoring its potential contributions towards the field.

Thus, in order to explore existing micro-thruster systems, it is needed to introduce the categorisation of the thrusters based on the conventional state of matter of the propellant. Scharlemann, C., et al. [24] classify propulsion technologies as chemical, cold gas, and electrical. Within this final branch, Takao et al. [25] propose one of the most detailed classifications for micro-electric propulsion devices, dividing the systems by comparing the propellant with the type of principal source of acceleration they employ: electro-thermal, electromagnetic, and electrostatic accelerations. To gain a broader perspective and identify the existing micro-propulsion mechanisms for nanosatellites, the following diagram on Figure 2-3 was created.

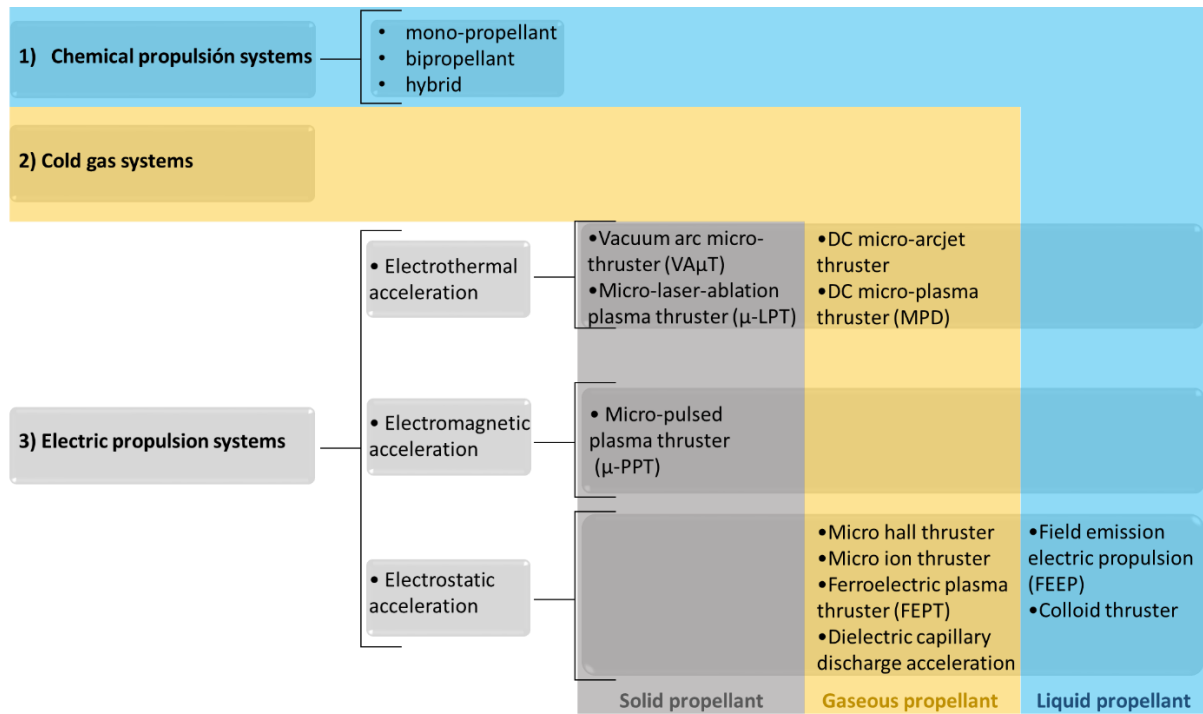


Figure 2-3. Micro-propulsion classification.

2.1.1. Electrothermal thrusters

Electrical power is originally utilised to heat propellant in a chamber in electrothermal devices. The propellant is expanded for acceleration using a converging/diverging nozzle [26]. Some types of micro-thrusters fall under this category: micro resistojets, arcjet thrusters, solid propellant micro-thrusters, liquid monopropellant micro-thrusters, and electrothermal plasma micro-thrusters.

i. Electrothermal plasma micro-thruster

The electrothermal plasma micro-thruster is becoming an attractive option due to its small volume, low cost, and lightweight. Argon (Ar) is a gas propellant requiring less than 10W to generate thrusts of the order of mNs and specific impulses of up to 85s. Radiofrequency (RF) or microwave radiation is typically used to generate thrust, and the heat generated by such a discharge process is used to heat the propellant. Collisions of charged particles and ambipolar plasma flow heat the gas, resulting in an electrothermal thruster [27].

Takahashi et al. [28] created a microwave electrothermal thruster (METs) that consists of a converging-diverging micronozzle of a 1mm quartz plate connected to an axis-aligned rod antenna shown in Figure 2-4. The metal rod antenna is encased in a dielectric envelope that produces high-

temperature plasmas at atmospheric pressures—accepting Ar flow rates between 10 and 70sccm at a maximum input power of 6W to generate 0.2mN to 1.4mN thrust and 50s to 80s specific impulses.

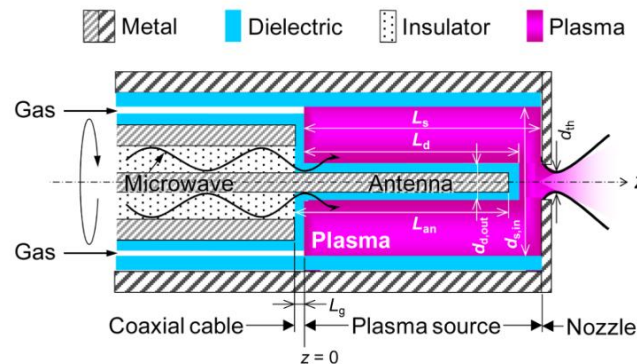


Figure 2-4. Schematic of the microwave electrothermal thrusters (MET) device [28].

ii. Arcjet thrusters

A direct current is supplied between two electrodes (Figure 2-5) of opposite polarity at either end of a constricting tube to generate a longer electric arc, thereby heating the propellant to increase its velocity through a diverging nozzle [29]. A high voltage between 1 kV and 4 kV ignites the arc, decreasing to 30 V to 50 V for low operating mode or 80 V to 160 V for high working mode. Arcjets typically offer four power levels, ranging from extremely low (100–300 W) to high (30–200 kW) [30]. Since an arc can generate significantly higher temperatures than a heating coil, arc jets are comparable to chemical thrusters and typically have three times the specific impulse of chemical rockets [31].

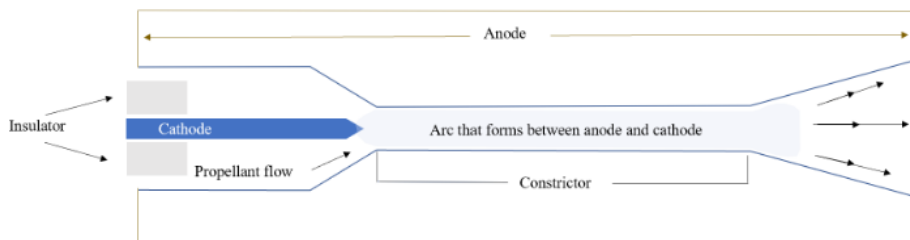


Figure 2-5. Schematic of an arcjet thruster [30].

Recent experiments have demonstrated that increasing propellant flow and decreasing throat diameter decreases the arc root transfer process, thereby increasing its lifetime [32]. Current arcjet research focuses on using different propellants, reducing erosion to increase durability, and

developing alternative designs to enable greater thrust forces. The most frequent occurrence of electrode and nozzle throat ablation is during startup [30].

Hydrogen arcjets with high power were studied for primary propulsion applications such as orbit transfer. Efforts were made to develop hydrogen arcjet thrusters in the early 1960s; Giannini Scientific Corporation [33] produced a 30 kW hydrogen arcjet with a 1000s impulse. The design extensively used regenerative heat transfer, which heated the thruster body and nozzle walls to prepare incoming propellant for injection into the arc. The design also incorporated an anode attachment zone for the mixing chamber immediately upstream of a diverging nozzle. This effort promoted the reassembly of dissociated gas molecules to reduce frozen flow losses.

Horisawa et al. [34] microfabricated an 800 μm x 100 μm x 1200 μm rectangular micro-arcjet nozzle on a quartz plate. Each anode had a 100 nm thick Au layer deposited on a divergent section of the nozzle. Also deposited on the inner wall surface of the cathode was an Au film. In this example, a constrictor section of the nozzle was electrically shielded to maintain high voltage mode discharges. Mass flow of 0.4 mg/sec of N₂, discharge current of 20 mA, 430 V (input power of 8.6 W, or specific power of 8.6 MW/kg), and plenum pressure of discharging chamber of 50 KPa produced a specific impulse of 147s [34].

iii. Solid propellant micro-thruster

Zhang et al. developed a planar solid propellant micro-thruster (SPM) with dimensions of 2200 μm x 1000 μm x 650 μm that contains a convergent-divergent micronozzle linked to a combustion chamber and an ignition slot fabricated on a silicon wafer and bonded to a glass layer via anodic bonding at 400°C and 1100 V (Figure 2-6). HTPB/AP/AL (adding aluminium) was selected as the solid propellant with an estimated thrust range of 0.76 mN to 4.38 mN and a total impulse of 1.16×10^{-4} Ns to 4.37×10^{-4} Ns at sea level and 1.25×10^3 Ns to 1.70×10^3 Ns in space [35]. The defining characteristic of an SPM with a planar structure is that all micro-thruster components are integrated on a single wafer, thereby minimising fabrication and bonding processes. In contrast to SPMs with vertical structures, the shape of the micronozzle can be easily altered to meet varying needs [36].

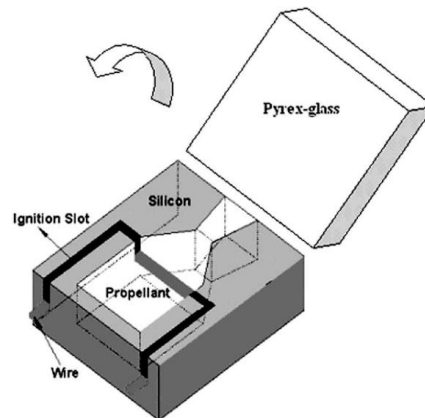


Figure 2-6. Schematic of a planar solid propellant micro-thruster (SPM) [35].

The 7 x 1 SPM array fabricated by Chaalane et al. [37] is another example of planar SPM structures (Figure 2-7). It consists of three layers: a silicon wafer layer with a top-side igniter and a micromachined nozzle, a ceramic (Macor) layer with the chamber extension bonded with the silicon layer, and a glass layer with H70-E epoxy glue. A homemade DB + x%BP solid propellant with a thrust range of 0.1 mN to 3.5 mN at a 100 μm throat width was utilised [36].

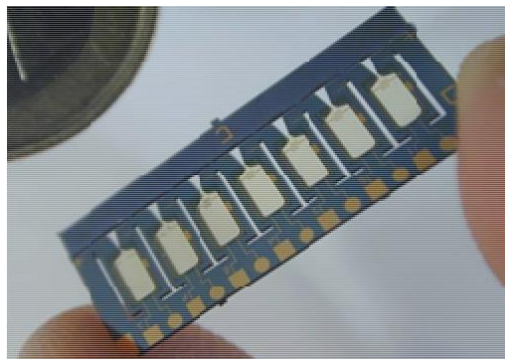


Figure 2-7. 7x1 silicon array micromachined planar SPM [37].

iv. Liquid Monopropellant Micro-thruster with Spark Ignition

Wu et al. [36] developed a spark ignition system by incorporating a pair of metal electrodes within the micro-thruster to make direct contact with the liquid propellant and deposit energy directly into the liquid propellant. As a propellant, hydroxyl ammonium nitrate (HAN) decomposes when a DC voltage of 20 V to 60 V is applied to produce a thrust of 100 mN to 200 mN. Three layers comprise the micro-thruster displayed on Figure 2-8: two for the electrodes, one for the combustion chamber and a micronozzle. The micro-thruster was fabricated using micro-punches in alumina (Al_2O_3)-based ceramics, with a pair of metal electrodes designed on the surfaces facing the micro-thruster chamber [38].

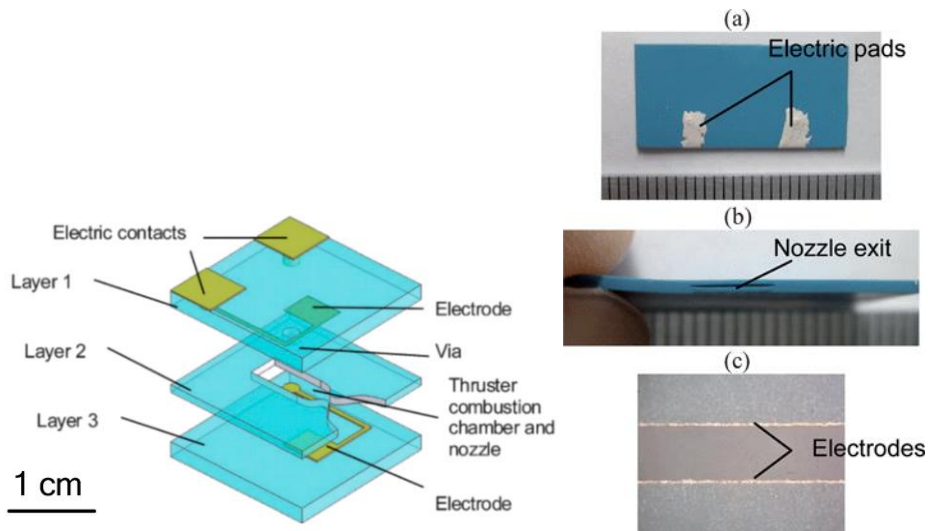


Figure 2-8. Electrolytic micro-thruster design [38].

v. Micro-resistojet

Microresistojet research was conducted at Delft University of Technology [39] as a safe and non-toxic propellant option for CubeSat propulsion systems. At low plenum gas pressure, a silicon heating chamber with a custom-designed silicon substrate was nanofabricated (Figure 2-9) to operate with sublimating solid water (ice). Propeller temperatures of 550 K and 773 K in the heating chamber at 5 bar pressure and a total propellant consumption of 50 g yield respective thrusts of 1.52 mN and 1.48 mN [39].

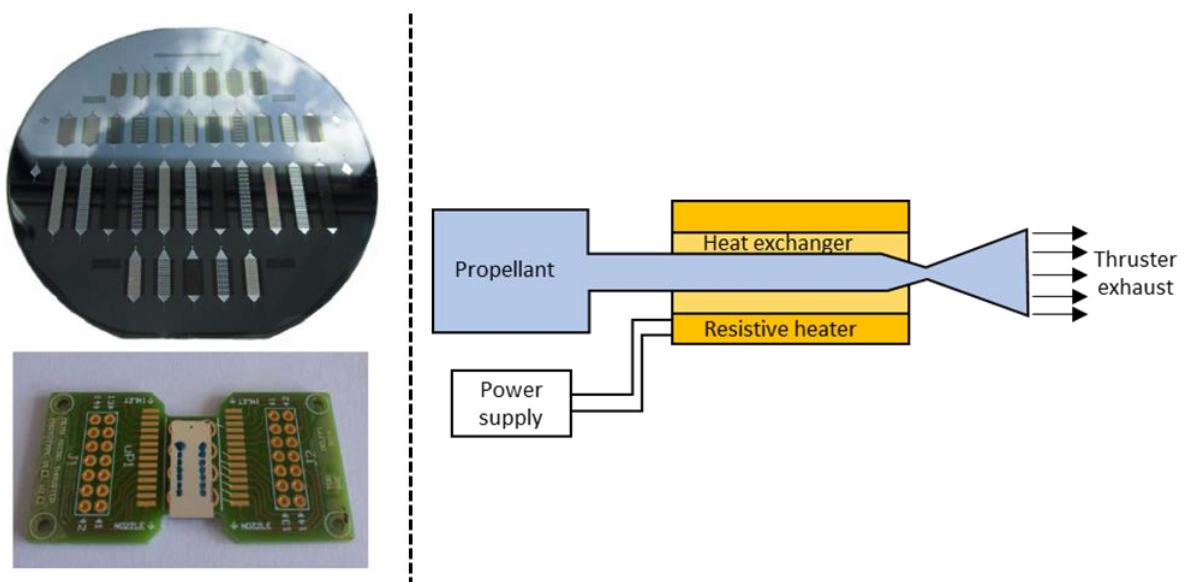


Figure 2-9. The Resistojet diagram is shown on the right side. Left side displays a silicon wafer with several thruster configurations on the top image, and a fully assembled thruster on the PCB is displayed on the bottom image.

2.1.1. Electromagnetic thrusters

Operation is based on the principle of electromagnetic fields interacting with charged particles. Making use of the Lorentz force, which is the force exerted on a charged particle in an electromagnetic field. The working fluid, usually a plasma (a hot, ionized gas), is accelerated by the interaction of electric and magnetic fields. [26]. Consequently, these systems may require greater power levels [30]. The electric field is typically created by electrodes or external power sources, generating a potential difference.

This field accelerates the ions in the plasma. Such as pulsed plasma thruster (PPT) that utilise a magnetic field to accelerate an ionised gas, where a cathode and anode produce the magnetic field at the exhaust nozzle. Thus, an electric current flows to ignite the gas into plasma and eject it, thereby providing the spacecraft with momentum. PPTs have high specific impulses with reduced power consumption and thrust overall. Due to its simple structure, excellent reliability, and low electrical power requirement for operation, polytetrafluoroethylene (PTFE) is commonly used as a propellant in PPTs [36] as early as the design presented by Guman et al. [40]. The AIS-gPPT3-1C Single-Channel Gridded Pulsed Plasma Thruster (Figure 2-10) is a great example of the use of PTFE as propellant from Applied Ion Systems [41]. It has dimensions of 18 mm x 19 mm x 21 mm, a thrust range of 0.22 N - 9.20 N, a specific impulse of 0.65 - 2.3 $\mu\text{N}\cdot\text{s}$, and operating voltage of 2 to 3.5 kV.



Figure 2-10. AIS-gPPT3-1C Single-Channel Gridded Pulsed Plasma Thruster [41].

Pulsed plasma thrusters also employ liquid propellants such as water or alcohol to reduce contamination, an schematic of the thruster is shown on Figure 2-11, low thrust performance, and non-uniform consumption caused by solid propellants (LP-PPT). Kakami et al. [42] created an LP-PPT with a thrust efficiency of 13% by utilising parallel electrodes as an igniter to operate the LP-PPT with a larger electrode gap, reaching 20 J of energy, a specific impulse of 4300s.

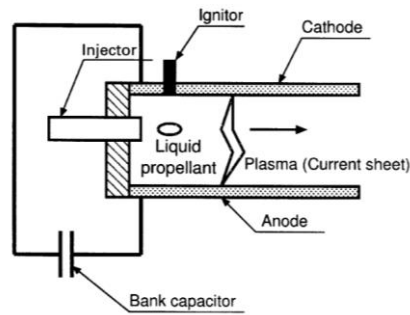


Figure 2-11. Schematic of a liquid propellant pulsed plasma thruster(LP-PPT) [42].

2.2.4. Electrostatic thrusters

Rely solely on the electrostatic forces for ion acceleration. In these thrusters, charged particles (ions) are accelerated directly by an electric field without the involvement of magnetic fields. This acceleration happens due to the Coulomb force, which is the attraction or repulsion between electrically charged particles. [30].

i. Electro spray thrusters

Electrospray thrusters use a charged particle ionic liquid sprayed onto a sharp tip externally or via a capillary. Ions or droplets are accelerated out of the tip with the aid of a static electric field on a metal extraction plate to form a Taylor cone [43]. Multiple Taylor cones are arrayed to form the thruster; the ability to have multiple Taylor cones makes these thrusters customizable [36].

Lenguito et al. [44] designed a multiplexed electro spray (MES) micro-thruster with a $31.1 \mu\text{N}$ thrust (Figure 2-12). The system comprises a nozzle unit and two electrodes, an extractor electrode and an accelerator electrode, with superior interelectrode insulation to maximise the applied voltage. The 37-MES achieved $31.1 \mu\text{N}$ at a voltage of 7.56 kV and an impulse of 1870s, while the 91-MES achieved $65.20 \mu\text{N}$ at a voltage of 7.35 kV and an impulse of 1140s.

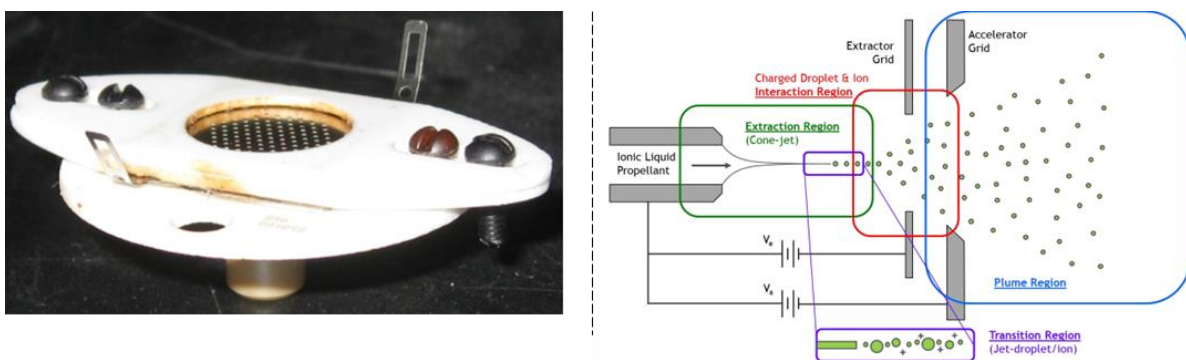


Figure 2-12. Left side shows the $31.1 \mu\text{N}$ electro spray micro-thruster [44]. On the right side the schematic of the electro spray thruster [45].

Martel, F. et al. [46] created one-of-a-kind ion electrospray thrusters (Figure 2-13) with no moving parts and unpressurized tanks containing zero-vapour-pressure liquid propellant with a specific impulse greater than 2500s. Where each Taylor cone weighs approximately one micro-Newton, the compact system consists of modules measuring 12 mm x 1 mm and 2.5 mm in thickness, with emitter arrays fabricated using electrochemical microfabrication techniques and emitter-to-emitter spacing measuring 450 microns, allowing attitude control and precise pointing on CubeSats [46].

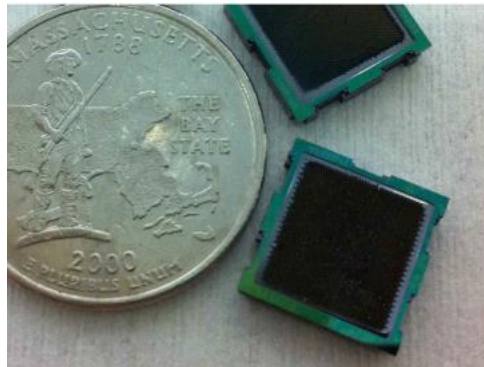


Figure 2-13. ion electrospray thrusters [46].

ii. Gridded micro Ion thruster

Micro gridded ion thrusters (GIT) produce ions by striking a propellant with a high-energy electron beam produced by a direct current (DC), radio frequency (RF), or microwave (MW) discharge [47]. The ions are then ejected through a series of electrically charged grids, a concept proposed for the first time in 1911 [47]. Due to their high atomic masses and ease of ionisation, mercury or cesium were utilised in the early stages of the GIT, despite their toxicity. Xenon, such as that used on NASA's first planetary defence mission, the Double Asteroid Redirection Test (DART) [30] [48], was employed on a newly constructed commercial Power Processing Unit (PPU) [49] to avoid the use of harmful chemicals. Small satellites can escape Earth's orbit by utilising PPU's with greater voltage ranges of 60–160 V at 7 kW of power [50]. Although it performs less efficiently than xenon, iodine is also used as a propellant because it is a safer and more abundant fuel source. Jinghua, Y., et al. [51] presented a 2.3 mN iodine radiofrequency ion thruster (IRIT4) with nominal power of 95.8 W and grid voltages of 1800 V, producing a specific impulse of 2361s shown on Figure 2-14.

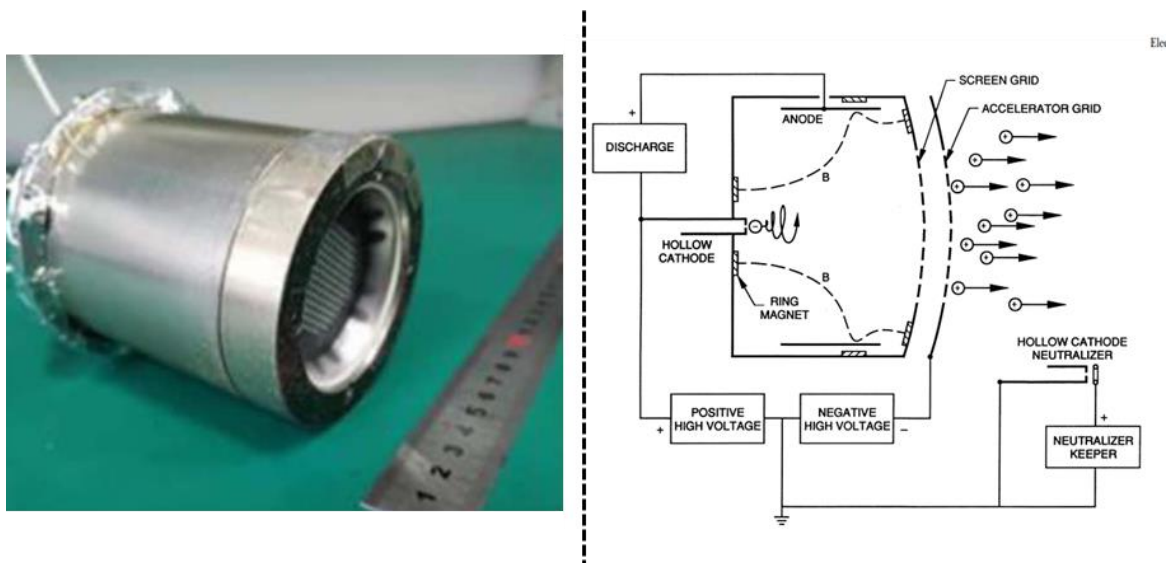


Figure 2-14. Left side shows the IRIT4 thruster [51]. Right side shows the Ion grid thruster schematic [52]

iii. Micro Ion thruster (IIT)

The IIT is a miniaturised version of a conventional ion engine, as it can be observed on Figure 2-15, in which an electron-generated cathode bombards a low-pressure gas discharge. Ions are extracted from the gas discharge and electrostatically accelerated to high velocities, approximately 30,000 m/s, in a set of 1 kV-charged accelerator grids. Currently, the Jet Propulsion Laboratory (JPL) is investigating a micro ion engine with a 3 cm diameter for micro spacecraft. The development of micro ion engines has not yet been conducted. Miniaturizing the subsystems of the device, such as the cathodes, neutralizers, and grids, has presented a number of technical challenges. Each of these subsystems requires in-depth technical research. Due to their extremely high specific impulse of 300 s, micro ion thrusters may be proposed as primary propulsion devices for micro and nano spacecraft. For a high DV requirement, a high level of specific impulse results in a decrease in propellant consumption. IIT could be useful in the field of attitude control for large spacecraft [53].

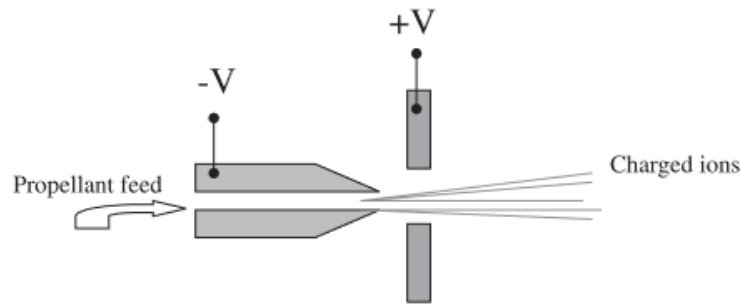


Figure 2-15. Schematic view of a micro ion thruster [53].

When it comes to miniaturisation, there is a gap between plasma thruster chips; the smaller they get, the more attention must be given to their design and performance. Trying to decrease the effects of electrode overheating due to their small volume when high voltage is applied, in conjunction with vacuum environments where materials tend to sublime/evaporate at lower temperatures.

To increase or maintain the device's lifetime during missions, thruster chips with converging/diverging micronozzle [26], combined with a microelectrode circuit, tend to be used as electrothermal thrusters, where the applied current-voltage is sufficient to heat propellant to accelerate it but not sufficient to generate a breakdown voltage (ionisation). Examples include the planar solid propellant micro-thruster (SPM) [35], the 7 x 1 silicon array micromachined planar SPM [37], the LTCC electrolytic micro-thruster design [38], and the microresistojet created by Delft University of Technology [39] where none of them is designed or capable of functioning as plasma thrusters with high enough power to ionise the gas.

Due to the heat and the possibility of sputtering or ablating the thruster's wall during ionisation, small plasma thrusters often do not attain a miniaturisation scale (microscale size), remaining on a centimetre scale. Examples include the microwave electrothermal thrusters (MET) device [28], the arcjet thruster [30], the electrospray micro-thruster [44], the IRIT4 thruster (gridded ion thruster) [51], and the halo hall-effect thruster [54] of ExoTerra.

In addition, the AIS-gPPT3-1C single-channel gridded pulsed plasma thruster (18 mm x 19 mm x 21 mm) [41], and the ion electrospray thrusters (12 mm x 1 mm x 2.5 mm) [46] are the thrusters that reach a micrometre size based on ionisation of the propellant in this survey, with the latter typically being closer in size to the proposed micro-thruster developed on the project goals included designing and fabricating a planar plasma-based micro-thruster chip with a micronozzle and an electrode circuit

as compact as possible without sacrificing the attribute of being easy-to-handle and covering a thrust performance range of nN to mN. The chip prototype is 5 mm x 7.4 mm x 0.75 mm and is used to investigate the micro-plasma effect simultaneously.

2.3. Calculation of the thrust force

Spacecraft use thrust to maintain orbit or manoeuvre. Thrust is produced by a change in the momentum of the propellant. Consequently, the thrust force F of a thruster can be determined by [55]:

$$F = \dot{m}v_e \quad \text{Eq. 1}$$

Being v_e is the effective exhaust velocity and \dot{m} is the mass flow rate. Where m can be determined from the nozzle exit area A_e , the gas density ρ_e and the exhaust velocity v_e , following shown [51]:

$$\dot{m} = \rho_e A_e v_e \quad \text{Eq. 2}$$

2.3.1. For electrostatic thrusters

Electrostatic propulsion systems, rely on the acceleration of ions using electric fields. The thrust F generated by an electrostatic thruster can be calculated using Eq. 1. Thus, the effective exhaust velocity can be determined by the potential difference V applied to the ions and their charge-to-mass ratio $\frac{q}{m}$ [51]:

$$v_e = \sqrt{\frac{2qV}{m}} \quad \text{Eq. 3}$$

Where q is the charge of the ion and m is the mass of the ion. Combining Eq. 1 and Eq. 3, the thrust can also be expressed as [51]:

$$F = \dot{m} \sqrt{\frac{2qV}{m}} \quad \text{Eq. 4}$$

Additionally, the power P required by the electrostatic system is given by [51]:

$$P = \dot{m} \frac{v_e^2}{2} = \frac{F^2}{2\dot{m}} \quad \text{Eq. 5}$$

2.3.2. For cold gas thrusters

Cold gas thrusters use the expansion of a pressurized gas to produce thrust. The thrust F generated by a cold gas thruster can be calculated using Eq. 1. Therefore, the exhaust velocity v_e can be approximated using the thermodynamic properties of the gas, assuming it behaves as an ideal gas from the following expression [56]:

$$v_e = \sqrt{\frac{2\gamma RT}{(\gamma - 1)M}} \quad \text{Eq. 6}$$

Being γ is the specific heat ratio, R is the universal gas constant, T is the temperature of the gas, and M is the molar mass of the gas.

2.3.3. Specific impulse

Additionally, Specific impulse I_{sp} is used to quantify the efficacy of propellant utilization in a propulsion system. It is the quantity of impulse produced by the engine divided by the weight of the propellant necessary to generate that impulse [57]. Specific impulse is calculated to be equal to engine thrust divided by propellant mass flow rate. Therefore, the specific impulse is defined as [58]:

$$I_{sp} = \frac{F}{g_0 \dot{m}} \quad \text{Eq. 7}$$

Being F the thrust, and g_0 is the gravitational acceleration. At a higher I_{sp} , less propellant mass is consumed for a given mission; therefore, a higher I_{sp} is generally preferable. In other words, the engine with the higher value of specific impulse is more efficient because it produces more thrust for the same amount of propellant.

2.4. Propellants analysis

The design of the micro-thrusters must accommodate both the use of gaseous propellants and an electric arrangement, as dictated by the DC discharge requirements, in order to transmit sufficient energy to break apart the gaseous bonds into ions.

Utilizing a gaseous propellant has the advantage of requiring less energy to vaporise. The search for denser gases so that the impulse per unit volume of propellant is maximised. With non-corrosive or

Chapter 2. Literature survey

inert (very low chemical reactivity) characteristics that prevent degradation or corrosion in the micro-propulsion system. Consequently, the essential characteristic of plasma formation is its ionisation efficiency. The following table, derived from the research of Greig, A. [5], Leomanni, M. et al. [59], illustrates some common propellants used in micro-propulsion systems:

Table 3. performance for micro-satellite propulsion.

Thruster Type	Propellant	Thrust (mN)	I_{sp} (s)	Power (W)
Cold Gas	Nitrogen	0.1-5	45-75	-
	Butane	53.00	>60	<1
Monopropellant	Hydrazine	1-4450	162-230	-
	H2O2	1-1.82	100-180	-
Solid Rocket	Various	157-325	196-257	-
PPT	Teflon	0.01-5	200-1500	2.5-30
FEFP	Cesium	0.001-1.4	9000.00	3-93
	Indium	0.001-0.14	2000-8000	1
Colloid	Various	<0.007	300-1500	2
Mini-Ion	Xenon	0.1-1.553	3000.00	20-60
Mini-Hall	Xenon	0.1-18	400-1718	20-300
Hollow Cathode	Xenon	0.002	85.00	55.00
Micro-Plasma	Argon	0.3-0.4	-	15-20
Mini-Helicon	Xenon	1.00	1000.00	50.00
	Argon	-	1200.00	50.00
Resistojet	Hydrazine	-	300-400	100-1000
	Water	0.13	127-150	100.00
	Xenon	100-200	50-75	80-100
	Helium	0.01 - 1	50-75	2.00
	Butane	20-100	90.00	15 -50
Arcjet	Various	109-335	93-385	167-506
	Helium	0.014-0.031	313.00	119.00
	Hydrazine	-	345-471	650-1400
	Ammonia	-	600-900	103 -104
	Hydrogen	-	700-1200	104.00
MET	Argon	0.2-1.4	50-80	6.00
	Helium	0.04-0.51	150-270	6.00
RFET	Argon	0.01-0.1	50-85	10-60
	Hydrogen	0.10	30000.00	100
	Xenon	0.3 - 1.6	300 - 3500	30 - 42

2.4.1. Inert gases

As shown in Table 3, the most commonly used propellants for plasma thrusters are Xenon and Argon. A closer inspection of the data in Figure 2-16, reveals that these two propellants have greater thrust and specific impulse:

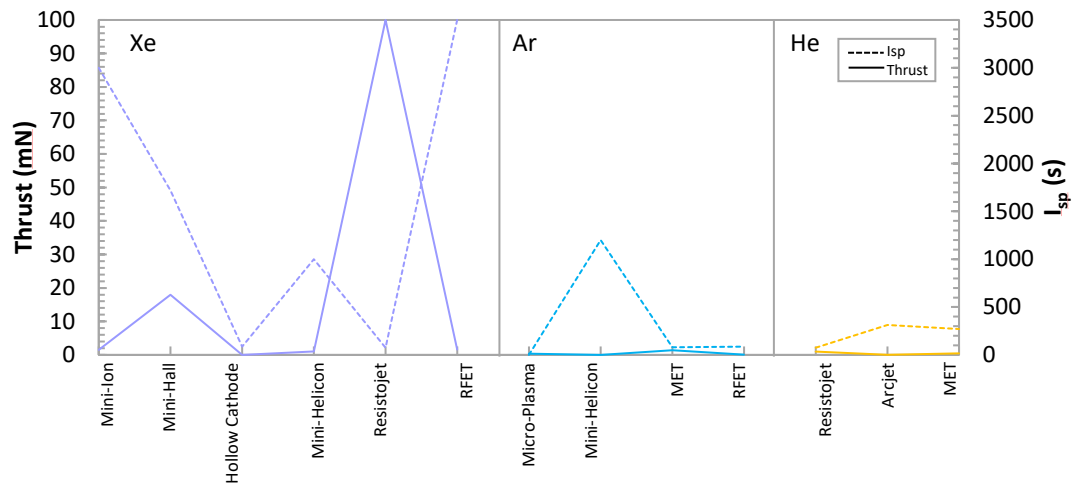


Figure 2-16. Inert gases performance for micro-satellite propulsion.

Xenon has the best performance, followed by Argon and Helium, where thrust and specific impulse are proportional to the ionisation energy and molecular weight of the element-specific gas particles.

2.4.2. Ionization energy

The final electron shell of inert or noble gases is wholly filled, deeming them stable because they have the least ability to gain, lose, or share electrons in chemical bonds. Ionisation energy is, therefore, the energy required to remove an electron from an atom. Consequently, inert gases have a filled shell structure, which makes it difficult to remove electrons from noble gases [60]. However, the stability of the elements makes them ideal as propellants, preventing chemical bonding between them and protecting the micro-devices from space contaminants. Increasing the number of electron shell configurations reduces the ionisation energy of an element. In other words, the greater the number of shells an atom has, the weaker the attraction of the electrons of the outermost shells to the nucleus (protons), necessitating a lesser amount of energy release, a representation it is shown on Figure 2-17.

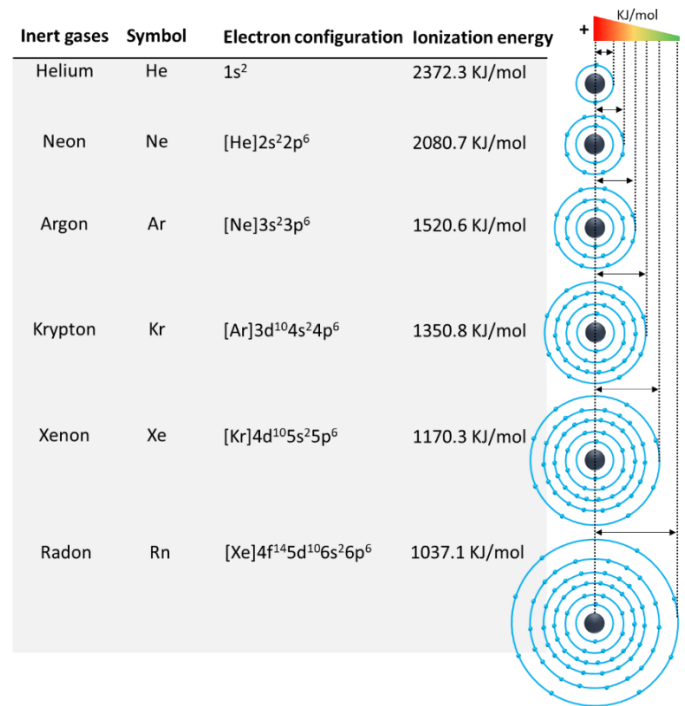


Figure 2-17. Ionization energy of inert gases. Representation of the relationship between the distance of the last shell and the ionization energy.

According to Table 4 by Micci, M. et al. [2], the specific impulse increases as the molecular weight of the propellant decreases. This data was collected for cold gas micro-thruster systems, which can be used for this micro-thrusters project due to the design's geometry, which operates as a cold gas system when the plasma actuator is turned off.

Table 4. Cold gas propellant performances [2]

Propellant	Molecular weight (Kg/Kmol)	Density (3500 psia, 0°C g/cm3)	Isp (s)	
			Theoretical	Measured
Helium	4.0	0.04	179	165
Nitrogen	28.0	0.28	80	73
Argon	39.9	0.44	57	52
Xenon	131.3	2.74	31	28

2.4.3. Propellant selection and relevance to micro-thruster operation

The propellant selection is key for optimum performance under different modes of operation in micro-thruster design as a cold gas thrusters and electrostatic thrusters. Nitrogen (N_2), Helium (He), Argon (Ar) and Xenon (Xe) are among the propellants that are of great interest in relation to the considered thruster, each having its own advantages depending on operational needs.

2.4.4. Selection for cold gas mode

Cold gas thrusters operate by expanding a gas through a nozzle to produce thrust without ionization or complex electrical systems. In this mode, the choice of propellant is mainly based on molecular weight and density which directly affect specific impulse (I_{sp}) as well as thrust efficiency [56].

- Nitrogen: This has an atomic mass unit value equal to 28 g/mol while its density is 0.28 g/cm³; thus nitrogen gives moderate specific impulse around 75 sec (Table 3). With relatively low molecular weight it becomes suitable for applications that require moderate thrust at reasonable efficiency levels [56].
- Helium: Although having the lowest possible molar value being 4 g/mol which also corresponds higher theoretical specific impulse, helium's inefficiency in providing large amount of drive stems from its lightness since it only weighs about 0.04 g/cm³. Nevertheless, non-reactivity may be necessary during certain missions so inertness coupled with low ionization energy makes this element a potential candidate for such cases.
- Argon: The atomic mass unit of argon stands at 39.9 g/mol while its density equals 0.44 g/cm³ hence giving lower specific impulse than both nitrogen and helium. However denser systems can benefit more from argon where additional mass flow is needed to produce thrust in cold gas systems with less volume constraints.
- Xenon: Having an atomic mass unit of 131.3 g/mol and density as high as 2.74 g/cm³, xenon displays the least specific impulse among others. Though not very effective for use in cold gas thrusters, it takes advantage of greater compactness per volume by providing more thrust for a given space and also better storage efficiency of propellant [56].

2.4.5. Selection for electrostatic mode

Ionization efficiency which is influenced by ionization energy and atomic properties of gas determines the choice of propellant in electrostatic mode where ions are accelerated through electric or magnetic fields after being created. The ionization potential becomes significant since these particles need to be accelerated through such fields but before that they must first get ionized.

- Xenon: For electrostatic thrusters including ion and hall effect types; xenon is preferred due to its relatively low ionization energy besides having higher atomic mass [55]. This results into high specific impulse together with large amount of thrust being generated at high level (up to 1.6 mN) specific impulse (up to 3500 seconds) according to Table 3. Moreover stability plus non-reactivity towards other materials used as components within thruster system are some additional advantages associated with this inert element.
- Argon: Although argon has lower atomic mass compared to xenon resulting into requirement for elevated levels of ionizing energies when considering it as an alternative propellant in electrostatic thruster designs [55]; argon based systems can still achieve relatively high values for specific impulses (upwards 1200 s [Table 3]) although typically providing lower amounts of thrust than those propelled by xenon. Cost effectiveness alongside wide availability makes argon suitable option especially during missions that have limited financial resources.
- Helium and Nitrogen: Although these gases may be used in an electrostatic thruster, they are not that common because of their small atomic masses which give reduced thrust per ionized particle. Due to its extremely low molecular weight, helium would need much more energy for ionization and acceleration thus resulting into lower efficiency altogether. On the other hand nitrogen being heavier than helium but lighter than argon or xenon is not as effective as them in terms of performance when used with high-power electrostatic thrusters.

All in all selection for consideration as propellants in this particular thruster; Nitrogen, Helium, Argon and Xenon are relevant because each has unique properties that match up well with both cold gas and electrostatic modes of the micro-thrusters operation requirements. For instance Ar ionises easily while Xe does so even better making them most suitable. All the properties of Xe, such as storage capacity, efficient ionization and ability to work well in electrostatic propulsion systems make it the best propellant for using in cold gas thrusters and electrostatic ones too. Nitrogen (N₂) and argon (Ar) are good substitutes when used under certain conditions but still overall xenon is preferred in dual mode thruster applications because it has a better combination of property balance.

2.5. Physics of gases

The quotient of N_A and R is Boltzmann's constant k_B , named after Austrian scientist Ludwig Eduard Boltzmann (1844–1906) [61], and it is calculated as follows:

$$k_B = \frac{R}{N_A} \quad \text{Eq. 8}$$

Where k_B is the Boltzmann constant and equals 1.3804×10^{-23} J/K, N_A is the number of atoms or molecules in one mole of a substance and equals 6.023×10^{23} , and R is the gas constant and equals 8.314 J/[mol*K].

2.5.1. Particle density

The particle density (n) is calculated by dividing the number of atoms or molecules in a given volume by the volume's size. In the kinetic gas theory for ideal gases, the following relationship is stated [61]:

$$n = \frac{p}{k_B \cdot T} = \frac{\rho}{m_t} \quad \text{Eq. 9}$$

Being n the particle density, T the thermodynamic temperature, p the pressure, ρ the density, m_t the gas molecule's mass.

2.5.2. Mean free path

The mean free λ_m is the distance between two particles before they collide (Figure 2-18); it is proportional to the probability of scattering cross-section, the kinetic diameter d_k of the gas molecules, and the gas density n in molecules per cubic metre, as demonstrated in [61]:

$$\lambda_m = \frac{1}{\sqrt{2}\pi d_k^2 n} \quad \text{Eq. 10}$$

In addition, the cross-section can be described as

$$\sigma = \frac{1}{n\lambda_m} = \pi(2r)^2 \quad \text{Eq. 11}$$

Where σ is the cross-section and r is the particle's kinetic radius.

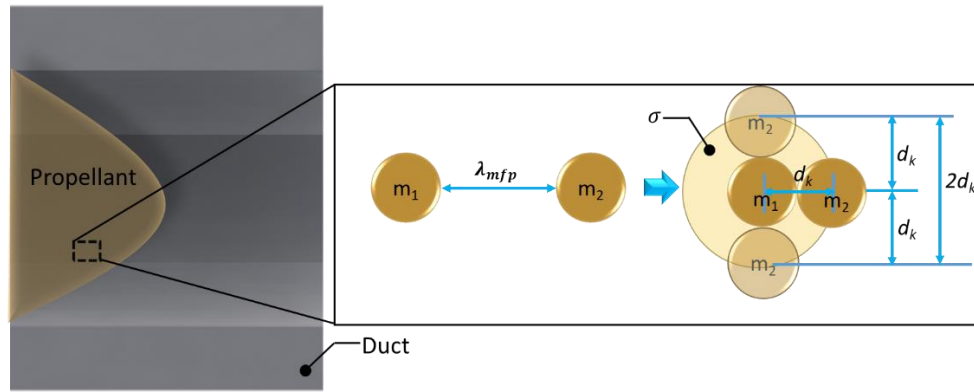


Figure 2-18. Mean free path and kinetic diameter representations for a gaseous propellant.

2.5.3. Kinetic diameter

The kinetic diameter d_k is a simplified model for representing the sizes of atoms and molecules in a gas as hard spheres that collide to determine scattering behaviour. It is essential to note that the kinetic and atomic diameters are not identical; the atomic diameter is smaller due to the atom's electron shell. The following d_k for some propellants are shown on Table 5.

Table 5. Propellants with their respective kinetic diameters.

Gas	d_k (nm)	
N2	0.368	[62]
He	2.560	[62]
Ar	0.340	[62]
Xe	0.396	[63]

2.5.4. Scattering cross-section

In a collision between two distinct particles or molecules, the scattering cross-section σ , is determined by the sum of the kinetic diameters of the two particles [61], which is given by the formula:

$$\sigma = \pi(r_{k,1} + r_{k,2})^2 \quad \text{Eq. 12}$$

Where $r_{k,1}$, and $r_{k,2}$ are the kinetic radius of each particle specie, respectively.

2.5.5. Knudsen number

The study of gaseous flows in micro-scale geometries is becoming more important for MEMS technologies, such as micro-thruster development. Microscale gas flows behave differently than predicted by macroscopic theory due to a combination of high gas rarefaction and a significantly increased influence of gas-surface interactions. Due to the micrometre length scales involved, the continuum fluid assumption may be invalid, and non-equilibrium events such as velocity slip, temperature jump, and thermal transpiration may need to be considered [64] [65]. Therefore, the Knudsen number Kn is used to determine the degree of gas rarefaction, as expressed by [61] [66]

$$Kn = \frac{\lambda_m}{L} \quad \text{Eq. 13}$$

Where L represents the characteristic length scale which, in this case, is usually the nozzle throat length as same as the electrode gap of the thruster (10 to 100 μm).

When a micro-thruster is designed with a diverging nozzle throat diameter of 10 to 100 μm , it is necessary to understand the flow regimes that will occur as the thruster operates over a pressure range from 0 to 100 kPa absolute. Knowing how flow behaviour is affected by the Knudsen number (Kn) in vacuum conditions where this micro-thruster is meant to be used can help optimize the design for different pressures.

Flow regimes may be classified according to the Knudsen number; these directly affect design and operation considerations for micro-thrusters:

- **Continuum Flow ($Kn < 0.01$):** This regime occurs at relatively higher pressures, typically near 100 kPa. At this pressure level, gas molecules' mean free path is much smaller than nozzle throat diameter; thus flow behaves like continuous fluid and conventional fluid dynamics equations such as Navier-Stokes can be applied [66]. Thruster design should focus on optimizing shape of nozzle for smooth gas expansion together with minimum viscous losses. However, since space forms primary operational environment for the device(vacuum), then this regime becomes more applicable during initial ground based testing or high altitude atmospheric phases.
- **Slip Flow ($0.01 < Kn < 0.1$):** Usually between 10 and 100 kPa. As pressure drops towards about 10 kPa where also lower end of given range when mean free path becomes comparable with throat length especially for very small sizes among listed values(10-100 μm), there occurs some slipping

near wall boundaries within nozzle whereby gas fails to adhere completely onto them [66]. This regime is more applicable during transitional phases like upper atmosphere operation or early space deployment.

- **Transitional Flow ($0.1 < Kn < 10$):** Occurs around 1 to 10 kPa. Within this region, flow indicated by the Knudsen number is neither fully continuum nor free molecular. Gas behaviour becomes more complicated requiring advanced modelling methods such as DSMC that can account for both continuum and molecular flow characteristics simultaneously [65] [66]. Altitudes just above Earth's atmosphere where pressure is low but not yet into full vacuum of space are critical for the micro-thruster operation therefore such a regime should be considered very important.
- **Free Molecular Flow ($Kn > 10$):** Below 1 kPa approaching vacuum i.e., space conditions. In a situation where pressure is effectively at near vacuity like what obtains in most parts of outer space, mean free path of molecules will tend to be very much greater than throat length; hence collisions between them become relatively less frequent compared with their impacts against nozzle walls at which point they collide significantly frequently amongst themselves than any other part within nozzle system [66]. Thus gas molecule-wall interactions become paramount in micro-thruster design under these circumstances since conventional nozzle designs may need modification so as achieve best performance when momentum transfer inefficiency due free-molecular flows are taken into account together with surface properties such as material choice and roughness which become more pronounced during this particular regime. This regime represents the main operational environment for the thruster in space.

For this reason, the micro-thruster's design has to take into account the various flow patterns it may undergo with the application of the Direct Simulation Monte Carlo (DSMC) method (Chapter 3) and should mainly focus on improving its performance while in outer space where free molecular flow is prevalent. It includes thinking critically about nozzle shape, surface characteristics, and types of substances employed so that they can function effectively at different pressure levels as well, being addressed in Chapter 4.

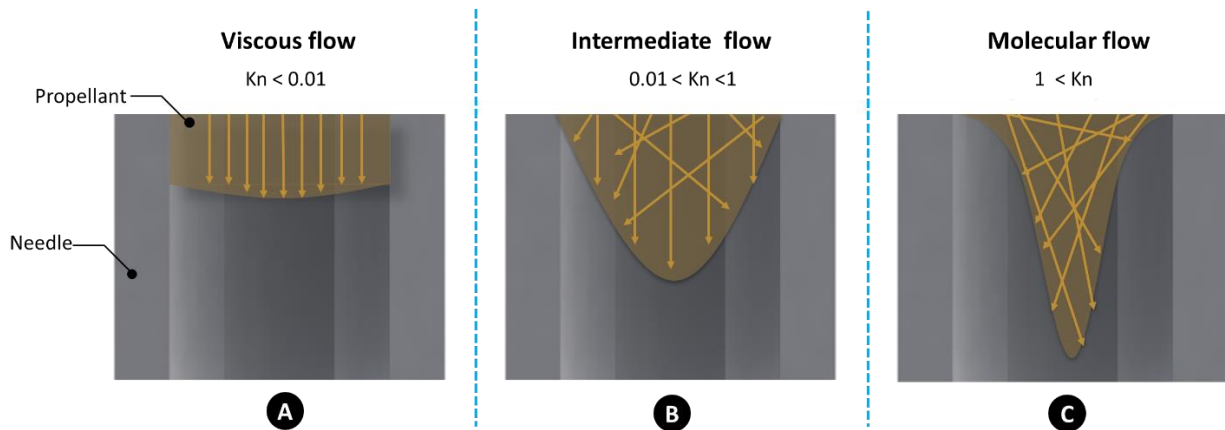


Figure 2-19. Flow regimen according to the Knudsen number on a duct [67].

Numerous MEMS were classified by Karniadakis, G., et al. [66] based on their Knudsen number profile and size shown on Figure 2-20. Micronozzles with a Knudsen number greater than 0.01 but close to it, where the regime between 0.01 and 0.1 is referred to as slip flow. This regime is a standard for micro-thruster development.

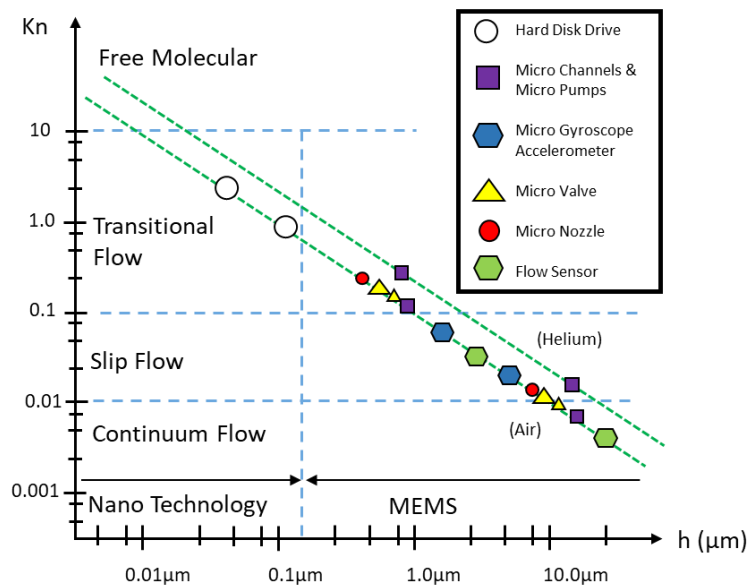


Figure 2-20. Knudsen number range for MEMS and nanotechnology applications [66].

2.6. Summary

Chapter 2 presented a literature review about the current status of plasma technology and its application in micro-thruster systems, which mainly focused on cold plasma and its relevance to micro-propulsion systems for CubeSats. The chapter started with an introduction to basic concepts of plasma by distinguishing between thermal and non-thermal (cold) plasmas. Non-thermal or cold plasmas were more particularly considered because they can keep low temperatures so that surfaces are not thermally damaged while efficient thrust is produced in micro-thrusters.

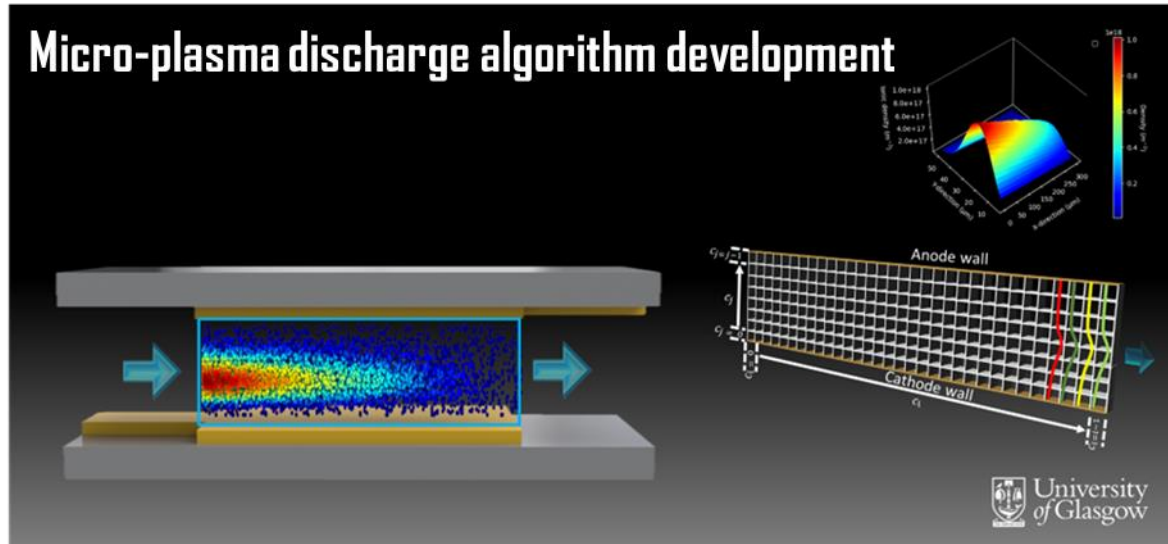
This section looked at operating parameters that are necessary for gas ionization in micro-thruster chip focusing on current, voltage, gap distance and pressure. It was highlighted certain current ranges (from 10^{-6} to 10^{-2} A) in order to achieve efficient ionization as well as maintain power limits and thermal considerations required for sustaining plasma states. Additionally, it examined how breakdown current varies with micro-gap size thereby showing how electron emission might be influenced by microscale environments leading into increased breakdown currents through ion generation.

Therefore, this portion went deeper into electron collision reactions during ionization which play crucial roles of keeping continuous plasma state within micro-thrusters. Such reactions would include elastic collisions, excitation of atoms or molecules, and ionization among others all contributing towards creating charged species needed for propulsion.

Moreover a technological snapshot about chip used in making up of thruster at microscopic level was provided; focused on the discharge characteristics with relevant ionization processes which powers its operations forward. The significance of plasma processes on performance improvements for smaller sized devices was emphasized; these included efficiency levels associated with ionizations besides their effect on thrusting capabilities directly. Different classifications of electrically heated electrothermal, electromagnetic and electrostatic thrusters were introduced as well particularly those applicable to CubeSats. Notably small sized low-cost power-efficient plasma micro-thrusters were singled out.

In summary, this chapter laid foundation for later development on new plasma technologies meant for enhancing design and performance of the plasma-based micro-thruster chip. Design decisions shall be influenced by findings from literature survey while experimental approaches will be guided by gained knowledge so that the present project can come up with more efficient and reliable micro-thrusters used in CubeSats during subsequent chapters.

Chapter 3



In recent years, MEMS have witnessed exponential growth in their employment as flow control devices and in CubeSats' on-board attitude and orbit control systems (AOCS) [68]. Applications of plasma on micro-scale AOCS thrusters yield nano-newton to micro-newton scale thrust, which has the potential for use in space applications in the near future [69] [70] [71]. Rarefied gases are an important factor to consider while troubleshooting the vacuum that MEMS must withstand for use in space. Therefore, the Boltzmann equation is required to provide a solution for the simulation of cases where molecular collision rates reduce, making the continuum fluid assumption in the Navier Stokes equations invalid due to the degree of rarefaction [72].

Flow rarefaction is defined by Knudsen numbers $Kn > 10$ in a free molecular regime, where intermolecule collisions are not an important factor in the transfer of mass, momentum, and energy [73] [12]. Therefore, rarefied flow simulations based on real scenarios involve the transition Knudsen number regime ($0.1 < Kn < 10$), where a solution to the Boltzmann equation must be sought, but intermolecular collisions are still an important process, which makes this equation difficult and numerically expensive to solve. Methods such as direct simulation Monte Carlo (DSMC), particle-in-cell (PIC) and test particle Monte Carlo (TPMC) [12] are widely used to obtain solutions to problems in the transition Knudsen number regime.

A significant problem is the inclusion of plasma in simulations due to the method's limitations and the high processing power requirements, which is a numerically expensive case. An electron-gas and ion-

gas particle interaction model needs to be simplified in order to replicate plasma phenomena in a more computationally efficient manner. There are two key capabilities that are not considered by the majority of the available methods; one is a phenomenon known as the quantum effect on microgaps, based on an increase in the electric field intensity by an enhancement factor when a voltage is applied to microgaps between electrodes. The second key is the macro view of the gas flow after electrons, gas particles, and ions' interactions. Herein lies the novelty of this work, which includes a method for simulating plasma that takes electric field enhancement and macroscopic flow analysis into account.

Particle-in-cell methods are used to model the movement/trajectory of charged particles within an electric field [13] for plasma simulations. Unfortunately, to model the effect of plasma within the flow, the methods usually do not consider the interactions between the particles [13] and the surface [12]. Some solvers, such as DEMOCRITUS [74], PicUp3D [75] and CPIC [76] are used to model the charging of satellites and instrument calibration [12].

DSMC simulations can reproduce the gas-surface interactions by modelling a single atom/molecule as a single particle that is representative of a large number of real gas atoms. Available DSMC solvers include dsmcFoam+ [73], MONACO [77], DAC [77], and SPARTA [78]. For applicability, dsmcFoam+ fulfils a similar role to other alternatives, but with the advantage of being an open-source (as is SPARTA) and implemented within OpenFOAM [79] (Open Source Field Operation And Manipulation), providing an open and extensible C++ based software package containing a wide range of libraries [73].

Combining the PIC capabilities to model the charged particles with the DSMC method for gas-surface interactions results in a hybrid PIC-DSMC method. Such PIC-DSMC codes are primarily focused on the research and design of plasma thrusters [12], such as PICLas [13] [14], and DRACO [15]. Additionally, PIC-DSMC solvers are commonly used to model orbiting objects in ionised environment, such as low Earth orbit, an example of which is the pdFoam solver [12] based in Open-FOAM. Unfortunately, PICLas [13] and DRACO [15] do not focus on the microscale effects on plasma, avoiding the variations and enhancements of the electric field due by the microgap between the electrodes. Furthermore, electron temperature (T_e) variation is essential in micro-plasma modelling to obtain an accurate electron density distribution between the microgap; the DRACO solver considers T_e to be constant [15]. Additionally, PIC-DSMC methods for modelling micro-scale plasma thrusters results in an exponential increase in computational resources when they are used to properly model number density by the difference between the densities of the charged particles (electrons) and the gas/neutral particles. To illustrate the challenge, each simulated particle in pdFoam represents a large number of real gas atoms/molecules.

Hence, for an inlet flow ranging from 1 KPa to 100 KPa, the gas particle density lies between 10^{23} m^{-3} to 10^{25} m^{-3} . Additionally, an estimated electron density range of 10^{11} m^{-3} to 10^{19} m^{-3} can be defined based on the electrical properties of the material, size, and the applied current-voltage. In PIC-DSMC methods, it is crucial to set the gas and electron densities as initial and boundary conditions. To ensure accurate collision statistics, it is recommended to have a minimum of twenty particles per cell when using dsmcFoam+ [80]. During initialization, some cells will only contain electron density. Therefore, with an electron density of 10^{19} m^{-3} , each equivalent particle must represent at least 10^{17} real atoms/molecules to meet the twenty-particle requirement. Consequently, inlet flows of 1 KPa and 100 KPa require 10^5 and 10^7 equivalent particles per cell, respectively, assuming the highest electron particle density value. As electron density decreases, the number of equivalent particles exponentially increases up to a maximum of 10^{15} particles per cell. Under this assumption, modelling a scenario of 1000 cells would entail approximately a minimum of 10^8 equivalent particles, demanding significant computational resources. For comparison, White et al [73] conducted parallel tests using the dsmcFoam+ solver, running millions of cells with varying equivalent particle counts on 960 cores on ARCHER, the UK's national supercomputing service. In contrast, executing a case for 1000 cells using the PIC-DSMC method would require up to 960 cores. Consequently, PIC-DSMC becomes costly and impractical for micro-thruster analysis.

Due to the flexibility and open-source nature of the solver, a dsmcFoam+ code was developed to optimize the modelling of the micro-plasma discharge effect on flow. This code combines particle-surface interactions from dsmcFoam+ with the numerical solution of the Fowler-Nordheim equation to simulate electrical charge interactions and ionization rates, enabling the simulation of the micro-plasma effect.

Consequently, a micro-plasma system with two inlets and a single outlet orifice was employed to showcase the application of the micro-plasma discharge algorithm in system simulation and analysis. Three electrode configurations were determined: (a) 1 anode/2 cathodes, (b) 2 anodes/2 cathodes, and (c) 1 anode extended/2 cathodes, positioned near the outlet to analyse the various flow profile variations caused by plasma.

3.1. Theory and Background

Since 1960, when Bird G. A. [81] proposed a non-equilibrium Knudsen number regime gas flow, the direct simulation Monte Carlo (DSMC) method has been utilised. As an alternative to costly molecular dynamics (MD) simulations, DSMC does not directly solve the Boltzmann equation. Still, it is based on kinetic theory to model the physics of the system for dilute gas and molecular chaos constraints.

Chapter 3 Micro-plasma discharge algorithm development

By incorporating the Boltzmann equation into the DSMC framework, researchers are able to simulate gas flows in a wide range of scenarios, from low-density environments in space to microscale devices where molecular effects dominate [82]. The kinetic theory underpinning the Boltzmann equation allows DSMC to capture non-equilibrium phenomena that cannot be easily described using traditional fluid dynamics approaches. The DSMC method works by tracking the motion and collisions of a representative sampling of gas particles. The particles are moved and collided stochastically, in accordance with the probability distributions derived from the Boltzmann equation [83]. This statistical approach enables DSMC to model the detailed physics of rarefied gas flows without the computational expense of a full atomistic simulation [82] [83]. The Boltzmann equation typically is written as follows,

$$\frac{\partial f}{\partial t} + \mathbf{v} \cdot \nabla_{\mathbf{x}} f + \mathbf{F} \cdot \nabla_{\mathbf{v}} f = \left(\frac{\partial f}{\partial t} \right)_{\text{collision}} \quad \text{Eq. 14}$$

where:

$f = f(\mathbf{x}, \mathbf{v}, t)$ is the distribution function, representing the number of particles at position \mathbf{x} with velocity \mathbf{v} at time t .

\mathbf{v} is the particle velocity.

\mathbf{F} is the external force acting on the particles.

$\nabla_{\mathbf{x}}$ and $\nabla_{\mathbf{v}}$ are the gradient operators with respect to position and velocity, respectively.

$\left(\frac{\partial f}{\partial t} \right)_{\text{collision}}$ represents the change in the distribution function due to collisions between particles.

In the field of plasma physics, the Boltzmann Equation is a crucial mathematical tool used to model and study the behaviour of particles in a plasma. Plasma is a state of matter consisting of highly ionized gases that contain a large number of charged particles, such as electrons and ions [84]. When modelling a plasma, the Boltzmann Equation is often chosen over the Vlasov equation due to its ability to account for collisions between particles [85]. The Vlasov equation is written as follows:

$$\frac{\partial f}{\partial t} + \mathbf{v} \cdot \nabla_{\mathbf{x}} f + \left(\frac{q}{m} (\mathbf{E} + \mathbf{v} \times \mathbf{B}) \right) \cdot \nabla_{\mathbf{v}} f = 0 \quad \text{Eq. 15}$$

where,

$f = f(\mathbf{x}, \mathbf{v}, t)$ is the distribution function, representing the number of particles at position \mathbf{x} with velocity \mathbf{v} at time t .

\mathbf{v} is the particle velocity.

q is the charge of the particles.

m is the mass of the particles.

\mathbf{E} is the electric field.

\mathbf{B} is the magnetic field.

$\nabla_{\mathbf{x}}$ and $\nabla_{\mathbf{v}}$ are the gradient operators with respect to position and velocity, respectively.

By considering these factor, the Boltzmann Equation provides a more comprehensive and accurate representation of plasma behaviour. The Vlasov equation is disadvantageous for plasma modelling due to its complexity, computational expense, neglect of collision effects, and difficulty in handling large plasma systems [84]. The Boltzmann Equation, on the other hand, simplifies the modelling process by considering collisional effects and assuming a Maxwellian velocity distribution for particles, making it more computationally efficient and manageable. Therefore, the Boltzmann Equation is a kinetic equation that describes the statistical behaviour of a distribution function, which gives information about the probability of finding particles with specific velocities and positions [84]. Thus, in a plasma, collisions occur frequently and play a significant role in determining the overall behaviour of the system. These collisions can lead to processes such as energy transfer, momentum exchange, and ionization/recombination. Consequently, even that Boltzmann Equation is not directly solve by DSMC method, but it entails the representation of a large number of real gas atoms or molecules as a single particle or equivalent particle, where the motion and collisions over short time intervals are calculated deterministically and stochastically, respectively.

3.1.1. Direct Simulation Monte Carlo (DSMC)

The DSMC method requires a computational mesh in order to retrieve macroscopic properties, but it is also used to simulate near-neighbour collisions. Typically, the cell size is set to one-third of the local mean free path to make collisions appear as realistic as possible. Therefore, the assumption of uncoupled particle motions and collisions is valid if the time step is significantly smaller than the mean collision time t_{mc} . DSMC is now universally acknowledged as the most robust technique to model highly rarefied, dilute gas flows in complex geometries. Modern modelling methodologies (such as analytical methods and hybrid approaches) are routinely compared to the outcomes of comprehensive DSMC simulations.

3.1.2. The DSMC algorithm

After determining the gas species characteristics, boundary conditions, and the number of actual molecules each DSMC particle represents F_N , the computational mesh is populated with DSMC

particles. The thermal velocities are derived from the equilibrium Maxwell-Boltzmann distribution at the translational temperature supplied. The number of DSMC particles inserted in each cell is determined using user-defined macroscopic density, temperature, and velocity parameters.

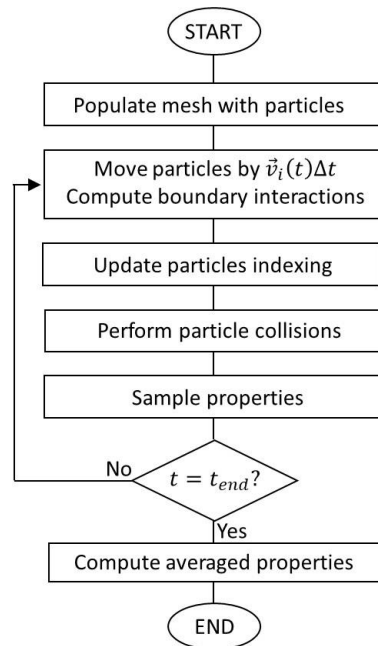


Figure 3-1. Flowchart of the DSMC algorithm.

The mesh is initially populated with DSMC particles in an equilibrium condition, meaning that the thermal velocity of each particle is sampled from a Maxwellian distribution at the specified macroscopic temperature and velocity. Figure 3-1 depicts the four steps that comprise the algorithm's main loop. 1) particle motion, 2) indexing, 3) collision method, and 4) sampling.

i. Particle movement

Transporting each particle i along its velocity vector c_i for one DSMC time step Δt , assuming that the velocity remains constant and no collisions occur. The velocity vector and time step are employed to move all particles. Any boundary interactions, such as a signal migrating from one processor to another or reflecting from a surface based on molecule-surface contact, are also handled at this level. In DSMC simulations, there are typically three major types of boundary conditions enforced:

- 1) Inflow boundaries – are utilised to achieve the required freestream conditions by inserting particles based on the equilibrium Maxwellian number flux [86]. In contrast, particles that come into contact with outflow boundaries are rapidly removed from the system.

- 2) Particle-surface interaction boundary – Maxwell's [87] specular and diffuse reflections are the most frequently used interaction model in DSMC. Specular reflection is a perfectly smooth surface with perfect slip where the tangential momentum of impacted particles is conserved. Diffuse reflection, on the other hand, denotes a microscopically rough surface where particles that strike the wall lose all of their tangential momentum.

- 3) Periodic boundary – When a particle traverses a periodic barrier, it simply re-enters the system with the same velocity and internal state at the mirror boundary.

Consequently, during this step, the macroscopic properties of solid barriers are calculated, typically as a function of the difference between the pre- and post-interaction properties (momentum and/or energy) of particles incident at the boundary.

ii. Indexing

After calculating particle motion and boundary interactions, each particle is indexed into a computational mesh cell based on its current position.

iii. Collision procedure

To replicate realistic collision rates, developing an appropriate collision modelling technique is necessary. Bird's no time counter (NTC) scheme [88] has become the standard method in DSMC due to its ability to produce accurate collision rates with minimal computational effort. A random selection of particle pairs(ij) is made within each cell or sub-cell, regardless of their position. Then, an acceptance-rejection approach is implemented. A collision is recognised for every pair of particles if [86],

$$\frac{(\xi_T c_r)_{ij}}{(\xi_T c_r)_{max}} > R_f \quad \text{Eq. 16}$$

where R_f is a random fraction uniformly chosen in the interval (0, 1), ξ_T is the total collision cross-section, and c_r is the relative velocity between the pair. Once a particle pair has been selected for collision, or if the pair has been rejected, a new particle pair is selected, and the acceptance-rejection mechanism is repeated until the required number of candidate particle pairs has been reached by, for example, selecting a new particle pair.

$$\frac{1}{2V_C} F_N \bar{N} (\bar{N} - 1) (\xi T c_r)_{max} \Delta t \quad \text{Eq. 17}$$

At each time step, pairs are selected from a cell, representing V_C the volume of the cell, \bar{N} the instantaneous number of DSMC particles in the cell, and F_N the number of real gas molecules represented by a single DSMC particle. $(\xi T c_r)_{max}$ represents the maximum product of collision cross-section and relative velocity of all feasible particle pairs in the cell and Δt represents the time step size.

If a particle pair is selected for collision, the collisions are merely simulated by resetting the velocities of both partners; their locations are not altered. In monatomic gases, particles i and j will only exchange translational energy, so that the collision will be entirely elastic. Using momentum conservation, it is possible to determine the post-collision velocities of each particle by,

$$c_i^* = c_m^* + \left(\frac{m_j}{m_i + m_j} \right) c_r^* \quad \text{Eq. 18}$$

where the superscript $*$ represents post-collision values. The collision has no effect on the centre of mass velocity c_m , i.e.

$$c_m^* = c_m = \frac{m_i c_i + m_j c_j}{m_i + m_j} \quad \text{Eq. 19}$$

The post-collision relative velocity c_r^* is calculated as follows:

$$c_r^* = c_r^* [(\sin \vartheta \cos \varphi) \hat{x} + (\sin \vartheta \sin \varphi) \hat{y} + (\cos \vartheta) \hat{z}] \quad \text{Eq. 20}$$

The conservation of energy implies that the collision has no effect on the relative velocity of the particles, as indicated by $c_r^* = c_r = \|c_i - c_j\|$. The scattering angles are uniformly distributed throughout a unit sphere, between 0 and 2π radians, according to the isotropic scattering law of the Variable Hard Sphere (VHS) model. The azimuthal angle, is equal to $2\pi R_f$, while the elevation angle, is equal to $\vartheta = \cos^{-1}(2R_f - 1)$. In the case of diatomic or polyatomic gases, each particle pair must be considered for rotational energy exchange, and collisions may be inelastic; the phenomenological Larsen-Borgnakke model can then be utilised to determine post-collision velocities.

iv. Sampling

When modelling real-world applications, engineers are frequently less concerned with microscopic information than they are with the fluctuation of macroscopic features. To achieve this, particle properties must be sampled following the processing of all collisions. The sampling procedure is

comparable to the kinetic theory [86], but it must be remembered that a single DSMC particle can represent any number of actual molecules. Given this presumption, the sampled number density is as follows:

$$n = \frac{F_N \bar{N}}{V_C} \quad \text{Eq. 21}$$

Where F_N is the number of actual molecules represented by a DSMC particle, \bar{N} is the average number of DSMC particles in the cell over the measurement time, and V_C is the volume of the cell.

After allowing a steady state problem to reach its steady state, properties are evaluated using a large sample size to reduce statistical error to an acceptable level [89]. Where by ensemble averaging can be used to reduce dispersion in transitory problems by repeatedly running the simulation.

3.1. Micro-plasma discharge algorithm

The micro-plasma discharge algorithm is an extension controller of the dsmcFOAM+ solver. This algorithm serves as an alternative method for modelling DC micro-plasma effects on flow, with a primary focus on the research and design of plasma thrusters. Rather than adding electrons and ions as particles in the mesh, the code focuses solely on determining the acceleration gradient of the preexisting neutral particles (gas species) in the mesh of the dsmcFOAM+ solver. It does this by calculating a numerical solution of the Fowler-Nordheim equation to emulate ionization, thus reducing computational requirements. Due to its simplicity, this approach does not provide high accuracy, however, correction factors (section 3.2.3 and 3.2.4).are introduced to approximate a more realistic scenario. Once the increase in acceleration is defined by the micro-plasma discharge algorithm, the exchange of energy during wall-particle or particle-particle collisions is handled by dsmcFOAM+.

In addition, it is important to emphasize that this algorithm does not consider the recombination in neutral/ion collisions on micro-gaps by the following advantages; firstly, it can significantly reduce the computational complexity of the simulation, as the inclusion of recombination processes can add significant overhead to the calculations. Secondly, by neglecting recombination, the simulation can focus on the dominant transport mechanisms, such as ionization (Eq. 30) and energy exchange (Eq. 18), without the added complexity of the recombination process. This approach may be particularly useful in situations where the recombination rate is relatively low compared to other relevant processes, or in cases where the micro-gaps are small enough that the impact of recombination is negligible. However, it is important to carefully evaluate for future works the validity of this assumption, as neglecting recombination may lead to inaccuracies in the simulation results,

particularly in regions where recombination plays a significant role in the plasma dynamics. In order to mitigate this effect correction factors are applied.

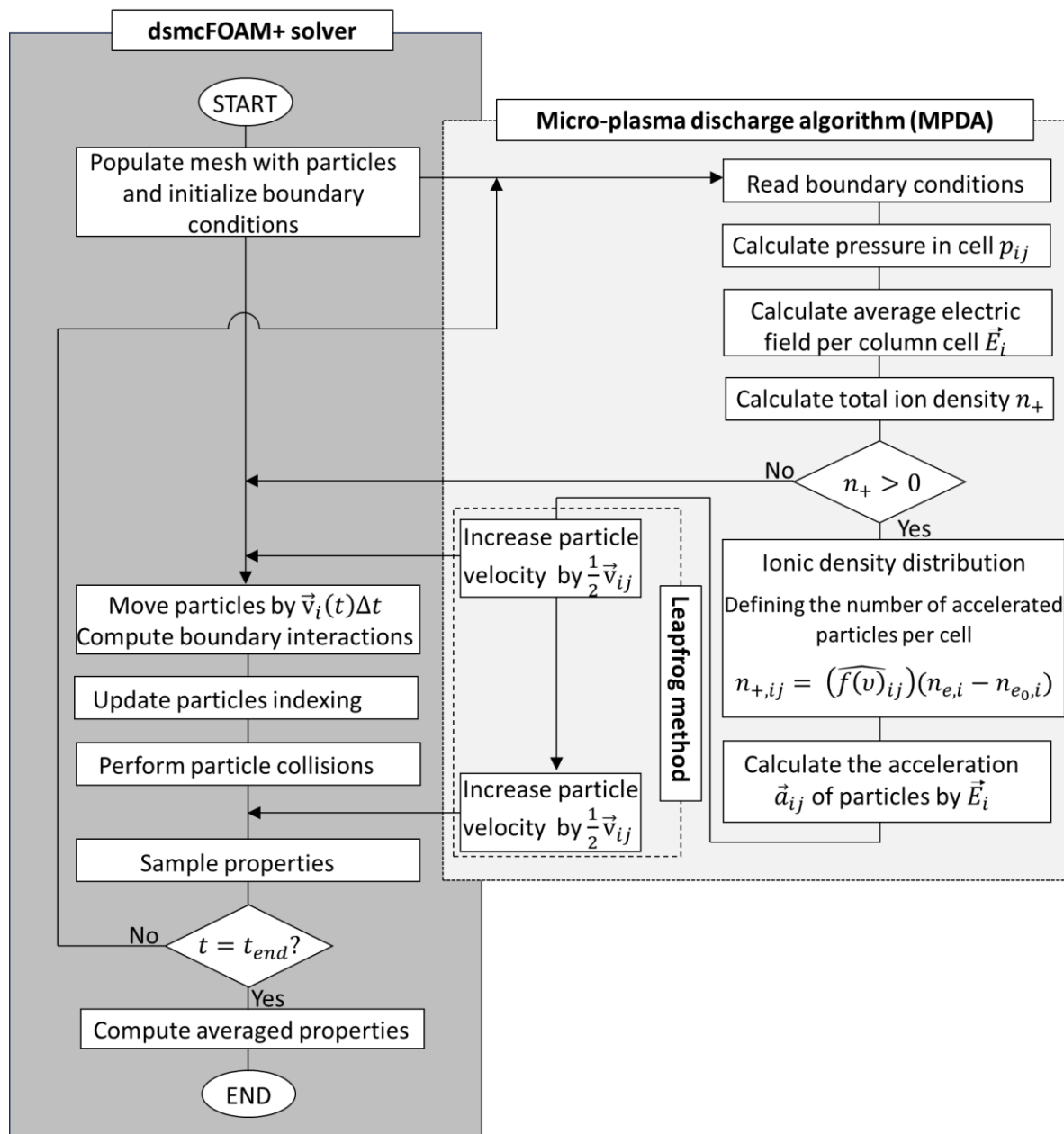


Figure 3-2. Flowchart of the micro-plasma discharge algorithm in dsmcFoam+.

3.1.1. How does the micro-plasma discharge algorithm (MPDA) works?

As previously mentioned, the micro-plasma discharge algorithm (MPDA) is an extension controller of the dsmcFOAM+ solver. Consequently, the algorithm cannot be run independently of the dsmcFOAM+. Generally, the micro-plasma discharge algorithm runs parallel calculations to obtain the acceleration gradient of the preexisting gas particles within the mesh of the dsmcFOAM+ solver, with

the goal of increasing their velocity for the next time step. Based on Figure 3-2, the procedure of the MPDA is as follows:

- 1) **Set dsmcFOAM+ Boundary Conditions:** Establish the type of gas, gas temperature, inlet pressure, outlet pressure, diffusion method for wall-particle collision, and time step (time step considerations are described in section 3.1.3).
- 2) **Set MPDA Boundary Conditions:** In addition to the boundary conditions in step 1, set the boundary conditions specific to the micro-plasma discharge algorithm (MPDA). These include electrode configuration (number of electrodes and type—anode/cathode), dimensions of the electrodes, distance between the electrodes, applied current, and voltage. Crucially, define the zone in the mesh where the cells are located between the electrodes. When the discharge occurs, gas particles in this zone will be accelerated in subsequent steps.
- 3) **Initialize dsmcFOAM+:** dsmcFOAM+ populates the mesh with gas particles (neutrals) and initialize boundary conditions from step 1.
- 4) **Initialize MPDA:** Read the boundary conditions from step 2.
- 5) **Calculate Pressure:** MPDA calculates the pressure by counting the number of gas particles in each cell of the mesh.
- 6) **Calculate Electric Field:** MPDA determine the resultant electric field vector for each cell inside the zone between the electrodes based on their location and configuration set in step 2 (calculation described in section Electric field calculations 3.1.4).
- 7) **Calculate Ion Density:** MPDA numerically calculate the total ion density according to the ionization factor per column of the mesh (calculation described from section 3.1.3 to section 3.1.6).
- 8) **Verify Ionization Conditions:** MPDA check if the conditions generate ionization. If the calculations in step 7 show ion density $n_+ > 0 \text{ m}^{-3}$, it indicates that the ideal conditions for a breakdown discharge are met (adequate pressure, voltage, gap distance, and current).
 - If $n_+ = 0 \text{ m}^{-3}$, there is no contribution to the acceleration ($\vec{a} = 0 \text{ m/s}^2$) of gas particles due to the MPDA effect. Directly jump to step 13.
 - If $n_+ > 0 \text{ m}^{-3}$, continue to step 9.
- 9) **Distribute Ions:** Once the identification of how many ions n_+ are produced per cell column in the region of interest, MPDA determines their distribution in each cell based on the ionic density distribution calculations (described in section 3.1.6).
- 10) **Calculate Energy Transfer and Acceleration :** With the assumption that an ion collides with a gas particle within the same cell. MPDA defines the energy transfer from the ion to the gas

particle collision to accelerate it. The MPDA calculations to determine the ion's energy and the gas particle's acceleration gradient are described in section 3.1.7. The kinetic energy of the ion is derived from the potential energy given by \vec{E} , and the transfer factor is defined to determine the acceleration gradient of the gas particle.

- 11) **Convert Acceleration to Velocity:** MPD converts the acceleration gradient to velocity magnitude to accelerate the particles in the dsmcFOAM+ solver.
- 12) **Apply Velocity (Leapfrog Method):** MPDA add half of the calculated velocity to the gas particle according to the leapfrog method to avoid non-physical energy increases in the DSMC particles during acceleration (described in section Leapfrog method3.1.8).
- 13) **Update Particle Positions:** The dsmcFOAM+ solver moves the gas particles within the mesh to other cells according to the velocities set by the boundary interactions and from the MPDA in step 12.
- 14) **Update Particle Indexing:** The dsmcFOAM+ solver updates the particle indexing after cell changes to track the gas particles (more information in reference [73]).
- 15) **Perform Collisions:** The dsmcFOAM+ solver performs collisions between gas particles (section 3.1.2– Collision Procedure) and walls (wall interaction described in section 3.1.9).
- 16) **Complete Velocity Update:** The MPDA adds the remaining half of the velocity to the gas particle according to the leapfrog method (described in section 3.1.8), only if $n_+ > 0 \text{ m}^{-3}$ in step 8.
- 17) **Extract Sample Properties:** The dsmcFOAM+ solver computes sample properties such as density, velocity, temperature, pressure, heat flux, etc.
- 18) **Check Time Step Completion:** The dsmcFOAM+ solver verifies if the last time step $t = t_{end}$ is reached.
 - If the last time step is not reached ($t < t_{end}$), the iteration restarts from step 4.
 - If the last time step is reached ($t = t_{end}$), proceed to step 19.
- 19) **Compute Average Properties:** The dsmcFOAM+ solver computes average properties such as average density, velocity, temperature, pressure, heat flux, etc.
- 20) **Finalize Simulation:** dsmcFOAM+ finalized the simulation.

3.1.2. Micro-plasma algorithm (MPDA) restrictions

- **No Ion Species in the Mesh:** The algorithm does not incorporate ion species into the mesh. Instead, ion density, ion density distribution, and their temperature are calculated numerically. The solver emulates the ion/neutral collisions, resulting in an acceleration gradient applied to a certain number of gas species in the mesh.
- **No Electron Species in the Mesh:** The algorithm does not incorporate electron species into the mesh. Electron density and temperature are calculated numerically to compute ion values (ion density and ion density distribution) based on the assumption of electron/ion pair formation.
- **No Recombination and Dissociation:** The algorithm does not consider the recombination and dissociation of electrons and ions.
- **No AC or RF Plasma Discharge Emulation:** The algorithm does not emulate plasma discharge through an applied alternating current (AC) or by inducing a radio frequency (RF) source.
- **Restriction to Planar Electrode Geometries:** The algorithm is restricted to planar electrode geometries due to the complexity of ordering mesh cells on curved geometries using BlockMesh and snappyHexMesh tools in OpenFOAM.

All these restrictions can be addressed in future work to improve the MPDA.

3.1.3. Time Step selection (Δt)

It is important to emphasize that only gas species particles are computed on the mesh, and they will be accelerated based on the numerical calculation of the micro-plasma discharge effect. Therefore, the computation of the mean collision time t_c , the cell residence time t_{res} , and the time step Δt focuses exclusively on gas species particles modeled as hard spheres [90]. This approach eliminates the complexity of dealing with different species, such as heavy ions and light electrons, and their velocities in the mesh, which simplifies defining the timestep. For all DSMC simulations and the micro-plasma discharge algorithm, which is a controller extension of dsmcFOAM+, the cell size is chosen to be smaller than the mean free path. To ensure realistic collisions, it is typically recommended that the cell size be one-third of the local mean free path [90]. This placement of enough cells throughout the domain allows for the recovery of macroscopic properties with sufficient resolution. Consequently, the time step is set to be smaller than the mean collision time and small enough for particles to spend multiple time steps within a single computational cell.

Thus, the time step should be a fraction of the local mean collision time [91] and the mean residence time [92]. The hard-sphere mean collision time t_c , can be calculated as [97] by:

$$t_c = \frac{\lambda}{v_{\infty,prob}} \quad \text{Eq. 22}$$

where λ the hard-sphere molecular mean free path and $v_{\infty,prob}$ is the most probable molecular speed. The cell residence time t_{res} is defined as the mean time it takes a particle to traverse a cell [92], given by the following relation [93],

$$t_{res} = \frac{\Delta x}{\bar{u}_{\infty}} \quad \text{Eq. 23}$$

where Δx is the cell size and \bar{u}_{∞} is the average cell stream velocity of the gas.

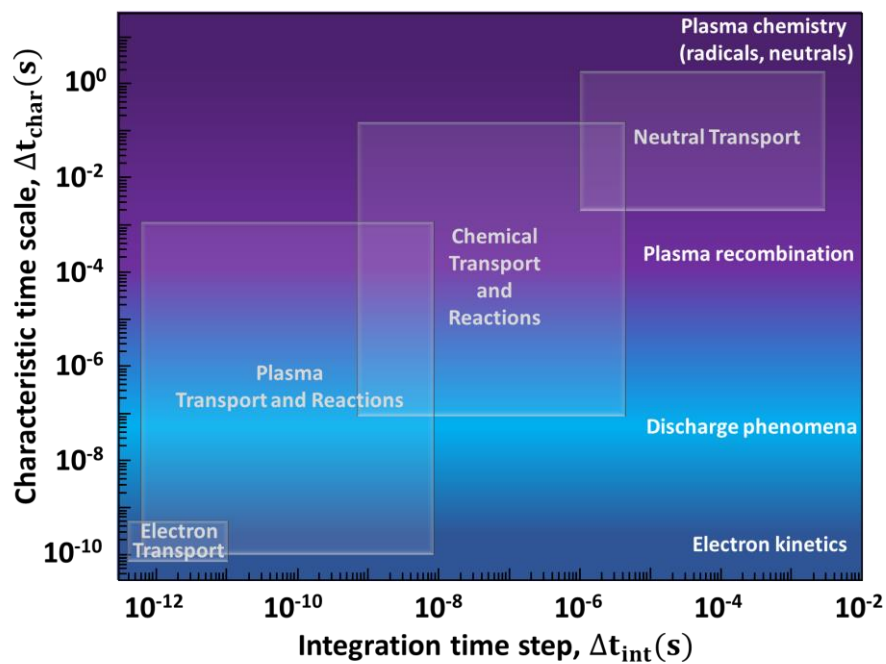


Figure 3-3. Time plot diagram contrasting the integration time step and characteristic time scale in plasma phenomena [94] [95].

The micro-plasma discharge algorithm imposes an additional restriction on the definition of the time step. As mentioned earlier, c

The focus on ion kinetics over electron kinetics means that the algorithm's time step (Δt) must align with the discharge phenomena time and the plasma transportation and reaction time, where ions are generated and begin to interact, as illustrated in Figure 3-3. If Δt is set lower than the discharge phenomena timing ($\leq 10^{-9}s$), the solver will compute it, but the resulting assumptions will be incorrect because the algorithm will prematurely calculate the total kinetic energy of the electrons.

To define an accurate Δt range, reference ranges are provided in Figure 3-3, based on data from References [94] and [95], which contrast the characteristic time scale Δt_{char} of the plasma effect with the numerical analysis of the integrated time step Δt_{int} .

Considering all these factors, the time step Δt must be greater than the characteristic time Δt_{char} of the electron kinetics but lower than the local mean collision time and the mean residence time:

$$\begin{cases} 10^{-9}s \leq \Delta t \\ \Delta t < t_{res} \\ \Delta t < t_c \end{cases} \quad \text{Eq. 24}$$

This restriction on the time step can be influenced by the simulation of larger geometries or extensive areas where cell size does not need to be refined, or in regions distant from the model's refinement focus. More research on the influence of the time step in simulations with larger geometries is necessary for future work.

3.1.4. Electric field calculations

For a given applied voltage V across a microgap distance d , the electric field is calculated based on the number and location of the electrodes. In this work, plane electrode plates are considered for all calculations of \vec{E} .

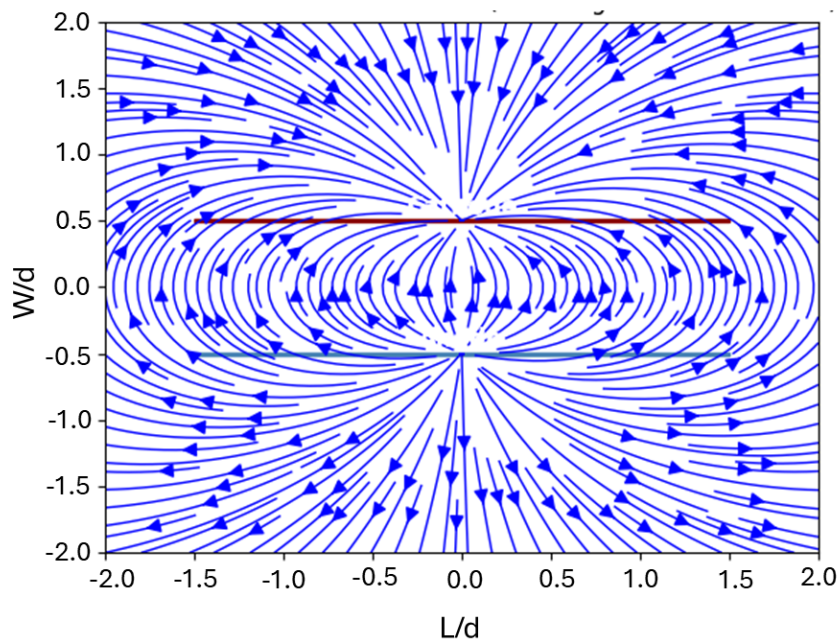


Figure 3-4. MPDA electric field lines from the computational mesh of a field \vec{E} between two parallel electrode plates with a gap distance d [cathode-red line][anode-blue line].

Chapter 3 Micro-plasma discharge algorithm development

To execute and demonstrate the application of the micro-plasma discharge algorithm, the electric field for three different micro-plasma electrode configurations must be defined. Therefore, electric field lines and values of \vec{E} are needed for:

- (a) 1 anode/2 cathodes
- (b) 2 anodes/2 cathodes
- (c) 1 extended anode/2 cathodes configurations

For the simplest case of parallel electrodes (one anode and one cathode), \vec{E} is uniform along the x-direction of the gap due to the consistent direction and average magnitude of the electric field lines. The electric field can be determined by the relation [96]:

$$\vec{E} = \frac{V}{d} \quad \text{Eq. 25}$$

Eq. 25 Equation 20 describes an ideal case with two parallel plates in a unidimensional context. If the electrodes are set in a two-dimensional context, such as in Figure 3-4, or if there is a displacement between them affecting their relative orientation, or an additional electrode plate is included, variations in the quantity, direction, and magnitude of \vec{E} at each point in space are introduced. This scenario can no longer be described by Eq. 25, and the modified electric field \vec{E}_n must be determined by the vector summation of the fields from the individual source charges q_j [96] [97]:

$$\vec{E}_n = \frac{1}{4\pi\epsilon_0} \sum_j \frac{q_j}{r_{ij}^2} \hat{r}_{ij} = \frac{Q}{4\pi\epsilon_0 r^2} \hat{r} \quad \text{Eq. 26}$$

where Q is the total charge to the source given by the sum of each individual charge on the field, ϵ_0 is the dielectric constant of the medium, r is the distance between the charges and \hat{r} is the direction denoted as a unit vector.

Figure 3-5 and Figure 3-6 illustrate that having more than two electrode (anode-cathode) plates, as in the presented configurations, modifies the electric field. The charge Q represents the total negative charge from its source (cathode), denoted as $Q_{cathode_n}$ for identification.

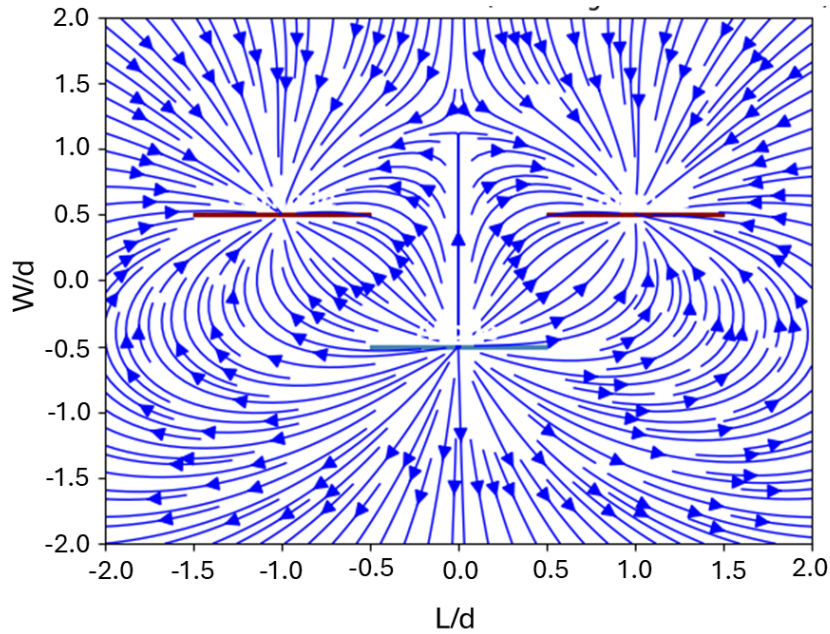


Figure 3-5. MPDA electric field lines from the computational mesh between an anode and two cathodes with a gap distance d [cathodes-red lines][anode-blue line].

An additional cathode plate is introduced to the system at the same height as the first cathode, with an anode placed between them on the opposite side of the microgap. The blue line represents the resulting vectors of the electric fields \vec{E}_1 and \vec{E}_2 . These vectors can be decompose into components \vec{E}_x and \vec{E}_y corresponding to the x-axis and y-axis respectively, can be calculated using the following expressions:

$$\vec{E}_x = \frac{Q_{cathode_1}}{4\pi\epsilon_0 r_1^2} \cos \theta_1 + \frac{Q_{cathode_2}}{4\pi\epsilon_0 r_2^2} \cos \theta_2 \quad \text{Eq. 27}$$

$$\vec{E}_y = \frac{Q_{cathode_1}}{4\pi\epsilon_0 r_1^2} \sin \theta_1 + \frac{Q_{cathode_2}}{4\pi\epsilon_0 r_2^2} \sin \theta_2 \quad \text{Eq. 28}$$

Additionally, if two pairs of parallel anode-cathode plates are placed near each other with a separation in the x-axis, as shown in Figure 3-6,, each parallel electrode pair experiences two electric fields: (1) the uniform field due to its own flux of charges between the parallel cathode-anode relation, and (2) the proximate field produced by its own neighbouring electrode plates, as described in Eq. 27 and Eq. 28.

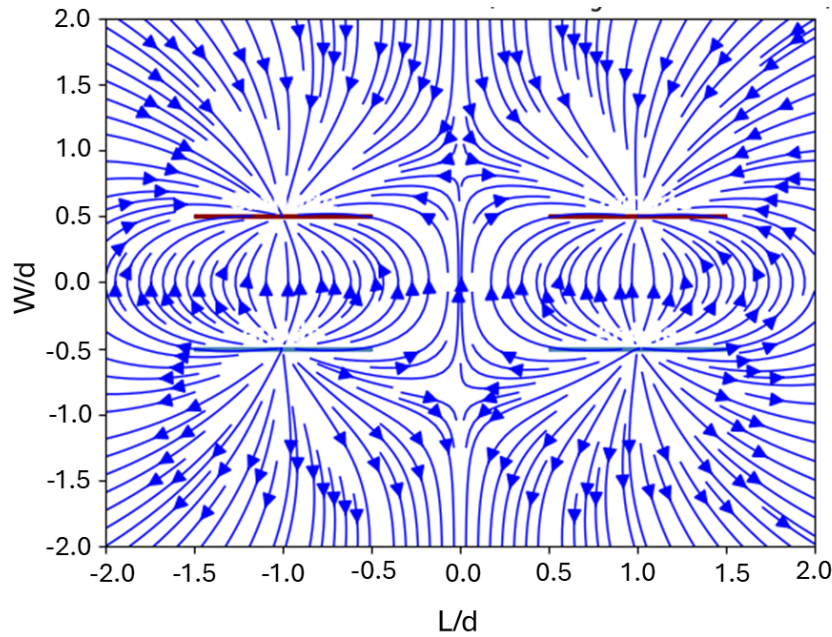


Figure 3-6. MPDA electric field lines from computational mesh between the two parallel pairs of anodes and cathodes with a gap distance d [cathodes-red lines][anodes-blue lines].

Thus, the total electric field \vec{E} experienced in a cell \vec{E}_{ij} located inside the electrodes region can be obtained by using Pythagorean Theorem on the calculated vector components \vec{E}_x and \vec{E}_y from

$$\vec{E} = \vec{E}_{ij} = \sqrt{\vec{E}_x^2 + \vec{E}_y^2} \quad \text{Eq. 29}$$

3.1.3. Townsend's first ionization coefficient (α)

In the breakdown of a gas, usually termed Townsend's breakdown, there are two primary mechanisms that contribute to a significant rise in carriers—gaseous charge production through electron impact;

- the process of ionization
- the process of the cathode charge production through secondary emission [11].

The coefficient α describes the number of electrons produced by a single electron moving 1 cm in the electric field direction during electron-neutral interactions [98]. The second electron produced by the first collision will repeat the same phenomena, impacting another neutral particle to create a third and subsequent accumulative electrons. Therefore, the number of electrons in the gap increases exponentially and this is known as electron avalanche. Through these collisions, ionization occurs at

the moment the neutral particle specie releases an electron, changing its charge [99]. Townsend's first ionization coefficient is expressed as

$$\alpha = Ap \exp \left[-\frac{Bp}{\vec{E}} \right] \quad \text{Eq. 30}$$

where p is pressure, \vec{E} is the electric field, and A and B are coefficients specific to the gas species. The rate of ion-electron pair production from a single electron after the subsequent avalanche on a distance x across the gap d is denoted \bar{n} and determined as [98] [100],

$$\bar{n} = \exp \int_0^d \alpha(x) dx = e^{\alpha d} \quad \text{Eq. 31}$$

Consequently, the electron number density n_e given by a current flowing in the gap after the avalanche effect is then given by [101],

$$n_e = n_{e_0} e^{\alpha d} \quad \text{Eq. 32}$$

where n_{e_0} is the initial electron number density.

3.1.4. Townsend's second ionization coefficient (γ_{SEE})

Secondary electron emission γ_{SEE} is described as the ratio of the secondary electron flux emitted from the cathode surface to the influx of the positive ion bombardment [101] [102].

$$\gamma_{SEE} = \left[\exp \left(\int_0^d \alpha(x) dx \right) - 1 \right]^{-1} \quad \text{Eq. 33}$$

Depending on the application, γ_{SEE} can be treated as a constant [22]. For a constant discharge, the electron density produced by positive ions bombardment, considering secondary electron emission, is defined as [101]

$$n_e = n_{e_0} \frac{e^{\alpha d}}{1 - \gamma_{SEE}(e^{\alpha d} - 1)} \quad \text{Eq. 34}$$

3.1.5. Field emission coefficient (γ_{FE})

Unfortunately, the previously presented equations (which are based on the Paschen curve) improperly describe the breakdown voltage and do not take into account the enhancement effect of the electric field in microgaps. In this micron scale regime, electron field emission plays a significant role in the breakdown phenomena. The Fowler-Nordheim equation takes into consideration the ion-enhanced field emission given by the effects of the electrodes' surface conditions for the breakdown voltage.

Consequently, Boyle and Kisliuk [103] took this approach and defined the field emission coefficient γ_{FE} as the ratio of field emission current incident to the ion current on the electric field \vec{E} given by [22]

$$\gamma_{FE} = K \exp\left(\frac{-6.8 \times 10^7 \phi^{1.5} v(y)}{\vec{E}\beta}\right) \quad \text{Eq. 35}$$

where K is a constant, with an approximate value of 10^7 [11], β is the field enhancement factor (typically for ideal polished metal surfaces this is equal to 50 [104] [11]), ϕ is the work function of the electrode's material, and $v(y)$ is a corrective function. It is insufficient just to consider the coefficients α and γ_{SEE} to estimate the electron density for an applied current-voltage in a micrometre gap separation between the electrodes. Furthermore, the incorporation of the γ_{FE} coefficient in Eq. 36 is needed to consider the field emission effect (FEE), resulting in the following expression [22]:

$$n_e = n_{e_0} \frac{e^{\alpha d}}{1 - (\gamma_{SEE} + \gamma_{FE})(e^{\alpha d} - 1)} \quad \text{Eq. 36}$$

This expression describes the rate of increase in the electron current density for an applied voltage in microgaps.

3.1.6. Ion density n_+

The ion density n_+ at the cathode is related to the total current/electron density in the gap [105]. Each additional electron generated from the initial current comes with an ion, forming an electron-ion pair. Thus, the following relation was made

$$n_+ = n_e - n_{e_0} \quad \text{Eq. 37}$$

Establishing the relation from Eq. 36 with Eq. 37, the ion density can also be expressed as

$$n_+ = n_{e_0} \left[\frac{e^{\alpha d}}{1 - (\gamma_{SEE} + \gamma_{FE})(e^{\alpha d} - 1)} - 1 \right] \quad \text{Eq. 38}$$

3.1.7. Corrective functions $t(y)$ and $v(y)$

According to Miller [106], $v(y)$ in Eq. 35 is a corrective function from the image force effect on the emitted electrons expressed by elliptical integrals in form of

$$y = 3.795 \times 10^{-4} \frac{\sqrt{\vec{E}}}{\phi} \quad \text{Eq. 39}$$

where $v(y)$ is expressed as [106],

$$v(y) = \left[\frac{1+w}{2} \right]^{\frac{1}{2}} [E(k) - (1-w)K(k)] \quad \text{Eq. 40}$$

To facilitate the computation of the corrective functions, a polynomial curve fitting equation were calculated for $v(y)$. Reference values were taken from Miller's table I [106] between values of 0 to 1 of $v(y)$ from Eq. 40, with intervals of 0.01:

$$v(y) = -0.7519y^2 - 0.2744y + 1.0161 \quad \text{Eq. 41}$$

3.1.5. Applied current density

For a given applied current I the following relation needs to be taken into consideration [107],

$$I = n_{e_0} v A = \frac{n_{e_0} q d A}{\Delta t} \quad \text{Eq. 42}$$

where n_{e_0} is the number of free charges per unit volume that flows through a volume segment Ad , q is the amount of charge on each carrier over a specific amount of time Δt . For the development of the dsmcFoam+ code, Δt is the iterative time value that represents the time-step size.

3.1.6. Ionic density distribution

A Maxwell–Boltzmann distribution is applied to determine the allocation and the specific electron-ion number of particles for each cell in the microgap region of the mesh.

At the beginning of the research, it was necessary to define the distribution of ion density, ion temperature, and electron temperature. Therefore, through an independent investigation of these topics, it was identified that all three parameters share the Maxwell–Boltzmann distribution, which will be explained.

To find a practical and straightforward solution that does not increase computational resource requirements for ion distribution along the mesh cell columns, the Boltzmann energy distribution was adopted based on elementary discharge behaviour (Figure 3-7). Initially, at time $t=0$, the electron and ion densities are uniformly equal (Figure 3-7-A). Subsequently, the low mass warm electrons quickly move to the wall, forming sheaths, and the bulk plasma becomes quasi-neutral (Figure 3-7-B) [108] [109]. In this phase, as shown in Figure 3-7-B, the ion density approximates a Maxwell–Boltzmann distribution curve similar to the electron density.

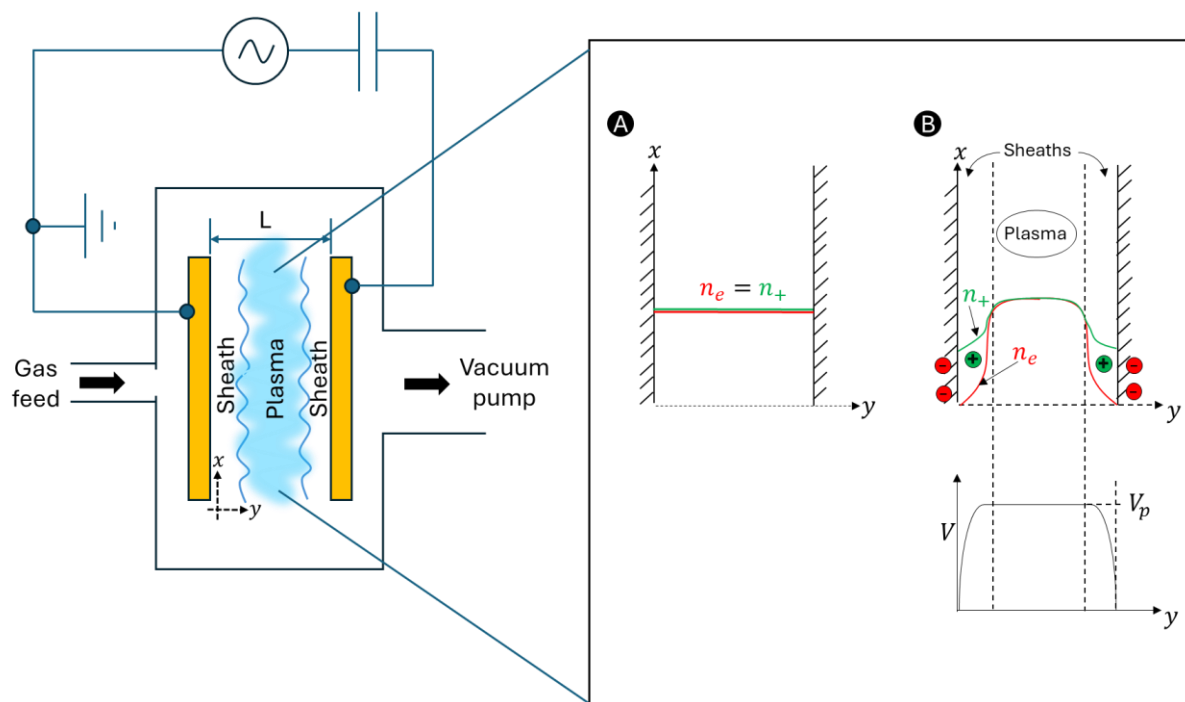


Figure 3-7. Elementary discharge behaviour diagram; A) Uniform electron and ion densities at $t=0s$. B) Quasi-neutral bulk plasma and its potential [108].

Concurrently, the potential follows a similar curve (Figure 3-7-B), where the ion temperature is calculated from the potential using the same Maxwell–Boltzmann distribution approach by converting the potential into energy, as detailed in section 3.2.4. This approach, due to its simplicity, does not provide high accuracy, specially at different electrode configurations, but correction factors (section 3.2.4) are introduced to approximate a more realistic scenario. For electron temperature, thermal equilibrium properties were considered, where electrons are generally near thermal equilibrium compared to ions, which generally are not [108]. The Maxwellian distribution for electrons is discussed in section 3.2.3.

Given the quasi-neutrality of the density of species where $n_e \approx n_+$, both ion and electron distributions in the elementary discharge behaviour are approximately the same. Therefore, the distribution is calculated from the following function [110] [111]:

$$f(v) = 4\pi v^2 \left(\frac{m_e}{k_B T_e} \right)^{3/2} \exp\left(\frac{-m_e \vec{v}^2}{2k_B T_e} \right) \quad \text{Eq. 43}$$

where $f(v)$ is the probability density for finding a particle with a velocity v , m_e is the electron mass, k_B is the Boltzmann constant, and T_e is the local electron temperature.

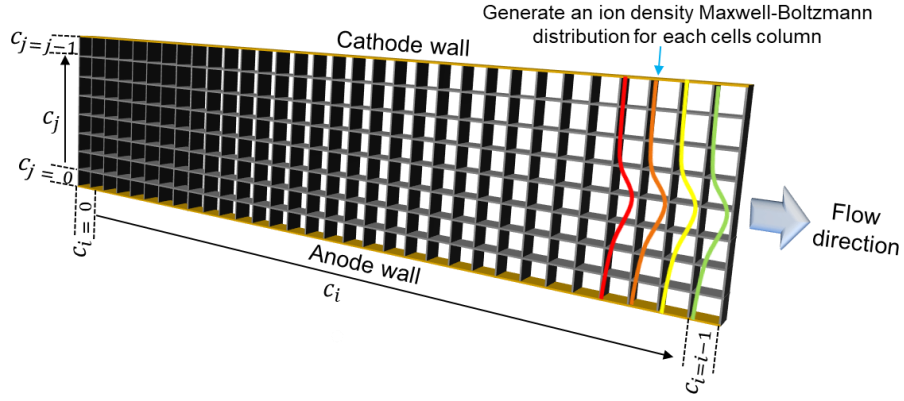


Figure 3-8. Micro-plasma discharge algorithm, representation of the ion density distribution per cell column in a mesh between parallel electrode plates.

In order to applied the Maxwell–Boltzmann distribution for the computational mesh based on the elementary discharge behaviour observed on Figure 3-7, the Maxwell–Boltzmann distribution is calculated for each cell column by integrating along the gap, as shown in Figure 3-8, and is a function of the temperature and the velocity of the electron, keeping the distribution shape on Figure 3-7-B. Thus, computing the distribution for each cell column allows the calculation of ion species by the different neutral/gas species located along the gap at the time Δt . Providing a simplistic method, but closely to a reliable scenario.

The calculation of the electron temperature in each column $T_{e,i}$ is possible once the average electric field \bar{E}_{ij} is obtained from the column of cells where the electron is located (Eq. 29) by the relation between the electric potential energy U_E and the average kinetic energy per particle K_E . Therefore,

$$U_E = \int_0^d q \vec{E}_{ij} dx = q \vec{E}_{ij} d \quad \text{Eq. 44}$$

where q is the charge of the particle exposed to an electric field \vec{E}_{ij} [96]. Additionally, the average kinetic energy per electron K_E is given by [110],

$$K_E = m_e \vec{v}_e^2 = \frac{3}{2} k_B T_e \quad \text{Eq. 45}$$

The change in the kinetic energy of the particle, in this case an electron, is equal to the change in its potential energy from the law of conservation of energy. Therefore the change in the potential of the electron in an electric field can be expressed as [96],

$$\Delta K = -\Delta U_E \quad \text{Eq. 46}$$

Solving for T_e , the temperature of the electron is

$$T_e = \frac{3 U_E}{2 k_B} \quad \text{Eq. 47}$$

To solve Eq. 43, once the temperature of the electron is obtained, the average thermal speed of the Maxwell–Boltzmann distribution can be calculated by [110] [112],

$$v_{e,ave} = \sqrt{\frac{8k_B[T_e]}{\pi m_e}} \quad \text{Eq. 48}$$

Additionally, the most probable speed of the distribution can be obtained as [110] [112]

$$v_{e,prob} = \sqrt{\frac{2k_B[T_e]}{m_e}} \quad \text{Eq. 49}$$

Therefore, for the assignation of a velocity from the Maxwell–Boltzmann distribution along a column of cells, the width of the curve needs to be obtained and segmented by the number of cells in the column. For this, the probability distribution, Eq. 43, is a function of the thermal velocity v , consequently, as v is the independent variable, the width of the curve can be found by calculating the approximation of the maximum thermal speed $v_{e,max}$, given by,

$$v_{e,max} = \sqrt{\frac{-2K_B T_e \ln(1 - k)}{m_e}} \quad \text{Eq. 50}$$

where $v_{e,max}$ represents the total width of the distribution curve, k is the confidence interval set as 0.998, an acceptable value allowing the width range to capture the distribution shape in the cell column. The closer k is to unity, it will cover more the width of the distribution curve tending to infinity. Then the distribution width is segmented by the total number of cells $\sum c_j$ in the column, as follows,

$$v_{seg} = \frac{v_{e,max}}{\sum c_j} \quad \text{Eq. 51}$$

Therefore, each cell c_j in the column of the mesh contains a corresponding thermal velocity expressed as v_{ij} . Where v_{ij} is the cumulative sum of the v_{seg} from the predecessor cells, starting from the lowest to the highest cell position of the column,

$$v_{ij} = \sum_0^j v_{seg} \quad \text{Eq. 52}$$

As result, the probability of the Maxwell–Boltzmann distribution for each cell is given by the function $f(v_{ij})$ from Eq. 43.

In order to use this probability as a distribution factor to calculate the electron density in a cell at (i, j) , $f(v_{ij})$ must be normalised through division by the probability distribution function of the average thermal speed, $f(v_{e,ave})$, obtained from Eq. 43 and Eq. 48:

$$\widehat{f(v)}_{ij} = \frac{f(v_{ij})}{f(v_{e,ave})} \quad \text{Eq. 53}$$

Thus, to calculate the electron density for each cell according to the position i and j it has in the mesh, $\widehat{f(v)}_{ij}$ is multiplied by $n_{e_0,ij}$ acquired from Eq. 32, as it is following shown:

$$n_{e_0,ij} = n_{e_0}(\widehat{f(v)}_{ij}) \quad \text{Eq. 54}$$

Therefore, to calculate the electron density after the breakdown voltage in a specific cell at (i, j) , the distribution factor $\widehat{f(v)}_{ij}$ is incorporated in the Eq. 36, resulting in the following expression,

$$n_{e,ij} = [n_{e_0}(\widehat{f(v)}_{ij})] \frac{e^{\alpha d}}{1 - (\gamma_{SEE} + \gamma_{FE})(e^{\alpha d} - 1)} \quad \text{Eq. 55}$$

Consequently, by the relation of electron-ion pairs where $n_e \approx n_+$ described in section 3.1.6 from Eq. 38, the ion density n_+ assigned to a specific cell at (i, j) is given by,

$$n_{+,ij} = [n_{e_0}(\widehat{f(v)}_{ij})] \left[\frac{e^{\alpha d}}{1 - (\gamma_{SEE} + \gamma_{FE})(e^{\alpha d} - 1)} - 1 \right] \quad \text{Eq. 56}$$

For the micro-plasma discharge algorithm, $n_{+,ij}$ represents the density of gas particles to be accelerated in a cell located at (i, j) to simulate the micro-plasma effect on the flow. In order to emulate the effects of ion interaction with gas particles as a simplistic method that provides a lightweight solution for plasma simulation in microgaps. Therefore, Eq. 56 provides the number of gas particles that need to be accelerated in each cell, moreover in the following section it will describe how much the gas particles requires to be accelerated by the ionic interactions.

3.1.7. Particle acceleration

Once the ion density and its distribution are obtained, the energy of the positive ions must be calculated to determine the acceleration of gas particles to be applied in dsmcFoam+.

The ion's kinetic energy $K_{E,+}$ is obtained by [113],

$$K_{E,+} = \frac{q\vec{E}_{ij}}{n_{gas}(\Delta t)\sigma} \quad \text{Eq. 57}$$

where \vec{E}_{ij} is the electric field experienced in the cell, $n_{gas}(\Delta t)$ is the gas particle density as a function of the time step and σ is the collision cross-section between the electrons and gas particles.

It is important to emphasise the discretisation of both particle densities n_{e_0} and n_{gas} as a function of the timestep Δt for the algorithm purpose. The first variable is already discretised solving n_e from Eq. 42, but for the case of n_{gas} , it follows that

$$n_{gas}(\Delta t) = \frac{N_A \rho}{M_{mass}} \Delta t \quad \text{Eq. 58}$$

where N_A the Avogadro constant, M_{mass} the molar mass, T_{gas} the gas temperature, and ρ the gas density.

Additionally, $K_{E,+}$ must consider the amount of energy transferred to a DSMC particle in a cell located at (i, j) . Each DSMC particle represents a large number of real gas atoms/molecules, F_N . If the ion particle density per unit volume $n_{+,ij}$ in the cell is less than F_N , $K_{E,+}$ needs to be multiplied by a transfer factor $C_{P_{DSMC}}$, the purpose of which is to assign the proportional amount of energy to a DSMC particle:

$$C_{P_{DSMC}} = \frac{n_{+,ij}}{F_N} \quad \text{Eq. 59}$$

Consequently, the ion energy $K_{E,+}$ assigned to a DSMC particle when $n_{+,ij} < F_N$, is defined as

$$K_{E,+} = \frac{q\vec{E}_{ij}}{n_{gas}(\Delta t)\sigma} C_{P_{DSMC}} \quad \text{Eq. 60}$$

Therefore, if $n_{+,ij} < F_N$ then just one DSCM particle in the cell at (i, j) will receive the ion energy. Afterwards, the kinetic energy is converted into the average thermal speed $v_{+,ave}$ through:

$$v_{+,ave} = \sqrt{\frac{8K_{E,+}}{\pi m_{gas}}} \quad \text{Eq. 61}$$

Then the average thermal speed is converted to the acceleration \vec{a}_{ij} on the DSMC particle by dividing $v_{+,ave}$ by the characteristic flow length, which is d , the gap between the electrodes [114]

$$\vec{a}_{ij} = \frac{(v_{+,ave})^2}{d} \hat{r}_{ij} \quad \text{Eq. 62}$$

If $v_{+,ave}$ is in function of the $K_{E,+}$ consequently \vec{a}_{ij} is in function \vec{E}_{ij} . Hence, the vector components x and y of \vec{a}_{ij} are defined by the unit vector \hat{r}_{ij} given from the distance r between the particle and its direction to the electric field.

Subsequently, the velocity vector \vec{v}_{ij} for a cell in the mesh located at (i, j) is calculated by

$$\vec{v}_{ij} = \vec{a}_{ij} \cdot \Delta t \quad \text{Eq. 63}$$

where Δt is the timestep set for each iteration. Finally, the DSMC particle is accelerated by adding the calculated \vec{v}_{ij} velocity to the current velocity $\vec{v}_{o,ij}$, resulting in the following velocity,

$$\vec{v}_{p,ij} = \vec{v}_{o,ij} + \vec{v}_{ij} \quad \text{Eq. 64}$$

This is an iterative process, whereby $\vec{v}_{o,ij}$ is updated in each cell when it is located between the defined electrodes area inside the mesh and experiences an ionization.

3.1.8. Leapfrog method

A leapfrog method is implemented in the code to avoid the non-physical increase of energy of the DSMC particles given by the numerical solutions during the acceleration. Since $n_{+,ij} \ll F_N$ is in the majority of the cases, only a small number of DSMC particles are accelerated. Therefore, Eq. 63 is split into two parts; half of the velocity is added to $\vec{v}_{p,ij}^t$ before the movement part of the DSMC algorithm, then the second half after the collisions with a velocity $\vec{v}_{p,ij}^{t+\Delta t/2}$ [115]. At the end of the timestep, the particle will be moving at $\vec{v}_{p,ij}^{t+\Delta t}$ [116] [117],

$$\vec{v}_{p,ij}^{t+\Delta t/2} = \vec{v}_{p,ij}^t + \frac{1}{2}\vec{v}_{ij} \quad \text{Eq. 65}$$

$$\vec{v}_{p,ij}^{t+\Delta t} = \vec{v}_{p,ij}^{t+\Delta t/2} + \frac{1}{2}\vec{v}_{ij} \quad \text{Eq. 66}$$

3.1.9. Wall-particle temperature exchange

The micro-plasma discharge algorithm is an extension controller of the dsmcFOAM+ solver. This algorithm does not compute any energy or temperature exchange from the collision of particles with the wall by its own; it focuses solely on determining the acceleration gradient of the preexisting neutral particles (gas species) in the mesh. Once the increase in acceleration is defined by the algorithm, the exchange of energy during wall-particle collisions is handled by dsmcFOAM+.

All simulations have been set with fully diffuse wall characteristics at room temperature (300 K), as defined by the dsmcFOAM+ solver. These simulations employ the Variable Hard Sphere (VHS) collision model along with the phenomenological Larsen-Borgnakke internal energy redistribution technique [90]. The Larsen-Borgnakke model is a phenomenological approach to handle the exchange of internal and translational energies during inelastic inter-particle collisions. More details about this method can be found in reference [118].

3.2. Algorithm validation

Cases from References [104] and [119] have been utilised to verify the accuracy of the micro-plasma discharge algorithm model's predicted ion density and distribution. Since the device and the geometry of the electrode positioning in a micro-gap are being proposed for the first time, no previous studies or test results are available for this specific electrode configuration. Consequently, the algorithm developed in this thesis was validated by comparing simulation results using a basic geometry—two parallel electrode plates with a micro-gap distance—a more common configuration for which ion density validation is well established. The primary objective, however, was to validate these computational results through experimental testing, which was attempted in Chapter 6 for validation of the flow velocity, thrust, and specific impulse.

3.2.1. Validation case 1

A 15 μm gap DC breakdown discharge based on a 1D PIC-DSMC simulation case was investigated in Reference [104]. The flow of charged particles across the gap between electrode plates may be seen using a 250 by 250 cell grid with a temporal resolution of 2.66 ns. A timestep at 2×10^{-14} s was used, with an applied voltage of 215 V in atmospheric conditions consisting of 78.8% N₂ and 21.2% O₂ at 300 K. The cathode is iron, the field enhancement factor (due to surface roughness) was taken as 50, and the secondary yield was set as 0.026. Similarly, a micro-plasma discharge algorithm case with 250 cells and a cell size of 0.06 μm was used, taking the boundary conditions from the PIC-DSMC case, with the exception of the timestep being set as 2.66 ns, fulfilling the requirements for Δt according to Section 3.1.3, an applied current of 1 μA and a work function for a 1 μm x 1 μm iron cathode of 4.5eV [120].

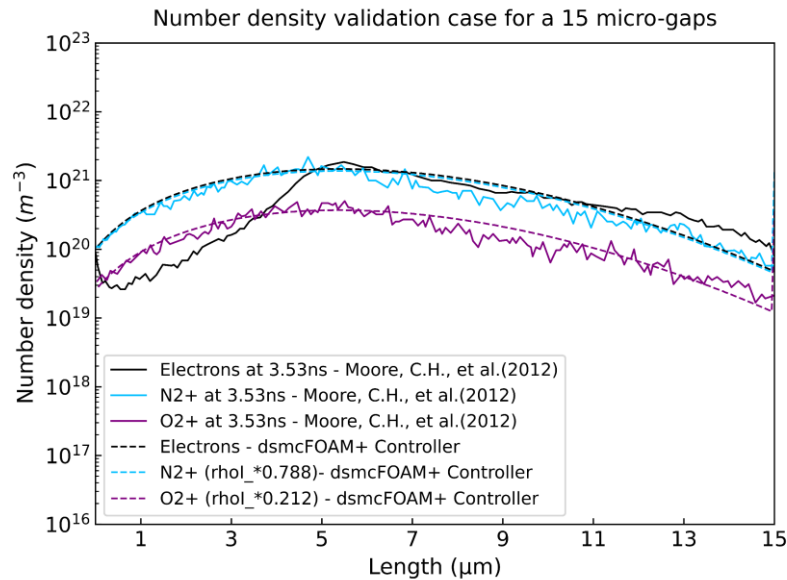


Figure 3-9. Ion and electron density results from 1D PIC-DSMC simulation [104] and micro-plasma discharge algorithm on a 15 μm gap at 2.66 ns and 215 V in atmospheric conditions.

The ion and electron densities were measured in each cell across the microgap and the results are shown in Figure 3-9. Dashed and solid lines represent the results obtained from the dsmcFoam+ code and Reference [104], respectively.

The code particle densities results show continuous values given by the calculation of the Maxwell–Boltzmann distribution from Eq. 43, meanwhile the 1D PIC-DSMC simulation presents the discretised solution of the densities by inserting electrons directly in the domain to interact with the gas particles. Due to the random character of the particle behaviour [111], the breakdown [100] and the field emission [121], it is challenging to acquire precise findings when it is compared with alternative methods. The results from dsmcFoam+ show a N2⁺ and O2⁺ ion density peaks of $1.34 \times 10^{21} \text{ m}^{-3}$ and $3.60 \times 10^{20} \text{ m}^{-3}$, respectively, both at 5.4 μm. The 1D PIC-DSMC solution predicts the highest density values of $2.2 \times 10^{21} \text{ m}^{-3}$ for N2⁺ at 4.7 μm and $5.03 \times 10^{20} \text{ m}^{-3}$ for O2⁺ at 5.5 μm. For the electron density, the PIC-DSMC results show an initial a decrease and a steeper upward tilt to the density curvature trend before reaching 5.5 μm along the gap. According to Reference [104] this occurs as a result of the Auger neutralization, where a quick stream across the gap creates ions, slowing down the acceleration during the process towards the cathode. However, the same stream neutralises some of the created ions, decreasing the number of electrons by recombination. The micro-plasma discharge algorithm calculates the total electron density from the applied current and the ionization of the gas species without any reduction in density by neutralisation interactions

between charged particles and has a continuous curvature shape. After reaching a peak value at around $5.5 \mu\text{m}$, both methods predict similar electron densities.

3.2.2. Validation case 2

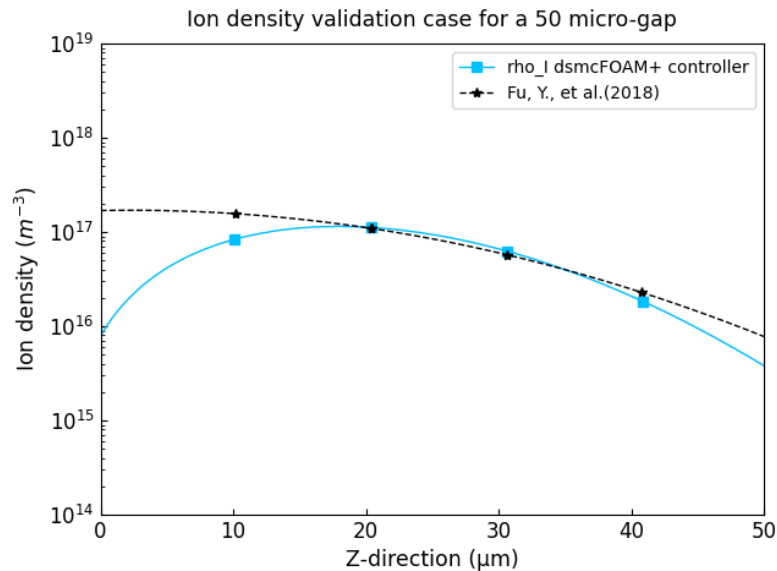


Figure 3-10. Ar^+ density distribution in a $50 \mu\text{m}$ gap Reference [119] and the micro-plasma discharge algorithm at 500 torr with 150 V.

In Reference [119], a two-dimensional fluid model was used to analyse the Townsend breakdown DC voltages in microgaps based on Paschen's curves. A $450 \mu\text{m}$ height hemi-ellipsoidal protrusion with a $200 \mu\text{m}$ radius was set on the $1000 \mu\text{m}$ radius cathode's surface, meanwhile the anode remains as a $1000 \mu\text{m}$ radius plane. A 150 V DC voltage is applied with a secondary emission coefficient fixed at 0.1. The working gas is argon at 300 K and 500 torr.

To compare the micro-plasma discharge algorithm with the model from Reference [119], the ion density was measured from the minimum point distance of $50 \mu\text{m}$ between the electrodes. The same boundary conditions were set as in the electrode plane plates case with additional considerations to fulfil the code's execution requirement; the electrode material was set as Au metal plates with a work function of 5.1 eV [120] and an applied current of 0.35 mA. The gas constants A and B were set as 12 and 180 respectively [122]. Therefore, the size of each cell in the mesh was set to $1 \times 1 \times 1 \mu\text{m}$, and the timestep was set to 1ns, which is less than the t_{res} value of 2.37ns.

As shown in Figure 3-10, the Ar^+ ion densities from both methods have similar values. Therefore, mismatches or major changes in the ion density distribution between $0\mu\text{m}$ and $20 \mu\text{m}$ along the Z-axis, as well as minor deviations between $40 \mu\text{m}$ and $50 \mu\text{m}$ are displayed. This is due to the fact that the values of the electric field enhancement will differ depending on the method utilised; for example, the electric field enhancement between the protrusion tip and the opposing electrode is described by

an exponential distribution in Reference [123]. Meanwhile, the micro-plasma discharge algorithm takes into account the electric field with the enhancement factor as an average value along the distance between the electrodes (Z-direction for this case), where the ion allocation is a function of the Maxwell–Boltzmann distribution (Eq. 53). Where the distribution of each method varies according to the shape of the function.

3.2.3. Electron temperature validation

Correction factors were required to take the theoretical electron temperature T_e closer to a more reliable values $T_{e_{ref}}$ satisfying the cases displayed on Table 6. Allowing for a more precise distribution curvature shape between the cell columns in the mesh for the micro-plasma discharge algorithm.

Table 6. Comparison between corrected electron temperature T_{e_c} and reference values $T_{e_{ref}}$ with their respective boundaries conditions. Showing a close approximation between T_{e_c} and $T_{e_{ref}}$. Timesteps (Δt) of 1 ns were set on cases where it was specified in the reference, denoted with (*).

Type	Gases	P (Torr)	Gap (μm)	E (V/m)	I (mA)	n_e (m^{-3})	Δt (ns)	$T_{e_{ref}}$ (eV)	T_{e_c} (eV)	Ref.
DC	Ar	450	10	2×10^7	.055	-	1*	2	1.52	[124]
DC	Ar	760	250	1.52×10^6	3.5*	-	10	2.25	2.21	[124]
DC	Ne/H2	0.74	100	5×10^6	.01*	-	1*	17	17.1	[125]
										[126]
DC	He/H2	0.66	250	2.8×10^6	.01*	-	1*	20	21.1	[125]
										[127]
DC	Ar	760	500	$\approx 1.85 \times 10^6$	-	3×10^{17}	1*	3	1.51	[128]
DC	Cs	1	30	2.3×10^5	.001	-	1*	0.07-	0.03-0.08	[129]
				3.3×10^5				0.08		[130]

To correct the electron temperature, the most probable speed $v_{e,i,prob}$ from Eq. 49 is obtained. Then, the electron energy requires to be recalculated by solving the kinetic energy K_E as a function of $v_{e,prob}$ and the addition of the correction factors $C_{e-n}C_p$, i.e.

$$K_E' = (m_e v_{e,prob}^2) C_{e-n} C_p \quad \text{Eq. 67}$$

Thus, the recalculated electron temperature is given by,

$$T_e = \frac{2 K_E'}{3 k_B} \quad \text{Eq. 68}$$

where K_E' is the corrected kinetic energy of the electron, C_{e-n} is the correction factor of the transferred energy,

$$C_{e-n} = \frac{2[m_e n_{e_0}][m_{gas} n_{gas}(\Delta t)]}{[m_e n_{e_0} + m_{gas} n_{gas}(\Delta t)]^2} \quad \text{Eq. 69}$$

and C_p a correction factor in function of the pressure,

$$C_p = \frac{P}{119700} \left[\frac{539 \left(\frac{P}{133} \right) - 350}{\left(\frac{P}{133} \right)^2 - 0.04 \left(\frac{P}{133} \right) - 0.383} \right] \quad \text{Eq. 70}$$

Both factors provide a closer approach to a more realistic electron temperature by taking into account the energy exchange between electrons and neutral gas particles.

The factor C_{e-n} was developed based on the transferred energy factor C_m during a collision between a sphere of mass m and another sphere of mass M [56],

$$C_m = \frac{2mM}{(m + M)^2} \quad \text{Eq. 71}$$

The adaptation of C_m is based on considering each sphere to have mass in proportion to the number density of the species it represents. Therefore, one sphere represents the electrons with mass m_e multiplied by the electron number density n_{e_0} from the applied current. Similarly, a sphere can represent the gas species with mass m_{gas} multiplied by the number density n_{gas} .

To provide a statistical analysis of the improvement achieved by adding the correction factors C_p and C_{e-n} to the theoretical electron temperature T_e to get closer to the reference temperature $T_{e_{ref}}$, it was performed the following steps for each case:

1. Calculate the absolute differences between $(T_{e_{ref}} - T_e)$, $(T_{e_{ref}} - T_e * C_p)$, $(T_{e_{ref}} - T_e * C_{e-n})$, and $(T_{e_{ref}} - T_e * C_{e-n} C_p)$.
2. Compare the mean absolute differences $(T_{e_{ref}} - T_e)$, $(T_{e_{ref}} - T_e * C_p)$, $(T_{e_{ref}} - T_e * C_{e-n})$, and $(T_{e_{ref}} - T_e * C_{e-n} C_p)$ to assess the improvement achieved by adding the correction factors.

Comparison of the Statistical mean difference in temperature T_e by the application of correction factors

Table 7. Comparison of mean absolute differences in electron temperature T_e calculations with variations of the correction factors

	$ T_{e_{ref}} - T_e $ (eV)	$ T_{e_{ref}} - T_e * C_p $ (eV)	$ T_{e_{ref}} - T_e * C_{e-n} $ (eV)	$ T_{e_{ref}} - T_e * C_{e-n} C_p $ (eV)
	30626.51	18316.3	0.54	0.48
	7382021.87	4417476.6	1.44	0.04
	315451.04	94146.5	40.29	0.10

	3769650.41	647564.8	102.83	1.10
	748.76	446.9	0.48	1.49
	6657.23	2425.5	0.10	0.00
Mean absolute difference	1917525.97	863396.11	24.28	0.54

- Theoretical T_e : This represents the mean absolute difference between the reference temperature and the original theoretical electron temperature without any correction factors applied. The average absolute difference is approximately 1,917,525 eV.
- With C_p correction: After applying the C_p correction factor to the theoretical electron temperature, the mean absolute difference decreases significantly to approximately 863,396 eV, although not as much as with the C_{e-n} correction.
- With C_{e-n} correction: Applying the C_{e-n} correction factor also reduces the mean absolute difference. The average absolute difference with the C_{e-n} correction is approximately 24.28 eV. This suggests that the C_{e-n} correction factor helps to bring the theoretical temperature closer to the reference temperature.
- With C_p and C_{e-n} correction: When both the C_p and C_{e-n} correction factors are applied simultaneously, the mean absolute difference decreases even further to approximately 0.54 eV. This indicates a very close alignment between the corrected theoretical temperature and the reference temperature.

Overall, the statistical analysis shows that adding both the C_p and C_{e-n} correction factors to the theoretical electron temperature significantly improves its alignment with the reference temperature, reducing the mean absolute difference to a very small value

A Pearson Correlation Coefficient analysis was done in order to estimate the approximation $T_e * C_{e-n}C_p$ where shows a coefficient of 0.992. This indicates a very strong positive linear relationship between the solver results and the referenced results. Obtaining a very low p-value of 0.0001 which confirms the statistical significance of this correlation. The uncertainty with a margin of error between 0.900, 0.999 in the correlation coefficient is reflected in the confidence interval, which is very close to 1, indicating high precision in the estimate of the correlation coefficient. Demonstrating the confidence of using both correction factor to estimate a more reliable electron temperature values.

3.2.4. Ion temperature validation

By contrasting the ion energy from several sources, the micro-plasma discharge algorithm verification was possible. The dependence of the thermal velocity ($v_{+,ave}$) as a function of the ion's energy ensures

a proper acceleration (\vec{a}_{ij}) value on gas particles for a valid flow profile, see Eq. 61. Solutions from $K_{E,+}$ (Eq. 60) without correction factors provides irrationally high energy values compared with conventional agreements [124], [131], [132], [133], and [134]. Three factors influence the proper calculation of $K_{E,+}$ values; (1) the stochasticity of the methods to describe and define the ion behaviour and its parameters, (2) the adaptation of discretised n_{e_0} , and n_{gas} in Eq. 60, and (3) the linear increase of the electric field in the function.

1. To approximate the ion's kinetic energy values closer to conventional agreements [124], [131], [132], [133], and [134], it is required to consider the stochasticity of the ion's energy by calculating the probability of its velocity by the Maxwell-Boltzmann probability distribution,

$$f(v_{+,prob}) = 4\pi v_{+,prob}^2 \left(\frac{m_+}{k_B T_+}\right)^{3/2} \exp\left(\frac{-m_+ v_{+,prob}^2}{2k_B T_+}\right) \quad \text{Eq. 72}$$

where m_+ is the ion's mass and the temperature T_+ can be calculated in similar manner as Eq. 47 but focusing on the ion energy instead,

$$T_+ = \frac{2K_{E,+}}{3k_B} \quad \text{Eq. 73}$$

where $v_{+,prob}$ is defined as,

$$v_{+,prob} = \sqrt{\frac{2k_B [T_+]}{m_+}} \quad \text{Eq. 74}$$

2. $K_{E,+}$ and σ are continuous equations, therefore the decrease in n_{e_0} and n_{gas} by being a function of Δt for discretisation affects the consideration of the continuity of the equations. Thus, discretised n_{e_0} and n_{gas} are taken as continuous values to calculate $K_{E,+}$. The resultant energy is increased by low densities in a continuous equation, where particles reduce the energy loss by having fewer collisions with other particles in their surroundings. To fix this problem, a dimensionless correction factor in the form of a collision cross section was implemented,

$$f(\sigma) = \frac{3.689(\log_{10} \sigma)^2 + 161.8 \log_{10} \sigma + 1774.3}{10} \quad \text{Eq. 75}$$

3. For the correction of the linear increase of the electric field \vec{E} to a more realistic exponential increase, the electric field correction factor $f(\vec{E})$ was set as,

$$f(\vec{E}) = \frac{2.11 \times 10^{-9} \vec{E}^{1.653}}{1 \times 10^5} \quad \text{Eq. 76}$$

Consequently, the corrected ion's kinetic energy is,

$$K'_{E,+} = K_{E,+} f(v_{+,prob}) f(\sigma) f(\vec{E}) \quad \text{Eq. 77}$$

where $K'_{E,+}$ replaces the kinetic energy from Eq. 57 with closer values to conventional agreements.

Table 10 shows five microgap DC discharge cases based in different works on micro-plasma effect analysis, providing the ion temperature in electronvolts (eV), making possible to contrast them with the temperature results from the micro-plasma discharge algorithm for dsmcFoam+. Corrected ion temperature T_{+c} , from $K'_{E,+}$ found from the code, shows a closer approximation to the reference temperatures, T_{+ref} .

Table 8. Comparison between corrected ion temperature T_{+c} and reference values T_{+ref} with their respective boundaries conditions. Timesteps (Δt) of 1 ns were set on cases where the timestep was not specified in the reference, denoted with (*).

Type	Gases	P (Torr)	Gap (μm)	E (V/m)	I (mA)	n_e (m^{-3})	Δt (ns)	T_{+ref} (eV)	T_{+c} (eV)	Ref.
DC	N2	760	50	7×10^6	5mA	-	1*	40	38.46	[131]
DC	N2	760	1	5×10^7	1 μA	-	943	15.6	15.65	[133]
DC	Ar	700	100	5.2×10^6	0.2 $\mu\text{A}/\mu\text{m}^2$	-	1*	0.83	0.93	[134]
DC	Ar	10	50	2.84×10^6	5 mA	-	1*	76	76.78	[132]
DC	Ar	760	250	1.52×10^6	3.5 mA	-	10	0.05	0.03	[124]

For the case of the ion temperature, to provide a statistical analysis of the improvement achieved by adding the correction factors $f(\sigma)$ and $f(\vec{E})$ to the theoretical ion temperature T_+ to get closer to the reference temperature T_{+ref} , it was performed the following steps for each case:

1. Calculate the absolute differences between $(T_{+ref} - T_+)$, $(T_{+ref} - T_+ * f(\sigma))$, $(T_{+ref} - T_+ * f(\vec{E}))$, and $(T_{+ref} - T_+ * f(\sigma) f(\vec{E}))$.
2. Compare the mean absolute differences $(T_{+ref} - T_+)$, $(T_{+ref} - T_+ * f(\sigma))$, $(T_{+ref} - T_+ * f(\vec{E}))$, and $(T_{+ref} - T_+ * f(\sigma) f(\vec{E}))$. to assess the improvement achieved by adding the correction factors.

Table 9. Comparison of mean absolute differences in ion temperature T_+ calculations with variations of the correction factors

$ T_{+ref} - T_+ $ (eV)	$ T_{+ref} - T_+ * f(\sigma) $ (eV)	$ T_{+ref} - T_+ * f(\vec{E}) $ (eV)	$ T_{+ref} - T_+ * f(\sigma) f(\vec{E}) $ (eV)
6.15	123.66	13.16	0.05
55.50	348.03	0.68	0.10

	12562.42	78200.33	63.60	0.78
	13.83	85.90	0.05	0.02
Mean absolute difference	3159.47	19689.48	19.37	0.24

- Theoretical T_+ : This represents the mean absolute difference between the reference temperature and the original theoretical ion temperature without any correction factors applied. The average absolute difference is approximately 3,159 eV.
- With $f(\sigma)$ correction: After applying the $f(\sigma)$ correction factor to the theoretical ion temperature, the mean absolute difference increases significantly to approximately 19,689 eV but brings the nominal value closer to the T_{+ref} when $f(\vec{E})$ is applied.
- With $f(\vec{E})$ correction: Applying the $f(\vec{E})$ correction factor also reduces the mean absolute difference. The average absolute difference with the $f(\vec{E})$ correction is approximately 19.37 eV. This suggests that the $f(\vec{E})$ correction factor helps to bring the T_+ closer to the T_{+ref} .
- With $f(\sigma)$ and $f(\vec{E})$ correction: When both the $f(\sigma)$ and $f(\vec{E})$ correction factors are applied simultaneously, the mean absolute difference decreases even further to approximately 0.24 eV. This indicates a very close alignment between the corrected theoretical temperature and the reference temperature.

Overall, the statistical analysis shows that adding both the $f(\sigma)$ and $f(\vec{E})$ correction factors to the theoretical ion temperature significantly improves its alignment with the reference temperature, reducing the mean absolute difference to a very small value.

Computing a Pearson Correlation, it was obtained a coefficient of 0.99985 indicates a very strong positive relationship between $T_+ * f(\sigma)f(\vec{E})$ and T_{+ref} . With a P-value: 0.000145 being a very small value close to zero, indicating that the correlation is statistically significant. This means that there is a very low probability that the observed correlation occurred by chance. This high correlation suggests that the corrected ion temperature ($T_+ * f(\sigma)f(\vec{E})$) is very closely aligned with the reference temperature T_{+ref} , indicating that the corrective model is quite accurate in this case.

3.3. Simulation cases

A $1\ \mu\text{m}$ deep and $50\ \mu\text{m}$ wide microchannel with two inlets and a single outlet is considered, as shown in Figure 3-11. Half symmetry and the mesh was constructed using blockMesh in OpenFOAM. A $2.5 \times 2.5 \times 1\ \mu\text{m}$ cell size was used, and there were a total of 4612 cells in the mesh. For all situations, the timestep Δt was adjusted to 1ns to satisfy the restriction imposed by Eq. 24. With a cell residence time t_{res} of 5ns and an average collision time t_c of 5.07ns. Considering a N2 particle number density of $2.41 \times 10^{20}\ \text{m}^{-3}$ with a λ of $2.14 \times 10^{-3}\ \text{m}$ and a mass of $4.64 \times 10^{-26}\ \text{kg}$. Temperature of the N2 gas was set at 300K and an estimated speed of 422.53m/s was computed.

Three plane-electrode configurations were set; (1) one anode/two cathodes, (2) two anodes/two cathodes, and (3) one anode (extended)/two cathodes. To simplify the naming of each configuration, they will be referred as configuration 1, 2, and 3, respectively. In each configuration, two cathodes were placed on the top surface of the microchannel and the location of the anodes are varied in each case.

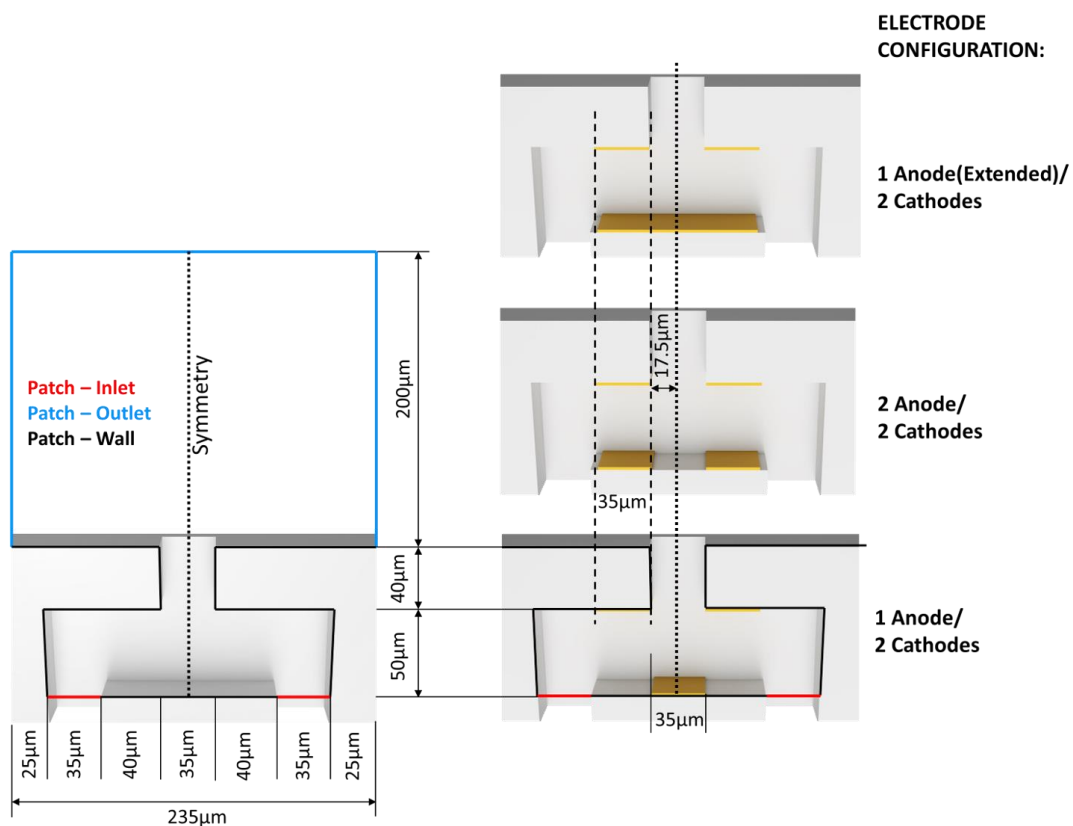


Figure 3-11. Geometry for a double inlet microchannel with a single outlet orifice. Orange, blue and dark lines represent the inlets, outlet, and walls respectively. On the right-hand side, three configurations are shown: (a) 1 anode/2 cathodes, (b) 2 anodes/2 cathodes, and (c) 1 anode extended/2 cathodes.

The electrode surface area was set as $35 \times 1 \mu\text{m}$, with the exception of configuration 1, where the anode surface was defined as $105 \times 1 \mu\text{m}$. The work function was taken as 4.5 eV as several different materials are near this value such as pristine gold (4.6), and a SEE coefficient of 0.02 to make a more general assumption on the selection of the electrode material.

The working gas was nitrogen at 300 K and three inlet pressures were tested; 10 kPa, 50 kPa, and 100 kPa. To simulate vacuum conditions an outlet pressure of 1 Pa was established, with a $200 \mu\text{m}$ wide external expansion region outside the efflux section.

Applied DC currents of $10 \mu\text{A}$, $50 \mu\text{A}$ and $100 \mu\text{A}$ were set for each tested voltage of 100 V, 400 V, 800 V and 1200 V for each inlet pressure case. There were therefore a total of 108 simulation cases run on a HP EliteDesk 800 G5 SFF Core i7-8700 3.2 with 32GB of RAM using one logical thread for each case.

3.3.1. Results and discussions

For the investigation of problems involving the flow of rare gases, the dsmcFOAM+ employs an explicit time-stepping solution with stochastic molecular collision [73]. Instead of trying to solve Newton's equations of motion for a very high number of individual atoms/molecules, an evolving simulation mimics the physics of a real gas in this way. Since dsmcFOAM+ is a time-evolving solver, the outcomes of the micro-plasma discharge algorithm likewise rely on the time dependency. To demonstrate the capabilities of the micro-discharge algorithm, Figure 3-12 shows the evolution of the N₂ flow velocity profile over time from 25 ns to 325 ns, before the plasma cases become steady, after the application of high voltage at 800 V with 50 μA across three electrode configurations. Separated by a $50 \mu\text{m}$ gap and an inlet pressure of 50 kPa in a 1 Pa pressure environment.

The results obtained from the micro-plasma discharge algorithm in dsmcFoam+ allows the visualization of pressure, velocity, and temperature for each case, as shown in Figure 3-12 and Figure 3-13 for time-evolution intervals and steady state flow, respectively. Additionally, dsmcFoam+ provides the mass density, number density, rotational, translational, and vibrational temperatures for each case.

Chapter 3 Micro-plasma discharge algorithm development

The plasma cases were performed after a continuous flow of 300 ns with a timestep of 1 ns, which is crucial to note. Then the micro-plasma discharge algorithm was activated and run until it reached a desirable interval, or up to 400 μ s for the analysis of the plasma steady flow cases.

Three main parameters; (1) highest temperature, (2) thrust, and (3) mean velocity, were taken from the steady state simulation results to evaluate the performance and feasibility of each of the three electrode configurations along with different current-voltage (I-V) values to be employed in plasma-based micro-thruster devices. The thrust was obtained from the cross-sectional area of the outlet, meanwhile, the highest temperature is the maximum value registered at any point inside the microchannel. This is critical to determine the feasibility of the electrode configuration and the operational range for the electrical parameters (I-V) in order to avoid values near to or higher than the sublimation point of the electrodes/thruster materials or any temperature range that can involve a risk for the nearby components.

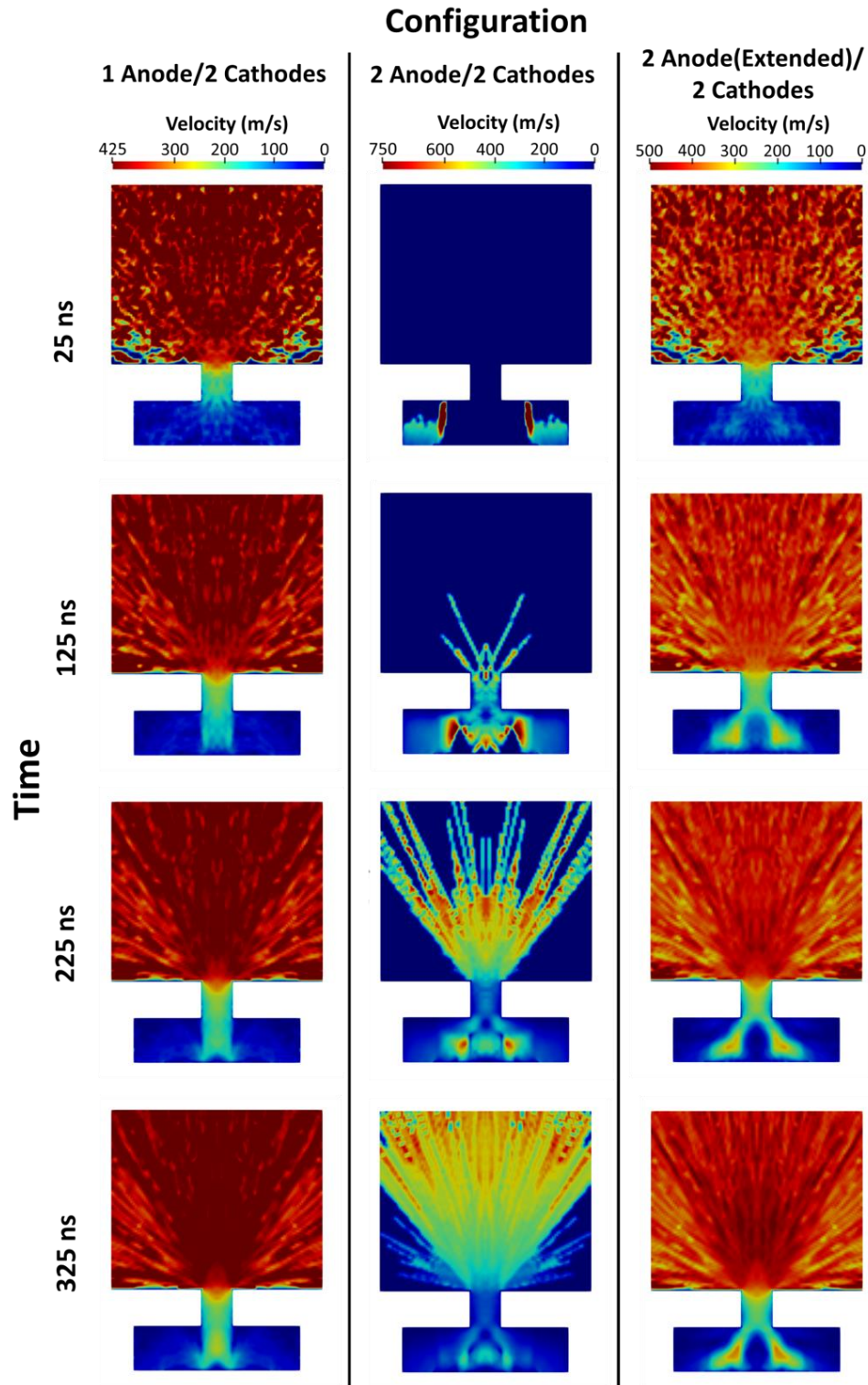


Figure 3-12. Time-evolution intervals of N₂ flow velocities in a 50µm gap microchannel at an inlet pressure of 50 kPa subjected to a continuous 50µA at 800V across the three distinct electrode configurations at 25, 125, 225, and 325 nanoseconds.

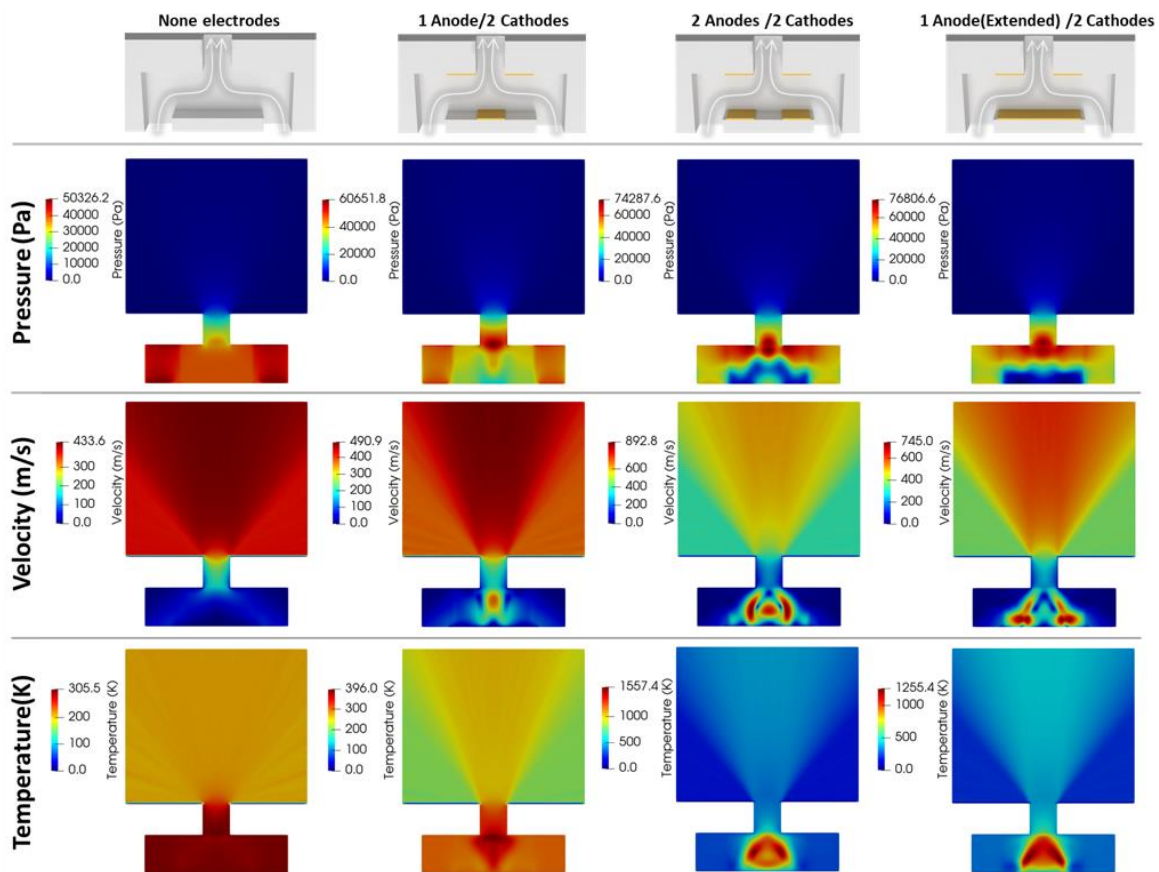


Figure 3-13. Steady DC micro-discharge simulation results for pressure, velocity magnitude, and temperature for N₂ flow at an inlet pressure of 50 kPa and an applied current of 50 μ A at 800 V with a 50 μ m gap for the three different electrode configurations.

i. Flow temperature analysis during discharge

Due to the emphasis on the macroscopic description of the flow, it is crucial to highlight variation in magnitude between temperatures in Figure 3-13. The electrode configuration has a considerable influence on the measured high temperatures. A configuration with two anodes and two cathodes produces the highest temperatures. This configuration strengthens the electric field in the discharge area, as it can be observed on the increase of intense \vec{E} lines on Figure 3-14, resulting in increased ionization and gas heating. Similarly, an extended anode arrangement produces higher temperatures due to its bigger surface area, which improves energy transmission and heating.

The temperatures measured in these models, which reached up to 1557.4 K, while high, are not unprecedented for micro-discharge situations. Because of the confined and strong energy input characteristic of microdischarges, such temperatures are feasible. The literature [135] [136] confirms the occurrence of temperatures ranging from 1000 K to 2000 K in similar circumstances, particularly under strong electric fields and high current conditions.

Chapter 3 Micro-plasma discharge algorithm development

In addition, it is important to emphasize the capability of the code to simulate theoretical cases beyond real scenarios where the temperature, pressure, and velocity rates can be greater than the material limits.

ii. Electric field simulation results

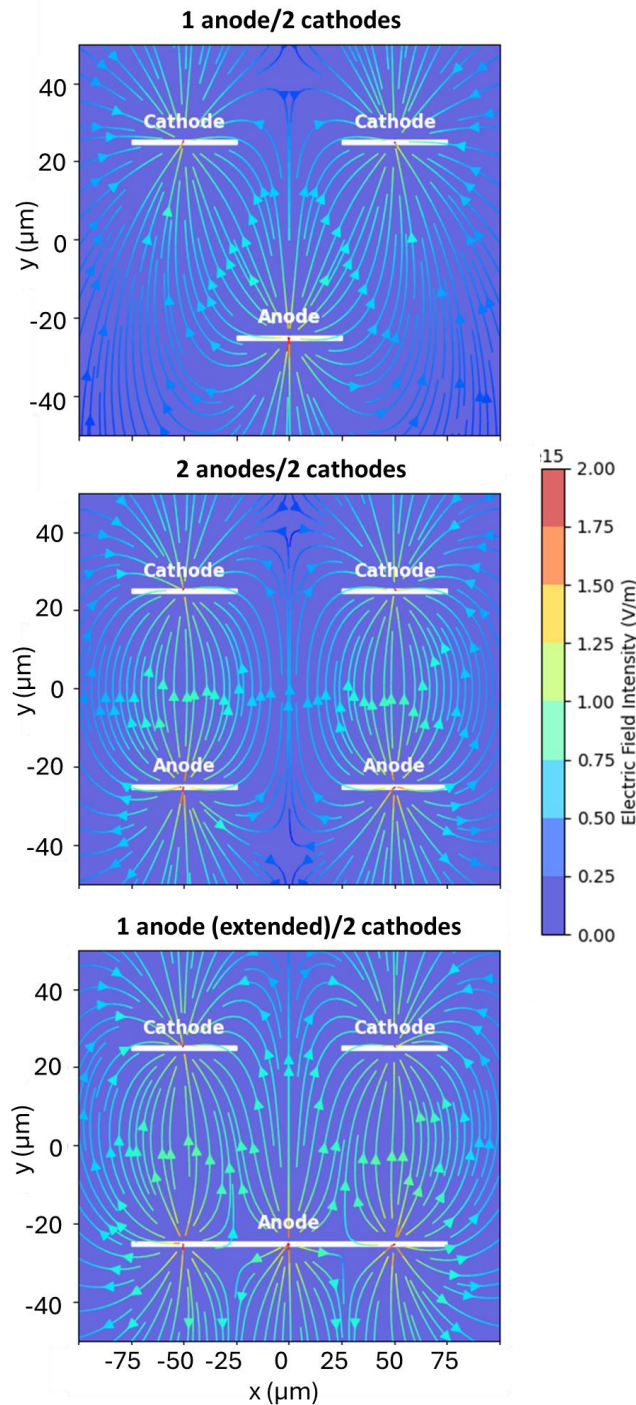


Figure 3-14. Electric field intensity results from the steady DC micro-discharge simulations at 800 V with a 50 μm gap for the three different electrode configurations.

Figure 3-14 depicts the electric field intensity and distribution results extracted from the micro-plasma discharge algorithm, with method describe in section 3.1.4, for three different electrode configurations used in a micro-discharge setup: the three possible configurations of the electrodes are 1 anode/2 cathodes, 2 anodes/2 cathodes, and 1 anode (extended)/2 cathodes. In the first configuration the field lines are equally spaced and are arranged in circles around a centrally placed single anode with two cathodes on either side, which leads to a region of high electric field density around the anode. The 2 anodes/2 cathodes configuration, where two anodes are positioned between two cathodes, has a more complex electric field distribution, with multiple zones of high strength caused by the anodes' superposition. This results in the formation of a greater surface area of high electric field intensity than when a single anode is used.

The third configuration exhibits a stronger and more consistent electric field distribution because its anode is elongated. The field intensity is highest near the edges of the elongated anode, with the electric field lines spreading out more evenly across its surface. The electric field intensities are shown in the color of the lines bases on the color bar, scaled from blue to red, ranging from 0.00 to 2.00×10^{15} V/m, for an applied voltage 800 V with a $50 \mu\text{m}$ gap, so that the strongest of them occupy regions near anode surface This visualization highlights the significant impact of electrode configuration on the electric field distribution and intensity in a micro-discharge setup, being crucial for optimizing the performance and characteristics of micro-discharges in practical applications.

iii. Simulations results analysis

Theoretical scenarios that exceed material limits can be simulated using the micro-plasma discharge algorithm (MPDA) especially when temperature, pressure and velocity rates are higher than what materials can withstand. This is important for analysing the increase in current-voltage (I-V) characteristics beyond the breakdown voltage. Analysis of the results based on Figure 3-15 and Figure 3-16 are the following:

Beyond material limits: The simulations reveal that at 1200 V and $100 \mu\text{A}$, with a pressure of 100 kPa, temperatures within the flow may reach unprecedented values— 7.1×10^5 K, 3.4×10^8 K, and 1.5×10^7 K for electrode configurations 1, 2, and 3 respectively. These temperatures are much higher than sublimation points of common electrode materials (such as gold at 1663 K, silver at 1285 K, copper at 1512 K, tungsten at 3475 K). Under normal conditions these high temperatures would cause these materials to evaporate well before reaching vacuum levels of around -1200 V

Reasons behind temperature increase: The exponential growth in ion densities at about -1200 V shown by Figure 3-15 happens due to cascade processes occurring in microgaps where electric field strength reaches $\sim 2.4 \times 10^7$ V/m which is much larger than breakdown voltage of about -350 V for a gap size ~ 50 μm at -100 kPa thus resulting into imaginary temperature levels as voltage doubles or more.

Voltage, current, and thrust Relationship: As voltage and current increase so does maximum temperature T_{max} as well as thrust F values according to Figure 3-15. For potentials between approximately -100 V and -400 V lower temperatures and thrust are observed since potential is not enough to reach necessary breakdown voltage for sustainable plasma; At these lower voltages, the configurations exhibit a steady temperature of 305 K, with thrust values of 410 nN and 820 nN for 50 kPa and 100 kPa, respectively—similar to a cold-gas micro-thruster.

Effects at higher currents: At higher current values such as 50 μA and 100 μA electron-ion densities ($\sim 10^{20}$ m^{-3}) become enough to accelerate flow unlike lower current of 10 μA where densities ($\sim 10^{19}$ m^{-3}) were found not enough to sustain breakdown even when required voltage(s) applied.

Insights from simulations: T_{max} values tend to have a maximum in configuration 2 followed by configuration 1 having the minimum while F has the maximum value for configuration number one followed by three then two. The reason behind this inverse relationship between T_{max} and F is because of differences in vorticity within microchannels as well as streamlines.

Flow dynamics and vortex formation: Flow dynamics are affected by vortex formation which depends on position of anode relative to outlet. In case there is no vortex being formed in configuration one there will be unrestricted flow hence lowest temperature but highest thrust while in other cases vortices located within micro-channel restricts flow towards outlet thus causing minimum thrust with maximum temperature; see Figure 3-16 for more details about size and location.

The micro-plasma discharge algorithm is used to analyse current-voltage simulations. The electrode configuration significantly affects the performance of micro-discharges with voltage and current. The capability of simulating conditions beyond material limits gives insights into temperature and thrust behaviour under extreme environments. Among the three settings, configuration 1 which does not form a vortex attains highest thrust with lowest temperatures thus being most efficient for practical applications. Configuration 2 achieves higher temperatures but is less efficient because there are flow restrictions caused by vortices. These results show that it is important to optimize electrode configurations for balancing temperature management against thrust performance in micro-

discharges which can be used as a basis for improving efficiency and effectiveness of such systems under real-world conditions.

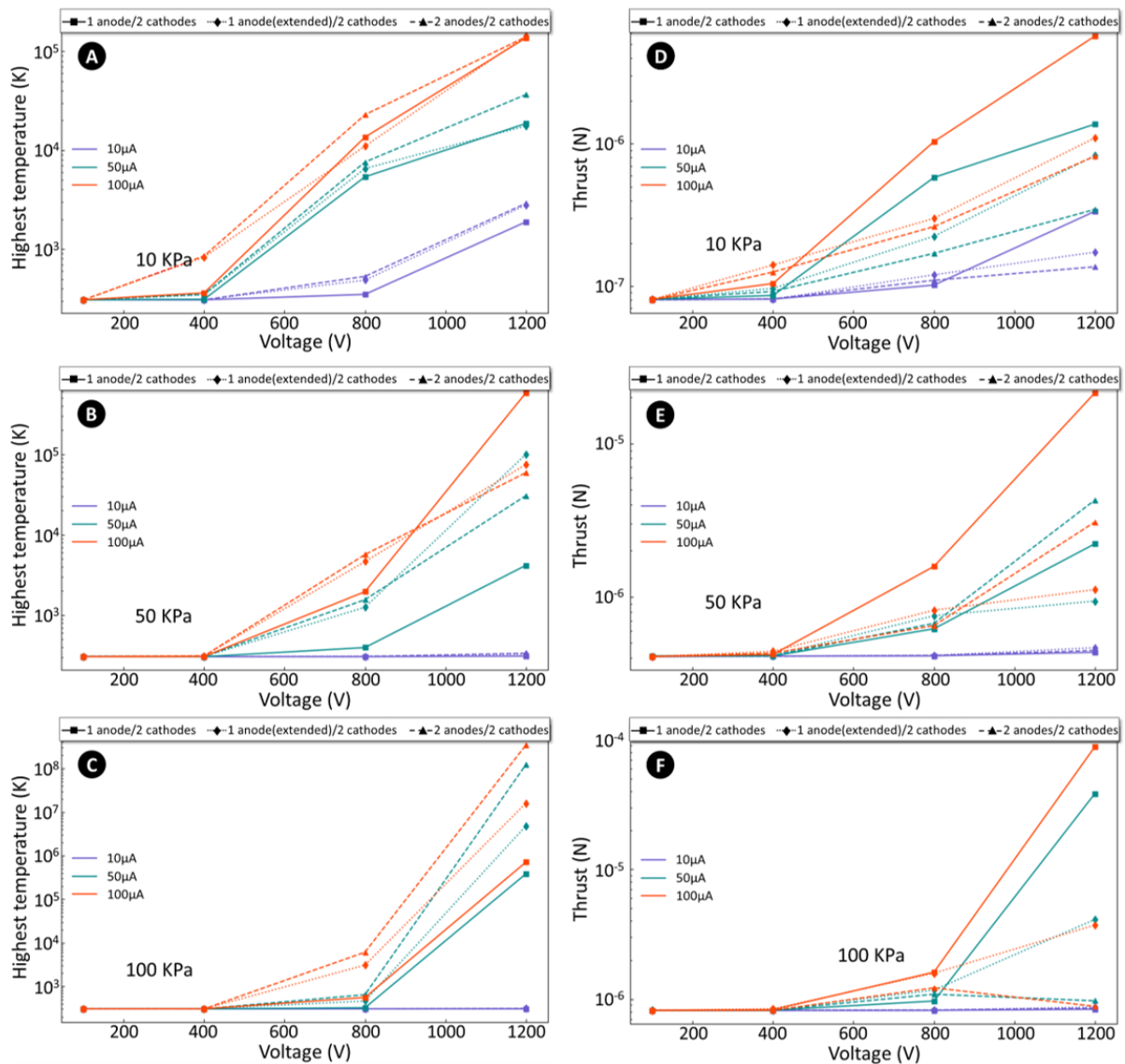


Figure 3-15. Highest temperatures and thrusts results at steady state from the simulations of three 50 μm -gap electrode configurations for ; (1) one anode/two cathodes, (2) two anodes/two cathodes, and (3) one anode (extended)/two cathodes for 100 V, 400 V, 800 V, and 1200 V. Results are split by nitrogen inlet pressures of 10 kPa, 50 kPa, and 100 kPa. The applied currents of 10 μA , 50 μA , and 100 μA are distinguished by purple, turquoise, and orange lines, respectively.

iv. Key factors behind temperatures results

The electrode configuration significantly influences the high temperatures observed in the results depicted on Figure 3-15, where the capability of the micro-plasma discharge algorithm to simulate theoretical cases beyond real scenarios where the temperature profile can be greater than the material limits. Thus, the configuration with two anodes and two cathodes shows the highest temperatures, especially at higher voltages and currents. This configuration increases the electric field strength in the discharge region, leading to more intense ionization and heating of the gas. Similarly, an extended anode configuration results in elevated temperatures due to its larger surface area, which enhances energy transfer and heating.

The impact of current and voltage is also crucial. Higher currents, like $50 \mu\text{A}$ and $100 \mu\text{A}$, combined with higher voltages such as 800 V and 1200 V , considerably increase the system's power input. This power is mainly dissipated as heat within the discharge region, raising temperatures significantly. This direct correlation between electrical parameters and temperature rise highlights the substantial power dissipation in micro-discharge environments.

Pressure variations further affect temperature profiles. Higher pressures, such as 50 kPa and 100 kPa , increase gas density, leading to more frequent collisions between electrons and gas molecules. These collisions enhance ionization and heating but also increase energy dissipation. The overall effect is a marked rise in temperature within the discharge region.

The $50 \mu\text{m}$ discharge gap is another critical factor. This small gap creates a very strong electric field for the given voltage, accelerating electrons to high velocities and increasing their kinetic energy. This energy is then transferred to the gas through collisions, causing significant heating. The confined space of the micro-discharge setup amplifies this effect, resulting in high observed temperatures.

In conclusion, the high temperatures observed in the simulations are reliable given by the strength of the electric field, the high currents, and voltages applied, along with specific electrode configurations. All of these factors work together to increase ionization and heat within the micro-discharge area, resulting in a high thermal profiles.

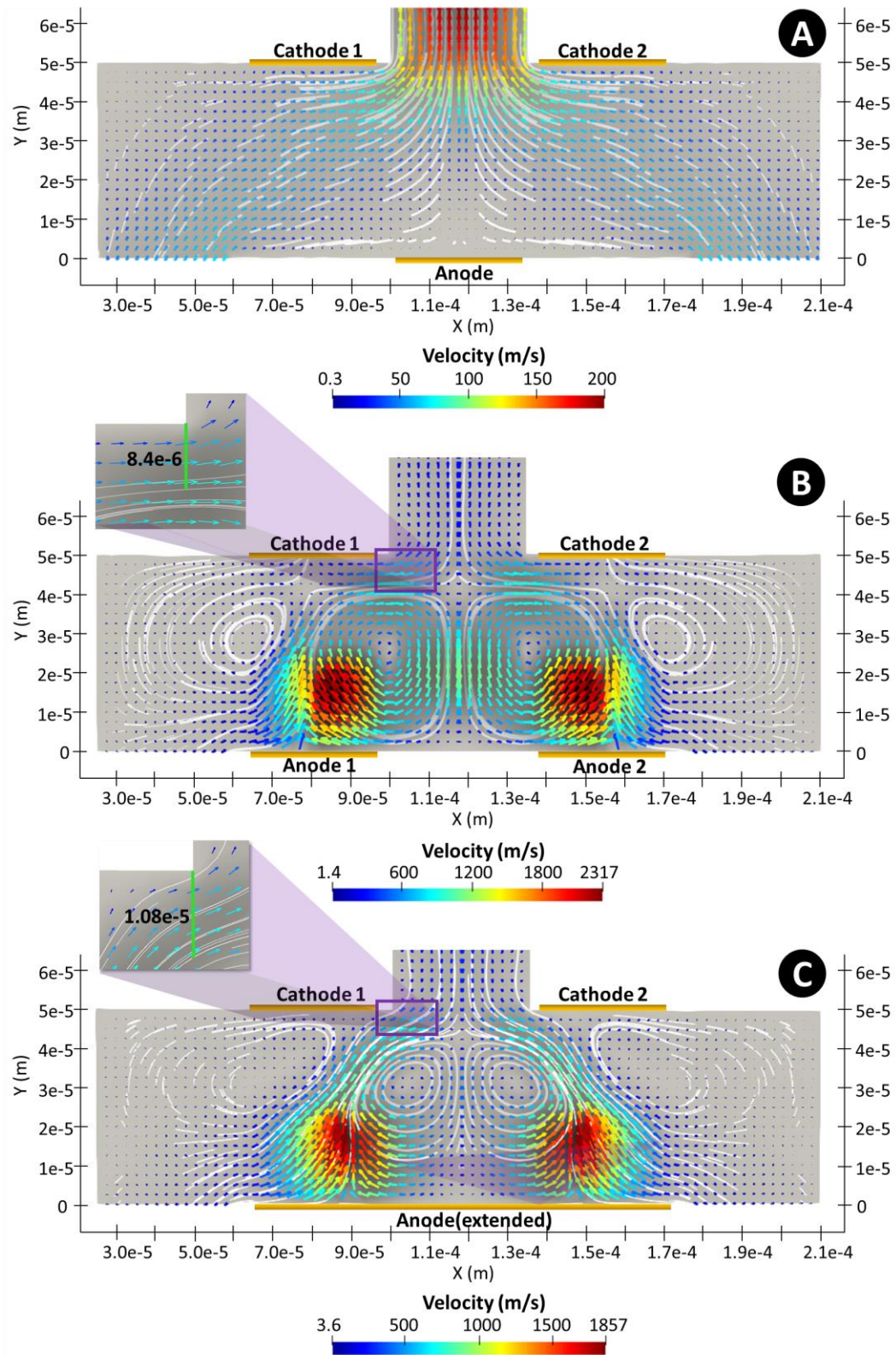


Figure 3-16. Velocity flow profiles at steady state on $50 \mu\text{m}$ gap at 800 V with an applied current of $100 \mu\text{A}$. The nitrogen inlet and outlet pressures were set as 100 kPa and 1 kPa ; Three configurations are shown: (a) 1 anode/2 cathodes, (b) 2 anodes/2 cathodes, and (c) 1 anode extended/2 cathodes. Vortex formation is present in (b) and (c), with a distance between the wall and the vortex of $84 \mu\text{m}$ and $108 \mu\text{m}$, respectively.

3.4. Summary

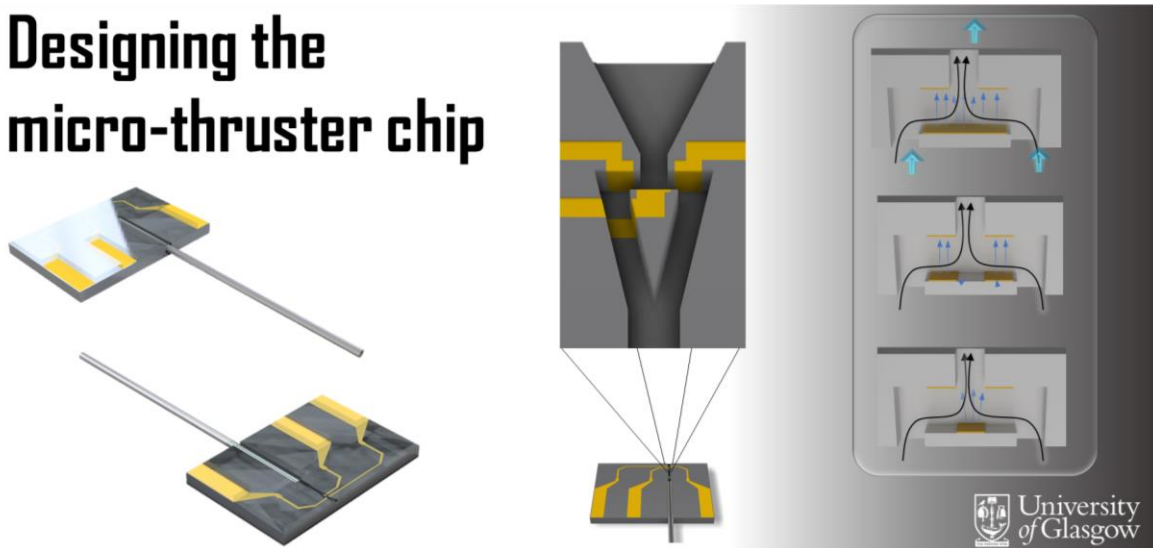
The micro-plasma discharge algorithm implemented in dsmcFoam+ solver is an alternative method to model DC micro-plasma effects on flow with the primary focus for the research and design of plasma thrusters. The code avoids adding electrons and ions as particles by accelerating an existing number of equivalent gas particles by calculating a numerical solution of the Fowler-Nordheim equation to emulate the ionization, reducing the computational requirements.

The applicability of the Micro-plasma discharge algorithm was tested by simulating three electrode configurations; (1) one anode/two cathodes, (2) two anodes/two cathodes, and (3) one anode extended/two cathodes. Inlet pressures were set as 10 kPa, 50 kPa, and 100 kPa, with an applied voltage of 100 V, 400 V, 800 V, and 1200 V, as well as an applied current of 10 μA , 50 μA , and 100 μA in a 50 μm gap. Configuration 1 shows the most effective electrode pattern, with the lowest increase in temperature between the configurations, and also the highest velocities and thrust values.

During the demonstration of the code application, it was identified that there must be a maximum difference between the electron and neutral number densities of 10^5 m^{-3} between the electrodes in order to provide enough charged particles to accelerate the flow. More work needs to be done to analyse the specific amount of current density required to contribute to the change in the acceleration of the flow. In addition, the code requires a performance test, contrasting it with other PIC-DSMC methods as future work to show its performance on the consumption of computational resources. The micro-plasma discharge algorithm is a promising tool for the prototyping simulation of plasma-based micro-propulsion systems for nano- and pico-satellites applications.

Chapter 4

Designing the micro-thruster chip



This chapter presents the procedure for defining the plasma-based micro-thruster chip design and the theoretical operational value ranges considering the heat transfer and the electrical and geometrical performances under thrust.

The chip's design must rely on a hybrid cold gas micro-thruster and a electrostatic plasma micro-thruster in order to test its performance if it is capable to provide a thrust between a nN to mN range while minimising power consumption with a reliable heat transfer range inside vacuum conditions to avoid sublimation.

In the design and operation of a micro-thruster chip that is based on plasma, a thermal model is very important to ensure its best performance as well as long life. This chapter gives an understanding of integrated thermal dynamics and where these calculations take place. Main components of this model include: heat transfer; breakdown voltage/current for plasma generation – affected by various operational conditions such as vacuum levels and material properties.

The device is a prototype and the first of its kind. There is no known data on the thrust performance; therefore, the major challenge in the development of the device is the thermal increase of the electrodes necessary to create an electric discharge without sublimating into a vacuum. Consequently, the intention is to determine in the future works the magnitude of thrust generated by the breakdown

Chapter 4. Designing the micro-thruster chip

parameters (I-V characteristics and temperature), where the functionality of the micro-device is a priority compare to achieving an specific range of thrust.

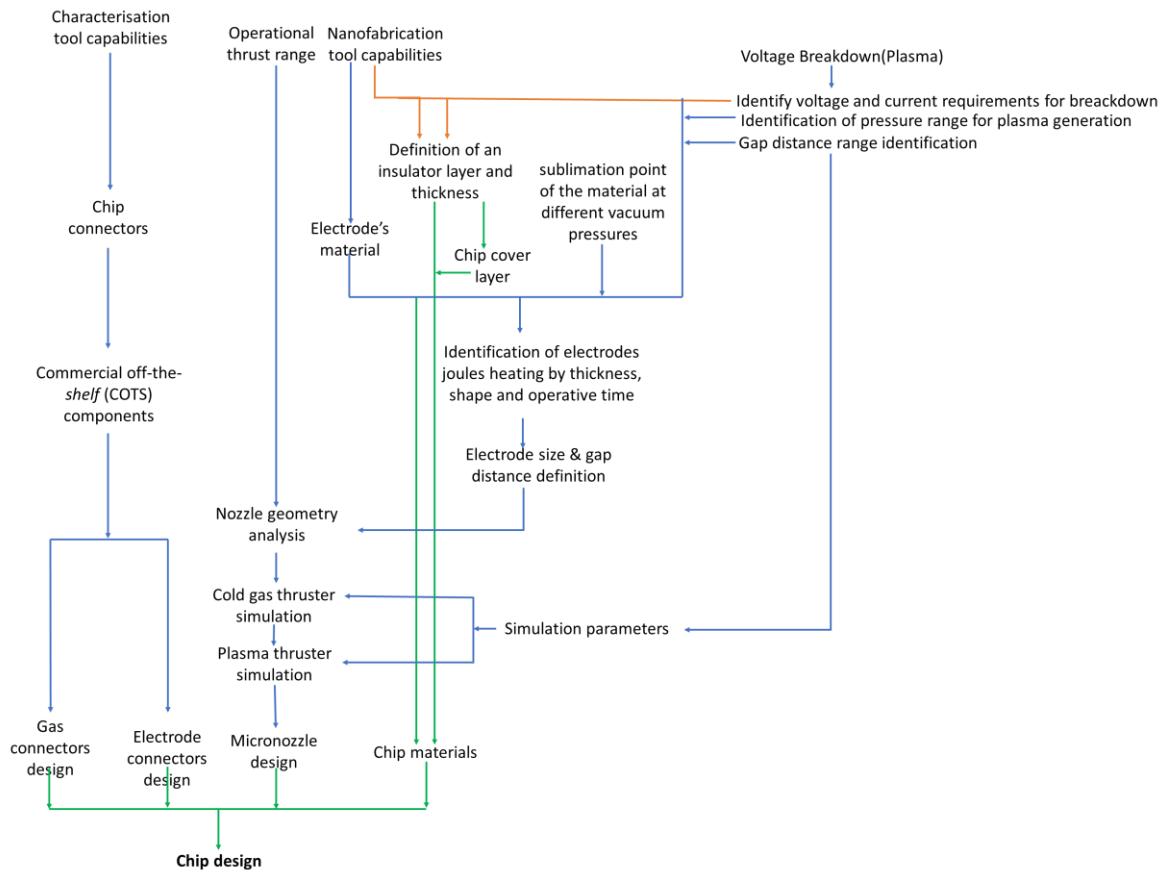


Figure 4-1. Design of a plasma-based micro-thruster chip procedure flowchart

i. Thermal model

The thermal model has critical elements which are:

1. Joule Heating: This refers to heat energy created when electric current flows through electrodes. Relationship is given as $q = I^2 R t$ where q stands for quantity of heat, I represents current R is resistance while t means time. In case of vacuum, one should be cautious enough not to allow sublimation of electrode materials because with decrease in pressure vaporization temperature decreases. Therefore, the thermal model requires to considerate the radiation heat q_{rad} (more description in section 4.5.1), conductive heat q_{cond} (section 4.5.4), and convective heat transfer q_{conv} (section 4.5.5) determine where heat loss occurs on electrodes. Commonly, heat loss is expressed in terms of heat flux (Watts), so the net heat transfer q_{net} of the system can be calculated as follows:

$$q_{net} = q_{Joules\ heat} - q_{rad} - q_{cond} - q_{conv} \quad \text{Eq. 78}$$

where $q_{Joules\ heat}$ is the Joule Heating flow rate and the heat can be emitted (+) or absorbed (-) depending on the sign.

To calculate $q_{Joules\ heat}$, q_{rad} , q_{cond} , and q_{conv} on parallel plates for micro-plasma generation, it is necessary to describe the heat transfer interactions in a system. These diagrams (Figure 4-2 and Figure 4-3) were created to assist with this analysis:

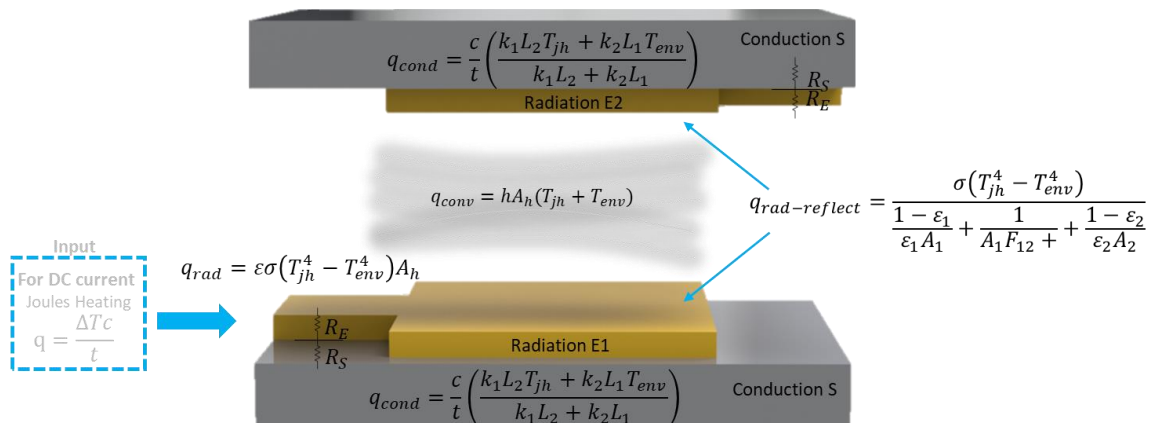


Figure 4-2. Schematic illustrating the mathematical modelling of heat transfer during plasma generation between two micro-electrode plates

Where, based on the mathematical modelling of the heating system, Eq. 78 can be written as follows:

$$P_{net} = \frac{c T_h}{t} - \left[\varepsilon \sigma (T_1^4 - T_0^4) (A_{CS} + A_E) + \frac{\sigma (T_1^4 - T_2^4)}{\frac{1 - \varepsilon_1}{\varepsilon_1 A_{ES1}} + \frac{1}{A_{ES1} F_{12}} + \frac{1 - \varepsilon_2}{\varepsilon_2 A_{ES2}}} \right] - \frac{c}{t} \left(\frac{k_1 L_2 T_{jh} + k_2 L_1 T_{env}}{k_1 L_2 + k_2 L_1} \right) - h A_h (T_{jh} + T_{env}) \quad \text{Eq. 79}$$

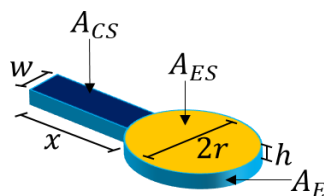


Figure 4-3. Surface area representation of an electrode

2. Breakdown Voltage and Current for Plasma Generation: Micro-thruster chip creates plasma by achieving breakdown voltage (section 4.2) that ionizes gas within microgap between two electrodes when an electrical current is applied (section 4.1). Paschen's Law modified to match microgap sizes given by [137] [138]:

$$V_b = \frac{B(p \cdot d)}{\ln[A(p \cdot d)] - \ln[\ln(1 + 1/\gamma_{sec})]} \quad \text{Eq. 80}$$

where A and B (considerations of constant are describe in section 4.4.24.3) are constants of the gas, γ_{sec} is the cathode's secondary electron emission coefficient, p is the pressure, and d is the distance between the electrode plates.

Radiative & Conductive Heat Transfer: Stefan-Boltzmann law describes radiative heat loss while conduction takes place through electrode material plus substrate. More details are displayed in sections 4.5.1 and 4.5.4.

ii. Environmental Conditions

Calculations are based on vacuum assumed to be present in space environment. Radiative heat loss and vaporization temperatures of materials are greatly affected by vacuum hence altering thermal behaviour significantly (section 4.5.4).

1. Heat Sink of Support Structure: The support structure should act like a sink for any heat generated by micro-thruster. This is aimed at ensuring that there is no accumulation of this energy within it which can lead to overheating or even damage.

2. Radiative Balance: It is important to consider radiant balance between structure itself and surrounding spaces. Therefore, there was no direct inclusion of plasma radiation among considerations made while developing the thermal model because:

- **Operational Current Range:** Plasma generation operates within current ranges of 10^{-6} to 10^{-2} amperes which ensures efficient ionization without much thermal radiation that may affect overall heat balance.
- **Thermal Energy:** Joule Heating and radiative losses from electrodes greatly exceed plasma radiation's impact in terms of heat production. When considered as part of general thermal activity, visible light energy released during plasma generation is almost insignificant.

This model integrates all thermal aspects and environmental fears into one whole which can be used to explain how the micro-propulsion chip should work thermally under space conditions where it will operate effectively and dependably.

The geometric dimension of the micro-thruster chip is crucial to the development of the chip. It is possible to fabricate nano- to micro-scale devices at the James Watt Nanofabrication Centre (JWNC), where each size range necessitates a new technique with its equipment and instrument-imposed limitations. As a result, three major considerations were made: 1) the constraints of the tools during fabrication, 2) the limitations of the equipment's resolution to characterise the chip's performance, and 3) providing a manageable size for the chip. Consequently, the processes shown in Figure 4-1 were utilised to define the design of the plasma-based micro-thruster chip discussed in this chapter.

4.1. Electrical current for plasma generation

As shown in section 2.1, gas ionization in micro-thrusters is influenced by four primary factors: current, voltage, gap distance, and pressure. The operational parameters, specifically the current range between 10^{-6} and 10^{-2} A, are critical for effective plasma formation [18] [19]. This current range is chosen based on gas breakdown detection, essential for ensuring efficient ionization of the propellant, which directly impacts thrust production in the plasma micro-thrusters.

Operating within this current range balances ionization efficiency, thermal stability, and power consumption. Currents above 10^{-2} A risk excessive heating, potentially damaging the micro-thruster, while currents below 10^{-6} A fail to sustain enough ionization, leading to reduced thrust. Hence, this range is vital for maintaining steady thrust output and long-term reliability of micro-device.

Further analysis of micro-gap breakdown currents reveals that current is 1.6 times higher in micro-gaps than in larger gaps due to several factors [20], including enhanced electron field emission, ion dynamics, and electrode surface effects. The increased electric field strength in micro-gaps leads to higher electron emissions from the cathode, which initiates and sustains the breakdown process. Additionally, the geometry and surface characteristics of the electrodes contribute to the observed higher breakdown currents.

In conclusion, the selected current range of 10^{-6} to 10^{-2} A is fundamental to achieving efficient and stable ionization, ensuring reliable thrust performance while addressing thermal and power constraints. Ongoing experimental and theoretical studies are needed to further validate the suitability of this current range for the system's specific thrust requirements.

4.1.1. Breakdown current considerations

The relationship between current and micro-gap size is a critical area of study in various technological fields. Researchers have explored the electrical breakdown behaviours in microgaps, which can provide valuable insights into this phenomenon. One key finding is that the current is 1.6 times greater in micro-gap environments compared to larger gaps [20]. Several causes leading to increased breakdown currents in microgaps have been investigated by researchers [21].

Firstly, electron field emission from cathode surface is one major cause for breakdown at microscale. As the size of the gap decreases the becomes electric field stronger at cathodes, resulting into very high levels of electron emissions. This enhanced electron emission can then initiate and sustain the breakdown process, resulting in the observed higher breakdown currents[150].

Additionally, the dynamics of ion generation and movement within the microgap also contribute to the increased breakdown current. The high electric fields in the microgap can lead to efficient ionization of the gas molecules, and the resulting positive ions can further enhance the field emission at the cathode, creating a positive feedback loop that sustains the breakdown.

Moreover, the unique geometry and surface characteristics possessed by electrodes in microgap can also influence the breakdown phenomenon. The surface roughness, material properties, and local field enhancements at the electrode edges or protrusions can all play a role in the breakdown process and contribute to the increased current observed [22][150].

The research community has made significant progress in understanding the mechanisms behind the 1.6 times current on microgap breakdown. By combining experimental, computational, and analytical approaches, researchers have gained valuable insights into the complex interplay of electron field emission, ion dynamics, and microscale electrode effects that underlie this intriguing phenomenon [22] [20] [21].

4.2. Breakdown voltage for plasma generation

In the case of voltage, the operational range is determined by the breakdown voltage given by the gap, the pressure, and the gas type. To ignite a plasma, the Paschen curve's breakdown voltage for the cold gas must be exceeded. This breakdown voltage (V_b) is dependent on the distance between

Chapter 4. Designing the micro-thruster chip

the electrodes and the pressure. As stated in Chapter 3, the Paschen curve cannot accurately describe the breakdown voltages in microgaps. For smaller gaps, the required breakdown voltages begin to increase exponentially. In this micron regime, electron field emission plays a significant role in the breakdown phenomenon, and the Fowler-Nordheim equation accounts for the ion-enhanced field emission ($E = \beta E_m$) caused by the surface conditions of the electrodes for the breakdown voltage in small gaps [11] [123].

The Paschen curve is combined with the Fowler-Nordheim equation to calculate the breakdown voltages of microgap gases. As a result, the equation governing the DC breakdown mechanism in micrometre gaps, also known as the modified Paschen curve, is [94]:

$$V_b = \frac{d(D + Bp)}{\ln[ApdK]} \quad \text{Eq. 81}$$

where K is assumed to be a constant material in order to calculate V_b as 1×10^7 [11] [139].

And D is the constant dependent on the gas (V/cm), which is defined as [94]:

$$D = 6.83 \times 10^7 \frac{\phi^{3/2}}{\beta} \quad \text{Eq. 82}$$

where ϕ the work function of the electrode material and β the field amplification factor.

Comparison between the Paschen curve, the Fowler-Nordheim, and the modify Paschen curve are displayed on Figure 4-4.

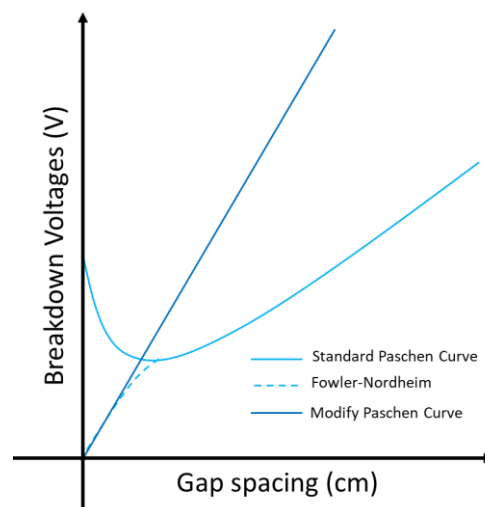


Figure 4-4. Paschen curve vs Fowler-Nordheim equation [11]

4.3. Breakdown voltage in function of A and B gas constants definition

A and B from Eq. 80 are constants used to approximate the breakdown voltage independently of the pressure, which just varies depending on the gas type, according to the reference [140], being A the gas constant related to the pressure and the mean free path by the equation [101]:

$$\frac{1}{\lambda_m} = Ap \quad \text{Eq. 83}$$

Therefore, B is a gas constant related to A and the ionising potential of the gas.

Typically, the definition of constants A and B are performed on a macroscopic gap with at least 1 mm distance. However, experimental results in references [20], [141], [142], [143], and [144] indicate that these constants no longer approximate the breakdown voltage from Eq. 81 within microgaps.

Nitrogen gas was selected as the species for these experiments due to its use as the main propellant during the experimental phase (Chapter 6). To align A and B values for N₂ with the reference values at pressures of 3, 10, 22, 30, 40, 50, 75, and 100 KPa, it is necessary to adapt the constants as a function of pressure, in addition to considering the conventional gas type. For vacuum conditions, a pressure range between 3 KPa and 100 KPa was chosen to simulate electric discharge in space environments.

To fit V_b in Eq. 80 with the referenced values, Eq. 36 from Chapter 3 was solved as a non-linear, multivariable system for constants A and B for each pressure case. This was done by taking the voltage as V_b at the point when the electron density reaches 1.6 times the threshold for a sustained electric discharge (plasma), as described in Section 4.1.1.

The average breakdown voltage curve for each N₂ pressure case was obtained and is depicted in the plots below in Figure 4-5.

Figure 4-5 presents the fitted breakdown voltage curves for nitrogen gas at varying pressures, with the model results depicted by blue lines and reference results by black lines. The following analysis examines the goodness of fit for each plot by comparing the model's predicted values with the reference data.

The nature of performing curve fitting of the breakdown voltage is aimed at finding the values of A and B that allow the approximation of V_b . These constants should, in principle, should provide consistent results independent of the gas pressure, being solely dependent on the type of gas.

Chapter 4. Designing the micro-thruster chip

However, these constants have been shown to be varied among different sources by reviewing reference values from [20], [141], [142], [143], and [144] with significant variation based on gas pressures on their test results.

To make the values of V_b more precise, as well as to make them agree with those in with the references ([20], [141], [142], [143], and [144]), it is essential that they should be adjusted so that they can be applied for all pressure levels. This means that apart from being taken as fixed numbers, V_b need also to be treated as variables depending on both the kind of gas involved but most importantly its pressure too.

On Figure 4-5, the fitting model curve fits well with reference values for gap sizes between 3 μm to 30 μm and 50 μm to 100 μm at around 3 KPa, especially within voltage range of 600 V to 1200 V. This means that the model represents initial ionization conditions accurately in those regions. The small differences observed between these two lines around gaps ranging from 30 μm to 50 μm ; however, the overall agreement is still good.

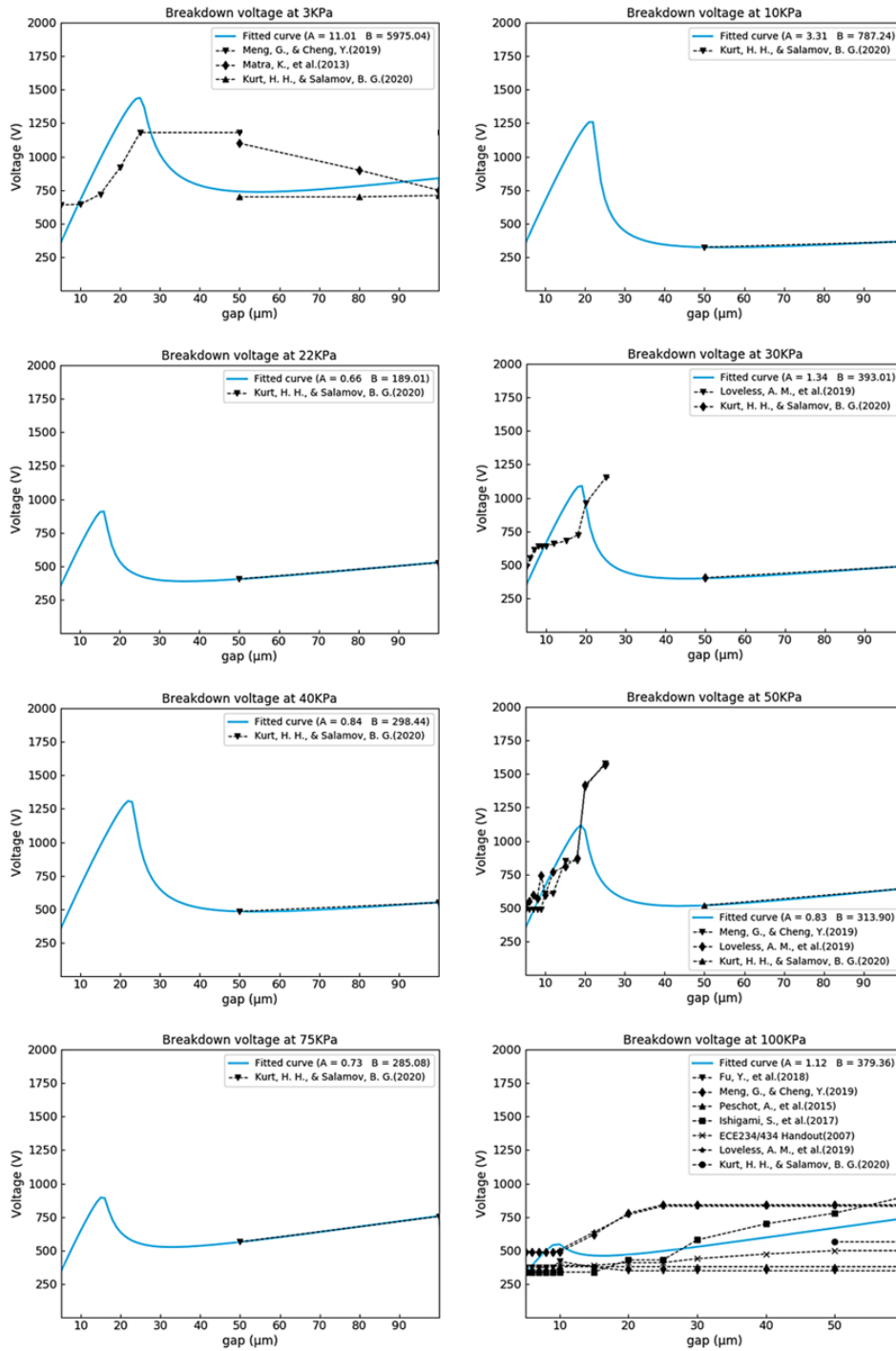


Figure 4-5. Fitted curves for the breakdown voltage of N2 at varying pressures

For four different pressures (10, 22, 40, and 75 KPa), fitted curves obtained track reference data curves very closely throughout most of their length. This fit is strongest when considering gaps from about 50 μm up to around or slightly beyond 100 μm where models reproduce the breakdown thresholds correctly.

Chapter 4. Designing the micro-thruster chip

The trend is the same in regard to 30 and 50 KPa for both models and reference curves — within the range of middle voltage (500 V to 1000V), fitting line is a little lower than reference lines. This means that model may underestimate it slightly because there are small differences between setups or errors of measurements were made by them. However, overall shape as well as steepnesses remain similar enough so they can be treated as correct representation of relations between variables.

At highest pressure examined at 100 KPa, fitted curves seem aligning more with results towards higher voltage side among other places where agreement between them could also be said strong enough even though slight disagreement occurring somewhere near ten micrometers down hundred micrometres within reference data does not appear too surprising given complexities of the breakdown voltage processes under such conditions. However, still it fits well at high voltages even if there are some deviations.

In order to consider small variations given to the experimental setup and conditions, the electrode type and material for each contrasting source are shown in Figure 4-5 of the Table 10 below:

Table 10. Electrode Types and Materials

Reference	Authors	Electrode Type and Geometry	Material of the electrode
[20]	G. Meng and Y. Cheng	Macro Electrodes: Spherical; Planar Electrodes: Metal on silicon substrate; MEMS Devices: Capacitive and ohmic RF-MEMS switches; Microelectrodes: Hemisphere tungsten	Tungsten, Aluminum, Copper, Gold, Platinum
[141]	A. Peschot, C. Poulain, N. Bonifaci and O. Lesaint	Planar Electrodes: Contact gaps ranging from 100 nm to 10 μm	Gold, Platinum
[142]	S. Ishigami, K. Kawamata and S. Minegishi	Planar Electrodes: Micro gap configurations for ESD study	Brass
[143]	ECE - University of Rochester	Planar Electrodes: Used in MEMS devices	Gold, Aluminum
[144]	A. M. Loveless, G. Meng, Q. Ying, F. Wu, K. Wang, Y. Cheng and A. L. Garner	Planar Electrodes: Used to understand microscale gas breakdown	Platinum

Chapter 4. Designing the micro-thruster chip

Taking the A and B values of N2 for each pressure case and fitting them to a function yielded (Figure 4-6) the following expression for the A constant:

$$A = 0.83 + \frac{15.5 - 0.83}{1 + \left(\frac{P}{4516}\right)^2} - 0.215 \quad \text{Eq. 84}$$

The equation was fitted with a P value of 0.998 and a R^2 of 0.9925.

following function was obtained for the case of constant B :

$$B = 317 + \frac{27735 - 317}{1 + \left(\frac{P}{1645}\right)^{2.24}} - 215 \quad \text{Eq. 85}$$

Having P value of 0.997 and a R^2 of 0.9996.

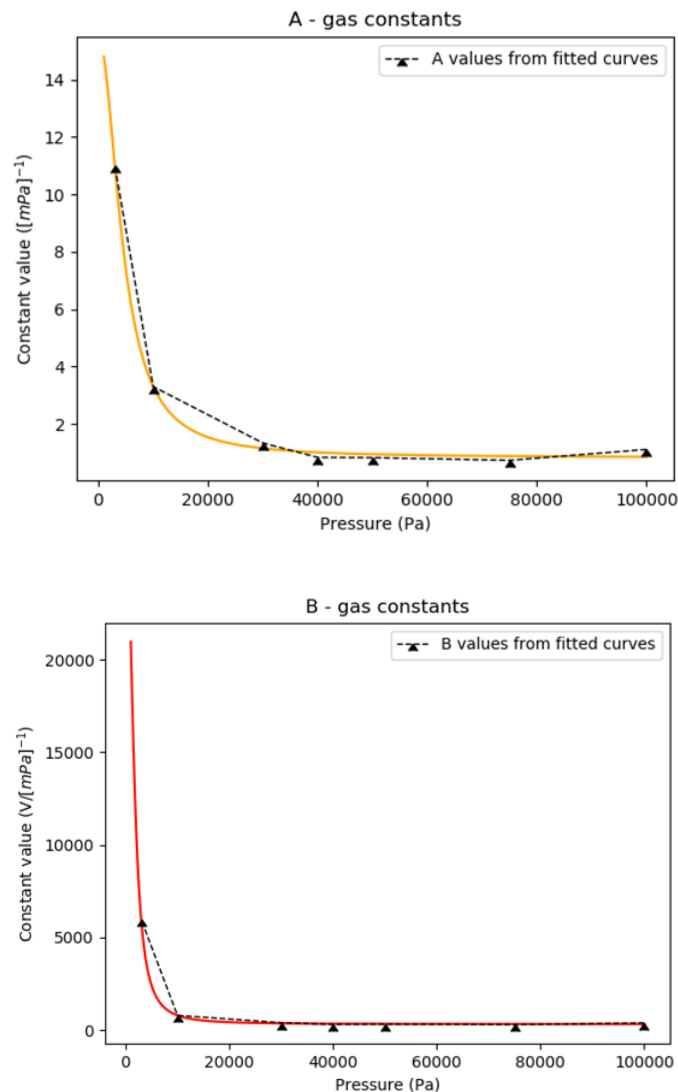


Figure 4-6. Redefined values of A and B gas constants for N2

Chapter 4. Designing the micro-thruster chip

Applying A and B from Eq. 84 and Eq. 85, respectively, to solve Eq. 36 in Chapter 3 for N_2 yields the following breakdown voltages curves based on the microgap distance between 10KPa and 100KPa:

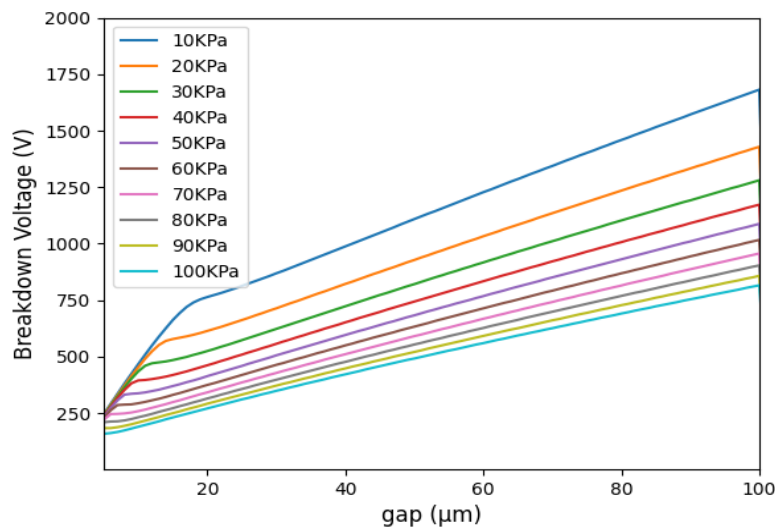


Figure 4-7. Breakdown voltages at different pressures based on the gap distance

The results of V_b showed in Figure 4-7 indicate a breakdown voltage range of 150 V to 1700 V for N_2 . While lower pressures result in a lower gas particle density and collision probability, a higher voltage is required to increase ionisation until it becomes self-sustaining. As a result of considering vacuum conditions as space environments for micro-thruster chip operations, the operative pressure ranges for a discharge during this stage were set between atmospheric conditions (100 KPa) and vacuum conditions (10 KPa). In addition, the gap must be as small as possible while taking into account the equipment's limitations (Chapter 6) for its characterisation. Consequently, a gap in the range of 1 μm to 100 μm was identified as a viable option for nanofabrication within JWNC and experimental analysis.

4.4. Heat transfer

Current and voltage applied to the electrodes of a plasma-based micro-thruster during operation significantly impact the device's longevity. When a current with a potential passes through electrodes, it produces Joule Heating or thermal energy. This thermal energy manifests as an increase in the temperature of the conductor material, which heats the microdevice.

Chapter 4. Designing the micro-thruster chip

4.4.1. Heat transfer considerations in space

Because the micro-thruster is intended for use in space, the components will be exposed to vacuum environments. As the vacuum level is decreased, the vaporisation temperature of the material drops (Figure 4-8). Metals tend to volatilise in vacuum furnaces at temperatures below their melting point [145]. Vacuum technology application in the micro-thruster necessitates knowledge of vapour pressure on materials to prevent sublimation during space missions.

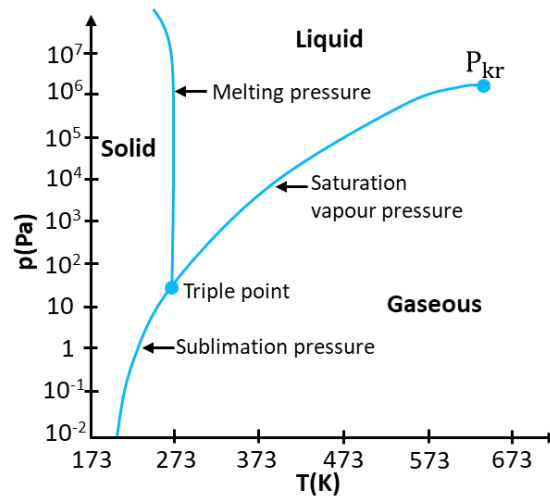


Figure 4-8. Dependence of melting temperature, sublimation and saturation temperature on pressure; 1)melting curve, 2) sublimation curve, and 3) saturation curve [146]

The vapour pressure can be calculated using the relationship [146],

$$\log P = f\left(\frac{1}{T}\right) \quad \text{Eq. 86}$$

The vapour pressure curves can be represented with sufficient accuracy for practical purposes as straight lines given by [146],

$$\log P = -\frac{B}{T} + A \quad \text{Eq. 87}$$

Being P the pressure in mbar, and A and B are material-specific values [146],

$$A = \log P_0 \quad \text{Eq. 88}$$

$$B = \frac{\Delta H \cdot \log e}{mR} \quad \text{Eq. 89}$$

where P_0 is the vapour pressure at standard temperature and pressure, ΔH is the transition heat, m is the mass of the gas, and R is the gas constant.

Chapter 4. Designing the micro-thruster chip

As described in section 5.7, the micro-thruster chip's materials were selected based on their availability and suitability for nanofabrication on the JWNC's Plassys II and Plassys IV for metallisation deposition. Therefore, the possible electrode materials on the micro-thruster chip are aluminium, gold, silver, copper, and tungsten, which are also frequently used for plasma actuator testing. Additionally, silicon is utilised as a substrate material due to its superior performance during the nanofabrication procedure. Consequently, the temperatures required to reach the sublimation point for these materials based on the ambient pressure are shown on Figure 4-9 [147]:

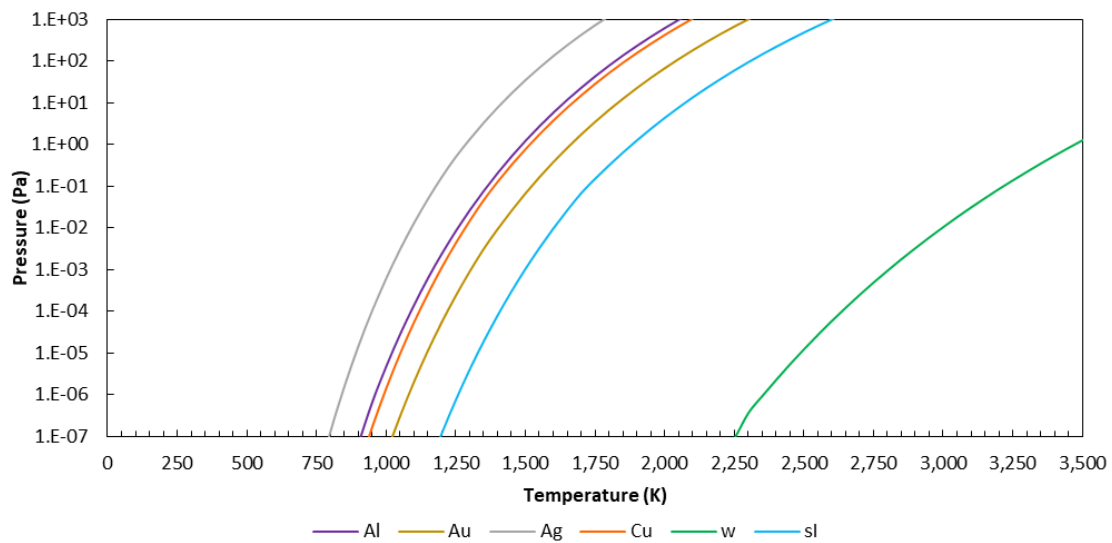


Figure 4-9. Vapor pressure of materials

4.5. Heat transfer calculation

The challenge is to determine the optimal microelectrode size so as not to exceed the temperature at which materials vaporise in vacuum. To calculate heat, one must first determine the supplied electrical energy E_{el} using equation [148],

$$E_{el} = \int P(t)dt = VIt \quad \text{Eq. 90}$$

where P is electric power in function of time, V is the voltage, I is the current and t is the time.

Furthermore, the thermal energy E_{th} is determined by [148],

$$E_{th} = \int_{T_0}^{T_1} c(T)dT = c(T_1 - T_0) = c\Delta T \quad \text{Eq. 91}$$

Chapter 4. Designing the micro-thruster chip

where c is the heat capacity dependent of the temperature, T_0 is temperature at start and T_1 becomes the temperature at end. Moreover, the heat capacity c can be calculated by the relation:

$$c = c(T) = S(T)m = S(T)V\rho \quad \text{Eq. 92}$$

where $S(T)$ is the specific heat in function of the temperature, m is the mass, V is the volume and ρ is the density of the material. Being the specific heat as a function of temperature T , as follows:

$$S(T) = a + bT + eT^2 + fT^3 \quad \text{Eq. 93}$$

where a , b , e , and f are empirical coefficients. Thus, if the specific heat is in function of the temperature consequently the heat capacity is in function of the temperature too.

According to the experiment from LD Didactic GmbH [148] the relation between the electric power and the heat energy on films is

$$E_{el} = E_{th} \quad \text{Eq. 94}$$

Taking Eq. 90 and Eq. 91 and solving for ΔT , it is determined

$$\Delta T = \frac{Pt}{c} = \frac{IVt}{c} \quad \text{Eq. 95}$$

Consequently, the heat transfer by Joule Heating flow rate q_{Jh} is defined by combining Eq. 95 and Eq. 92, as follows:

$$q_{Jh} = \frac{c\Delta T}{t} = \frac{Sm\Delta T}{t} = \frac{SV\rho \Delta T}{t} \quad \text{Eq. 96}$$

4.5.1. Radiation heat transfer

For heat losses, if a hot object radiates energy to its cooler surroundings, the net radiation heat flow rate q_{rad} is expressed as [149]

$$q_{rad} = \varepsilon\sigma(T_h^4 - T_c^4)A_h \quad \text{Eq. 97}$$

Chapter 4. Designing the micro-thruster chip

where ε is the emissivity coefficient of the object, σ is the Stefan-Boltzmann constant equal to 5.6703×10^{-8} , T_h is the hot body absolute temperature, T_c is the cold surroundings absolute temperature and A_h is the area of the hot object.

4.5.2. Between Two-Surface Enclosure

If both micro-electrode plates are facing each other, radiation heat transfer between two-surface enclosures must be considered due to the microgaps between the electrodes. Thus, the net exchange of radiation between surfaces can be expressed as [150]

$$q_{rad\ 1\ to\ 2} = \frac{\sigma(T_1^4 - T_2^4)}{\frac{1 - \varepsilon_1}{\varepsilon_1 A_1} + \frac{1}{A_1 F_{12}} + \frac{1 - \varepsilon_2}{\varepsilon_2 A_2}} \quad \text{Eq. 98}$$

$q_{rad\ 1\ to\ 2}$ represents the net heat flow rate, which depending on its value, can be emitted (+) or absorbed (-). T_1 is the absolute temperature of the hot body, T_2 is the absolute temperature of the cold body, A is the surface area of the object, and F_{12} is the view factor between bodies 1 and 2.

4.5.3. Radiation View Factors

The analysis of the energy exchange by radiation between two surfaces relies heavily on the comprehension of view factors, the precise evaluation of which is crucial for a variety of applications. View factor between two components is influenced by their geometry, orientation, and relative position. The geometric view factor is defined as the ratio of two isothermal, black, diffusely emitting and reflecting surfaces, as calculated in [151],

$$F_{ij} = \frac{1}{A_i} \int_{A_i} \int_{A_j} \frac{\cos \theta_i \cos \theta_j}{\pi R^2} dA_i dA_j \quad \text{Eq. 99}$$

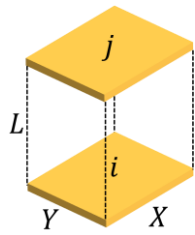
It follows from the solution of the integrals in this equation that [151]

$$A_i F_{ij} = A_j F_{ji} \quad \text{Eq. 100}$$

This expression can be utilised to determine one view factor given knowledge of the other [150].

As demonstrated by Gupta, M.K., et al. [152], there are numerous methods for calculating the view factor, such as integration, unit sphere, cross string, Monte Carlo, ray casting, and matrix.

The cross string method was chosen for this study due to its low computing time for evaluating the view factor on aligned parallel rectangle electrodes provided by Incropera, F.P. et al. [150]:



$$\bar{X} = \frac{X}{L} \quad \text{and} \quad \bar{Y} = \frac{Y}{L}$$

$$F_{ij} = \frac{2}{\pi \bar{X} \bar{Y}} \left\{ \ln \left[\frac{(1 + \bar{X}^2)(1 + \bar{Y}^2)}{1 + \bar{X}^2 + \bar{Y}^2} \right]^{1/2} + \bar{X}(1 + \bar{Y}^2)^{1/2} \tan^{-1} \frac{\bar{X}}{(1 + \bar{Y}^2)^{1/2}} + \bar{Y}(1 + \bar{X}^2)^{1/2} \tan^{-1} \frac{\bar{Y}}{(1 + \bar{X}^2)^{1/2}} - \bar{X} \tan^{-1} \bar{X} - \bar{Y} \tan^{-1} \bar{Y} \right\} \quad \text{Eq. 101}$$

4.5.4. Thermal conductivity

The metal of the electrodes heats up due to the current flowing through the circuit. This temperature increase is proportional to the metal-strip element's temperature coefficient of resistance. The interior heat is then transferred to the substrate or surrounding materials via surface contact. Taking into account the heat loss of the electrodes, it can be described by the following relation [149]

$$q_{cond} = \frac{dQ}{dt} \quad \text{Eq. 102}$$

where q_{cond} is the net heat conduction flow rate, dQ is the difference of heat transfer over a given period time denoted by dt .

Typically, heat conduction calculations are based on the Fourier law, which establishes an empirical relationship between the conduction rate in a material and the temperature gradient in the direction of energy flow and is expressed as [149].

$$q_{cond} = -kA \frac{dT}{dx} \quad \text{Eq. 103}$$

Being k is the thermal conductivity of body material, A is the cross-sectional area normal to direction of heat flow and $\frac{dT}{dx}$ is the temperature gradient. Similar definitions are associated with thermal conductivities in the y - and z -directions, but the thermal conductivity of an isotropic material is independent of the transfer direction.

In the event that two bodies are in contact (Figure 4-10), the corresponding equation is [149]:

$$\frac{dQ}{dt_1} = \frac{dQ}{dt_2} \quad \text{Eq. 104}$$

Consequently,

$$\frac{k_1 A (T_{jh} - T_x)}{L_1} = \frac{k_2 A (T_x - T_{env})}{L_2} \quad \text{Eq. 105}$$

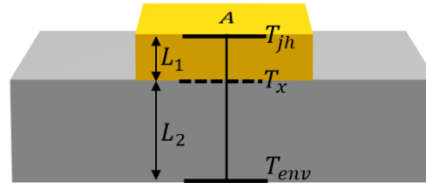


Figure 4-10. Diagram of the heat conduction between an electrode and the substrate

Solving for T_x , it is obtained,

$$T_x = \frac{k_1 L_2 T_{jh} + k_2 L_1 T_{env}}{k_1 L_2 + k_2 L_1} \quad \text{Eq. 106}$$

Given that ΔT from Eq. 95 equals T_x from Eq. 106, the net heat conduction flow rate can be expressed as:

$$q_{cond} = \frac{c(T_x)}{t} = \frac{c}{t} \left(\frac{k_1 L_2 T_{jh} + k_2 L_1 T_{env}}{k_1 L_2 + k_2 L_1} \right) \quad \text{Eq. 107}$$

i. Thermal conductivity k

Films thicker than $1 \mu\text{m}$ are regarded as bulk material; therefore, thin films have a lower thickness [153]. In the case of micro-plasma thrusters, the thickness of the electrodes is approximately 500 nm , making them eligible for classification as thin films. Consequently, variations in thermal conductivity relative to bulk materials must be considered.

To determine if thermal conductivity varies, a study on the thermal conductivity of thin films was conducted, which can reveal changes in the value of k as the film thickness decreases. Consequently, a factor f_k for thin films was derived from the behaviour of bulk k using the following relationship [154]:

To determine whether thermal conductivity varies, a study was conducted on thermal conductivity, defined as:

$$f_k = \left(\frac{k_{film}}{k_{bulk}} \right) \quad \text{Eq. 108}$$

Chapter 4. Designing the micro-thruster chip

where k_{film} and k_{bulk} represent, respectively, the thermal conductivity of thin films and bulk materials. For Cu [155], Al [156], Au [154], W [157] and Ag [158], f_k values of 0.90, 0.72, 0.70, 0.5, and 0.45 were determined.

Using the predefined thermal conductivity values for bulk films [150] and f_k , thin film thermal conductivity is calculated as follows on Figure 4-11:

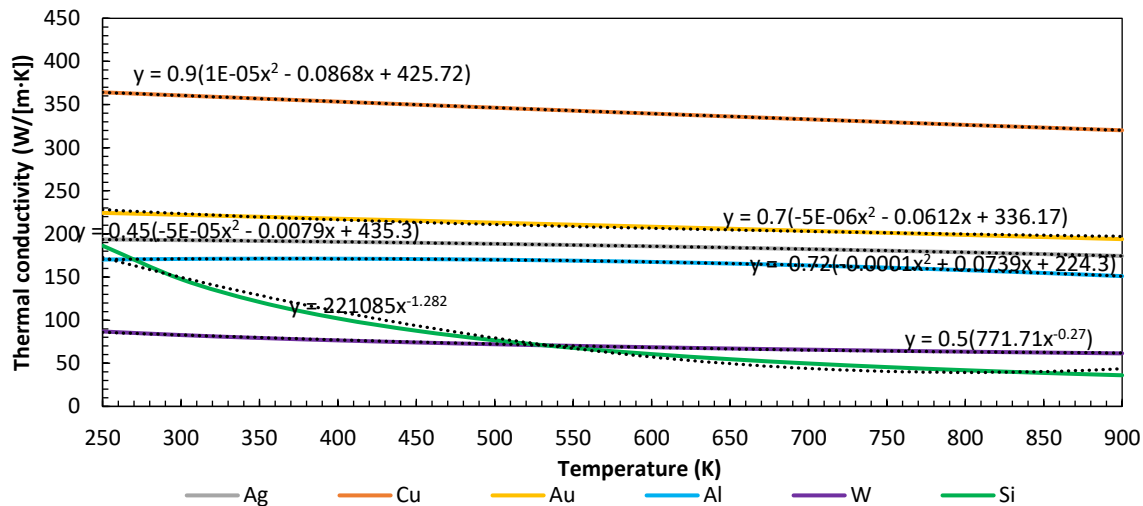


Figure 4-11. Thermal conductivity formula for each material considered for micro-thruster chip electrodes.

The following expressions describe each k material curve:

Material	K(T) equation (W/[m·K])
Ag	$k(T) = 0.45(-5 \times 10^{-5}T^2 - 0.0079T + 435.5)$
Cu	$k(T) = 0.9(1 \times 10^{-5}T^2 - 0.0868T + 425.72)$
Au	$k(T) = 0.7(-5 \times 10^{-6}T^2 - 0.0612T + 336.17)$
Al	$k(T) = 0.72(-1 \times 10^{-4}T^2 - 0.0739T + 224.3)$
W	$k(T) = 0.5(771.71T^{-0.27})$
Si	$k(T) = -221085T^{-1.282}$

4.5.5. Convection

The equations below describe the heat transfer between the gas particles and the electrode surface.

$$q_{conv} = hA_h(T_{jh} + T_{env}) \quad \text{Eq. 109}$$

Where h is the heat transfer coefficient and determine the heat generated in the electrodes and the maximum temperature they can withstand requires calculating the system's heat loss. Radiation heat q_{rad} , conductive heat q_{cond} , and convective heat transfer q_{conv} determine where heat loss occurs on electrodes. The heat transfer coefficient h can be expressed as [159]:

$$h = \frac{N_u k}{L} \quad \text{Eq. 110}$$

Where N_u is Nusselt number, k thermal conductivity and L characteristic length.

For this specific case, as a reference value for the micro-thruster chip, the thermal conductivity k for nitrogen (N₂) is given by [160]:

$$k(T) = 0.024 + 7.53 * 10^{-5} * T - 1.26 * 10^{-8} * T^2$$

Where k approximately 0.04657 W/m·K at 300K, for natural convection over a vertical plane plate, a $N_u \approx 4.89$ [161] is assigned, and for the characteristic $L = 50 \mu\text{m}$, giving a heat transfer coefficient value of $h \approx 4554 \text{ W/m}^2\text{K}$. It is important to emphasise that the heat transfer rates in microchannels are often different from those observed in macroscopic systems due to their size and enhanced mechanisms of transferring heat [162].

4.6. Electrode geometry shape analysis

To determine the optimal electrode shape and thickness for minimising power loss in micro-thruster chip operation. First, on Figure 4-12, A) a square and two circular electrode shapes were evaluated, with the square having dimensions of 500 x 500 x 250 μm and a volume of $6.25 \times 10^{-11} \text{ m}^3$. B) For one of the circular shapes, the dimensions were determined to be 500 μm in diameter and 250 μm in thickness, with a volume of $4.91 \times 10^{-11} \text{ m}^3$, while maintaining the same diameter and thickness as the square electrode. To maintain the same volume as the square shape, C) the second circular shape was given a diameter of 500 μm and a thickness of 318.31 μm .

In the second case (Figure 4-13), the effect of different thicknesses on five squared shapes [A-E] was evaluated while the volume was held constant at $6.25 \times 10^{-11} \text{ m}^3$ to determine whether radiation or conductivity contributes more electrical conductivity power. In both cases of analysis, it was assumed that all electrodes were affixed to a silicon substrate with an electrical power of 5 mW, a view factor of 1, and a continuous operation time of 15 seconds. An ideal electrode as a superconductor is one

Chapter 4. Designing the micro-thruster chip

that conducts the 5 mW set for this analysis; the difference between this power and the net power flow rate is the power lost as heat.

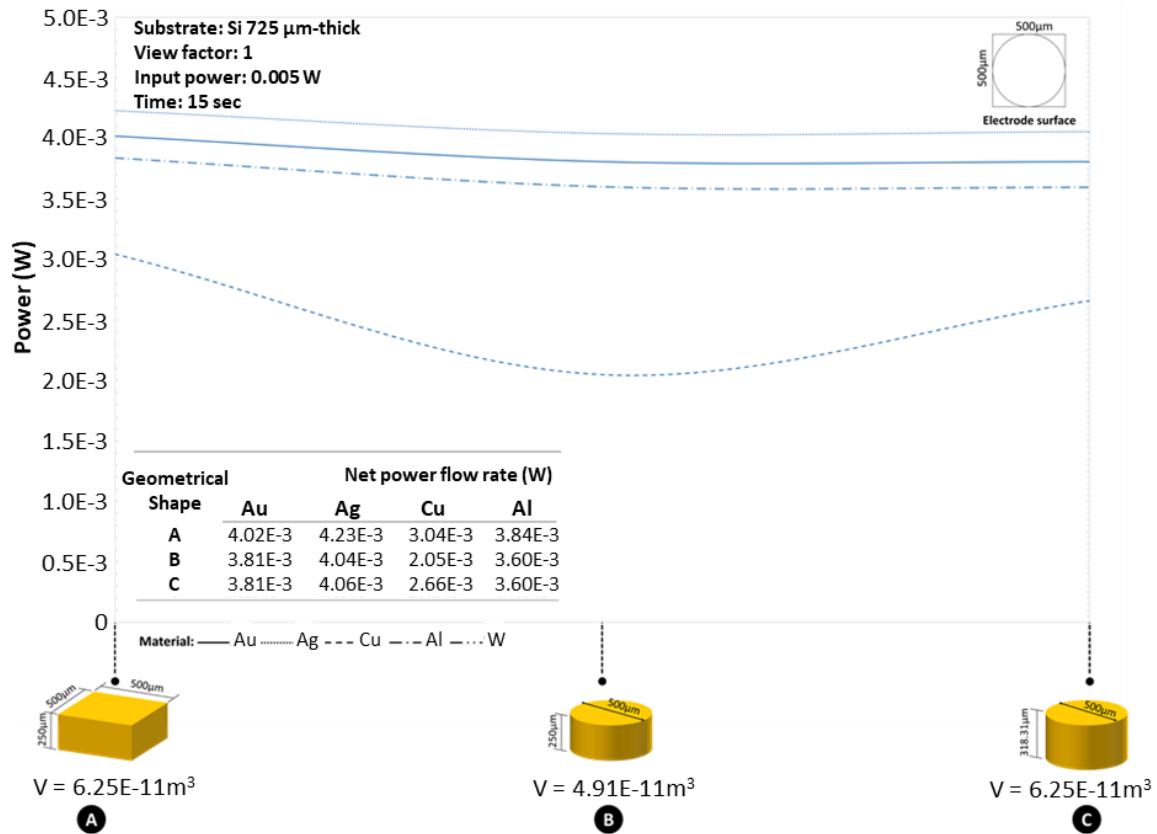


Figure 4-12. Electrical net power flow rate on electrodes modelling based on their shape made of Au, Ag, Cu, and Al materials.

The results in Figure 4-13-A shows that the larger the area of the micro-electrode surface, the less heat is retained and the higher the power flow rate is present. In the absence of a propellant, only two types of heat loss can be observed in a vacuum: radiation and conduction heat. As a result, the larger the surface area, the more heat can escape decreasing the molecular instabilities in the material while also losing less electrical power in the form of heat. The square shape has the greatest surface area because it covers more space than the circular shape with the same value of square length on its radius. As a result, larger surfaces become a better option for the electrodes.

The thickness also plays an essential role in dissipating heat by increasing the exposed surface. It was observed that materials with the greater thickness (Figure 4-13) but the same volume have lower electric conductivity because heat dissipates better through conduction than through radiation. As a

Chapter 4. Designing the micro-thruster chip

result, the Joule Heating of the electrode dissipates faster when its surface area comes into contact with another cooler body (substrate) where the electrical power conduction losses less.

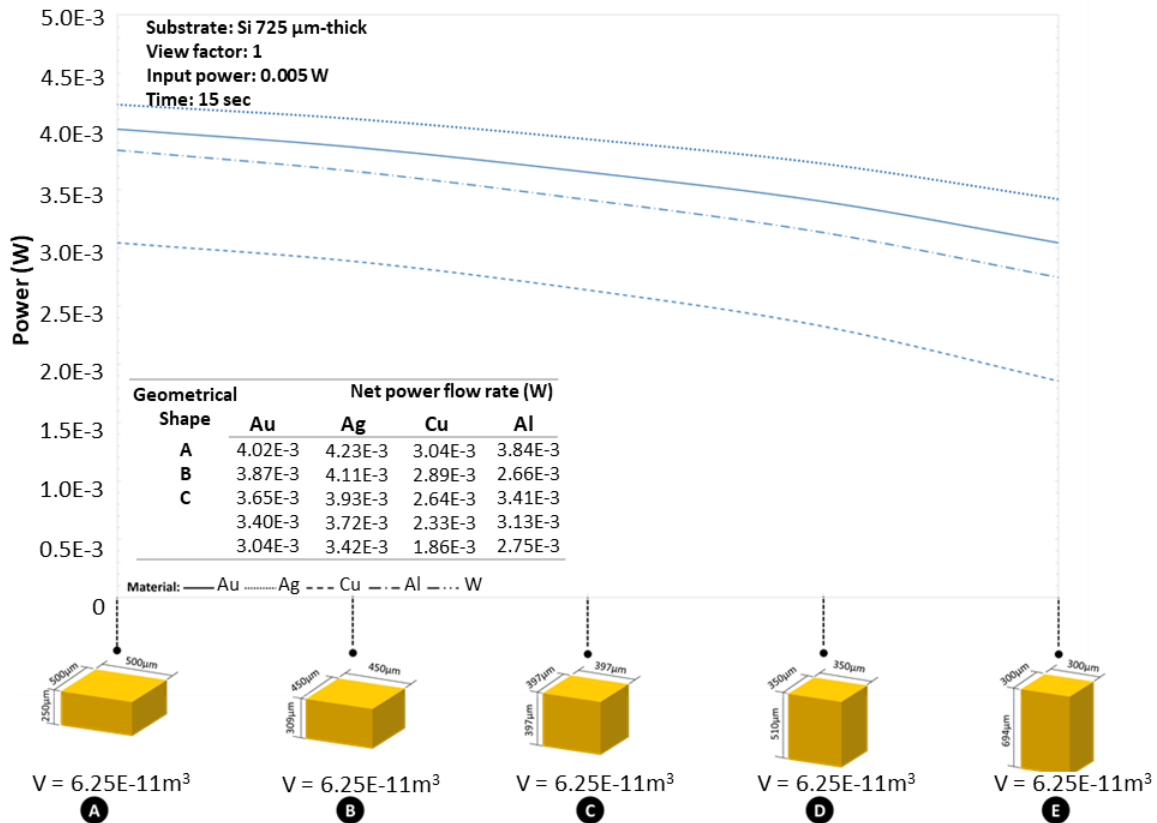


Figure 4-13. Electrical net power flow rate on electrodes modelling based on their thickness made of Au, Ag, Cu, and Al materials.

The decision to use flat, rectangular electrodes is also motivated by the desire to have uniform electric fields between simulation and experimental setups. However, the algorithm for simulating micro-plasma discharges can only model flat electrodes and not curved ones. In this case, simulations should be able to verify the experiments directly if a rectangular design is adopted thus providing a clear link from theoretical models to practical applications.

Shown in Figure 4-12, it is clear that the shape of an electrode greatly affects its thermal as well as electrical performance. The research examined square and circular electrodes where they found out that rectangular shapes have larger surface area than circular ones thereby enhancing heat dissipation with reduced heat retention; this leads into higher power flow rates coupled with decreased risk of overheating. More heats can escape through bigger surfaces which results in lower molecular instabilities besides reducing heat loss due to electrical power.

Chapter 4. Designing the micro-thruster chip

From the manufacturing point of view, flat and rectangular electrodes are much easier to produce and handle compared to their counterparts. They match up with resolution capabilities of fabrication tools available so far hence ensuring that they are made according to required specifications for optimum performance. Circular or irregular shaped electrodes may introduce extra challenges during fabrication thereby causing defects or variations affecting micro-thruster's performance.

4.7. Electrodes heat over time

To identify the limits of heat on micro-electrodes on the micro-thruster chip, the volume- ΔT plot below displays the results of the net power that is still conducted through the electrode plate after power losses (radiation and conductive heat) at various time intervals (from 10^{-8} s to 10^{-5} s) as determined by Eq. 79. The supply power is in the range of 0.001 W to 0.01 W to maintain the current (10^{-6} to 10^{-2} amperes, as previously discussed) and voltage in the range of 1 kV to 10 kV (common values for breakdown voltages) when the environmental vacuum pressure is 0.01 Pa.

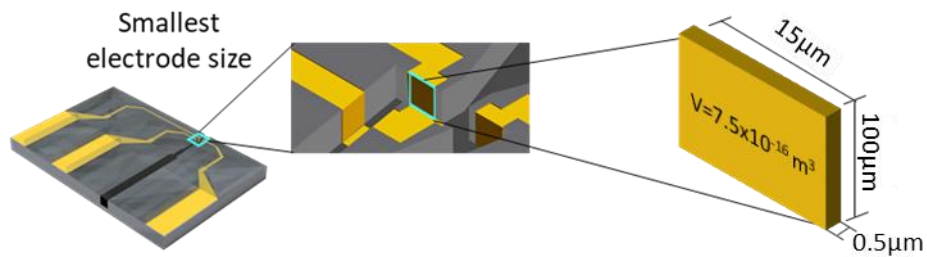


Figure 4-14. Size and location of the smallest electrode on the micro-thruster chip.

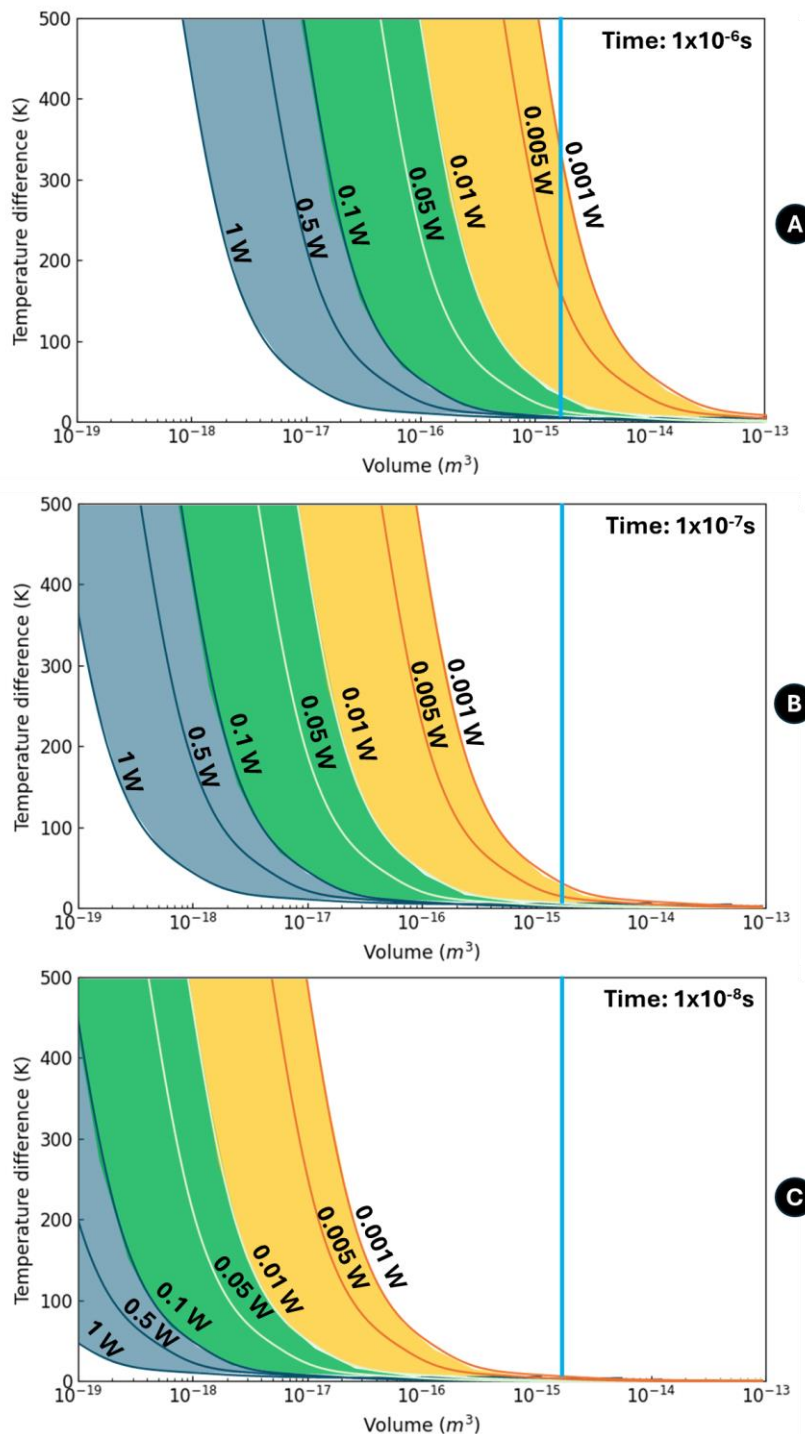


Figure 4-15. Temperature increase on electrodes subjected to electrical power ranging from 0.001 to 1 W. The response is observed for three different DC pulses during 60 seconds: A) 1 μ s, B) 0.1 μ s and C) 0.001 μ s.

To figure out and maximize the performance of the micro-thruster chip, it is important to know how the electrodes react dynamically to different electrical power inputs. According to Figure 4-15, which shows temperature increase (ΔT) on electrodes with respect to power ranging from 0.001W to 1W under three different DC pulse durations over 60s A)1 μ s, B)0.1 μ s and C)0.001 μ s. The critical elements of analysis output are the followings:

Chapter 4. Designing the micro-thruster chip

Power Supply and Activation Time: Joule Heating occurs in the microelectrodes due to two main parameters: power supply and operational time (activation time). The shorter the pulses are, the less heat will accumulate which means there is no risk of reaching melting or sublimation points for electrode materials.

Electrode Volume and Material: When volume decreases, heating effect increases because smaller amount can hold less heat dissipation capacity. In this plot ΔT is plotted against volume & materiality of an electrode as seen in Figure 4-15 where smallest volume used was $7.5 \times 10^{-16} \text{ m}^3$ (dimensions: $15 \times 100 \times 0.5 \text{ }\mu\text{m}$). Based on power between $10^{-8} \text{ s} - 10^{-6} \text{ s}$ DC pulses at electrical powers ranging from 0.001W to 1W;

Reference Line and Safe Operation Range: The vertical dark line at minimum volume value serves as reference line for measuring safety margins during electrode operation shown by Figure 4-15 if ΔT curves move away from this line towards larger volumes overheating likelihood decreases conversely such that exponential increase in ΔT intersects with reference line then there is risk of overheating followed by potential sublimation.

Safe DC Pulse Durations: For preventing overheating according to modelling results are as follows:

- Pulses should be less than $1 \times 10^{-5} \text{ s}$ if power is between 0.001W and 0.01W.
- Pulses should be less than $1 \times 10^{-6} \text{ s}$ if power ranges from 0.01W to 0.1W.
- Pulses should be less than $1 \times 10^{-7} \text{ s}$ if power varies between 0.1W and 1W.

Temperature Threshold: To avoid electrode melting or sublimation during atmospheric-to-high vacuum pressure transitions, maximum ΔT was limited at 500K which can be determined by subtracting 300K from the highest-vaporizing temperature of a metal(800K for Ag in HV).

In conclusion, within these limits, micro-thruster chips can operate safely while retaining their functionality under space conditions where heating may cause overheating leading to material loss through volatilization

4.8. Considerations on design

On the design of the micro-thruster chip, several factors must be considered. Depending on the mission, the micro-thruster chip will operate in Low Earth Orbit (LEO) or space, providing nN to mN

thrust ranges for high-precision manoeuvring for altitude control and displacements. This study aims to test and analyse the DC micro-plasma phenomenon as a thrust source by creating a micro-thruster chip device. Due to microplasma generation, the micro-design thrusters must consider the device as a finished product, with the operational risks of sputtering, degradation, and sublimation on the electrodes. To keep the device operational during missions where replacement or maintenance of micro-propulsion system components in nanosatellites and picosatellites is impossible, the micro-thruster chip must be designed as a hybrid propulsion device, combining the characteristics of a DC plasma thruster with a cold gas thruster, in the event that the electrodes, the high voltage, or the power source fail. Utilising the need for a gas propellant for plasma ionisation, consider it a cold gas propellant in which a nozzle geometry is required to control the flow rate, direction, and velocity to produce a gas jet.

To define the nozzle geometry, four primary factors were considered: (1)the electrode location, (2)the electrode size, (3)the flow acceleration by the expansion of the nozzle, and (4)the goal of fabricating the smallest size possible while still being characterisable with current PIV equipment (Chapter 5) and manipulable with conventional tweezers or hand.

4.8.1. Electrode location

For microplasma generation, the location of the electrodes is crucial for minimising heating and directing plasma acceleration toward the outlet to increase thrust. The parallel electrode plates perpendicular to the outlet were the first placement option considered for the micronozzle's electrodes (Figure 4-16-A). Positive ion formation is likely to be attracted to the cathode, which is perpendicular to the flow through the outlet, resulting in a change in direction opposite the outlet. The accelerated particles will collide with the electrodes and walls of the microchannel, resulting in turbulence flow and a decrease in flow speed and thrust.

As an alternative, a microchannel with a double inlet and a single outlet orifice was idealised to force the flow to travel between the electrodes and direct the cathode towards the outlet to accelerate of positive ions. The anode(s) is/are mounted on the wall opposite the outlet, while the cathode(s) is/are mounted on the surrounding walls near the outlet.

Three electrode configurations were analysed based in section 3.3; Configuration 1:one anode/two cathodes (Figure 4-16-B), Configuration 2: two anodes/two cathodes (Figure 4-16-C), and Configuration 3: one anode(extended)/two cathodes (Figure 4-16-D), keeping the same configuration

Chapter 4. Designing the micro-thruster chip

number as chapter 3. The three configurations were evaluated in terms of velocity, temperature, and thrust based on the simulations presented in section 3.3. Configuration 1 with one anode and two cathodes demonstrates the most effective electrode pattern, with the lowest increase in temperature among the configurations, as well as the highest velocities and thrust values being selected for implementation in the plasma-based micro-thruster chip design.

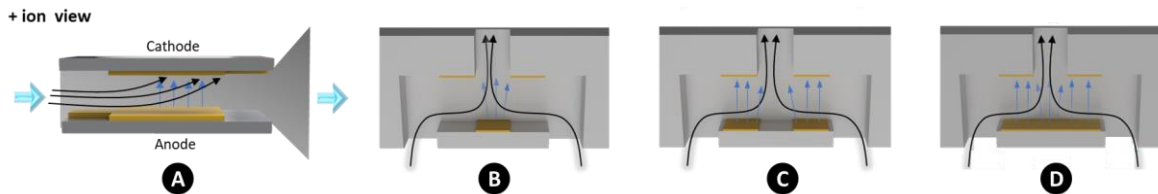


Figure 4-16. Alternatives for electrode placement. A) Perpendicular electrode plates parallel to the outlet. There are three parallel plate layouts where the cathodes towards the outlet: B) configuration 1: one anode/two cathodes, C) configuration 2: two anodes/two cathodes, and D) configuration 3: one anode(extended)/two cathodes.

Once the electrode location was determined, two geometry shapes for the walls that conduct the flow through the outlet on the microchannel with a double inlet and a single outlet orifice were considered.

After determining the location of the electrode, two geometries were considered for the outlet walls of the microchannel with a double inlet and a single outlet orifice (Figure 4-17). Alternative (E) depicts parallel walls and a neck/microchannel connecting the outlet orifice. Alternative (F) is characterised by sloped walls that converge at the outlet orifice. Where the convergence of wall thickness decreases near the outlet, which is undesirable due to the material degradation caused by plasma and the easy removal of the thinner walls that surround the outlet. The contribution of the uncontrolled outlet expansion complicates the plasma analysis for measuring the increase in velocity and thrust during the characterisation phase. In contrast, alternative (E) has a low probability of altering the outlet dimension due to plasma degradation resulting from the geometry's thicker walls.

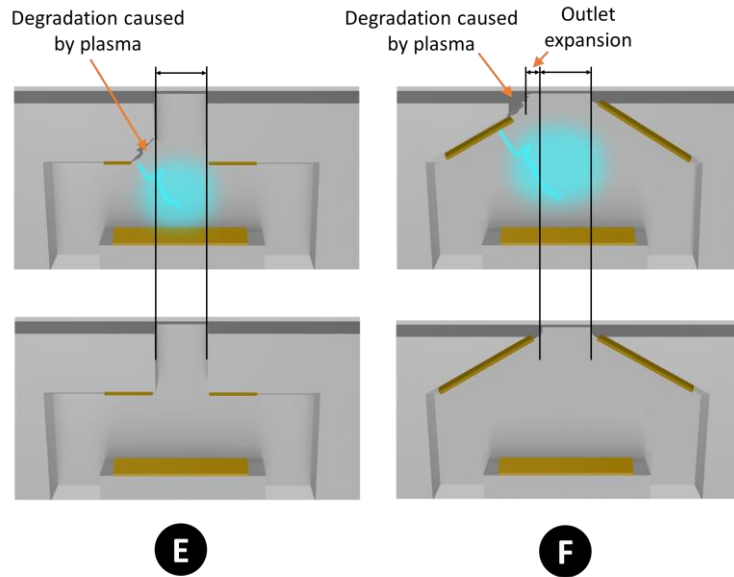


Figure 4-17. Degradation on walls caused by plasma according to the outlet geometry.

In addition, this is the first time the Aerospace Sciences Division has created a microdevice. In order to keep the geometry of the nozzle as simple as possible during the initial fabrication testing, it was determined that the limitations of nanofabrication techniques and equipment were not well understood at the outset. In addition, there are no geometric constraints because this is the first time a plasma-based device has been designed.

4.8.2. Electrode size

As stated in section 4.7, the cathodes comprise the smallest electrode sizing area of the electrical routes, with a minimum volume of $7.5 \times 10^{-16} \text{ m}^3$ for a $15 \times 100 \times 0.5 \text{ }\mu\text{m}$ size. Set the width of the electrode to $100 \text{ }\mu\text{m}$ in relation to the depth of the microchannel so the enough volumetric flow can be exhausted and detected by the PIV system during characterisation (Chapter 6). In terms of electrode thickness, the thicker it can be, the less likely it is that the electrode will overheat; therefore, for physical vapour deposition of electrode material, the tool within JWNC is restricted to a maximum single deposition of $0.5 \text{ }\mu\text{m}$ – thick.

4.8.3. Flow acceleration caused by nozzle expansion

After determining the location, configuration, and minimum size of the electrodes, the nozzle was created using the outlet wall design from section 4.8.1 alternative (E). By connecting a divergent nozzle to the single outlet of a microchannel with double inlets, an expansion is generated to accelerate the exhaust flow and increase thrust. Micro-tubing, such as a hypodermic needle, was believed to have

Chapter 4. Designing the micro-thruster chip

supplied the propellant gas to the double inlet channel. As a result, the hypodermic needle adds weight and size to the micro-thruster chip device, making it inefficient to use a needle to connect each inlet channel. As a result, a single needle was idealised to connect both inlet channels via a triangular geometry, thereby distributing the inlet flow across both channels.

The micronozzle geometry contains ten main parameters on its design. As it is shown on Figure 4-18;

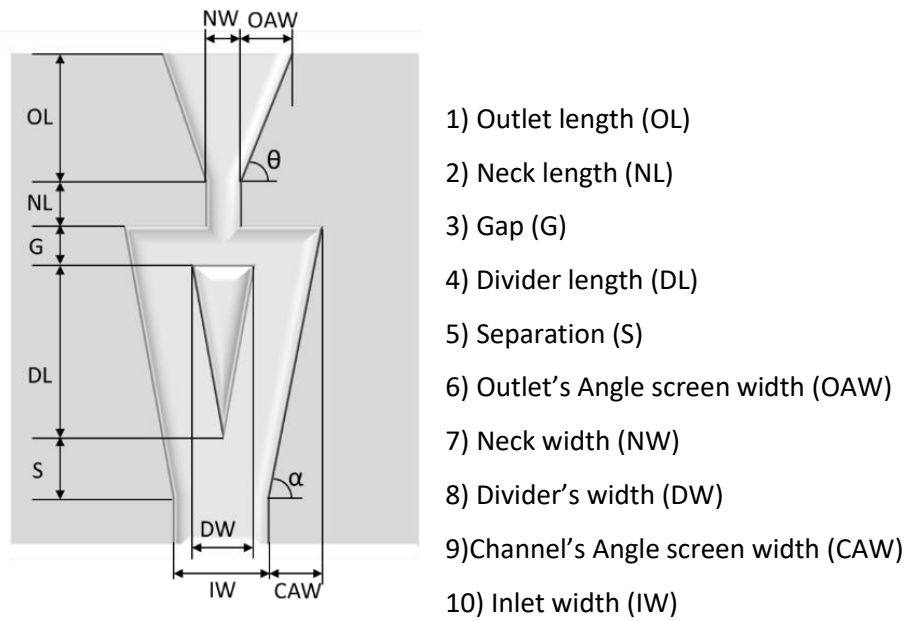


Figure 4-18. Layout of the micronozzle.

For consistency, the DL of each column of 63 chips is 90, 180, 300, or 400 μm , depending on whether the chips are classified as XS (extra-small), S (small), M (medium), or L (large). Each chip has a unique code that can be used to determine its geometry and electrode form. Therefore this categorization will continue to show up in subsequent chapters. Thus, the code consists of first supplying the DL size, then a number representing the gap distance between the electrodes in micrometres, and finally, a code to identify the electrode configuration, of which there are two alternatives, E3 and E5, as shown in Figure 5-6 of Chapter 5.

4.8.4. Microtubing definition

Therefore, a conduit must be constructed to connect the needle to the IW section of the micronozzle to supply the gas propellant. This channel, known as the microtubing channel, must have the same dimensions as the outer diameter of the needle for it to be introduced within the micro-thruster chip (O.D.). To create the smallest microdevice possible, the 34G(O.D. 0.159 mm) and 32G(O.D. 0.235 mm) needles available on the market were considered. In contrast, a metal tapered is essential for safety during tests to allow for higher pressures in the event that the device becomes clogged. Therefore, a

Chapter 4. Designing the micro-thruster chip

30G needle with an outer diameter of 0.310mm and a stainless steel taper was chosen. In addition, the needle must have a blunt needle point (type 3) to prevent any damage to the microchannel wall during the nanofabrication process.

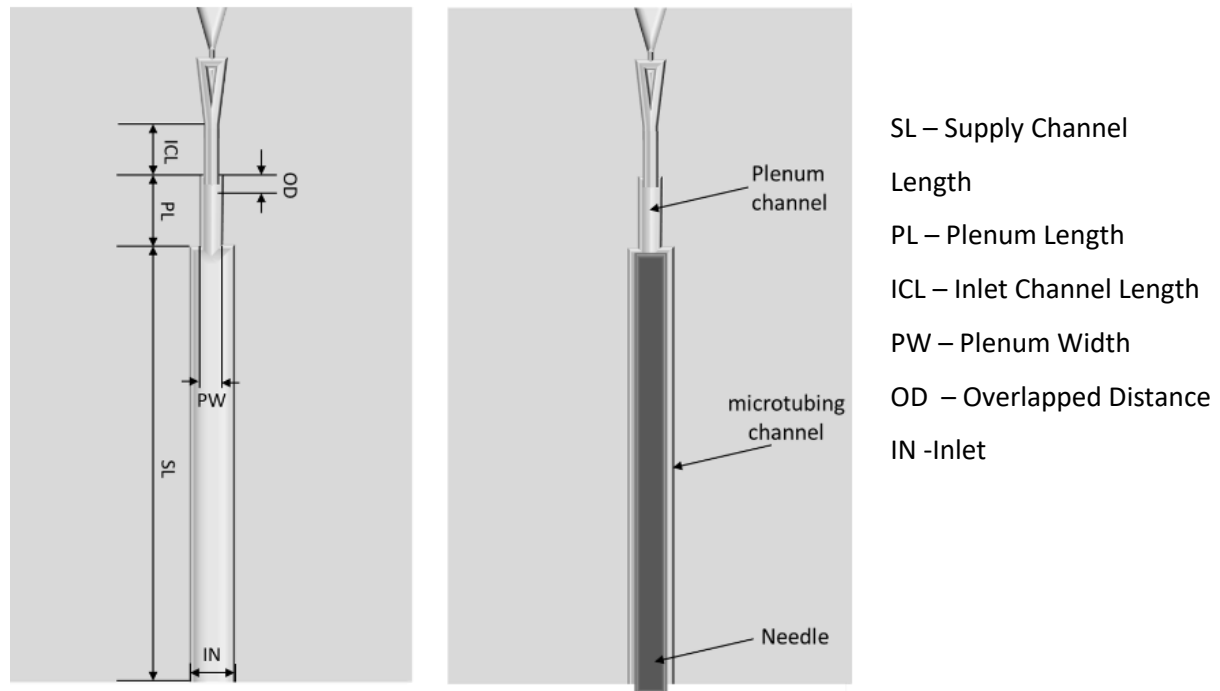


Figure 4-19. Layout of the micro-tubing channel.

Due to the abrupt difference in size between the microtubing channel and the inlet width of the micronozzle inlet, if the 30G is placed until it reaches the inlet walls of the micronozzle, there is a high probability that the needle will become obstructed by the needle's wall, or that high turbulence flow will be created since the inlet. To prevent these issues, a plenum channel, shown on Figure 4-19, was installed between them to allow the propellant gas flow to become laminar.

Determine the thrust performance of the micronozzle and how it varies as the size of its geometrical structure is altered according to the eight parameters depicted in Figure 4-20. Using OpenFOAM-2.4.0-MNF and the dscmFOAM+ solver, various 2D simulations were conducted with the micronozzle as a cold gas propulsion system. Each case was assigned a fixed parallel run of 10 cores on the Buckethead cluster at the University of Glasgow, where a total of 96 simulations were executed. The gas propellant was set to nitrogen (N₂) at 300 K with inlet pressures of 1 KPa and 30 KPa and an exit pressure of 1Pa to simulate vacuum conditions in order to run slim particle cases. With a 50 μm wide expansion region external to the efflux section. A timestep of 1ns was set to run for a maximum of 0.5×10^{-4} s, with `dsmcLiouFangPressureOutletSpecifiedMolarFraction` and `dsmcWangPressureInlet` as boundary models for the outlet and inlet, respectively.

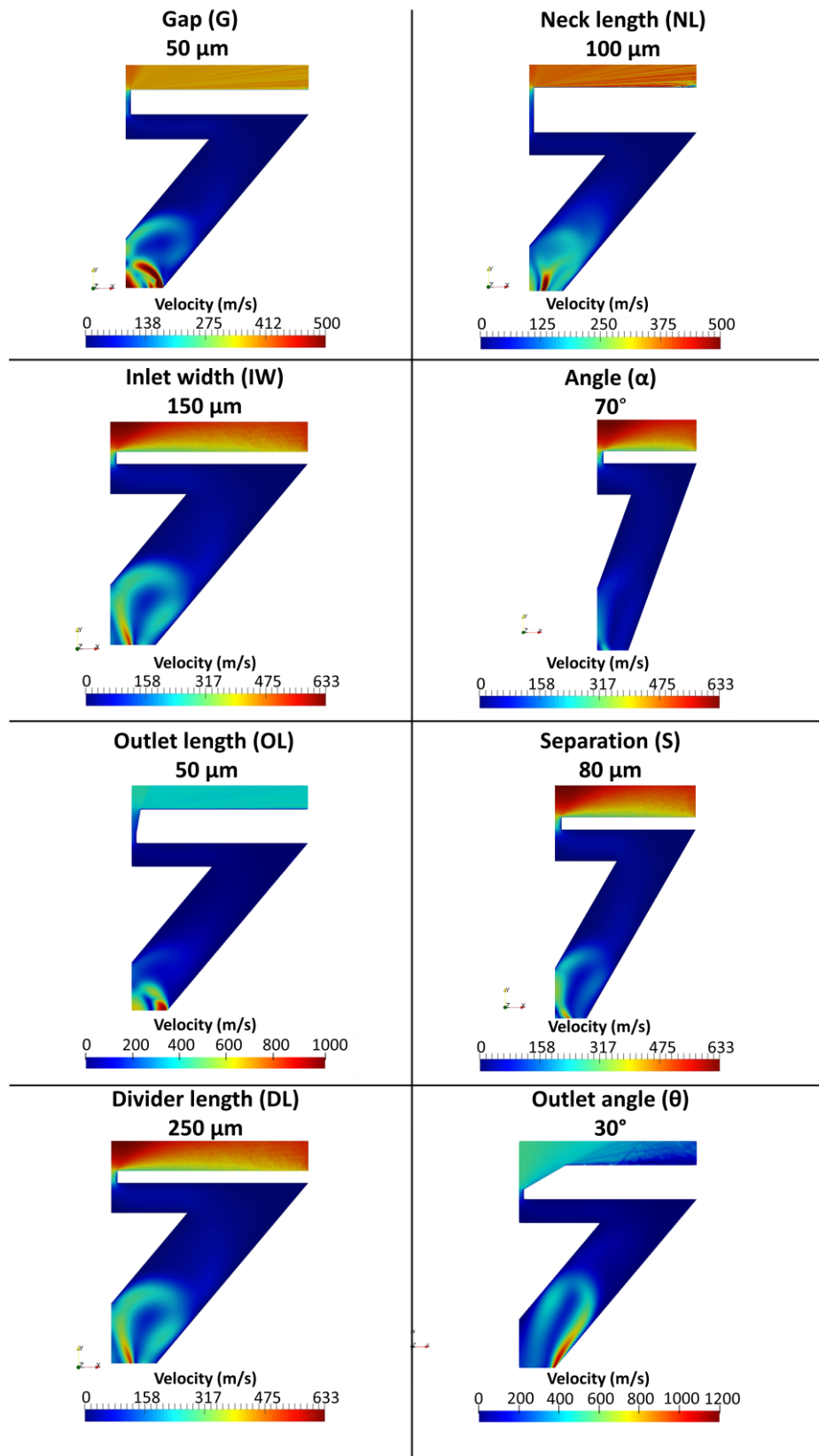


Figure 4-20. N2 dsmcFOAM+ simulation results for the velocity magnitude on the micronozzle as a cold gas thruster with an inlet pressure of 30KPa and an outlet pressure of 1Pa.

Chapter 4. Designing the micro-thruster chip

For the purpose of identifying and analysing the geometrical size contributions of the micronozzle on each of the eight parameters, the thrust T was calculated for each example using the expression.

$$T = \dot{m}v_e + (p_e - p_0)A_e \quad \text{Eq. 111}$$

Where p_e is the exhaust pressure and p_0 is the free stream pressure. Similarly, v_e is the exhaust velocity and A_e is the exhaust area. All variable values and post-processing were collected from simulated cases utilising ParaView 5.9.1. Where the \dot{m} is the mass flow rate, defined as

$$\dot{m} = \rho v_e A_e \quad \text{Eq. 112}$$

Figure 4-21 depicts thrust values; each plot depicts the change in size or angle on a single geometric parameter while holding the other parameters constant to identify variations in thrust at the nozzle outlet. Size-related information is expanded upon in Appendices - "A. Geometrical dimensions of the micro-thruster chip". When thrust increases, pressure increases from a range of 1.54 nN to 4.96 nN at 1 KPa to a range of 87.39 nN to 678.42 nN at 30 KPa. Increasing the separation can alter the thrust by up to 35.6 nN at 30 KPa and 1.05 nN at 1 KPa, whereas changing the angles from 20° to 80° results in a ΔT of 1.35 nN to 229.3 nN and 2.01 nN to 334.36n N for 1 KPa and 30 KPa inlet pressures, respectively. Inlet widths(IW) between 150 μm and 840 μm , divider length(DL) between 200 μm and 500 μm , neck length(NL) between 20 μm and 100 μm , gap(G) between 5 μm and 100 μm , and outlet length (OL) between 50 μm and 300 μm have a ΔT between 0.152 nN(1 KPa) and 87 nN(30 KPa), 1.68 nN(1 KPa) and 218.27 nN(30 KPa), 1.78 nN for both 1 KPa to 30 KPa, and 2.85 nN(1 KPa) to 494 nN(30 KPa), respectively.

As this is the first time a plasma-based structure has been designed and nanofabricated in the aerospace division, there are no geometrical size restrictions. Minitab Statistical software was used to run a design of experiments (DOE) based on factorial regression to identify the geometrical parameters that contribute most to the thrust performance of the micro-nozzle. Figure 4-22 depicts the main effects plot for thrust, while Figure 4-23 depicts the Pareto chart.

Minitab generates the main effects plot by plotting the means for each value of a categorical variable, such as distance, angle, inlet width, etc. Each block contains a line representing the mean thrust in nN for each geometrical parameter, where the line determines the presence or absence of the main effect for a categorical variable. The blue line is the overall mean reference line. Thus, when the line is horizontal (parallel to the x-axis), the current variable has no main effect, indicating that the response means the same across all factor levels for this particular micronozzle's geometrical parameter. In contrast, there is a primary effect when the line is not horizontal. The average response varies across all factor levels. The major effect magnitude is proportional to the line slope.

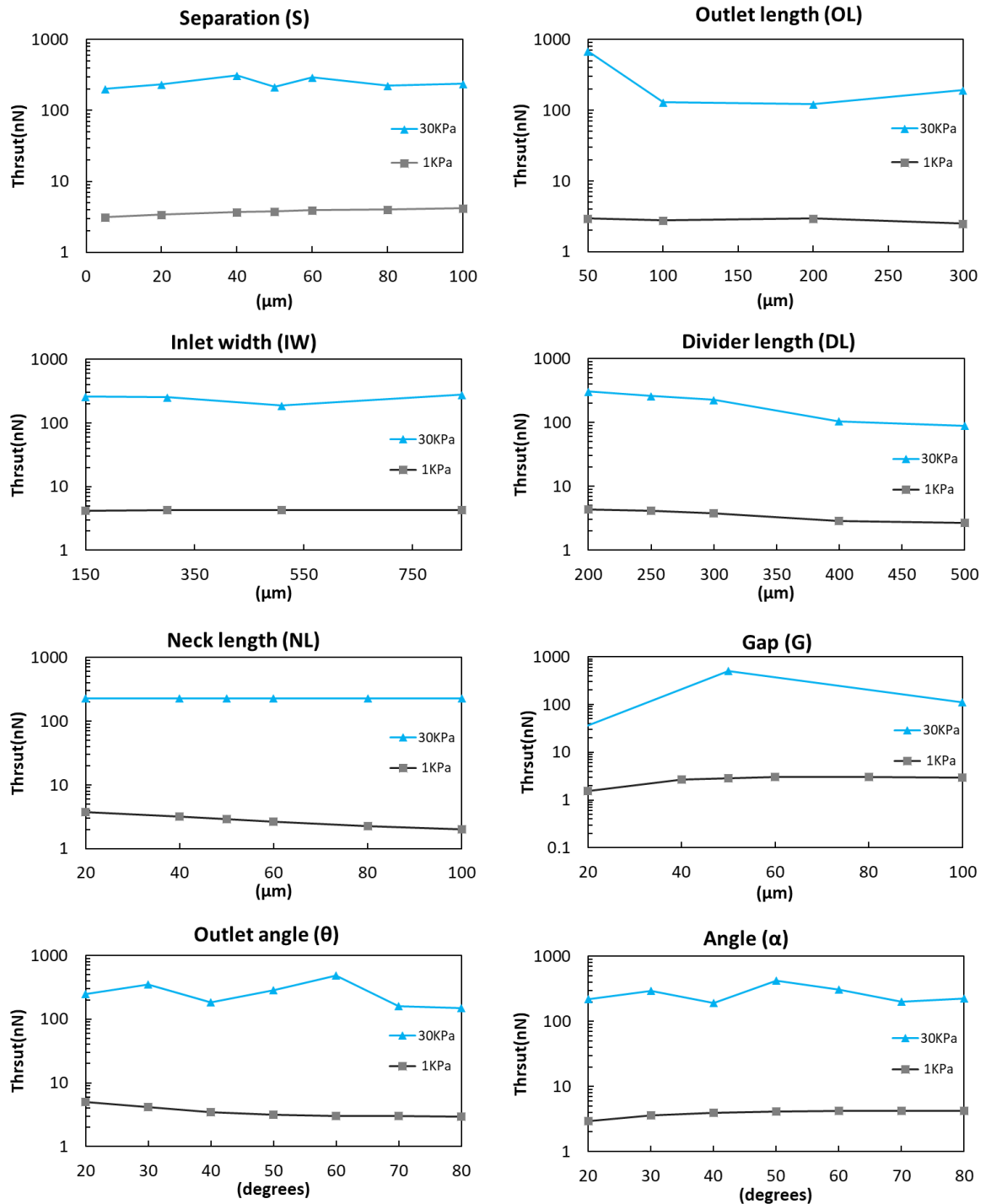


Figure 4-21. Thrust performance based on the geometric parameters of the micronozzle with 1KPa and 30KPa inlet pressure and 1KPa outlet pressure.

According to the factorial analysis in Figure 4-22, there are no significant effects of variations in dimensions on the separation (S) and outlet length (OL). Consequently, variations in angle (α) have a minor impact on thrust, where the greater the angle, the lower the thrust, and the wider the inlet

Chapter 4. Designing the micro-thruster chip

width (IW), the greater the thrust. The length (DL) of the micronozzle has a greater impact on thrust as it increases, while the gap distance (G) has a greater impact as it increases. The outlet angle (θ), in which the thrust raises as the angle increases, and the outlet length (OL), in which the thrust decreases as the length increases, are the two parameters whose variation on the micronozzle's dimensions has the most significant effect contribution.

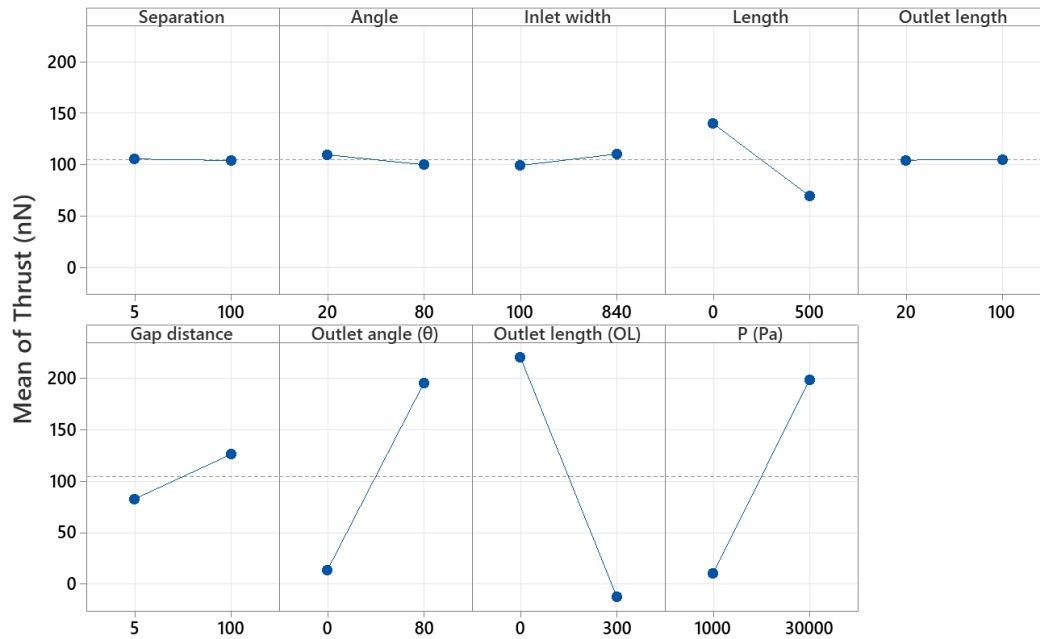


Figure 4-22. The main effect plot for thrust based on the geometric parameters of the micronozzle; Separation (S), Angle (α), Inlet width (IW), Divider length (DL), Neck length (NL), Gap (G), Outlet angle (θ), Outlet length (OL), P (Pa)

The Pareto chart displays the absolute values of the standardised effects of the geometrical factors contributing to thrust, from the greatest to the most negligible impact. The standardised effects are computed using t-statistics, which are employed to test the null hypothesis that the effect is nullified. The significance level (denoted by α) establishes the line of statistical significance. The results correlate with the significant effects plot, confirming that the outlet length (OL) is the most important parameter contributing to the nozzle thrust performance, followed by outlet angle (θ).

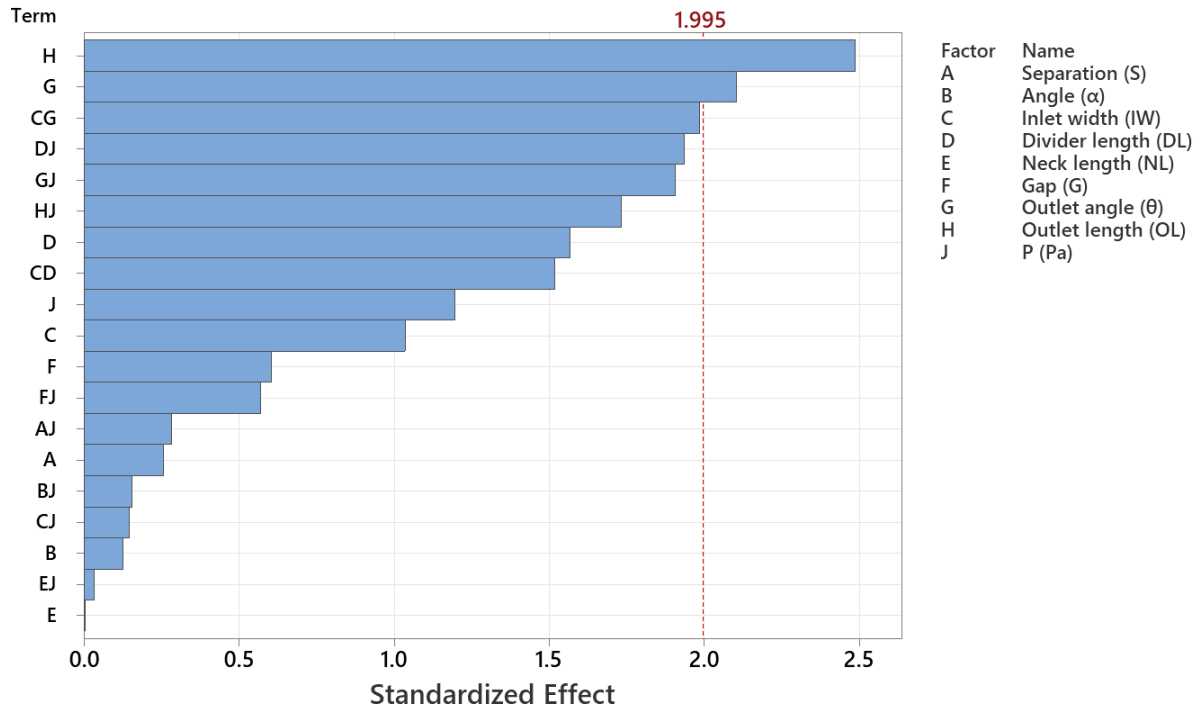


Figure 4-23. Pareto chart of the standardised effects (with 95% confidence) based on the reaction of thrust (nN) supplied by micronozzle geometry variations.

The expression in Eq. 113 describes the thrust of the micronozzle as a cold gas thruster in function of separation (S), angle (α), inlet width (IW), divider length (DL), neck length (NL), gap (G), outlet angle (θ), outlet length (OL), and gap (G) can be described as:

$$\begin{aligned}
 T_{\mu\text{Nozzle}} = & [-11 + 1000(S) + 30000(\alpha) + 1500(IW) + 20000(DL) - 31000(NL) \\
 & - 4000(G) + 0.01388(p) + 7(S \times p) - 0.00001(\alpha \times p) - (IW \times p) \\
 & - 27(DL \times p) + 2(NL \times p) + 30(G \times p)][1 - 0.019(\theta) - 0.072(OL) \quad \text{Eq. 113} \\
 & + 0.00093(\theta \times OL) + 0.000009(\theta \times p) + 0.000092(OL \times p) \\
 & - 0.000001(\theta \times OL \times p)](1 \times 10^{-9})
 \end{aligned}$$

Chapter 4. Designing the micro-thruster chip

Thus, the approximation of Eq. 113 to the thrust simulation results using N2 propellant is displayed on Figure 4-24.

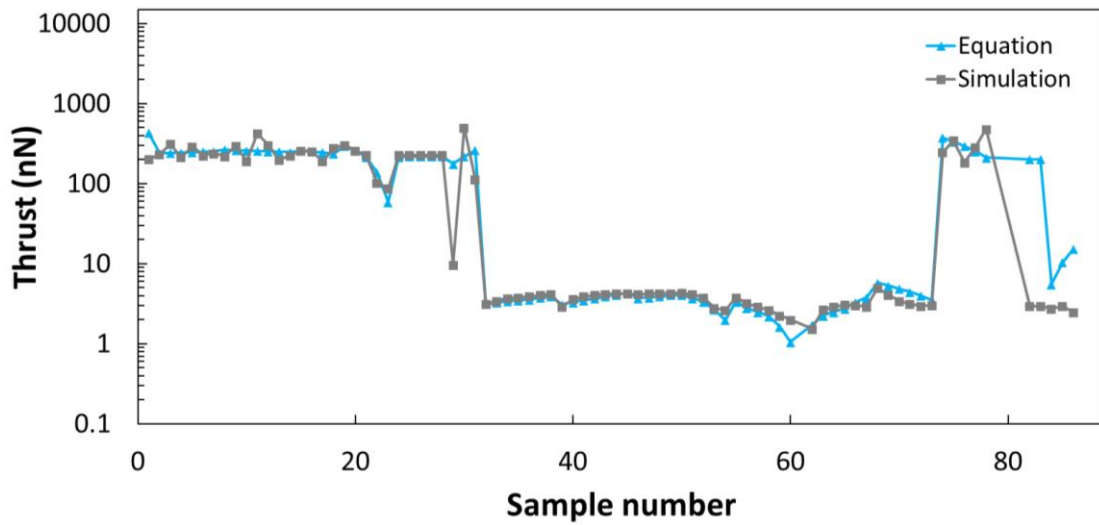


Figure 4-24. Comparison between simulations results and $T_{\mu\text{Nozzle}}$ equation

To calculate the performance of the micronozzle as a DC plasma-based micro-thruster, 180 simulations were performed. To have a broad mapping of numerical thrust values within the most possible operational electrical parameters to form plasma, not only as initial reference values, but also for subsequent validation of the micro-plasma discharge algorithm with experimental results. Therefore, electrical currents of 1×10^{-3} A, 1×10^{-4} A, 1×10^{-5} A, and 1×10^{-6} A were simulated, along with voltages of 200V, 400V, 800V, 1200V, and 1600V for each current case. At each voltage, a gap distance of 10 μm , 50 μm , and 100 μm was utilised. And for each gap, the inlet pressure was set at 10 KPa, 50 KPa, and 100 KPa, with 1 Pa as the outlet pressure, as shown in the diagram below on Figure 4-25.

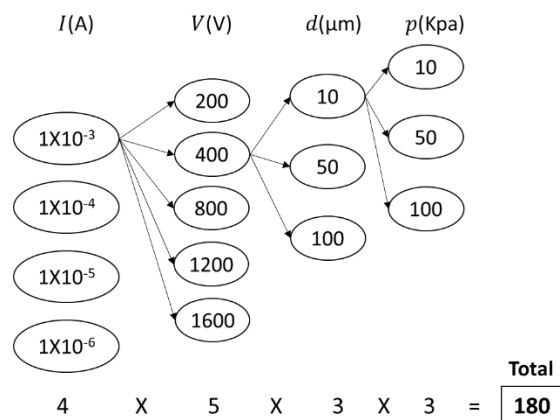


Figure 4-25. Diagram illustrating the number of computational simulations based on parameter permutations (current, voltage, gap, and pressure)

To make the thrust results from the plasma simulation cases comparable, it was assumed that the increase in thrust on this equation could be accounted for by multiplying it by a normalised factor that describes the contribution of plasma to the results, while searching for an expression that can be combined with Figure 4-24. This normalised factor is influenced by the electrical current, voltage, distance between the gaps, and pressure. The plasma simulation result was used to derive the normalised factor $T_{\mu Plasma}$, which was then applied to calculations of thrust from the plasma simulation $T_{\mu Plasma}$ over simulations of thrust from the nozzle as a cold gas thruster $T_{coldGas}$, given by

$$\hat{T}_{\mu Plasma} = \frac{T_{\mu Plasma}}{T_{coldGas}} \quad \text{Eq. 114}$$

Figure 4-26 is a diagram depicting the outcome of $\hat{T}_{\mu Plasma}$. For 10 μm from voltages of 200 V or higher, regardless of inlet pressure, 1 μA and 10 μA produce comparable thrust values because the microgap is so small that it is already choked, preventing a greater mass flow rate from passing through the outlet with a constant thrust even as the voltage and current increase to 10 μA . As a result, for the 10 μm , the thrusts decrease slightly at 1200 V due to increased turbulence that prevents the flow from flowing directly to the outlet. This is caused by increasing the current to 100 μA and the voltage, which provides more electrons with a greater potential, causing the ionisation to choke flow and resulting in turbulence. Due to the increased ionisation caused by the proximity of the gap, the normalised values for this gap are significantly greater than those for the 50 μm and 100 μm gaps, by a factor of up to 500 for an inlet pressure of 100 KPa. Where a voltage of 200 V, which is the starting value for the voltage in these simulation cases, is too high for a 10 μm gap and will overheat in a real scenario, causing sublimation on electrodes, the controller would still be able to go beyond the real situations and cover theoretical ones, where the ionisation can exponentially increase the thrust as the voltage is increased based on Eq. 38.

It is essential to remember that pressure has a substantial effect on the thrust performance of the micronozzle; the higher the inlet pressure, the greater the thrust. As discussed in Chapter 1, as the pressure between the electrodes increases, so does the probability of ionisation for the plasma phenomenon. Consequently, micronozzle thrust performance has no impact on the increase in ionisation probability. Due to a smaller number of particles with which the electron collides, more energy is transferred to the ionised gas particle when an ion is formed in an environment with low pressure. As a result, because there are fewer particles in its surroundings, this ionised particle will lose less energy through collision, thereby increasing the velocity of the flow and generating a higher thrust profile.

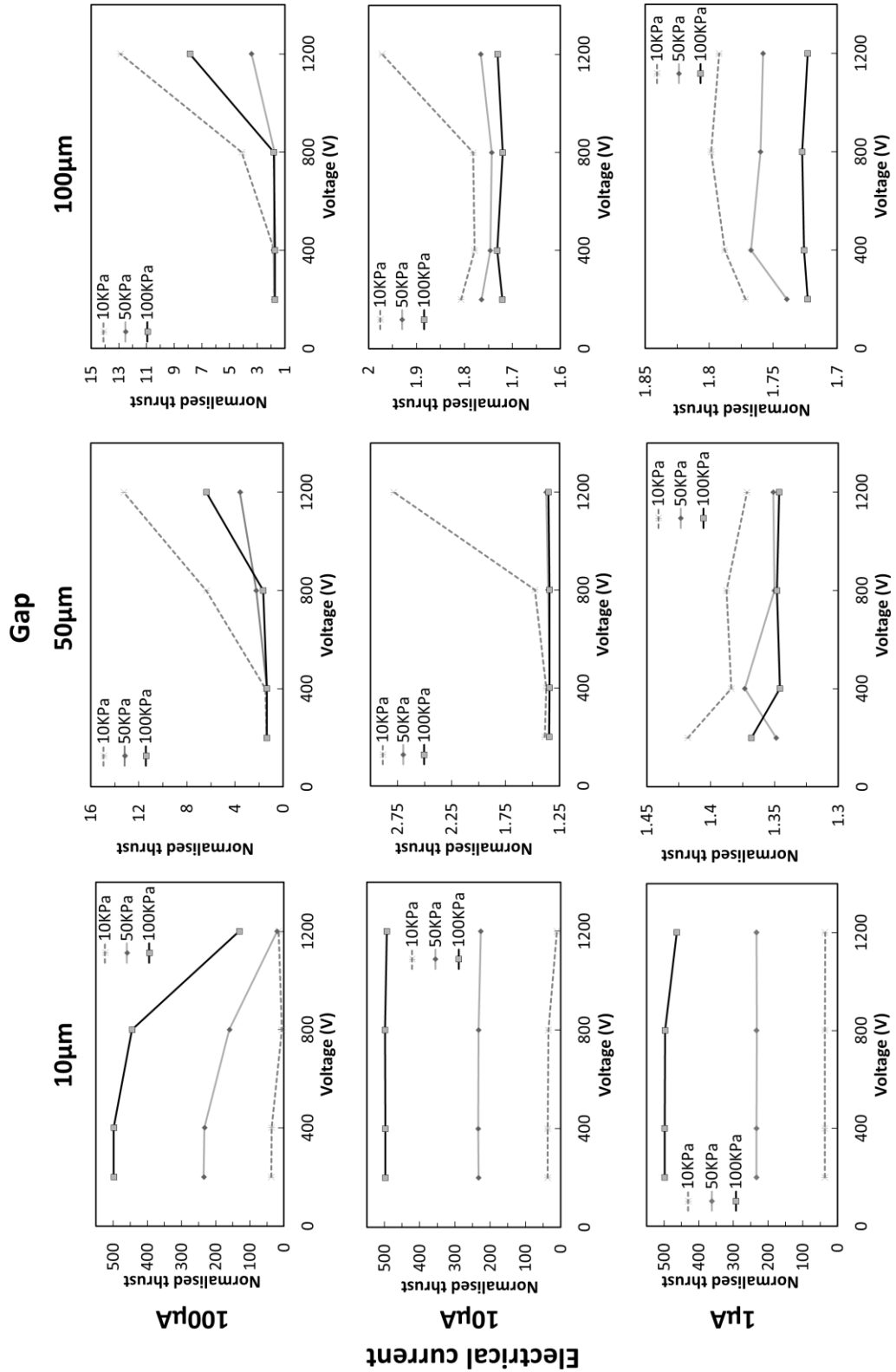


Figure 4-26. Normalized thrust performance based on the plasma effect on microgaps' main parameters: current, voltage, gap, and pressure.

Chapter 4. Designing the micro-thruster chip

In the case of a 50 μm gap, at 10 μA , the 50 KPa and 100 KPa exhibit a slight increase in thrust (by a factor of 1.25) as the voltage increases, which is almost imperceptible when compared to the $\hat{T}_{\mu\text{Plasma}}$ results from 10 KPa, which reach up to a factor of 2.75 at 1200 V, as discussed in the previous paragraph. When a current of 100 μA was applied, a greater number of electrons were introduced between the gap, thereby increasing the ion density generation. In consequence, the increase in $\hat{T}_{\mu\text{Plasma}}$ as the voltage rises is more apparent in Figure 4-26, where the highest $\hat{T}_{\mu\text{Plasma}}$ values at 1200 V are 13.3, 3.6, and 6.4 for 10 KPa, 50 KPa, and 100 KPa, respectively.

$\hat{T}_{\mu\text{Plasma}}$ for the three applied current cases of 1 μA , 10 μA , and 100 μA for the 100 μm gap simulation is more notable that the thrust increase proportional to the voltage increase. Therefore, at 1 μA , exhibits a nonexponential behaviour in which an increase in voltage on a wider gap does not result in an increase in thrust due to the limited number of electrons, resulting in a nearly constant trend. Where the majority of electrons are unable to provide sufficient energy for ionisation as a result of energy loss caused by collision with a greater gas particle density (higher pressure).

In order to obtain an expression for determining the value of $\hat{T}_{\mu\text{Plasma}}$ on Eq. 114, the simulation results shown in Figure 4-26 were used to establish the following equations:

In the case of microgaps < 50 μm , the following equation must be used:

$$\hat{T}_{\mu\text{Plasma}} = |-13.5 + 0.18d - 0.06I - 0.0057V + 4.59p + 0.0003dI| \quad \text{Eq. 115}$$

As a result, for microgaps greater than 50 μm , the expression is as follows:

$$\hat{T}_{\mu\text{Plasma}} = |0.77 + 0.0115d - 0.0318I + 0.0004V + 0.031p|$$

Thus, the following equation describes the thrust of the micronozzle:

$$T_{\mu\text{Thrusterchip}} = \hat{T}_{\mu\text{Plasma}} \times T_{\mu\text{Nozzle}} \quad \text{Eq. 116}$$

Where $\hat{T}_{\mu\text{Plasma}}$ is only 1 when the performance is evaluated as a cold-thruster with no electrical influence.

Figure 4-27 depicts the approximation of Eq. 115 and Eq. 116 to the simulation results for normalised thrust when using N2 propellant.

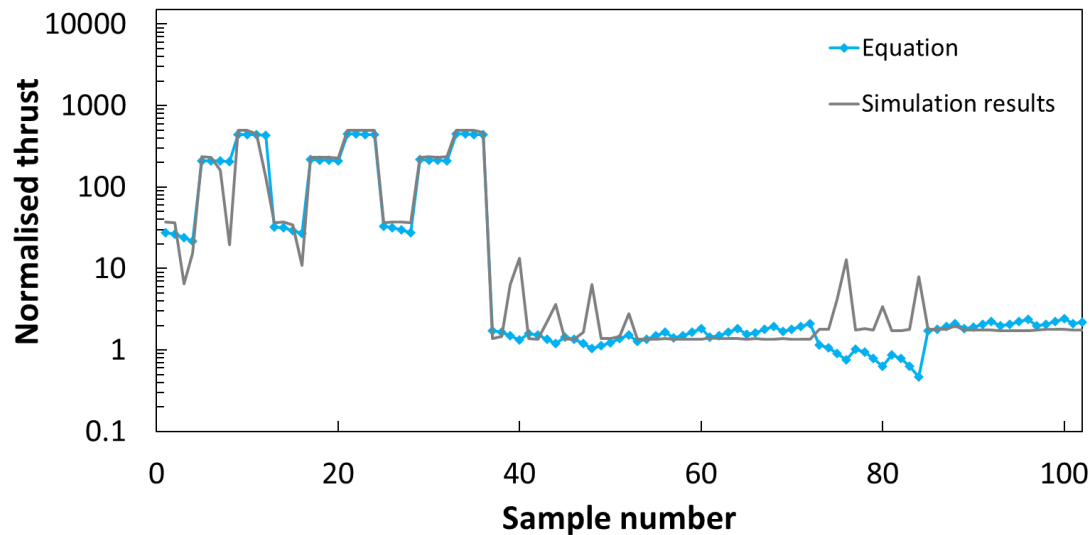


Figure 4-27. Comparison between simulations results based on $\hat{T}_{\mu Plasma}$ and Eq. 115 and Eq. 116

Several factors can cause the fitting equation to differ from the actual results on Figure 4-27. Model complexity is one such factor. The model may not fully catch the intricate relationships between features (GAP, Voltage, Current, Pressure) and target variable (Normalised Thrust). Even when a model includes more complexities, it might still fail to represent all patterns that underlie it. Another important thing is data quality whereby presence of outliers within datasets greatly affects how models perform. Consequently, outliers can distort findings which leads to disparities between predicted values and true values. Thirdly, the interactions among terms could be more elaborate than those shown by features.

A correlation coefficient of 0.84 was obtained through correlating normalized thrust values derived from simulation results against those gotten using theoretical equation. Such a value implies that there exists significant positive relationship between predicted and observed thrusts thus indicating that the theory captures most essential dynamics of experimental data very well. Although there is some scatter around this line but because high correlation supports validity of model; it means also provides reliable representation for real thrust behaviour in simulations. Theoretical models do not always match with actual figures but closeness between sets normalizing spinners demonstrates strength underlying assumptions them making useful tooling materials science researches on plasma-based micro-thruster chip

4.8.5. Handleable chip design

To facilitate its manipulation and connection to an electrical circuit for generating the plasma discharge, the size and shape of the micro-thruster chip must be taken into account. The chip (Figure

Chapter 4. Designing the micro-thruster chip

4-28) must be small enough to be considered a micro-device, but not so small that it cannot be moved with conventional tweezers or hands, avoiding the need for a specialised vacuum tweezers that would complicate its manipulation and portability during nanofabrication and testing.

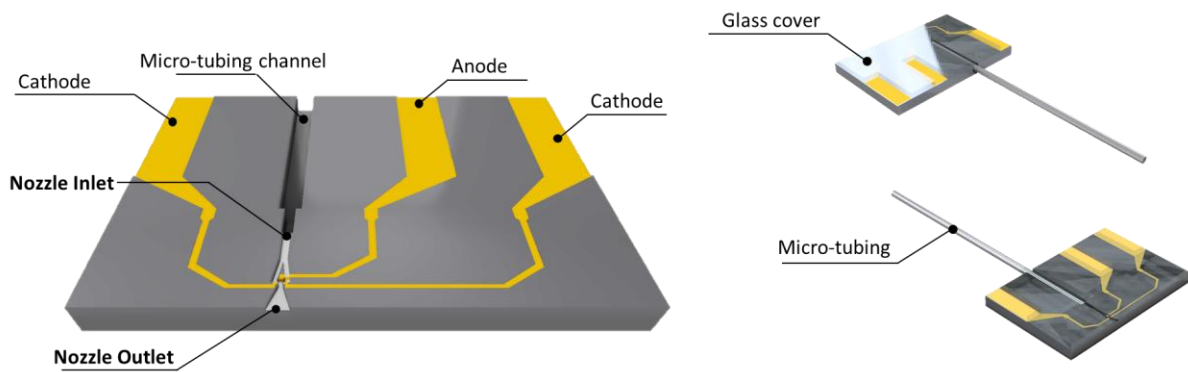


Figure 4-28. Design of a plasma-based micro-thruster chip and its components

Therefore, the design must incorporate existing electrical connectors on the market, specifically commercial off-the-shelf (COTS) components, to become a viable and cost-effective micro-thruster option, thereby reducing the complexity of designing and assembling the high voltage electrical circuit. As a result, the micro-thruster was envisioned as a chip that can be connected to a high voltage power source using a microSD card adapter. Therefore, the micro-thruster chip requires that its electrodes be spaced as far apart as the microSD connector's pins (Figure 4-29). Each electrode (two cathodes and one anode, shown on Figure 4-30) has its pin-connected electrical routing. It was planned to have a separate routing for each electrode to ensure the chip's performance in the event of nanofabrication errors (Figure 4-31), with the option to continue the experiments even with two active routing electrodes.

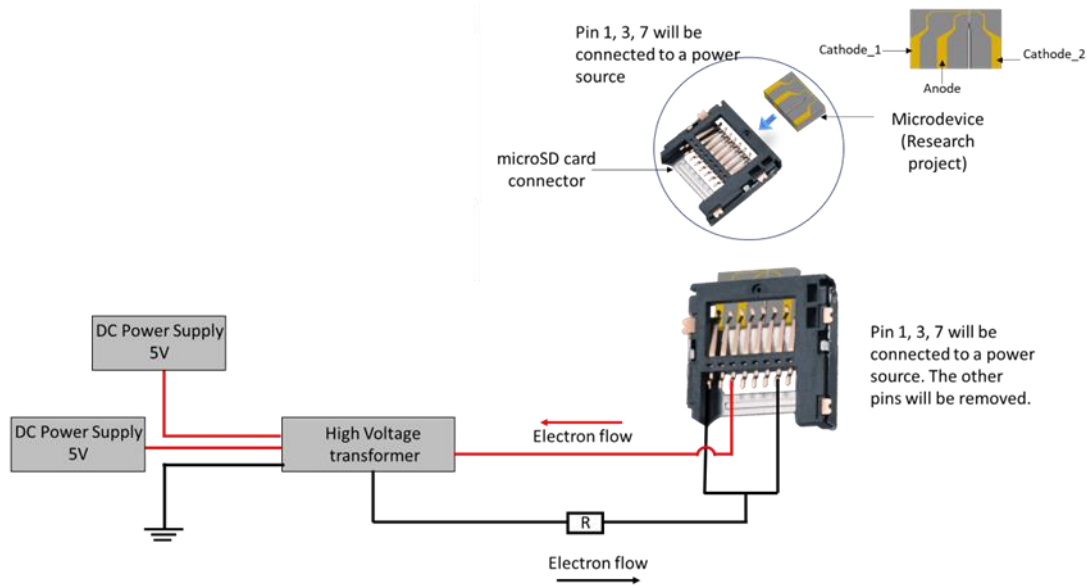


Figure 4-29. A microSD connector connection diagram for the micro-thruster chip's electrical layout.

A gap of 1.4 mm is created between routings to prevent arc discharge. It is necessary to modify the microSD connector so that only three of its eight pins are retained. As a result, the micro-thruster chip's rectangular dimensions were determined to be 5 x 7.4 x 0.75mm, as depicted below:

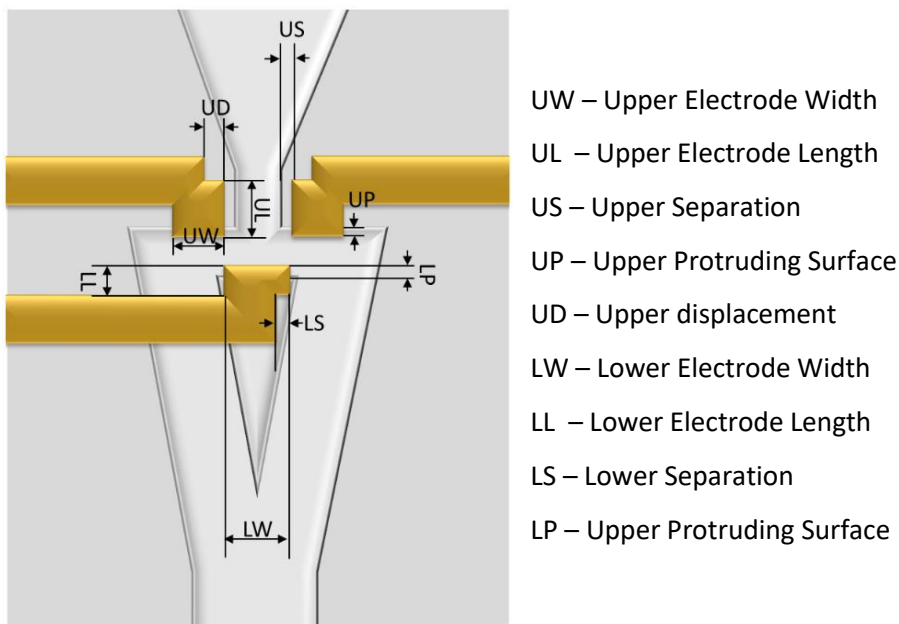


Figure 4-30. Electrodes design on the chip's micronozzle.

In addition, to make the micro-thruster chip more compact and efficient, it should integrate the cathode beside the anode. In this case, the electrodes can be incorporated into the chip without using extra space which is necessary to keep device dimensions and functionality.

Chapter 4. Designing the micro-thruster chip

The anode was located in triangular/divider area (Figure 4-30) of micronozzle geometry hence it required conformal deposition for electrical routing during nanofabrication. This means that routing on walls was a complex part of nanofabrication process. If instead of anode, cathode electrodes were put next to each other; then one of these cathodes would need additional conformal routing to cross neck side of micronozzle thereby making routing process more complicated and may change gas heating effect in microchannels thus affecting performance of micro-thruster. Such increased complexity would also challenge matching simulation results with experimental findings because such cases are difficult to correlate. In worst plasma discharge condition when routing of cathode starts being destroyed by degradation or conductivity failure due to being situated within electrical discharge zone.

These potential problems are avoided when we position a cathode next to an anode because this allows design simplicity as well reliability throughout fabrication steps. Therefore, this arrangement ensures that there is no disruption in electrical routing while minimizing any chances where performance may deteriorate due thermal or even electric discharge effects during operation.

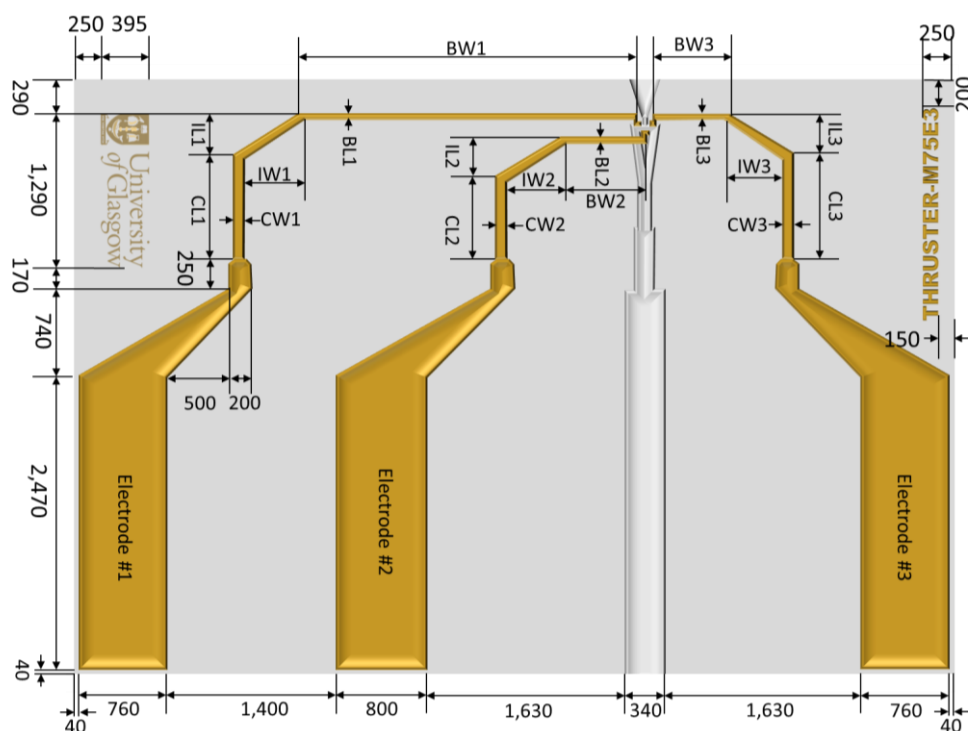


Figure 4-31. Layout of the plasma-based micro-thruster chip.

In addition, an insulator layer will be necessary to prevent arc discharge in any undesirable region of the chip during operations. During the nanofabrication stage, it was proposed that a wafer of silicon serves as the substrate (Chapter 5). Consequently, SiO₂ or SiN are considered as insulating layer

Chapter 4. Designing the micro-thruster chip

deposited on top of the substrate; depending on the quality of the SiO₂ or SiN, it can have a relatively high voltage strength of up to 10 MV/cm [163] and 12 MV/cm [164], respectively. But for a more conventional rate, a breakdown voltage can occur at a 5µm-thick SiO₂ layer when 5kV is applied. And for the case of 5µm-thick SiN the breakdown occurs when 6kV is applied.

To calculate the breakdown voltage V_b according to the insulation thickness layer, can be obtained using the formula:

$$V_b = \text{Breakdown Field Strength} \times \text{Thickness} \quad \text{Eq. 117}$$

Thus, Figure 4-32 shows the point where a 5µm thick layer of SiO₂ at 5kV breakdown is represented by the red line. A 5µm thick layer of Si from wafer at 5kV breakdown at 1.5 kV is represented by the blue line. The breakdown voltage for SiN is represented by the green line. Each of these has specified points for 5 µm thick SiO₂ and SiN layers which are marked and named accordingly. Dashed orange lines represent about how much it would take to operate an electrode gap that is 10 µm, 20 µm, 50 µm or 100 µm wide This shows the maximum limits within which it can work safely with both materials (SiO₂ and SiN). More discussion about the election of the insulation layer can be found on section 5.5.5.

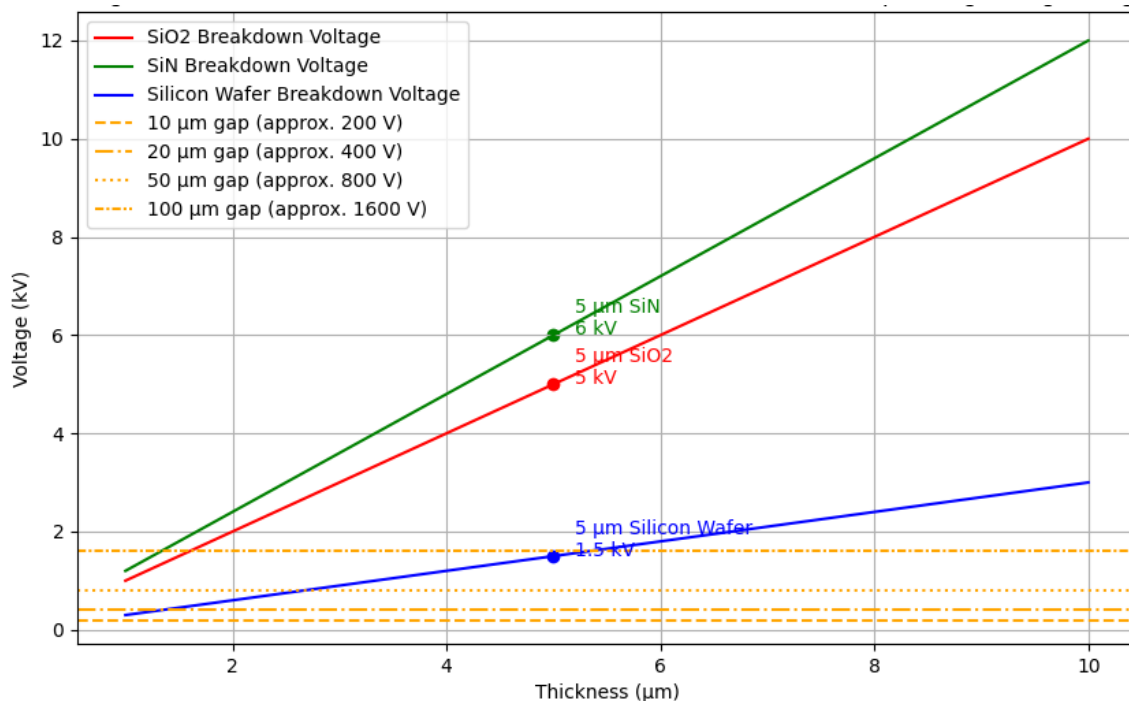


Figure 4-32. Voltage breakdown characteristics of SiO₂, SiN and Silicon wafer with operating voltage ranges

Chapter 4. Designing the micro-thruster chip

Breakdown voltage depends on electrode spacing as well for the electrode configuration. In the design, the micro-thruster operates between 200 V to 1600 V for electrode gaps that vary from 10 μm to 100 μm under some N₂ gas pressure which allows plasma creation.

Hence, electrostatically operating system limits must take into account these breakdown properties. In order not to experience any electrical breakdown but achieve continuous performance it is necessary to keep working voltages far below SiO₂ layer disruptive potential and according to safe distances between electrodes requirements. This will make the micro-thruster lifetime longer while still being useful in real life applications.

Such evaluations need to be included into designing process of the micro-thruster chip in order to operate safely and effectively over its specified voltage ranges while also being able to withstand electrical faults throughout other parts of the system hence making it more reliable in different application areas.

4.9. Quantitative Operating Regime of the Device

To this extent, the micro-thruster's quantitative operating mode has been identified from the simulation results from previous sections and defined as follows:

Operating Pressure

- **Electrostatic Mode:** 10 KPa to 100 KPa

Operating Voltage

- **Electrostatic Mode:** 200 V to 1600 V

Operating Current

- **Electrostatic Mode:** 1 μ A to 10 mA

Power Range

- **Electrostatic Mode:** 0.001 W to 1 W

DC Pulse Durations

- **0.001 W to 0.01 W:** Less than $1 \times 10^{-51} \times 10^{-5}$ s
- **0.01 W to 0.1 W:** Less than $1 \times 10^{-61} \times 10^{-6}$ s
- **0.1 W to 1 W:** Less than $1 \times 10^{-71} \times 10^{-7}$ s

Anticipated Performance in Electrostatic Mode

- **Thrust:** Up to 68.7 μ N
- **Specific Impulse:** Approximately 3059 seconds

Performance in Cold Gas Mode

If the supply pressure in cold gas mode is the same as that in electrostatic mode:

- **Thrust:** Up to 4.4 μ N
- **Specific Impulse:** Approximately 81.55 seconds

To make certain that the micro-thruster functions well under given circumstances and at the same time generates maximum thrust and specific impulse in all modes of operation, these criteria have to be followed.

4.10. Summary

As a starting point, the electrical current range from 10^{-6} A to 10^{-2} A was determined to obtain a visible normal glow effect for the plasma phenomenon. Next, the voltage needed to generate breakdown was identified as 200 V to 1600 V for 10 μm to 100 μm gaps distance between the electrodes dependent on the gas pressure for plasma formation with N₂.

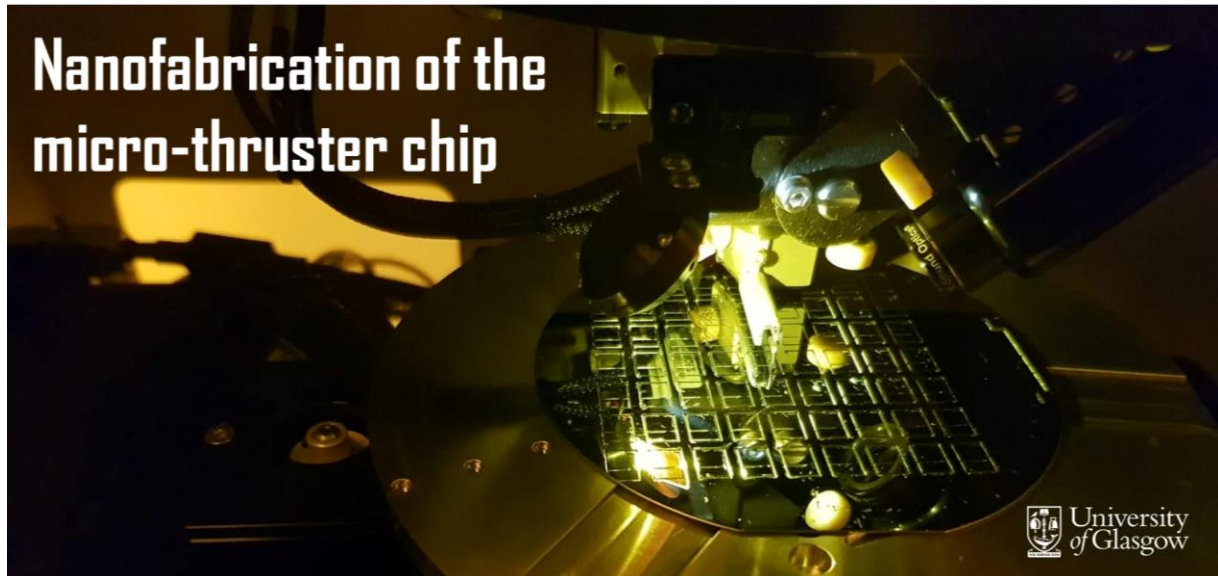
After identifying the current and voltage, the power range of 0.001 W to 1 W for the Joule Heating calculation for the electrodes could be calculated. Whereas, according to the functionality of the micro-thruster for space applications, it will be exposed to vacuum environments where the materials tend to sublime at lower points, taking 800 K from Ag as the maximum temperature the electrodes can increase as the lowest sublimation point of the chosen metals.

The smallest electrode volume was defined as 7.5×10^{-16} m³ for a 15 μm x 100 μm x 0.5 μm size with a square shape due to its increased heat dissipation efficiency and a larger contact area with the substrate.

To safely apply a DC pulse to the electrodes in space conditions (vacuum) while minimising the risk of sublimation over a continuous operation of 60s, DC pulses lower than 1×10^{-5} s were identified as appropriate for 0.001 W to 0.001 W, 0.01 W to 0.1 W lower than 1×10^{-6} s, and 0.1 W to 1 W lower than 1×10^{-7} s. A triangular geometry was idealised for the electrode location evaluation, dispersing the flow via both inlet orifices. A single 30G needle with a 0.310 mm O.D. and a stainless steel taper was used to feed a gas propellant to the microdevice. A 320 μm x 320 μm channel was idealised to insert the needle, connecting to the plenum microchannel and then to the micronozzle.

Various 2D simulation cases were run on OpenFOAM-2.4.0-MNF using the dscmFOAM+ solver, with the micronozzle acting as a cold gas and plasma-based propulsion system. Thrust was estimated for each example and represented using Eq. 113 for cold gas, resulting in an operational thrust range of 1.06 nN to 4.4 μN . Based on numerical calculations, the thrust range of a plasma-based micro-thruster was found to be between 1.06 nN and 68.7 μN . Finally, the micro-thruster chip was described as 5 mm X 7.4 mm X 0.75 mm with three routing electrodes separated by 1.4 mm, which can be connected to a high voltage power source via a microSD card socket.

Chapter 5



The primary innovation of this project is the fabrication of a tangible micro-thruster chip from the designs presented in the previous chapter using a defined nanofabrication process.

Taking into account any misalignment or non-uniformity caused by a differential levelling (inclination) on the wafer surface caused by the holders or stages on each tool. Wider or larger microchannel patterns were allocated further from the wafer's centre (Figure 5-1), allowing for greater size tolerance. The further pattern is from the wafer's axial (centre), the further it is from the horizontal axis (levelling reference). Experiencing overprocessing or under-processing depending on whether the pattern is above or below the horizontal levelling line. Having a non-uniform procedure or outcome across a wafer's surface.

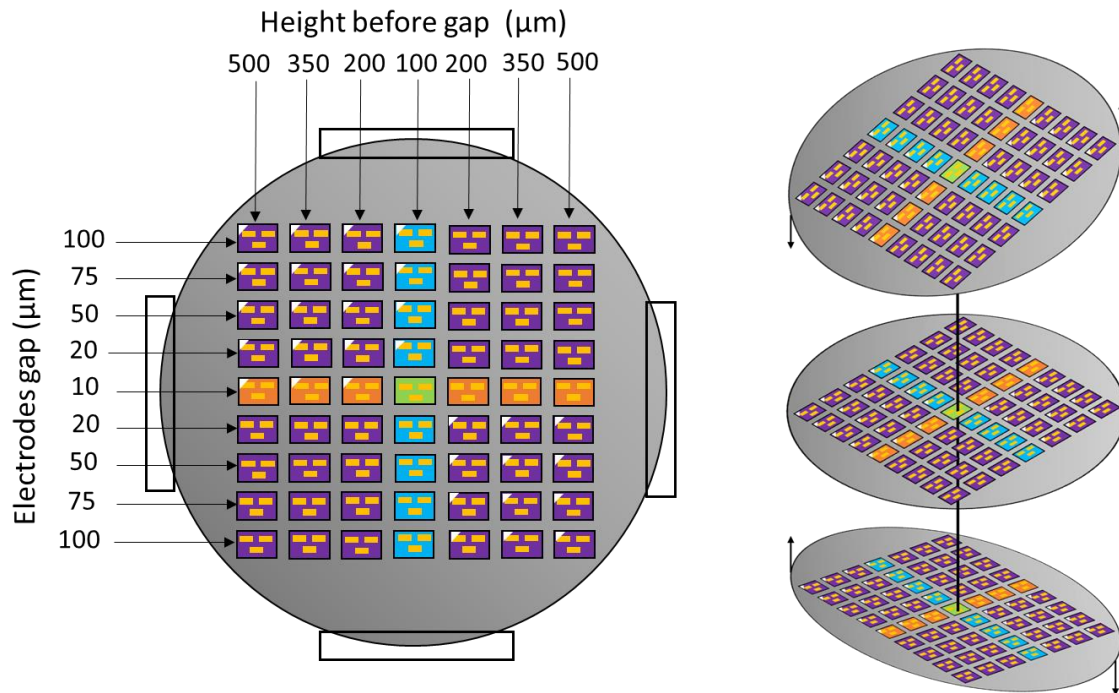


Figure 5-1. The configuration of 63 micro-thruster chips on a 4-inch Si wafer. Micro-thrusters were ordered according to the distance between electrodes (column) and the height of the triangular channel pattern(rows). 1) 31 original designs (marked white in the upper left corner) and 2) 32 extended mode designs were distributed. The right-hand diagram depicts the differential levelling considerations for wafer holders or tool stages. Thus, allocation of the smallest pattern (green) is placed at the axial and crossing this point, 10 µm gap patterns (orange) and 100 µm long triangular channels (blue) are assigned.

This process describes various nanofabrication techniques, such as photolithography, spin coating, development, dry etching, metallisation, and lift-off, for the microdevice's replicability.

5.1. Photolithography

The development of the micro-thruster chip as MEMS necessitates the use of micro- and nanofabrication techniques to transform the design into a reliable pattern structure on a substrate surface. Depending on the size of the MEMS, these patterning structures can be created using either photolithography or e-beam lithography (EBL) [165]. The University of Glasgow's James Watt Nanofabrication Centre (JWNC) provides the necessary equipment to implement micro- and nanofabrication techniques. Being photolithography by UV light a more conventional method for patterning structures with dimensions greater than 1 µm, and a more reliable method for mass production, such as the fabrication of microelectronic chips for the semiconductor industry [165]. In

contrast, electron beam lithography (EBL) generates structures below $1\mu\text{m}$ covering the nanometre range by exposing electrons as contrasted to UV light, avoiding the limitations of optical diffraction [165]. As a point of comparison, the EBL equipment (PG) utilised by JWNC has a resolution of 0.5 nm , making the EBL process significantly slower and more expensive than photolithography. In addition, using EBL requires a more specialised tool and training [166]. According to the chip designs for nozzles, the width of the microchannels ranges from $5\mu\text{m}$ to $320\mu\text{m}$. Thus, these pattern's sizes exceed the $1\mu\text{m}$ requirement of the EBL, making them suitable for the application of photolithography.

To provide a more comprehensive description, photolithography is typically carried out by projecting a pattern from a photomask onto a photoresist film [165]. First, a thin layer of photosensitive polymer, also known as photoresist or resist, is spin-coated onto a substrate. The substrate is then exposed to a UV light source via a photomask, as depicted in Figure 5-2. Depending on the type of photoresist, the UV-exposed area will either dissolve in a developing solution (positive photoresist) or not dissolve at all (negative photoresist). In either instance, the pattern on the photomask is transferred to the photoresist film that will serve as the mask for coating or etching the substrate [167].

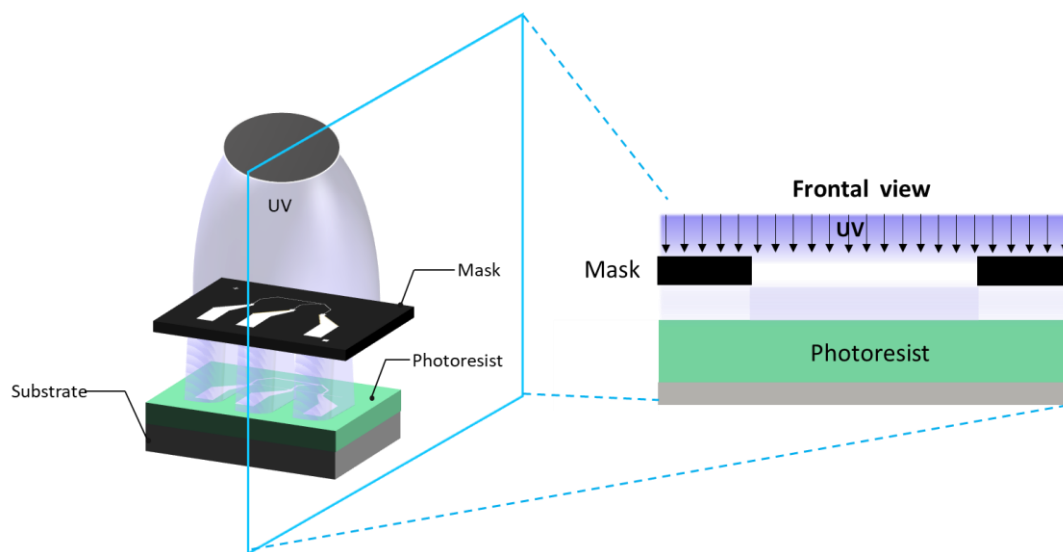


Figure 5-2. Representation of the photolithography technique for the micro-thruster nozzle patterning on a photoresist-coated substrate.

During the nanofabrication of chips, the photolithography process presented three major challenges: 1) the degree of alignment error, 2) the exposition dose intensity, and 3) the exposition dose timing.

5.1.1. Photomask

There are two types of photomasks: 1) "hard" made from quartz or borosilicate glass, and 2) "soft" made from soft plastic [168]. The most common material for photolithography is a quartz plate with

a thin layer of chromium on it. Even though quartz is a more expensive option, it has two main advantages; 1) the low expansion of the material by heat during the photolithography process due to its low thermal expansion coefficient of 0.42 ppm/°C compared to soda lime's 9.5 ppm/°C [169], which minimises the distortions in the pattern size caused by heat. 2) its transparency, which enables deeper ultraviolet wavelength exposure below 200 nm compared to 295 nm for borosilicate, which is more opaque [169]. Therefore, quartz was selected as the optimal material for the micro-thruster chip photomasks. The designs for the photomasks were created in L-Edit using the GDSII file format and then sent to Compugraphics-photomasks for production.

Therefore, the micro-thruster chip nanofabrication required three photomasks (Figure 5-3): Mask #1 for the microtubing channel, Mask #2 for the micronozzle, and Mask #3 for the electrode pattern.

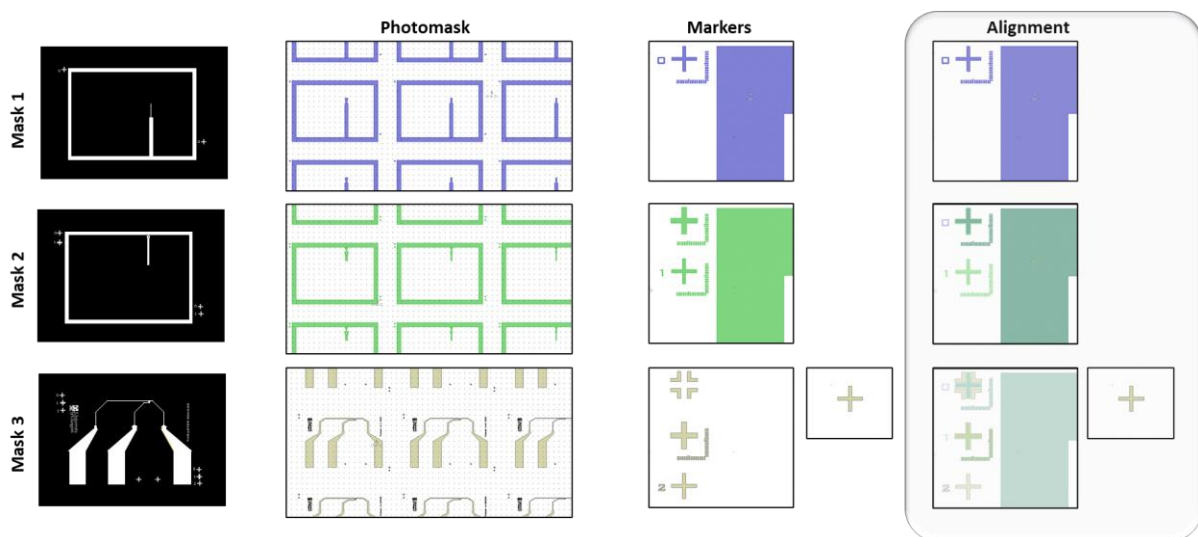


Figure 5-3. Masks alignment representation on L-edit based on the three photomasks required for micro-thruster chip nanofabrication. The alignment markers on each photomask should be followed by their overlapping sequence.

The microtubing and micronozzle patterns were assigned to two individual photomasks for major control of the final depth of etching on the chip. Providing flexibility to define the depth for gauge size of the microtubing (needle) independently of the restrictions on the micronozzle depth for the metal deposition to obtain a conformal coating on its walls for the electrode routing discussed in section 5.7.1.

5.1.2. Alignment markers

Alignment markers were used to avoid misaligning subsequent photomask patterns on the substrate. For the photolithography patterning of the chip, each photomask includes markers on the upper left and lower right sides of each chip pattern on the wafer (Figure 5-4).

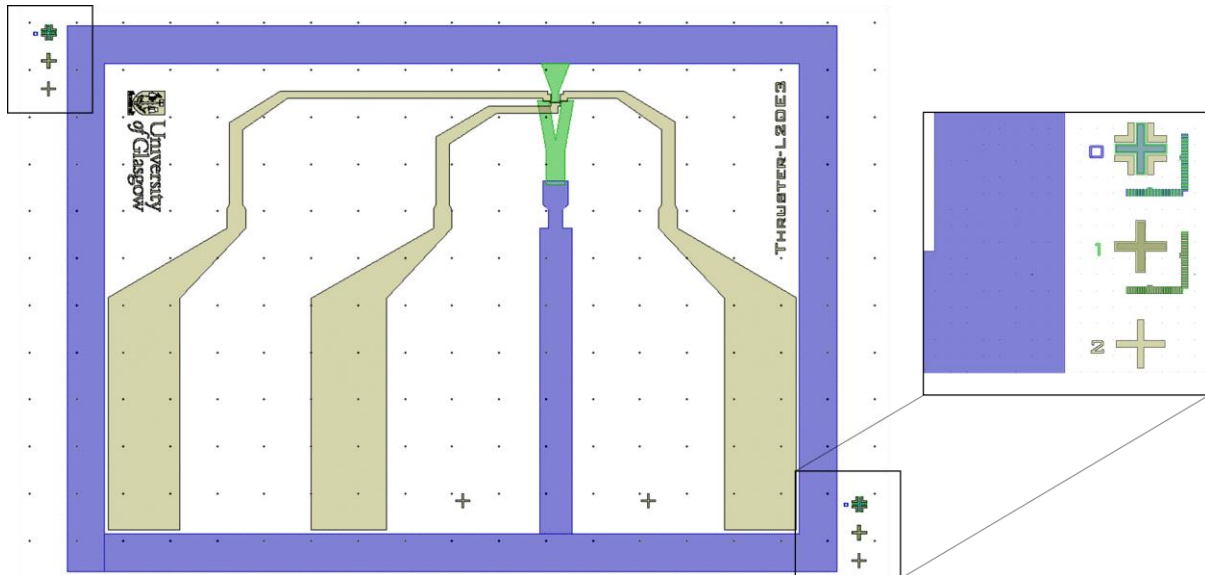


Figure 5-4. Allocation of photomask alignment markers in the upper left and lower right corners of a single chip pattern.

Mask #1 comprised 20 μm -wide and 150 μm -long marks. In contrast, Mask #2 contains two marks: 1) a 30 μm -width and 160 μm -length mark intended to be overlapped on the patterned mark from Mask #1, and 2) a second marker placed below with the same dimensions as the first marker (150 μm x 20 μm) to maintain a reference point without distortions caused by the overlap of patterns (Figure 5-5), thereby facilitating the alignment of the third mask. Mask #3 contains three marks: two to be aligned and patterned on top of its predecessors, and as with Mask #2, a new mark devoid of distortions, as this mask will be used twice: for the etching and metal deposition stages.

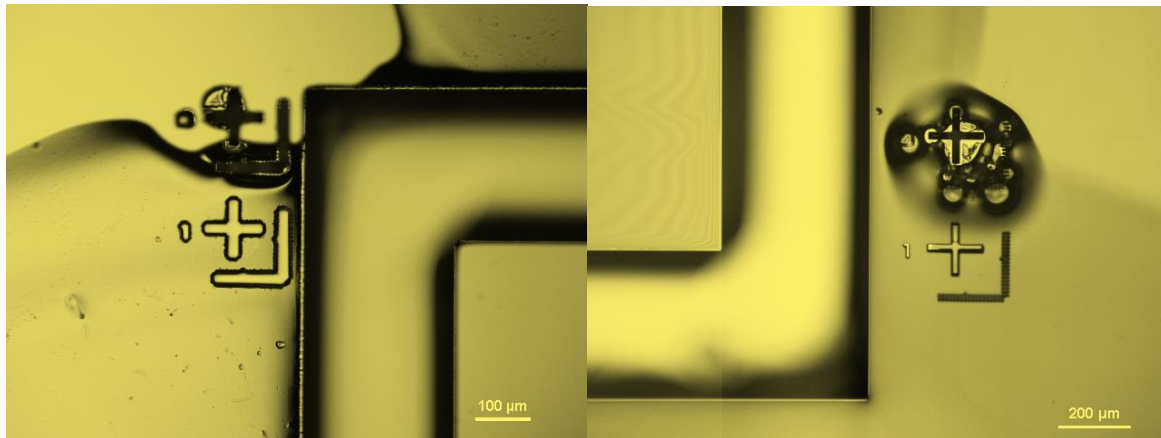


Figure 5-5. Deterioration and deformation of the overlap on alignment markers after a deep dry etch. Images captured by optical microscope.

As previously stated, the widths of the alignment markers are 20 μm and 30 μm ; therefore, the difference between them, 10 μm , is the controlled degree of error during manual alignment on the MA6. In addition to this error, several factors, such as the sensitivity of the rods to alignate the mask, the contact distance between the mask and all points of the substrate, and the human error caused by the manual manipulation of the tool, can make obtaining a proper alignment of the patterns challenging. In consideration of these variables, the electrode patterns on Mask #3 were separated into two categories (Figure 5-6) by extending the electrode plates to the nozzle neck. Increasing the level of misalignment tolerance (Table 11) in the x-direction to ensure, in the worst-case scenario, the nanofabrication of a partial quantity of micro-thruster-devices from a single wafer, thereby preventing the complete loss of patterns.

Table 11. Alignment tolerance on the electrode photomask (mask #3)

Alignment tolerance						
	Size	x-direction	y-direction	Size	x-direction	y-direction
		(μm)	(μm)		(μm)	(μm)
Mask#3	XS	5	5	XS-extended	10	5
	S	10	8	S-extended	19	8
	M	10	18	M-extended	29	18
	L	10	18	L-extended	29	18

As seen in Table 11, the x-direction tolerances for XS, S, M, and L on Mask #3 are so tight as to increase the probability of fabrication failure. Since this was the first time the Aerospace department wanted to nanofabricate a micro-thruster device, 32 of the 63 chip patterns on the mask were given an extended mode design to make the tolerances wider. Modification of the electrode designs is shown in Figure 5-6 and their distribution is shown in Figure 5-1, where the electrodes extend beyond the micronozzle's outlet neck, increasing the alignment tolerance by 100 percent in the x-direction.

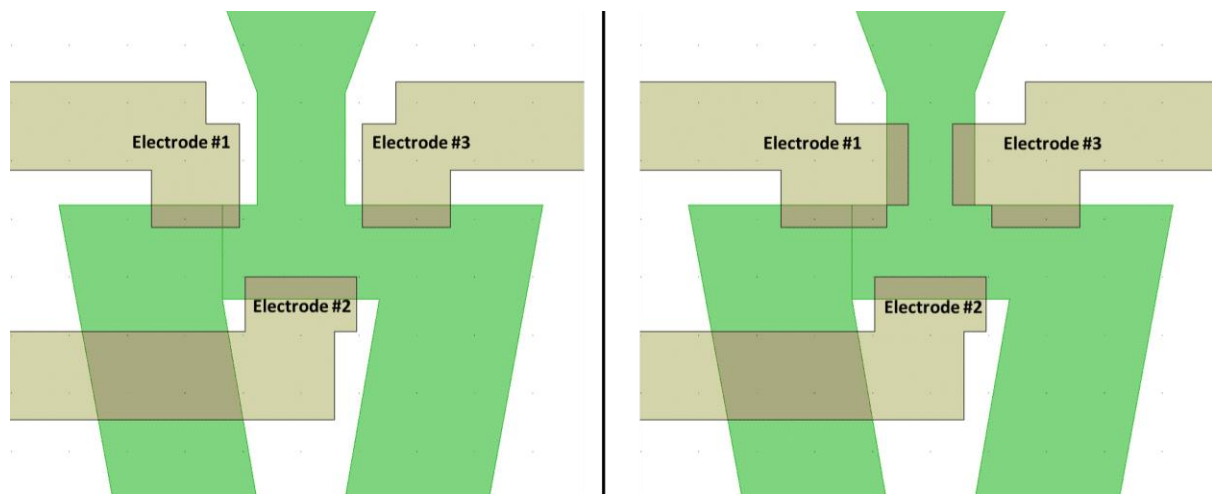


Figure 5-6. Comparison of the "original design" (left) and the "extended mode design" (right). Electrodes #1 and #3 were enlarged to make contact with the nozzle neck surface in the extended version.

In addition, the extended electrode design pattern serves as a precautionary (backup) option in the case that the conformal gold coating (section 5.7.1) on electrode #2 cannot be connected/bridged successfully. Changing the electric current polarity of one of the electrodes at the chip's end can restore its functionality. Therefore, this modification will alter the performance and location of the plasma at the outlet neck of the nozzle.

5.1.3. Photoresist

Resists are radiation-sensitive materials (polymers) that, after exposure to UV light and development (section 5.3) in a solution, produce the desired patterns in relief [170]. There are two types of photoresist that can be used in the microfabrication process: 1) Positive resist, in which the UV-exposed resist becomes soluble upon contact with the developer; thus, unexposed resists have very low solubility in developer [171]. 2) Negative resist, opposite to positive resist, the unexposed resist is soluble in developer but becomes insoluble when exposed to light [171].

Table 12 illustrates the distinguishing characteristics between positive and negative photoresists for nanofabrication:

Table 12. Comparative analysis of conventional positive and negative photoresists [172].

Characteristics	Resist type	
	Positive	Negative
Adhesion to Si	Fair	Excellent
Available compositions	Many	Vast
Contrast γ	Higher, e.g. 2.2	Lower, e.g. 1.5
Cost	More expensive	Less expensive
Developer	Aqueous based (ecologically sound)	Organic solvent
Developer process windows	Small	Very wide, insensitive to overdeveloping
Influence of oxygen	No	Yes
Lift-off	Yes [usually with multiple-layer resist (MLR)]	Yes, with new types of negative resists [single-layer resist (SLR)]
Minimum feature	0.5 μm and below	$\pm 2 \mu\text{m}$
Opaque dirt on clear portion of mask	Not very sensitive to it	Causes printing of pinholes
Photospeed	Slower	Faster
Pinhole count	Higher	Lower, e.g. 1.5
Pinhole in mask	Prints mask pinholes	Not so sensitive to mask pinholes
Plasma etch resistance	Very good	Not very good
Proximity effect	Prints isolated holes or trenches better	Prints isolated lines better
Residue after development	Mostly at $< 1\mu\text{m}$ and high aspect ratio	Often a problem
Sensitizer quantum yield ϕ	0.2 to 0.3	0.5 to 1
Step coverage	Better	Lower
Strippers of resist over		
Oxide steps	Acid	Acid
Metal steps	Simple solvent	Chlorinated solvent compounds
Swelling in developer	No	Yes
Thermal stability	Good	Fair
Wet chemical resistance	Fair	Excellent

The use of a photoresist for photolithography requires specific considerations, such as the exposure dose in light, its sensitivity given by the contrast, the proximity of the mask and the substrate, whether the photoresist was previously baked or just dried, and the environmental temperature and humidity, which all affect the printed pattern directly. The requirements of the nanofabrication process that necessitates the use of a resist are the primary determinant of the photoresist's characteristics.

Chapter 5 Nanofabrication of the micro-thruster chip

Rohm and Haas Electronic's SPR220-7 photoresist [173] was selected for the nanofabrication of the micro-thruster chip. The following reasons are listed:

- 1) SPR220-7 is made up of three compounds, like most positive photoresists. About 70% of it is an organic solvent, 20% is the novolac resin (which acts as a glue or matrix), and 10% is the photoactive compound Diazonaphthoquinone (DNQ). Where the DNQ–novolac system can provide a process with a higher resolution and greater thermal stability [174] [175]. Being ideal for dry etching procedures due to its thermal stability during plasma exposure.
- 2) SPR220-7 has a higher thickness capability of <10 μm film in a single coat with excellent uniformity [173]. Ideal for use as a protective resist mask during dry etching (section 5.4) and for a good lift-off quality after metal deposition, maintaining a minimum 1:5 thickness ratio.
- 3) Within the JWNC, photoresists from the SPR220 series are used for the automated spinner "Suss RCD8 Positive Resist", which is one of the few spinners where the user can adjust the spinning acceleration to control the coating thickness.

Table 13. MA6 input parameters for UV exposure on SPR220-7 during each nanofabrication stage.

		Resist: SPR220-7			
		microtubing channel	Micronozzle	Electrodes	
		Dry etching	Dry etching	Dry etching	Metal deposition
Parameter	Description	Value			
Power (W)	Power of exposure light	260	260	260	260
Exposure Type	Type of exposure	Hard	Hard	Hard	Hard
Exp. Time (s)	Time of exposure	37	37	39	41
Wait Time(s)	Pause between the expose cycles, using Multiple Exposure	N/A	N/A	N/A	30
Exp. Cycles	No. of cycles, using Multiple Exposure	N/A	N/A	N/A	3
Al. Gap	Alignment distance during the alignment	100μm	100μm	100μm	100μm
Exp. Gap	Distance during the exposure proximity	50μm	50μm	50μm	50μm

5.1.4. Photoresist: Exposure dose and resist contrast

To determine the exposure dose E for photoresists to light, it is given by

$$E = I * t \quad \text{Eq. 118}$$

Where I is the light intensity, and t is the exposure time.

The thickness of the photoresist remaining after development is determined by E , where

$$\frac{T}{T_0} = \gamma \log \frac{E_1}{E} \quad \text{Eq. 119}$$

Being T_0 the initial resist thickness, and γ is the contrast provided by

$$\gamma = \frac{1}{\log \frac{E_1}{E_0}} \quad \text{Eq. 120}$$

In the case of a positive photoresist, E_1 is the dose above which the resist is totally removed, whereas E_0 is the dose at which the developer begins to attack the resist. In contrast, for negative photoresist, E_1 is the dose necessary to achieve 100 percent of the initial resist thickness, and E_0 is the dose at which crosslinking begins [170].

According to the data sheet for the SPR220-7 from Rohm and Haas Electronic [173], the E_1 dose required to remove a 7 μm -thick film is defined as 470 mJ/cm^2 . For E_0 , it is set to 18.4470 mJ/cm^2 by the standardised light intensity I of 18.4 mW/cm^2 at 365 nm, and 34.8 mW/cm^2 for 405 nm (no filters) and a lamp power of 350 W on the MA6 based on data from the JWNC derived from measurements of Suss(fabricant) [176].

The default UV wavelength for internal users on MA6 is 365nm, but the default lamp power varies. For an ideal lamp power of 350 W, contrast a value of 0.71(Eq. 120) with an intensity of 18.4 mW/cm^2 and $t = 25.54$ seconds are required to completely remove a 7 μm -thick film. In practice, the lamp power is set to 260 W, causing the exposure time to increase by $t = 33$ seconds and the light intensity I to change to 14.24 mW/cm^2 .

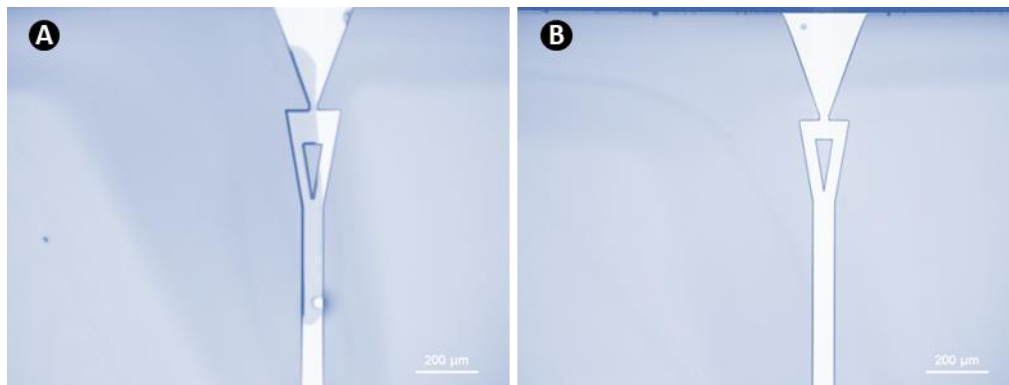


Figure 5-7. Comparison of exposure times for micronozzle patterning in the photoresist. A) Resist partially removed due to underexposure with an exposure time of 27 seconds at 275W. B) Correctly expose the resist after 33 seconds at 275W. SPR220-7 was used as a photoresist and was developed for 3 minutes with MF-CD-26.

5.1.5. Photoresist: profile

For nozzle nanofabrication, it is essential to consider how optical absorption affects the profile (Figure 5-8). After the development process, the profile's edges should ideally become straight. Since the top of the resist is overexposed compared to the bottom, light absorption on positive photoresist causes profiles to become narrower at the top than at the bottom. Negative resists have an undercut profile that is narrower at the bottom than at the top. Again, the top of the resist is overexposed in comparison to its base [177]. Due to the change in geometry, metrology issues and variations in expected outcomes are brought about.

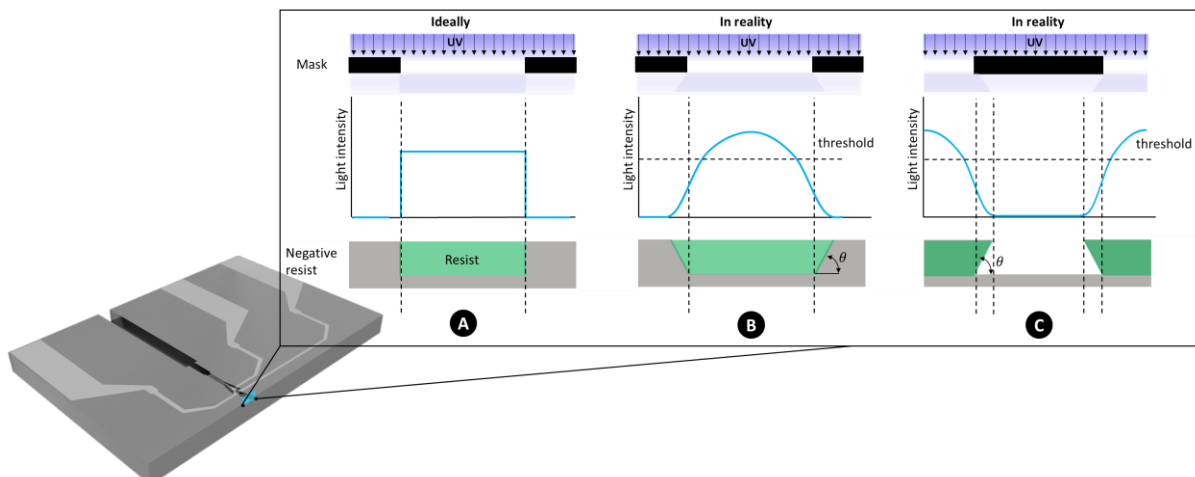


Figure 5-8. Photoresist profiles of the cross-sectional area of the nozzle exhaust following the development process; (A) a perfectly straight profile. (B) A photoresist with a highly steep profile is assigned to fill the void. (C) Extremely steep profile of a negative photoresist assigned to the gap edges [178].

In photolithography, light is transmitted through the mask's aperture. Due to the laws of diffraction, this intensity diffuses into the shadowy regions surrounding the transmitted beam [179]. Where the width of the exposed area is greater than the aperture of the mask, causing a change in geometry. Figure 5-9 illustrates various photoresist profile overviews based on dose, developer influence, the development rate of the exposed region (R) over the development rate of the unexposed region (R_0), and the resist contrast (γ).





Profile	Dose	Developer influence	R/R_0	γ	Uses
A a) Positive resist undercut 	High (often with back scatter radiation)	Low	> 10	> 6	Ion implant Lift-off Not good for plasma etching Often only obtained through image reversal
b) Vertical 	Normal dose	Moderate	5 - 10	< 4	Lift-off Reactive ion etch Wet etch Ion beam etch Perfect fidelity
c) Normal of overcut 	Low	Dominant	< 5	< 3	Typical for positive resists Wet etch Metallization $< 20\%$ resist loss
B Negative resists Undercut 	Dominant	Little influence	< 0.1	< 3	Permanent resist Larger devices MEMS

Figure 5-9. Photoresist profile overview. (A) Positive resist. (a) Desired resist profile for lift-off, exposure-controlled profile (undercut). (b) Perfect fidelity image transfer by applying normal exposure doses and relying moderately on the developer. (c) Receding photoresist structure with thinning of the resist layer (overcut). (B) Negative resist. The profile is mainly determined by exposure. Development swells the resist slightly but has no influence on the wall profile [172].

5.1.6. Shadow printing resolution

During light exposure, the printed shadow on the surface of the photoresist affects the resolution of the printing pattern. The proximity of the mask to the resists or wafer plays a significant role in determining the width and steepness of the pattern's edges (Figure 5-10).

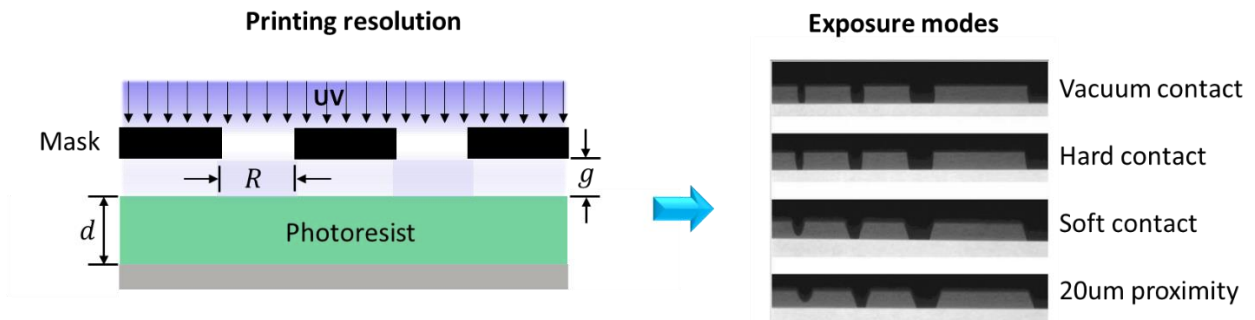


Figure 5-10. Shadow printing (Contact and Proximity) diagram in which R is the resolution (width), g is the distance between the mask and the resist, and d is the thickness of the photoresist. Next to the diagram are the results of various exposure modes.

The mask can be placed in direct contact with or close to the resist surface. These allocations are categorised into four exposure modes:

- Proximity: Also known as projection lithography, this technique involves programming a predetermined distance between the mask and the substrate. Mask features are greater than the final pattern [178]. Mask reduces damage, but reduces resolution as well. This mode has a resolution of roughly $2.5\ \mu\text{m}$ [170].
- Soft contact: Also known as contact lithography, slight mechanical pressure is applied to the mask and substrate to produce contact. Mask features and final pattern have identical dimensions [178]. The resolution is $2\ \mu\text{m}$ [170].
- Hard contact: Similar to soft contact, additional substrate force is applied. Resolution has enhanced ($1\ \mu\text{m}$).
- Vacuum contact: The contact between mask and substrate is optimised by evacuating the gap. This mode provides the highest possible resolution. The resolution is $0.7\ \mu\text{m}$ [170].

Where the resolution (R) is given by

$$R \approx \sqrt{\lambda \times \left(g + \frac{d}{2}\right)} \quad \text{Eq. 121}$$

Be λ the wavelength of the light, g is the gap thickness and d is the resist thickness [178].

In addition to the separation between the wafer and the mask, other factors that affect printing resolution are the lack of uniformity of the wafer or the mask, which can cause variations in their flatness, debris on the mask or photoresist layer, the size of the photoresist edge bead, the photoresist thickness, and the exposure wavelength by a different source of light [178].

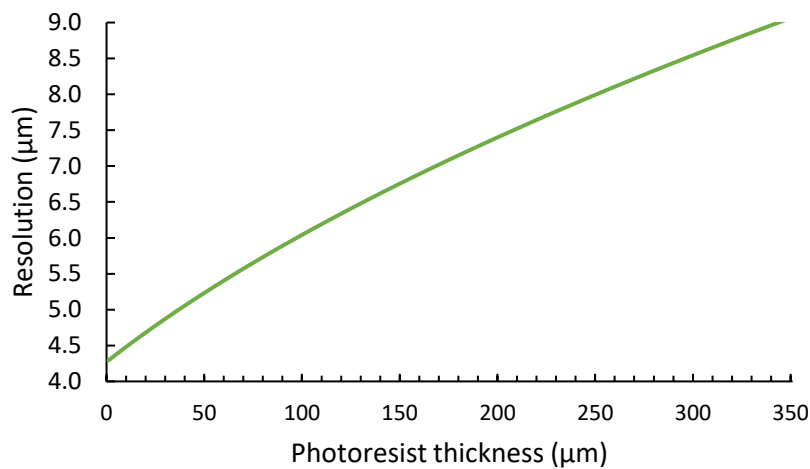


Figure 5-11. Shadow printing based on the thickness of the photoresist.

Consequently, the specific resolutions for each nanofabrication stage at various resist thicknesses are as follows:

Table 14. Shadow printing resolution on every micro-thruster chip nanofabrication stage.

Nanofabrication stage	Printing pattern	Wavelength (nm)	Gap thickness (µm)	Resist thickness (µm)	Resolution (µm)
Stage 1	Microtubing channel	365	50	7.0	4.42
Stage2	Micronozzle	365	50	7.0	4.42
				320	8.75
Stage3	Electrodes	365	50	30	4.87
				100	6.04

5.1.7. Photoresist: processing

Spin coating is utilised to obtain a uniformly distributed layer of resist on the substrate's surface. The spin resist thickness (T) is proportional to viscosity (η), spin speed (ω), and solvent evaporation rate (E), as shown in [180], respectively.

$$T \sim \sqrt[3]{\frac{\eta E}{\omega^2}} \quad \text{Eq. 122}$$

According to the manufacturer [173], the relationship between spin speed and resist thickness for the SPR220-7 and SPR220-4.5 in the RCD8 automated spinner for 4-inch substrates is as follows on Figure 5-12:

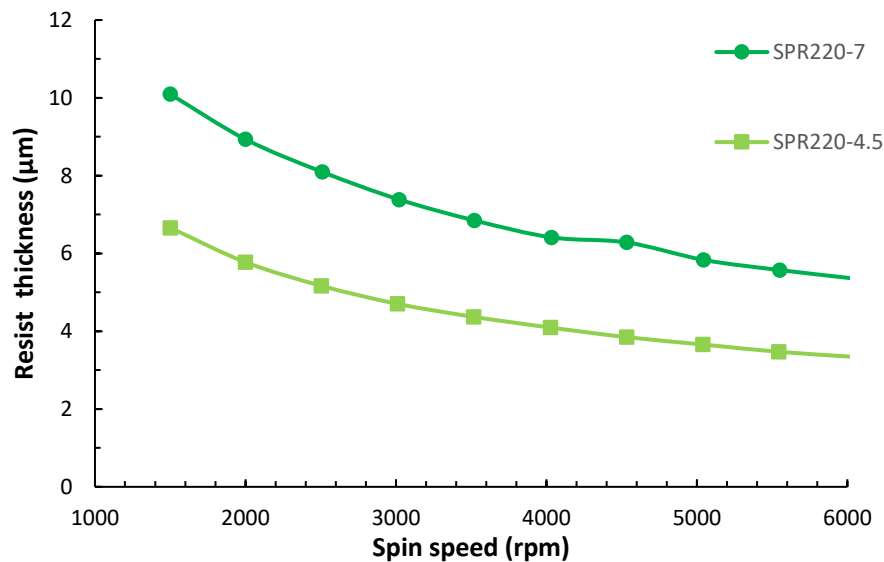


Figure 5-12. SPR220-7 and SPR220-4 thicknesses based on the spin speed ω for 4" wafer.

Where the relationship between the spin speed and the resist thickness for the SPR220-7 can be simplified by

$$T \sim 283.87\omega^{-0.455} \quad \text{Eq. 123}$$

And for the SPR220-4.5 is

$$\sim 249.47\omega^{-0.495} \quad \text{Eq. 124}$$

For the nanofabrication of micro-thruster chips, the Spinner Suss RCD8 Positive Resist (Figure 5-13) was utilised as a pin coating instrument within the JWNC to produce thicker resist films.



Figure 5-13. RCD8 spinner at the JWNC.

The RCD8 automatically applies a uniform coating using a mechanical pump, dispensing photoresist in the centre of the wafer through an arm, with the option to programme the chuck's rotational speed to a maximum of 10,000 rpm and acceleration to a maximum of 7,000 rpm/s [181].

Table 15. RCD8 process description recipe for SPR220-7 deposition

Step	Time (s)	Speed (rpm)	Acceleration (rpm/s)	Functions
1	10	20	1000	Until Arm1
2	3	20	1000	Resist 1 C1 Pudder
3	60	70	400	
4	30	1200	1200	
5	2	0	1500	

The spinning recipe comprises five steps (Table 15). The first step involves moving the dispensing arm from its resting position to its initial position (wafer's edge). Step 2 entails dispensing the resist as the arm moves from the wafer's edge to its centre and the chuck rotates at 20rpm. Creating a spiral distribution of the resist to improve the SPR220 surface coverage on the wafer. Before attempting to obtain a thin film coating, Step 3 focuses on increasing the spin speed while keeping it low in order to spread the resist over the entire wafer surface. The absence of this step can result in areas lacking resist coating due to the abrupt acceleration of the wafer's spindle, which causes the majority of the

resist to fall off before it can cover the entire wafer surface. Step 4 is 30 seconds of spinning with the specified spin speed (ω) for the desired thin resist film thickness (T). Step 5 causes the chuck to decelerate to a resting position, and as a result, the wafer no longer spins.

The values of the spin speed ω for the desired SPR220-7 thicknesses T based on the nanofabrication stage requirements for micro-thrusters are as follows:

Table 16. Spinning parameters for each nanofabrication stage of the micro-thruster chip

Nanofabrication stage	Printing pattern	Time (sec)	acceleration (rmp/s)	ω (rmp)	T (μm)
Stage 1	Microtubing channel	30	1200	1200	7
Stage2	Micronozzle	30	1200	1200	7
Stage3	Electrodes	30	800	800	13.6
			450	450	17.6

During the spinning of the SPR220-7, two major challenges arose:

1) the appearance of bubbles on the resist, causing inhomogeneities in the coating and resulting in undesirable unprotected/exposed micro-areas; and 2) the inability to spin the SPR220-7 at high speeds. The appearance of bubbles on the resist can be caused by a number of factors. By their incorporation into the liquid resist during transportation of the resist bottle or refilling the tool tank [182]. As stated in section 5.1.3, SPR220-7 is a positive photoresist based on DNQ. During the gradual thermal decomposition of this photoactive compound, nitrogen is re-released, expanding the resist and forming bubbles when it dissolves [182].

2) The resist coating for conformal walls on deep trenches of the wafer's pattern (stage) results in an overabundance of resist thickness to ensure coating of conformal surfaces. This increase in thickness increases the appearance of the bubbles, necessitating an additional spin coating to cover the remaining exposed areas and bubbles, as shown in Table 16 at stage 3.

5.2. Baking

Typically, the next step after coating is baking the resist. Depending on the thickness of the resist film and the solvent used, the solvent concentration in resists ranges between 10 and 35 percent [183]. Where the primary objective of baking is to reduce this residual solvent concentration to prevent the resist or remaining impurities from adhering to the mask during contact exposure. In addition, improve the adhesion of the resist to the substrate and prevent bubble formation by evaporating the solvent when the coating substrate must undergo metallisation or dry etching. Primarily, baking prevents the formation of standing wave patterns on the surface of the resist after exposure to light provided by monochromatic plane wave incident light [183]. The waves are then reflected by the mirror-like surface of the wafer or substrate. These interferences between reflected and incident light produce "standing wave" modulation on the photoresist profile [178].

According to the SPR220-7 manufacturer [173] in Table 17, soft baking parameters are recommended. Unlikely, there are no suggestions for thicknesses greater than 10,0 μ m. Thus, reference [184] was used as a starting point for a thicker resist layer, which included an additional oven step after the contact hot plate procedure.

Table 17. Soft baking conditions for thicker SPR220-7 resist layers(>1 μ m)

Thickness (μ m)	Layers	Soft bake		Equipment	Source
		Temperature ($^{\circ}$ C)	Time (min)		
1.1 - 4.0	1	115	1.5	Hot plate	[173]
4.0 -10.0	1	115 (step-down)	0.5	Hot plate	[173]
1.0 - 18.0	1	90	1	Hot plate	[184]
18.1 - 36.0	2	90	1	Hot plate	[184]
			55	Oven	
36.1 -54.0	3	90	1	Hot plate	[184]
			90	Oven	

The necessity of searching for soft bake parameters as a foundation for thicker resist films stems from the presence of deep trenches (microchannels) that were filled with resist during spin coating (Figure

5-14). Table 18 displays the optimised values for the soft baking of the SPR220-7 during the nanofabrication of micro-thruster chips.

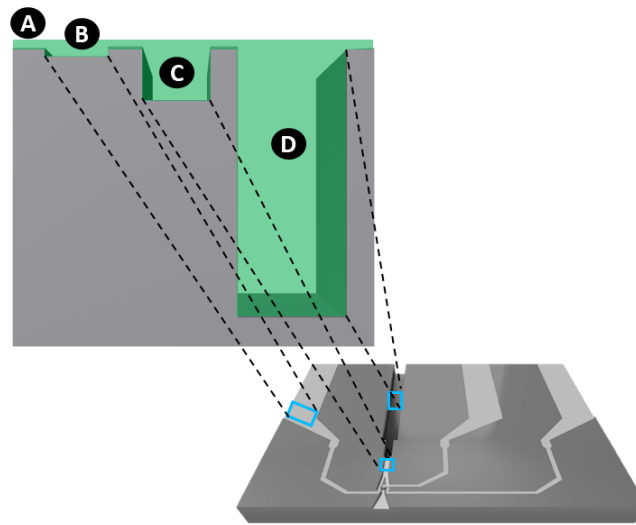


Figure 5-14. Trenches flooding representation by photoresist on the microthruster chip; green layer represents the SPR220-7 photoresist. A) Wafer surface coated with resist. Three main depth trenches conform the microdevice; B) 500nm depth trench for a further metal deposition on the electrodes pattern, C) 50µm-100µm depth trench for micronozzle patterning, and D) 320µm depth trench for microtubing channel pattern.

Table 18. Practical soft baking parameters based on resist thickness in micro-thruster trenches.

Thickness (µm)	Layers	Soft bake		
		Temperature (°C)	Time (min)	Equipment
1.0 - 14.0	1	120	1.5	Hot plate
		80	1.5	Hot plate
14.1 - 40.0	1	90	20	Oven
		80	1.5	Hot plate
36.1 - 100.0	2	90	20	Oven
		120	20	Oven
		120	20	Oven

5.3. Development

When positive photoresists, such as SPR220-7, are exposed to UV light during photolithography, a polymeric chain scission or cross-linking occurs, which is subsequently removed by a developer solution.

There are three primary development techniques [185]: 1) immersion, in which the wafer is immersed in a developer-filled container for a predetermined amount of time. 2) Spray the development while the wafer is spinning through a sprayer. 3) The Puddle method combines immersion and spray.

Immersion is the quickest and most cost-effective technique, so Microposit MF-CD-26 from Rohm and Haas Electronic was utilised to develop SPR220-7 on a 4-inch Si wafer. Two 250ml containers were filled with MF-CD-26, and the wafer was placed in one for 110 seconds before being transferred to the other for 75 seconds, followed by five minutes of DI water. The purpose of utilising two containers is to minimise the development efficiency loss from the 250ml of MF-CD-26 due to saturation caused by the dissolution of SPR220-7.

5.4. Etching

Based on its design, the fabrication of the micro-thruster required multiple etching processes. It is essential to consider the etching direction (Figure 5-15), etching rate, and selectivity [186]. There are two main types of etching: wet etching, which uses an aqueous solution to create an isotropic (uniform in all directions) etching profile, which uses a chemical solution. And the dry etching utilises etchant gases or plasmas to remove substrate materials and provide an anisotropic etch (uniformity in the vertical direction) [187].

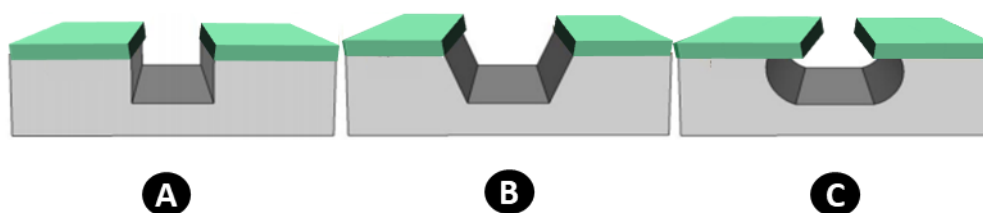


Figure 5-15. A) Completely anisotropic. B) Partially anisotropic. C) Isotropic etching of silicon [187].

To determine how fast the material is removed when it is exposed to the etchant is given by

$$Etch\ rate = \frac{\Delta d}{t} \quad \text{Eq. 125}$$

Where $\Delta d = d_0 - d_1$ (Å) is thickness change, and t is the exposition time to the etchant [188].

The following equation can be used to calculate the non-uniformity (NU) etch factor in determining the quality of the etching:

$$NU(\%) = \frac{E_{max} - E_{min}}{2E_{ave}} \quad \text{Eq. 126}$$

Where E_{max} is the maximum etch rate measured, E_{min} is the minimum etch rate measured, and E_{ave} is the average etch rate [188].

Aspect Ratio (A/R) is the ratio between the etched feature depth H and the feature width w [189], given by

$$A/R = \frac{H}{w} \quad \text{Eq. 127}$$

A/R plays a significant role in deep reactive ion etching (DRIE) when it exhibits several effects at the bottom of the etched feature, such as sidewall tapering, etch termination, and DRIE lag. Providing a sidewall that is not vertical ($\theta \neq 90^\circ$) degrades the performance of the microfabricated device. This effect is typically a result of the limited Knudsen transport of gas species at deeper etchings, which depletes reactive species [189].

Due to the A/R and the ambiguity of the ion bombardment on the volatility of the dry etching, it is always a matter of engineering judgement to highlight the etching capability of a material under particular conditions [190].

According to the micro-thruster chip design (section 4), a deep anisotropic etching profile is required, with dry etch being the primary etching technique. Therefore, within the JWNC, the Oxford Instruments Estrelas 100 ICP RIE Deep Silicon Etch system is the etching instrument capable of providing a deep reactive ion etching (DRIE). DRIE is an extension of reactive ion etching (RIE), in which physical and chemical effects are combined to remove material from a wafer's surface. Enabling rapid etching of deep and narrow structures, as shown in Figure 5-16:

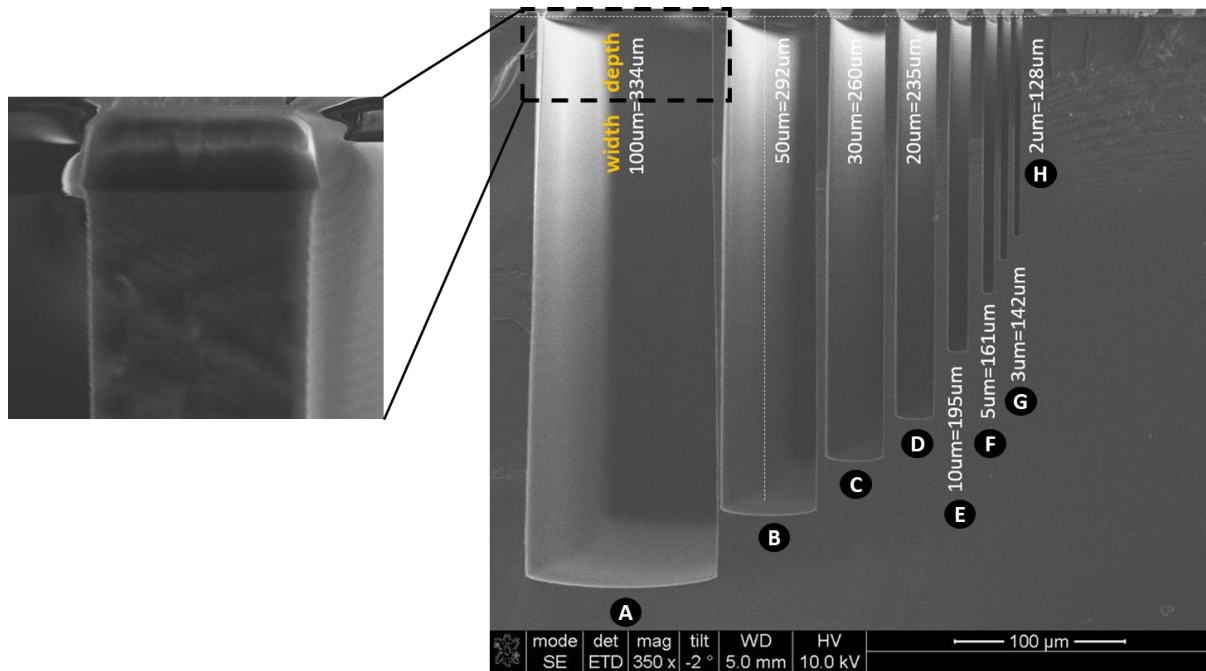


Figure 5-16. Variations in depth were obtained by different widths, including narrow structures, on a single Si substrate test for a deep etching process supplied by JWNC. The procedure was executed in Estrelas using the J00 BSH J05 IC fpl 25-99- TWE R08T7 DbE2b LF60W recipe for cycle[152, 153, 154, 154] at 56.53 minutes on eight widths. The left image depicts the profile of the sidewall where repeated isotropic etching steps produce an anisotropic silhouette [191].

Four process modes are permitted in Estrelas:

- 1) Bosch Deep Silicone Etching (DSIE), which provides high anisotropic etching rates up to $25\mu\text{m}/\text{min}$ with a uniformity around 3% on silicon, permitting a maximum aspect ratio of 60:1 and a selectivity to PR up to 250:1 on silicon, silicon-on-insulator (SOI), and silicon on glass substrates [192].
- 2) Silicon (Si) Mixed Etching offers a continuously passivating anisotropic or sloped etch with a maximum rate of $5\mu\text{m}/\text{min}$ providing smooth sidewalls with uniformity of 5%, permitting aspect ratios of up to 7:1 and a maximum selectivity to PR of 10:1 [192].
- 3) Si Cryo Etch (DSIE) permits deep Silicon anisotropic or sloped etching at cryogenic temperatures at a rate of up to $5\mu\text{m}/\text{min}$ with uniformity of 5% on maximum aspect ratios of 30:1 and selectivity to PR of 100:1 [192].
- 4) Silicon(Si) Isotropic Etching with a maximum rate of $25\mu\text{m}/\text{min}$ and selectivity of 400:1 for PR and 800:1 for SiO_2 [192].

5.4.1. Bosch deep silicon etching (DSIE)

Thus, DSIE was utilised for the microtubing channel etching, where a $320\mu\text{m}$ -deep trench with a 1:1 aspect ratio was required for the subsequent allocation of a 30G needle based on the micro-thruster chip design. Then, two Si Mixed etching processes, one for the micronozzle pattern with a $50\mu\text{m}$ -depth trench for 2:1, 1:1, and 1:2 aspect ratios, followed by an electrode pattern etching with a $0.5\mu\text{m}$ -depth trench, were processed.

Combining isotropic silicon etching from SF_6 and C_4F_8 for multiple sidewall passivation steps yields anisotropic profiles [193]. As depicted in Figure 5-17, the Bosch procedure consists of a three-step cycle: deposition of C_4F_8 for passivation, breakthrough or passivation removal at low pressure, and isotropic etching with SF_6 at high pressure [192].

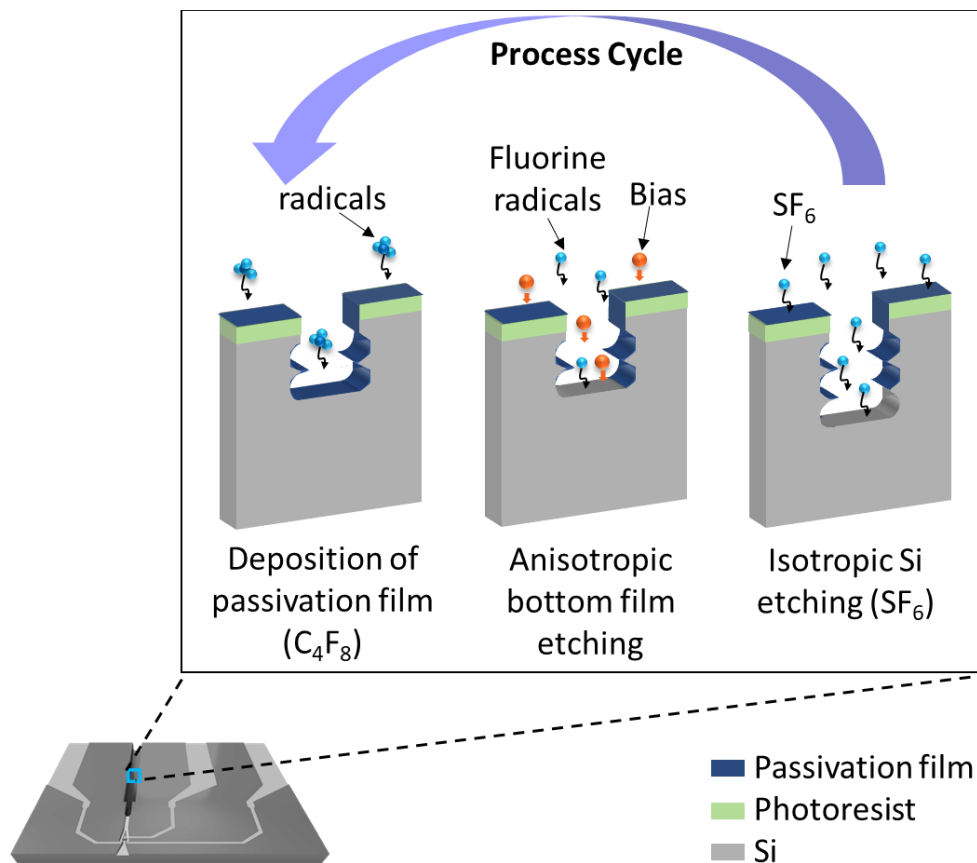


Figure 5-17. Diagram of the Bosch etching process applied to the deep etching of the microtubing channel on the micro-thruster chip. In each cycle, the isotropic etch and fluoropolymer steps are repeated to produce an anisotropic profile.

Each cycle was run with the following parameters:

Table 19. Estrelas DSIE parameters for an A/R of 1:1 etch along 320 μ m-width

PARAMETER	VALUE
ICP POWER (D)	1500
ICP POWER (B)	1800
ICP POWER (E)	1800
LF POWER (D) W	10
LF POWER (B) W	60
LF DUTY CYCLE (%)	25
LF PULSE FREQUENCY (HZ)	990
PRESSURE (D) (MT)	50
PRESSURE (B)	30
PRESSURE (E) (MT)	35
C4F8 (D) (SCCM)	200
C4F8 (B) (SCCM)	10
C4F8 (E) (SCCM)	10
SF6 (D) (SCCM)	10
SF6 (B) (SCCM)	200
SF6 (E) (SCCM)	200

The etching of a 320 μ m-deep trench on silicon with a 1:1 aspect ratio requires a total of 613 cycles. By assigning distinct times, these cycles will be divided into four stages. As [cycles] [152, 153, 154, 154] for [stage1, stage2, stage3, stage4] respectively. Where the cycle times were defined as [5.25, 5.45, 5.65, 5.85] seconds per stage, the total time for the Bosch process was 56 minutes and 53 seconds.

To determine the DSIE processing time according to the Aspect Ratio (A/R) required for the 1:1 microtubing channel with a 320 μ m width, the etching test results from the Bosch process during 56.53 minutes provided by the JWNC in Figure 5-16 were utilised.

Table 20. Etching rates for Bosch Deep Silicone Etching (DSIE) from JWNC

Profile	Time (min)	Depth (μm)	Width (μm)	Aspect ratio	Depth rate reference	etch rate ($\mu\text{m}/\text{min}$)
A	56.53	334	100	3:1	1	5.9
B	56.53	292	50	6:1	0.88	5.2
C	56.53	260	30	9:1	0.79	4.6
D	56.53	235	20	12:1	0.72	4.2
E	56.53	195	10	20:1	0.6	3.4
F	56.53	161	5	32:1	0.5	2.8
G	56.53	142	3	47:1	0.44	2.5
H	56.53	128	2	64:1	0.41	2.3

The etching rate varies based on the A/R, and the reference data covers a range from $2\mu\text{m}$ to $100\mu\text{m}$ trench width; thus, to calculate the etched depth for the required $320\mu\text{m}$ -width, the depth is normalised by taking the $100\mu\text{m}$ -width as unity, obtaining the following normalised depths from three tests(R08T5, R07e, R07e-DbE2b) [191]:

Table 21. DSIE normalized average depth

Width	Depth reference R08T5	Depth reference R07e	Depth reference R07e-DbE2b	Normalized Average depth
100	1.00	1.00	1.00	1.00
50	0.88	0.91	0.89	0.89
30	0.79	0.83	0.81	0.81
20	0.72	0.76	0.74	0.74
12	0.60	0.65	0.62	0.62
7	0.50	0.55	0.51	0.52
5	0.44	0.49	0.47	0.46
4	0.41	0.47	0.37	0.42

Where the normalised average depth (Figure 5-18) in relation to the width follows a behaviour in which the increase in depth slows as the open area becomes wider (greater than 30 μm):

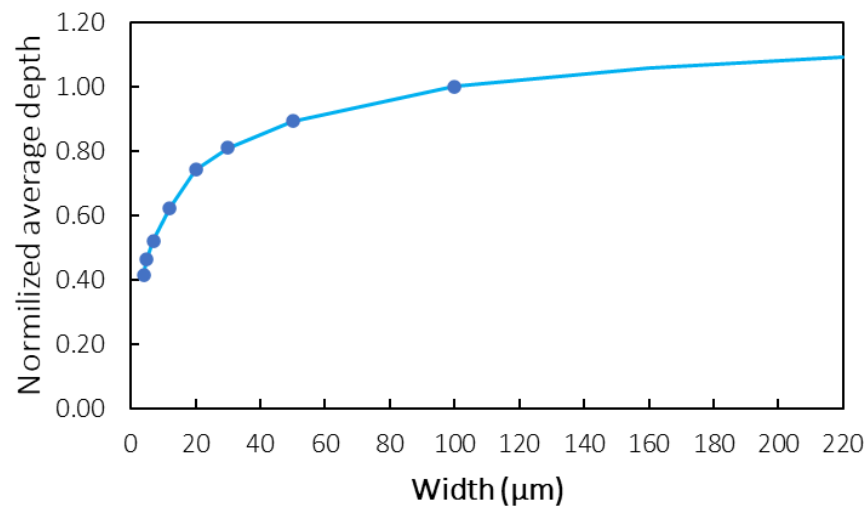


Figure 5-18. Normalized average depth factor for DSIE based on the open area width.

Where the trend of the normalised average depth H_{Norm} can be expressed as,

$$H_{Norm} = 1.483552 + \frac{(0.3003207 - 1.483552)}{\left[1 + \left(\frac{w}{4.020896}\right)^{1.759396}\right]^{0.1574458}} \quad \text{Eq. 128}$$

Where w is the open area's width in microns on the Si wafer.

Based on Eq. 128, Table 22 was created to identify the normalised depth difference ΔH_{Norm} between two widths during the same Bosch procedure and timing. Where a 320 μm -wide open area has 14 percent deeper etching than the 100 μm -wide reference point.

Table 22. Normalized depth difference between different micro-trench widths using 100µm-width as the unitary reference.

Width (µm)	0	10	20	30	40	50	60	70	80	90	100	160	200	220	320
10	0.59	0													
16	0.69	0.10	0												
26	0.78	0.19	0.05	0											
40	0.86	0.27	0.13	0.05	0										
50	0.90	0.31	0.16	0.09	0.04	0									
56	0.91	0.32	0.18	0.11	0.05	0.02	0								
70	0.95	0.36	0.22	0.14	0.09	0.05	0.02	0							
76	0.96	0.37	0.23	0.15	0.10	0.06	0.04	0.01	0						
90	0.98	0.39	0.25	0.18	0.12	0.09	0.06	0.04	0.02	0					
100	1.00	0.41	0.27	0.19	0.14	0.10	0.07	0.05	0.03	0.01	0				
150	1.05	0.46	0.32	0.24	0.19	0.15	0.12	0.10	0.08	0.07	0.05	0			
200	1.08	0.49	0.35	0.27	0.22	0.19	0.16	0.13	0.12	0.10	0.08	0.03	0		
230	1.10	0.51	0.37	0.29	0.24	0.20	0.17	0.15	0.13	0.11	0.10	0.04	0.02	0	
320	1.14	0.55	0.41	0.33	0.28	0.24	0.21	0.19	0.17	0.15	0.14	0.08	0.05	0.04	0

Recipe: 00_BSH_J05_IC_fpl_25-99-_TWE_R08T7_DbE2b_LF60W Cycle [152, 153, 154, 154] Times [5.25, 5.45, 5.65, 5.85] for a total time of 56.53 min

5.4.2. Silicon (Si) mixed etching

For the micronozzle and electrode pattern etching in Estrelas, the Si Mixed Etching mode [192] was utilised. Compared to DSIE, the mixed processes or pseudo-Bosch process provides a low roughness etched profile on sidewalls and bottoms, ideal for minimising flow performance variations during experiments caused by drag on the micro-thruster. In addition, sidewall uniformity is desired for a continuous conformal gold coating during metallisation (section 5.7.1). This is achievable by combining the passivation, silicon etching processes, and adjusting the gas ratios between SF6 and C4F8. Producing insufficient sidewall passivation under constant ion bombardment for high aspect ratio etching where structures can collapse [194].

Therefore, the mixed etching recipe 000 MIX J05 Ic fpH RYT1 HF Test was executed in Estrelas with the following parameters:

Table 23. Parameters for the Si Mixed Etching procedure

PARAMETER	VALUE
ICP POWER (E)	600
HF POWER (E) W	11
LF DUTY CYCLE (%)	25
LF PULSE FREQUENCY (HZ)	990
PRESSURE (E) (MT)	11
C4F8 (E) (SCCM)	50 (63)
SF6 EXT. (SCCM)	50

This process's etching rate is 1.55 $\mu\text{m}/\text{min}$, with a 100 μm -depth micronozzle etching pattern taking 1 hour, 4 minutes, and 31 seconds. The electrode pattern was etched for an additional 20 seconds at a 510 nm depth during stage three.

5.4.3. Carrier wafer procedure

Before running, a 4-inch wafer must be adapted to fit within the 6-inch holder of the Estrelas 100 ICP RIE, regardless of the process mode. Thus, the 4-inch wafer must be attached to a 6-inch carrier wafer with a 5 μm -SiO₂ layer on the top surface as a mask to prevent the over-etching of contaminant-causing material during the process.

Santovac is an oil used as a bonding agent to mount a 4-inch wafer onto a carrier wafer due to its low volatility, chemical and radiation attack resistance, and thermal degradation resistance at maximum temperatures of 450°C for extreme environments, such as, are resistant to chemical and ionising radiation attack [195], which makes their use suitable for the plasma within the dry etch process.

Thus, the following steps were taken for the attachment of the carrier-wafer:

1. Preheat 1-2 ml of Santovac in a 4 ml vial in a vial heater at 95 degrees Celsius.
2. Warm the 4-inch sample wafer to 80 C on a hotplate for one minute.
3. Take the oil along with the pipette.
4. Place a Santovac drop of 3mm diameter in the centre of the carrier surface.
5. Place the preheated 4-inch sample wafer on the Santovac drop immediately.
6. Press around the perimeter of the sample wafer and wait an additional 1-2 minutes.
7. Place on a flat surface until cool.

After the dry etch is complete, the wafer must be demounted from the carrier by:

1. Set vacuum hotplate to 80°C.
2. Place the carrier wafer on the vacuum holder and activate the vacuum.
3. Wait approximately two minutes for the carrier, Santovac, and sample heating.
4. Demounting the sample wafer by sliding it across the carrier onto a watch glass.
5. Remove Santovac using acetone.

5.5. Electrical Breakdown within the device

There are several reasons why the micro-thruster chip can have electrical breakdowns which include the nanofabrication process and materials themselves. Choosing and applying appropriate dielectric materials is of paramount importance in preventing such a breakdown. The dielectric layer acts as an insulator by stopping unnecessary electric discharges between the silicon substrate and metallic electrodes.

Therefore, SiO₂ was selected due to its lower dielectric constant of 3.9 compared to SiN's 7.5, making SiO₂ less capable of storing electrical energy, despite both materials having dielectric strengths of 10⁷ V/cm [163]. An essential property of the insulator layer is its density, which is 2.2 g/cm³ for SiO₂ and 3.1 g/cm³ for SiN, with SiO₂ being the most feasible option for minimising the increase in satellite load by adding an insulator layer. Depositing SiO₂ involved using Plasma-Enhanced Chemical Vapor Deposition (PECVD) method whereby films with uniformity over large areas could be formed at relatively low temperatures ranging from 60 °C up to 300 °C .

Moreover, it is necessary that metal layers should be deposited conformally so as not only to provide robustness but also increase reliability across electrical paths throughout the device. Any breaks or cracks in metal routing create localities where there are excessively strong electric fields hence raising chances that dielectrics may break down locally due to these regions being points with highest vulnerability towards such failures. The electron beam evaporation technique under Physical Vapor Deposition (PVD) category was specifically used during metal depositions because it allowed one control thickness levels along with evenness across various parts.

Generally speaking, among risk management measures taken at different stages during nanofabrication processes involved in making micro-thruster chips, the selection of proper dielectric materials; use of advanced deposition techniques as well ensuring uniformity and integrity of metal layers remain key strategies against electrical breakdowns.

5.6. Insulator layer deposition

As it was mentioned in the previous section, the plasma-based micro-thruster chip necessitates a dielectric layer acting as an insulator to prevent any breakdown voltage on undesirable areas between the Si substrate and the electrode's material (Au). Thus, SiO₂ was chosen as insulator layer by its lower dielectric constant of 3.9 and its low density.

SiO₂ is deposited using Plasma-Enhanced Chemical Vapor Deposition within JWNC (PECVD). Plasma induces the decomposition of the sourced gases, such as silane (SiH₄), tetramethoxysilane (TMOS), or hexamethyl-disiloxane (HMDS), into radicals that react with oxygen to form SiO₂ [196].

This is a well-established technique for deposition of a wide variety of films. PECVD is a low-cost process where, depending on the temperature (ranging from 60 °C to 300 °C), the roughness, refractive index, stress, electrical characteristics, and wet chemical etch rate of the film properties can be controlled, resulting in films with excellent uniformity and high rate [197] [198].

For the nanofabrication of micro-thruster chips, a standard SiO₂ deposition on PECVD SPTS Delta was implemented for the 5µm-thick SiO₂ layer on the 4-inch Si wafer. This standard procedure utilised SiH₄, N₂O, and N₂ at 7 sccm, 146 sccm, and 85 sccm at a controlled temperature of 300 °C and a chamber pressure of 1000mTorr. With a 65nm/min deposition rate and compressive stress of 40 MPa, a 5 µm-thick SiO₂ layer can be deposited in 1 hour and 16 minutes [199].

5.7. Metal deposition

Metal deposition involves depositing nm-thick metallic films into the openings of a resist mask. Physical vapour deposition (PVD), chemical vapour deposition (CVD), atomic layer deposition (ALD), molecule beam epitaxy (MBE), oxidation, plating, spin or spray coating, blade coating, and printing are all methods for thin film deposition [185]. Plassys Bestek, the manufacturer of the MEB550S Plassys Electron Beam Evaporator [200], is commonly used to process metallic thin film deposition on PVD inside the JWNC [201].

PVD comprises sputtering plasma and thermal evaporation by electron-beam deposition (Figure 5-19). A sputtering plasma deposition consists of two parallel electrodes in a vacuum chamber, with the anode serving as the sample stage and the cathode containing the deposition material (metal). A high DC voltage is applied between the electrodes. Then argon is introduced, colliding with the free electrons to produce ions, acquiring of additional electrons and Ar⁺ through ionisation. Sputtering occurs when Ar⁺ ions are accelerated toward a metallic material (target), producing free metal atoms

with sufficient kinetic energy to deposit on the surface of the sample and its surroundings [185]. Electron-beam deposition, on the other hand, uses an electron gun to evaporate the source material under vacuum conditions. A DC high voltage supply heats the electrons to 3000 °C, eliminating the need for a resistively heated evaporation source [185] [202].

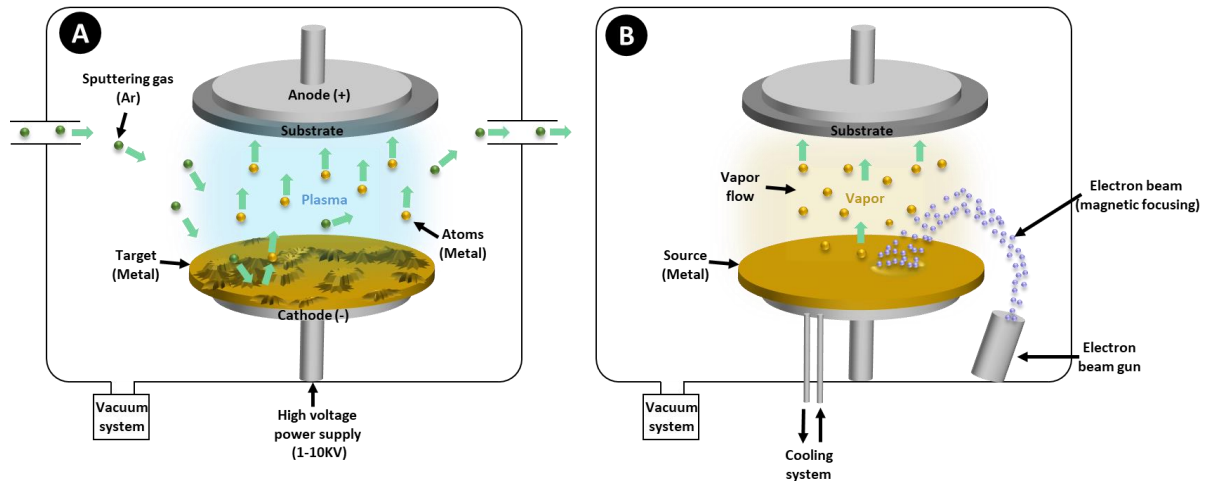


Figure 5-19. Metal deposition process; A) Plasma sputtering deposition. B) Electron-beam physical vapor deposition.

The formula for determining the thin-film deposition rate R_{dep} by thermal evaporation is as follows:

$$R_{dep} \propto \frac{\cos\theta \cos\varphi}{r^2} (P_s - P_c) \quad \text{Eq. 129}$$

Where r is the distance between the source of evaporation and the sample, θ is the angle of the sample to the axis of evaporation, and φ is the surface orientation angle of the sample (Figure 5-20). In addition, P_s is the pressure of the source material, which varies with the heating temperature, and P_c is the chamber pressure.

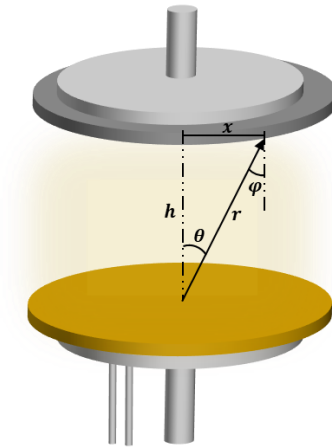


Figure 5-20. Schematic of the position of the source relative to a flat sample for thin film deposition.

Generally, the greater the distance from the centre on flat samples, the thinner the film deposition will be. Consequently, to obtain the thickness of an off-centre location, the formula t_x follows[84]:

$$t_x = \frac{t_0}{\left[\left(1 + \frac{x^2}{h^2} \right)^2 \right]} \quad \text{Eq. 130}$$

Where t_0 is the thickness of the deposited film at the centre of the sample perpendicular to the axis of the evaporation source, x is the distance of the off-centre location from the centre of the sample, and h is the height.

5.7.1. Conformal deposition

According to Sarkar, J. [203], a conformal film has a nearly constant thickness on both horizontal and vertical surfaces. According to the micro-thruster chip design specifications, there is a region where the metallic thin film route of the anode must cross a portion of the micronozzle channel to connect the electrode with the voltage supply (section 4.8.5). Thus, deposition techniques such as physical vapour deposition (PVD) or atomic layer deposition (ALD) can provide conformal films with uniform growth in 3D structures with complex shapes and high aspect ratios [204].

Two techniques provide a conformal film coating without altering the vapour's orientation within the chamber, instead tilting the sample (Figure 5-21). The first technique is oblique-angle deposition (OAD), which involves tilting a planar sample at a fixed angle between 0 and 90 degrees during the thin film deposition process to produce high-fidelity conformal coatings [205]. Rarely can protruding structures at a deposition angle create a shadowed region that prevents or prohibits the formation of thin films [206]. As a second technique to mitigate this issue, conformal-evaporated-film-by-rotation

(CEFR) was considered; it is a variant of OAD that improves the uniformity of coating thickness by adding an axial rotation to the sample. Being simultaneously rotated and tilted, the sample provides complete coverage of the 3D structures on the substrate [205].

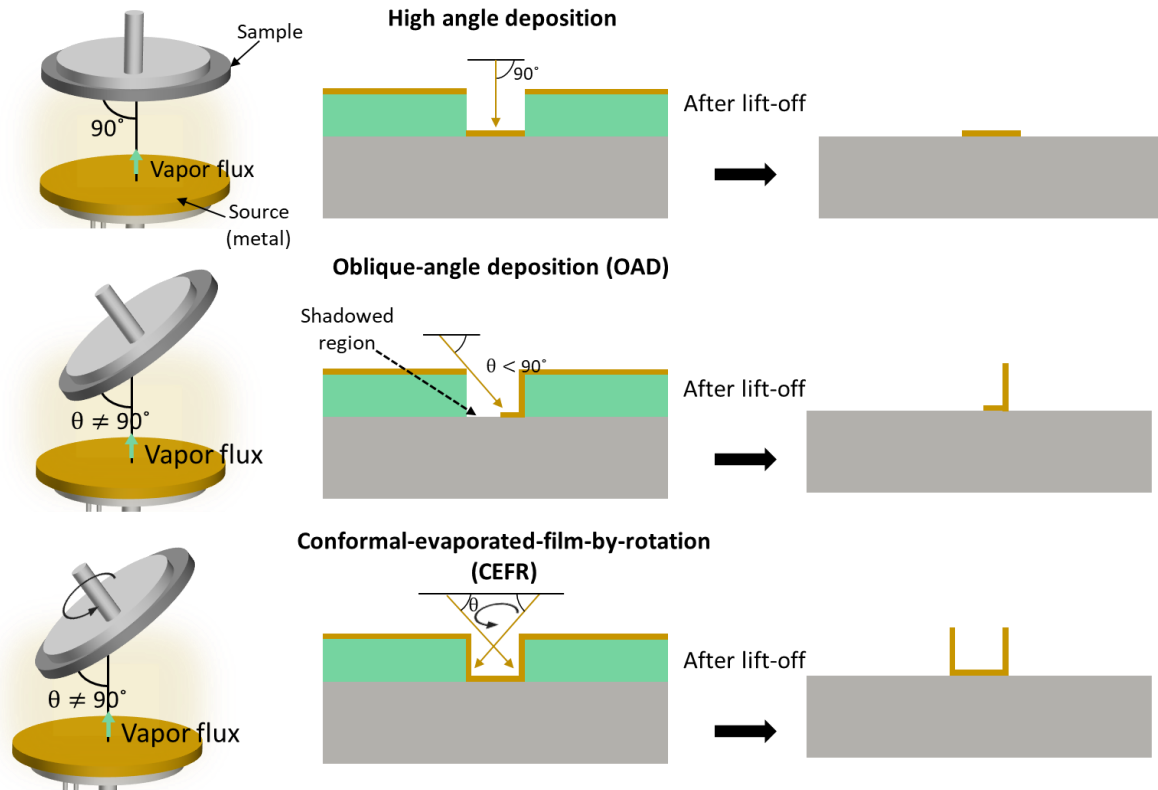


Figure 5-21. Sample's directionality and rotation during vapour deposition.

The following ratios were defined to quantify the conformal structure. The bottom coverage is determined by the ratio of the film thickness at the bottom of the feature (t_b) to the nominal film thickness on the flat region (t_n) [203],

$$\text{Bottom coverage} = \frac{t_b}{t_n} \quad \text{Eq. 131}$$

To calculate the left-side step coverage (Figure 5-22), divide the film thickness (t_{s1}) at the side of a feature by the nominal thickness of the film on the flat region (t_n) [203]:

$$\text{Step coverage}_L = \frac{t_{s1}}{t_n} \quad \text{Eq. 132}$$

For the right-side,

$$\text{Step coverage}_R = \frac{t_{s2}}{t_n} \quad \text{Eq. 133}$$

Therefore, [203] describes the asymmetry between the two conformal coatings on a trench.

$$Asymmetry = \frac{t_{s2}}{t_{s1}} \quad \text{Eq. 134}$$

The conformity K is determined by vertical and horizontal growth in a practical sense. Consequently, based on the average growth of each side of the vertical and horizontal films, it is defined as

$$K = \frac{(t_{s1} + t_{s2})}{(t_n + t_b)} \quad \text{Eq. 135}$$

Where the reentrance is r on Figure 5-22.

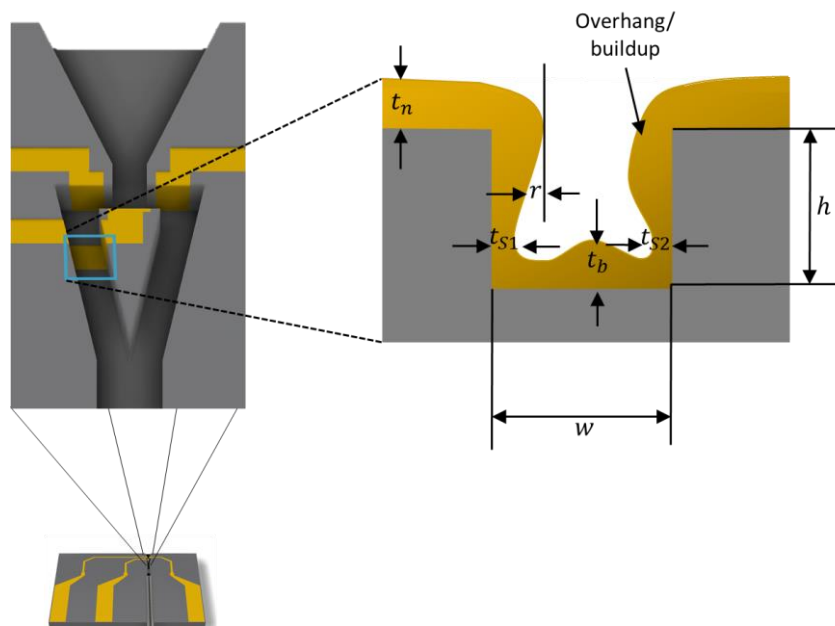


Figure 5-22. Schematic of the conformal Au-coat routing for electrodes on the micro-thruster chip, showing the aspect ratio, step coverage, bottom coverage, asymmetry, and reentry.

Plassys MEB550S was used to deposit 30 nm-thick titanium (Ti) thin film with a 99.995% purity from Kurt J. Lesker Company, followed by a 500 nm-thick gold (Au) thin film with a 99.99% purity from Pi-KEM Ltd. on a 4-inch wafer. With a deposition rate of 0.5 nm/s at a frequency of 5.8 MHz and a chamber pressure of 1.1×10^{-8} mbar using the conformal-evaporated-film-by-rotation (CEFR) technique with an oblique angle of 30 degrees.

5.7.2. Covering issues

The directionality (angle) of the deposition is crucial for obtaining a good additive metallic pattern transfer during lift-off. Good step coverage by thin films makes resist removal difficult by preventing the solvent from coming into contact with the resist [185]. Consequently, tilt metal deposition provides a conformal coating on the side walls between the top and bottom resist patterns (Figure 5-24), encapsulating the resist with a metallic coating layer that prevents the resist from dissolving and renders lift-off impossible.

The solution to this problem is to use a pipette and a solvent (acetone) to generate a jet capable of penetrating the resist and breaking the metallic coating. Two factors were considered for the implementation of this method: 1) the increase of the resist thickness to soften the resist surface where the coating is deposited to generate cracks, and 2) the incorporation of an adhesion interlayer to strengthen the bond between the SiO₂ surface of the sample and the gold coating for a more aggressive (pipette jet) lift-off technique.

1) Increasing the resist thickness substantially increases the likelihood of resist coverage on step patterns by decreasing the spinning speed (section 5.1.7). In addition, the greater the separation between the metallic thin film coating and the sample surface created by a thicker resist layer, the softer the resist becomes, thereby accelerating the formation of cracks on the coating. As a result, a metallic coating on a thicker resist layer is easier to crack or remove by applying pressure with a pipette. In addition, a thicker resist will allow a greater volume of solvent to permeate and flow through the resist gap, facilitating its removal during the lift-off.

2) There is a high probability that the pressure from the pipette's jet applied to the metal coating adhered to the sample will be removed if adhesion is poor. Therefore, adhesion must be enhanced by incorporating a titanium thin film interlayer between SiO₂ and Au, which provides exceptional bonding strength, in order to improve adhesion. Ti is frequently employed as adhesion or adhesive layer between ceramic or dielectric films and a metal conductor [207]. Moreover, during thin-film deposition, Ti is partially oxidised, allowing it to readily bond with SiO₂ on the sample's surface [208]. Afterwards, during the Au deposition, Ti forms a perfectly bonded alloy.

5.7.3. Lift-off

Lift-off is the only way to pattern many metallic materials, making it the most common technique [185]. After the deposition of metallic thin films, a chemical solvent is applied to dissolve the resist layer, causing the metallic coating on its surface to peel off. In contrast, the metallic coating deposited on the resist pattern openings on the substrate remains. Thus, the micro-thruster chip nanofabrication launch consisted of placing the 4-inch Au-coated wafer inside an acetone-filled glass container.

Then, a plastic pipette was used to generate a jet to break or remove portions of the 500 nm-thick Au film to allow the acetone to dissolve the resist. The Au deposited on the patterned areas is not removed by force ejected from the pipette due to the incorporation of a 30 nm-thick Ti interlayer that bonds flawlessly with the SiO₂ surface layer of the wafer. The wafer is then placed in a beaker of acetone and in a warm bath for at least 30 minutes for lift-off to occur.

After the entire resist has been dissolved, the remaining metallic fragments adhered to the thin film pattern but not bonded to the wafer can be effortlessly removed using the pipette jet.

The wafer was cleaned for three minutes by placing it in another beaker containing DI water that was running from a tap.

5.8. Glass cover fabrication

Using a Trotec speedy 300 laser engraver by Trotec Laser GmbH, the pattern was etched onto 18 x 18 mm borosilicate glass slides with a thickness of 170 nm from Paul Marienfeld GmbH & Co. KG.

The Trotec speedy features both laser cutting and laser engraving modes. In the case of glass materials, the tool can only engrave glass surfaces without cutting using a CO₂ laser mode ranging from 30 to 120 watts. Using the default parameters for glass engraving supplied by Trotec, the etch was not deep enough to facilitate its fracture on the etched lines to obtain the required cover shape from 170 µm-thick glass slide. Etch depth was measured with a Bruker Dektak XT Height Profiler within JWNC, displaying a value of 30 µm ± 2 µm. Consequently, it was manually set to cutting mode to increase the etching depth with 40 W power, 15 m/s speed, and 10,000 PPI/Hz with 10 passes, displaying 83 µm depth on the Dektak XT, thereby facilitating the fracture on the etching lines.

During the process, cracks will appear on glass slides if the power is increased to >40 W or the speed is decreased to 15 m/s. After obtaining the etch pattern from Trotec, the fracture was created by pulling the segment of the glass pattern in the same direction as the laser etch until it broke.

5.9. Bonding

Bonding involves adhering to two or more substrates with or without using intermediate layers [209]. According to nanofabrication requirements, there are several well-known bonding techniques. Commonly used for bonding Si-glass and SiO₂-glass, anodic bonding that consists of adhering substrates by exposing them to temperatures around 400°C and a high voltage. Adhesive bonding utilises an intermediate layer of an adhesive solution to attach materials together. Polymeric bonding in which the surfaces are heated above the glass transition temperature (T_g), and the structure is then

sealed by applying pressure. Another method is fusion bonding, which involves high-temperature annealing the two surfaces (1000°C) [209].

Unfortunately, anodic bonding cannot be used to bond the glass cover to the SiO₂ surface of the micro-thruster chip. SiO₂ is an insulating layer that prevents current flow; therefore, for it to be bonded to a glass surface, the glass must contain a mobile ion, such as Na⁺ [210]. Even though most Na⁺ ions will be neutralised when a high voltage is applied during the bonding process, the remaining active ions will alter the insulator properties of the surface junction, thereby reducing the voltage strength. Having a negative impact on the micro thruster chip's efficiency because it raises the risk of a catastrophic failure throughout the whole microdevice surface outside of the control zone.

To bond the glass cover to the substrate of the micro-thruster chip, regardless of the method employed, it is necessary to use a process or instrument that provides alignment control to ensure the correct placement of both components.

Therefore, within JWNC, the Flip Chip Bonder Model 850 was utilised, as it is the only device capable of bonding the glass cover and chip substrate via alignment and heating. Utilising a vacuum tip and stage with maximum temperature controls of 200°C and 400°C, respectively. In the event that a heat-curing adhesive is utilised, the Flip Chip Bonder can only perform adhesive bonding. Due to the tool's maximum temperature (400 °C) limitation, polymeric and fusion bindings were not possible, as borosilicate requires a minimum T_g of 525°C [211].

As a result, Cyclotene 3022-57 Series Advanced Electronics Resins derived from B-staged bisbenzocyclobutene (BCB) were selected as a bonding adhesive agent due to their low dielectric constant and low dielectric loss materials, as well as their low moisture absorption, lack of outgassing, low-temperature cure, and excellent planarisation [212]. It was utilised as a bonding layer between the glass cover and chip substrate. According to the specifications, the adhesive can be cured at approximately 260 °C. BCB was placed on both extreme sides of the glass cover using a stick. The glass cover was then placed on the vacuum tip of the Flip Chip Bonder, and the chip substrate was placed on the stage and heated simultaneously at 200 °C and 260 °C for 10 minutes.

The needle was then introduced into the micropiping channel for attachment within the micro-thruster chip. To secure the needle and seal the orifice, BCB was injected into a plastic pipette so that a drop could be deposited on the micro-piping channel inlet. The needle and chip are then placed vertically on a peaker and placed in a 260 °C oven for 20 minutes.

5.10. Process traveller for the plasma-based micro-thruster chip nanofabrication

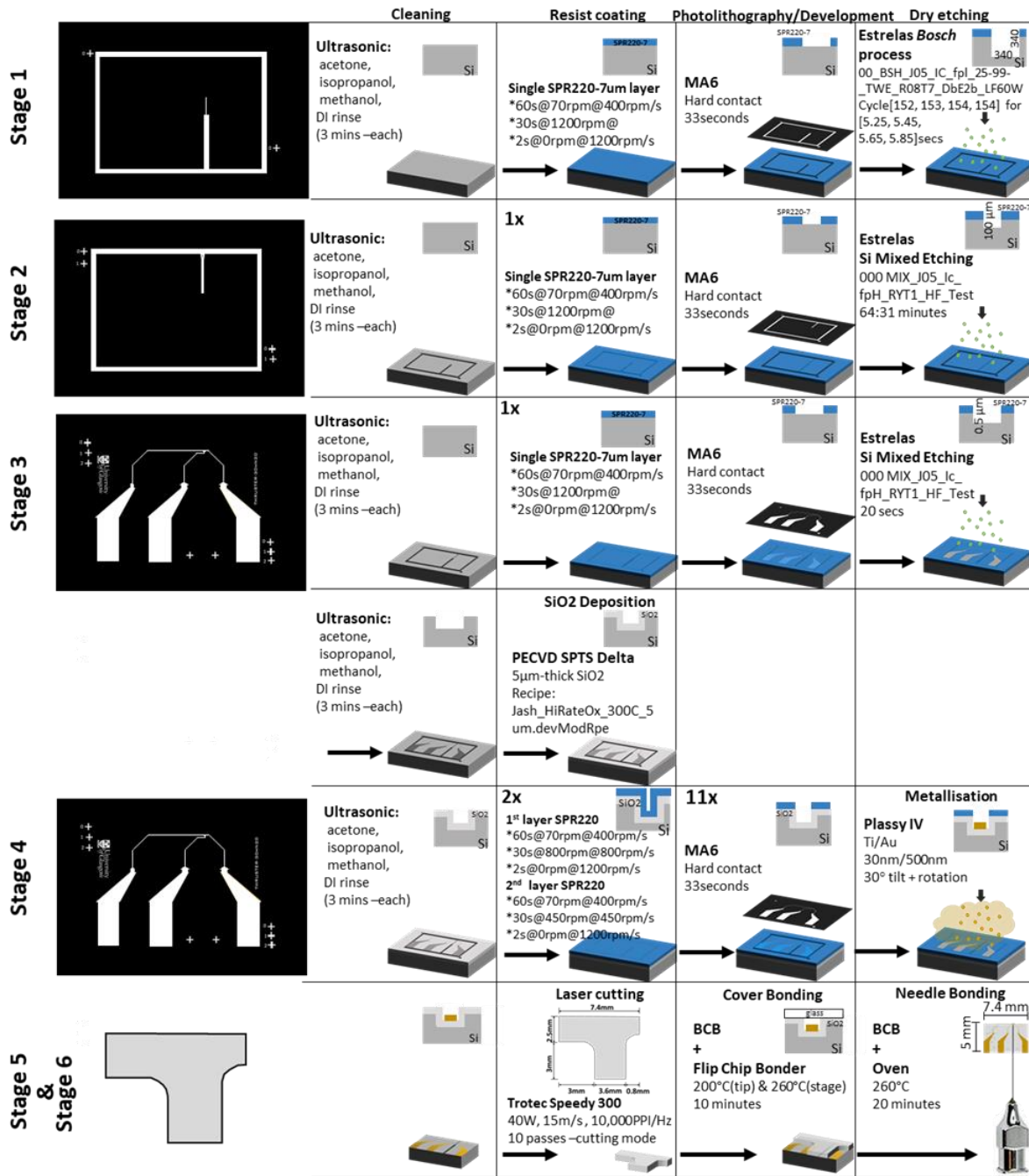


Figure 5-23. General scheme of the nanofabrication processes for the micro-thruster chip

More detail on the nanofabrication procedure shown on Figure 5-23 for the plasma-based micro-thruster chip can be found in section Appendices D.

5.11. Characterisation

The primary objective of micro-thruster characterisation is to define the quality of geometric/design parameters that can affect the device's performance and their replicability with the original design and expected results. The contact profiler Dektak XT and SEM S4700 were used as the primary instruments for characterising the nanofabrication quality of the plasma-based micro-thruster chip. The quality parameters centre on the microdevice's surface topography, analysing the depth of the microchannels, surface roughness, symmetry of the shapes/borders, and surface condition and attachment of the metal in search of cracking and discontinuities in the electrical routing path. Where defects in the topography or geometry of the micro-thruster would affect the flow conditions, creating turbulence, or the possibility of plasma generation between the electrodes gap would be avoided due to the abrupt break in the continuity of the metal routes, preventing the electric current from reaching the area of interest.

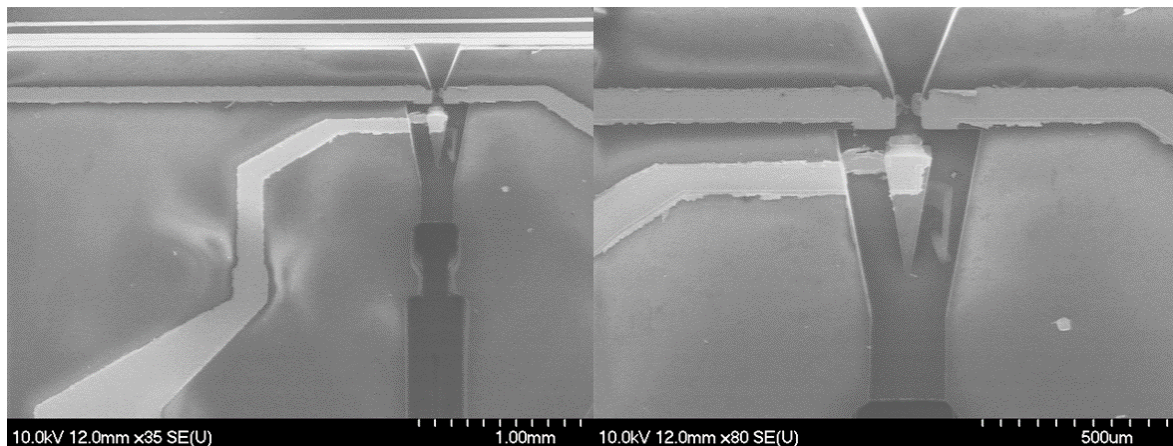


Figure 5-24. SEM image of the micro-thruster chip from top view.

5.11.1. Depth analysis in microchannels

For depth analysis, the Dektak XT profiler was used, which consists of making contact with the sample using a stylus with a diamond tip. Then, as the tip slides across the sample to be traced, the instrument maintains a constant stylus force; therefore, the change in the position of the diamond-tip permits the measurement of step heights and lateral dimensions of the surface topography of the sample.

Based on the different depths discussed in section 5.4, three primary microchannels were chosen to be characterised by depth: A) a 320 μm -deep trench for microtubing channel pattern to accommodate a 30G needle, B) a 50 μm -100 μm -deep trench for micronozzle patterning, and C) a 500 nm-deep trench for the metal routing path. Where this analysis was replicated on seven distinct locations of the wafer, as depicted in the following diagram:

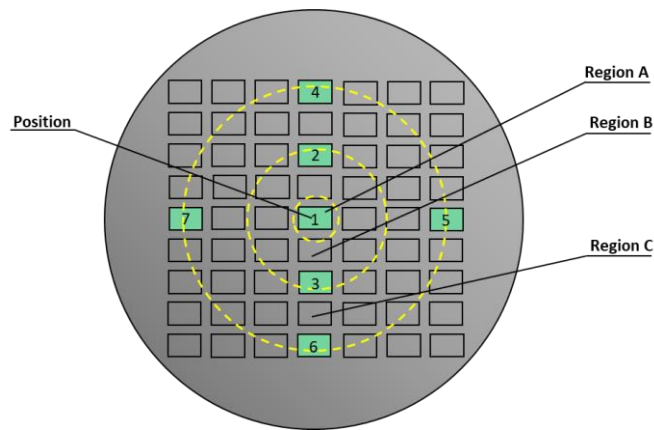
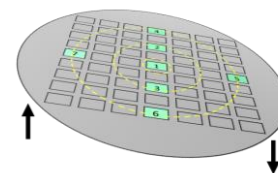


Figure 5-25. Diagram for depth etching analysis, seven microdevices on a Si wafer are used to divide the regions.

Several factors, including ion distribution within the dry etching tool, tilt of the wafer by the attachment of the carrier wafer, and positioning of the tool holder, make it difficult to achieve uniformity in depth etching along the wafer. Consequently, a mapping of regions (A, B, and C) based on depth variations was conducted (Figure 5-25), using seven characterised microdevices to assess a trend in the depth variations. A quick data analysis was performed to determine if depth changes are smaller in one quadrant of the wafer and greater in the other. Thus, it can be assumed that the differences are due to the tilt of the wafer, with the direction of the inclination being indicated by the wafer's lowest and highest etched depths. Consequently, if the depth difference is more pronounced in the middle region, variation by inclination can be disregarded, and ion distribution can be considered the primary cause.

Table 24. After the dry etching process on the microtubing channel, variations in depth contrast with the intended design outcome.

Position	Region	microtubing channel $z(\mu\text{m})$	Expected depth $z(\mu\text{m})$	Δz (μm)	% error
1	A	322	320	2	0.62
2	B	319	320	-1	-0.31
3	B	314	320	-6	-1.91
4	C	320	320	0	0.00
5	C	308	320	-12	-3.90
6	C	310	320	-10	-3.23
7	C	319	320	-1	-0.31



Chapter 5 Nanofabrication of the micro-thruster chip

The microtubing channel depths show a minimum of 305 μm at position 6 and a maximum of 322 μm at position 1, as opposed to the expected 320 μm . Given that the deepest etch was in the centre of the wafer (region A) and that etch depth decreases as one approaches the wafer's edges, it is possible to conclude that ion distribution contributes to the changes in depth. Furthermore, region C with the shallowest depth of 308 μm and 310 μm , respectively, contributed the most to the inclination of the wafer. Positions 4 and 7 exhibited the highest values, 320 μm and 319 μm , indicating a wafer tilt in the quadrant between positions 5 and 6. Furthermore, the deviation from the intended depth is less than 5%, indicating that any major fluctuations in the flow conditions and needle fittings within the micro-thruster are disregarded, making the etching parameters and process acceptable for these 320 μm -depth channel etchings.

Table 25. Variations in depth after the dry etching process on the micronozzle patterning in contrast to the intended design outcome.

Position	Region	micronozzle patterning $z(\mu\text{m})$	Expected depth $z(\mu\text{m})$	Δz (μm)	% error
1	A	102	100	2	1.96
2	B	101	100	1	0.99
3	B	102	100	2	1.96
4	C	98	100	-2	-2.04
5	C	98	100	-2	-2.04
6	C	97	100	-3	-3.09
7	C	97	100	-3	-3.09



Regarding the etched depth of the micronozzle patterning, the results are as follows: In terms of the etched depth of the micronozzle patterning, the results indicate a null difference between regions A and B that are closer to the expected 100 μm , but the depth decreases slightly as it approaches the wafer's edge, which may be due to ion distribution during etching. When the difference in depth between them is almost identical, inclination-induced variations can be disregarded. Additionally, the difference in etch depths ranges from -3.09% to 1.96%, less than 5%, when the flow conditions within the microchannel do not experience a significant change in flow profile.

Table 26. Variations in depth after the dry etching process on the metal routing path in contrast to the intended design outcome.

Position	Region	metal routing path z(μm)	Expected depth z(μm)	Δz (μm)	% error
1	A	0.51	0.5	0.01	1.96
2	B	0.50	0.5	0	0.00
3	B	0.49	0.5	-0.01	-2.04
4	C	0.49	0.5	-0.01	-2.04
5	C	0.48	0.5	-0.02	-4.17
6	C	0.48	0.5	-0.02	-4.17
7	C	0.49	0.5	-0.01	-2.04



Similar to the previous case, the metal routing channel depths vary due to ion distribution during dry etching, with the deepest value of 510 nm at region A and a nearly uniform depth distribution across the wafer surface. Where the error percentage from the expected depth of 500 nm is between -4.14% and 1.96%, the performance of the micro-thruster is unaffected.

5.11.2. Symmetry of the shapes/borders analysis

The SEM S4700 was used to characterise the symmetry of the shapes and borders of the microchannels within the micro-thrusters in order to observe differences in size and geometry during nanofabrication procedures according to the design, which can impact the performance of the microdevice.

Figure 5-26 exhibits the frontal view of the micronozzle from the outlet, with an outlet dimension of 287.54 X 99.19 μm and an area of 0.0285m² for a micro-thruster size M (medium) and a throat length of 54.6μm, which is close to the expected length of 50 μm. It provides an undercut shape profile on the microchannel with a length difference of 50.9 μm on its upper side compared to 54.6 μm on its lower side. With a difference of 1.85 μm on both sides of the wall and an undercut angle of 91.07°. Defects on the outlet wall indicate surface irregularities, but there are no structural cracks that could lead to propellant leakage. As a result, surface imperfections develop in the top region of the device with an approximate area of 0.0023 m² due to the SiO₂ layer deposition produced by the brilliant thin layer in Figure 5-26, which covers the entire device surface. These protrusions do not represent a

significant difference in wall thickness that can influence flow conditions relative to the volume of open space through which propellant flows.

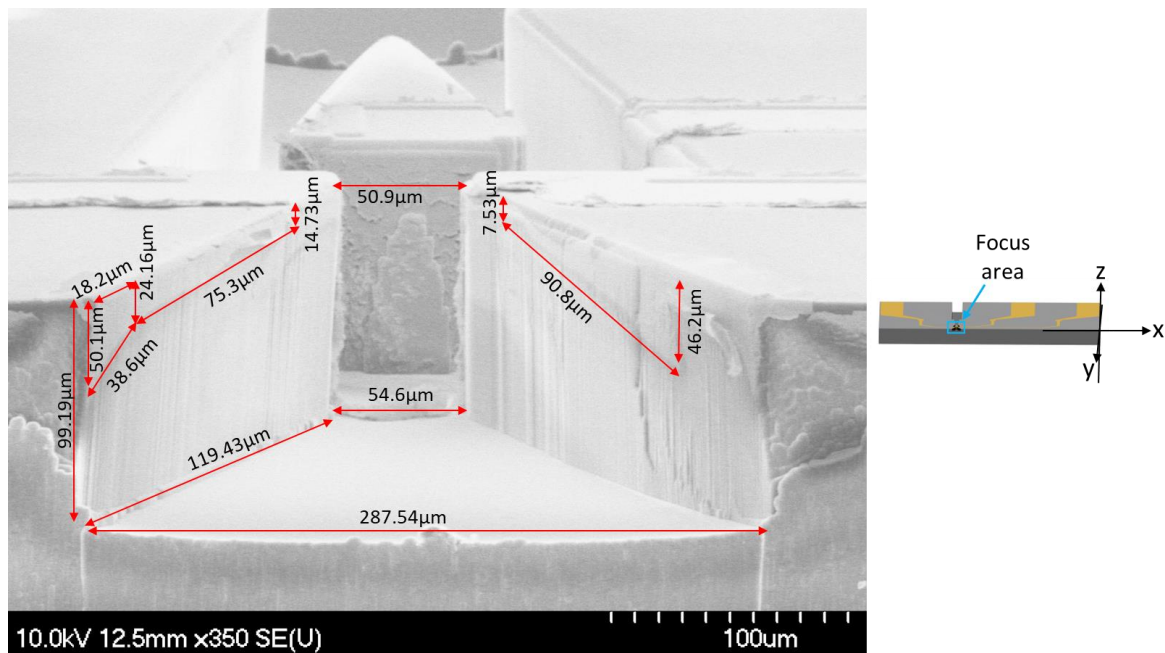


Figure 5-26. Frontal SEM image of the outlet of a medium-sized (M) micro-thruster.

Figure 5-27 shows in greater detail the micronozzle geometry after nanofabrication of the micro-thruster. The conformal metallisation on the micronozzle's wall is visible (section 5.7.1). The transition of the metal routing path from a transverse to a vertical plane (conformal) exhibits no discontinuities or cracks in any routing sections, creating the ideal structural conditions for the electrical circuit routings on the micro-thruster. The most challenging procedure was the deposition of the metal routing that runs from the upper surface down to cross the microchannel, where the conformal layer with dimensions of $83.1 \mu\text{m} \times 85.13 \mu\text{m}$ and an area of 0.007 m^2 successfully adhered to the wall. For the anode with dimensions of $85.13 \mu\text{m}$ to $78.88 \mu\text{m}$, the roughness provided by the wall finish was adopted. For the anodes, the metal face plate from the nozzle neck has dimensions of $78.21 \mu\text{m} \times 62.27 \mu\text{m}$. As a result, the metal deposition on the etched routes was increased from $8.96 \mu\text{m}$ to $17.58 \mu\text{m}$, with a 500 nm gap added for the bonding thickness of the glass cover and the micro-thruster. These metallisation anomalies were caused by UV light overexposure, where the photolithography exposure was repeated 11 times (process 38 and 39 of the traveller recipe on section 5.10) to remove the flood resist of the microchannel for conformal deposition. These anomalies have irregular shapes that surround the routing patterns that are slightly unfolded by the lift-off procedure. Still, none represent a substantial modification to the micro-thruster's design.

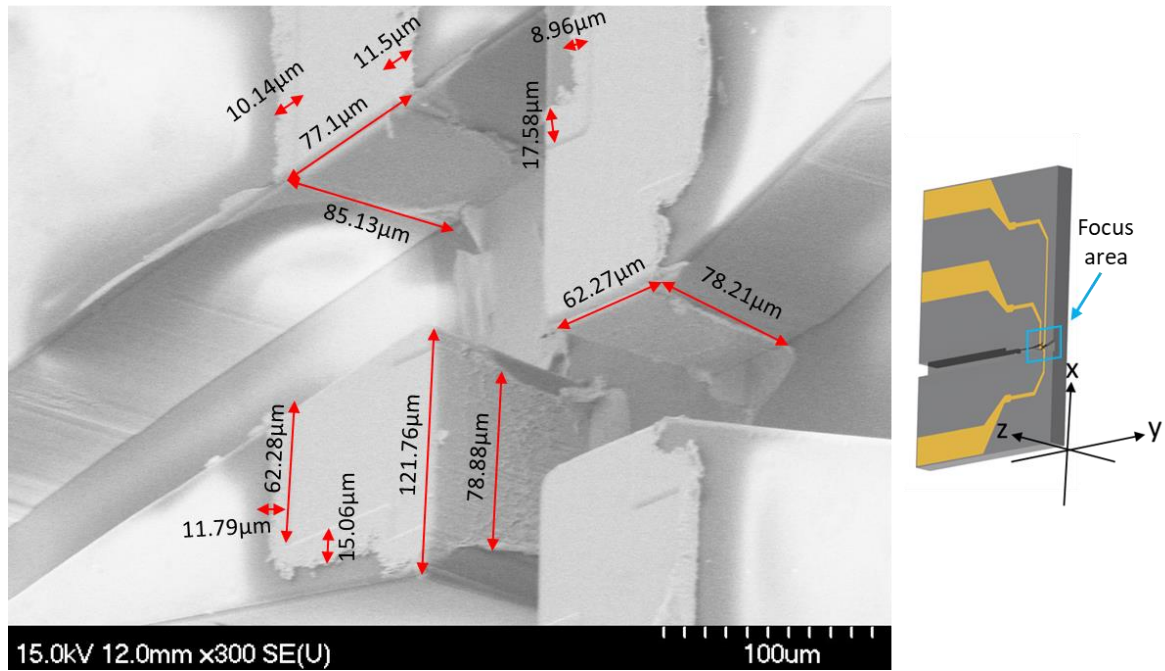


Figure 5-27. Top-lateral SEM image displaying conformal deposition of a medium-sized (M) micro-thruster.

Figure 5-28 displays the connection between microtubing and micronozzle channels through a $166.63 \times 275.3 \mu\text{m}$ plenum microchamber. The input gap of the plenum is $202.7 \mu\text{m}$ wide, and the length of the protrusion walls is $105.713 \mu\text{m}$, preventing the needle from reaching the micronozzle's walls and becoming wholly or partially obstructed. In addition, the microtubing channel width of $335.21 \mu\text{m}$ is adequate for accommodating the 30G needle with an outer diameter of $310 \mu\text{m}$.

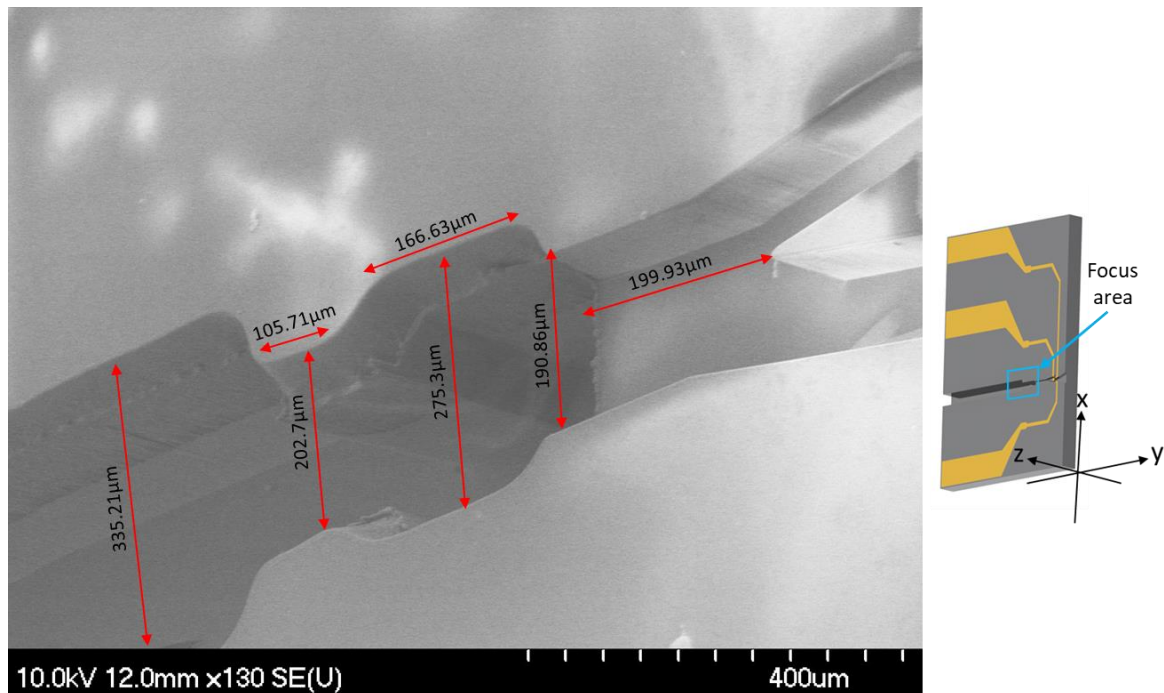


Figure 5-28. Top-lateral SEM image of the plenum microchamber of a medium-sized (M) micro-thruster.

5.12. Summary

The nanofabrication of an in-house micro-thrusters chip at James Watt Nanofabrication Centre (JWNC) was accomplished as the first time a micro-thruster device was intended to be nanofabricated at the Aeroscience department.

Sixty-three devices of various sizes were nanofabricated on a single wafer to increase the degree of tolerance by misalignments or non-uniformities caused by differential levelling (inclination) on the wafer by the holders or stages on each tool.

The implementation of three photomasks has used the photolithography process to fabricate the micro-thruster: Mask #1 for the microtubing channel, Mask #2 for the micronozzle, and Mask #3 for the electrode pattern. All photomasks have markers on each chip pattern's top left and bottom right sides. Mask #1 has 20 µm-width and 150 µm-length marks, whereas Mask #2 has 30 µm-width and 160 µm-length marks that overlap with Mask #1's markers. And Mask #3 comprises three marks, two of which must be aligned and patterned on top of their predecessors.

SPR220-7 photoresist was chosen by providing a higher thickness capability of <10 µm film. Being ideal as a protective resist mask during dry etching(section 5.4), particularly deep etching. Being able to maintain a good lift-off quality after metal deposition and capable of keeping a minimum of 1:5 thickness rate.

During the spinning of the SPR220-7, two main challenges became presented for conformal metal deposition: 1) the over increase of the resist thickness at the point the microchannels become flood adopting the thickness of the trench-depth. This increase of thickness rises 2) the bubble appearance requires an additional spin coating to cover the exposed areas and the bubbles.

Estrelas was used to dry etch on a silicon wafer. Consequently, a Bosch Deep Silicone Etching (DSIE) was run for the microtubing channel etching where it was needed a 320 μm -depth trench. Afterwards, two Si Mixed etching processes were run, one for the micronozzle pattern with a 50 μm -depth trench for 2:1, 1:1, and 1:2 aspect ratios, followed by a 0.5 μm -depth electrode pattern etching.

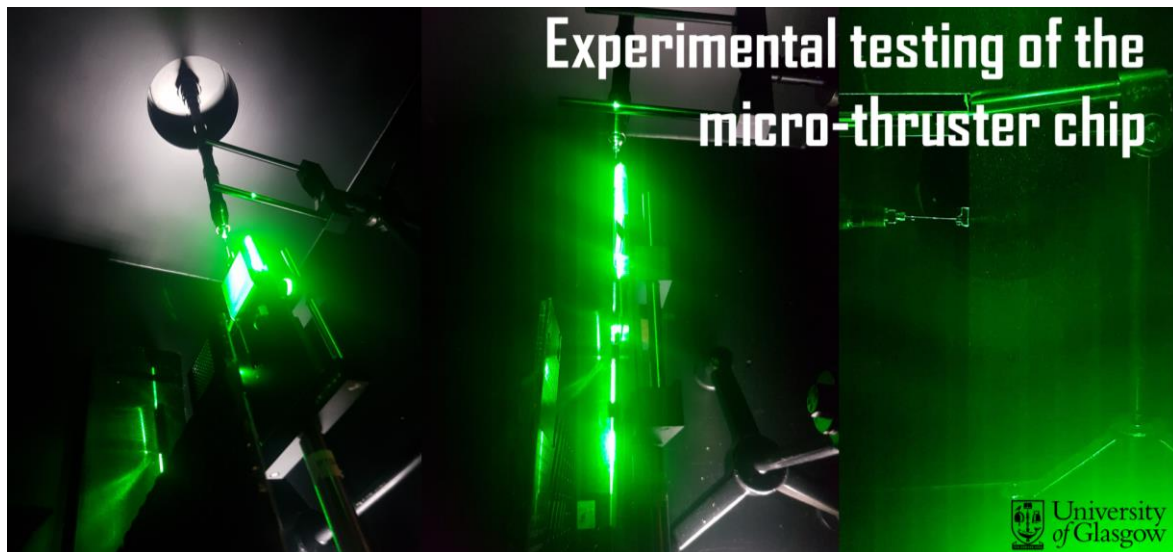
A standard SiO_2 deposition on PECVD SPTS Delta with a controlled temperature of 300°C was implemented for the 5 μm -thin SiO_2 layer on the Si wafer for the insulator layer of the micro-thruster chip.

Conformal deposition of 500 nm-thick Au(gold) through a 100 μm trench was achieved by physical vapour deposition (PVD) using SPR220-7 positive photoresist as a mask. A 30 nm-thick thin film titanium (Ti) followed by a 500 nm-thick thin film gold (Au) using a Plassys MEB550S. With a deposition rate of 0.5 nm/s and an oblique angle of $\Theta = 30^\circ$. Metallisation anomalies were discovered during the SEM image analysis, including irregular shapes that surround the electrical routing patterns that are slightly unfolded by the lift-off process and the presence of extended metal deposition out of the pattern borders by 8.96 μm to 17.58 μm , caused by the overexposure of the UV light, when the exposure for photolithography was repeated 11 times (process 38 and 39 of the traveller recipe on section 5.10) to remove the flood resist. Therefore, none of them constitutes a substantial change to the micro-thruster's design.

The difficulty of resist removal was demonstrated during lift-off due to the thin films' thorough step coverage and the resist's encasement in a metallic coating layer, which prevented contact with the developer and caused the resist to dissolve. The solution to this issue involves creating a jet using a pipette and an acetone-based solvent that can penetrate the resist and break the metallic layer.

Using a Trotec Speedy 300 laser engraver, borosilicate glass slides measuring 18 mm x 18 mm x 0.17 mm were etched to create the glass cover. As a result, the adhesive bonding agent Cyclotene 3022-57 (BCB) was selected to bond the glass cover with the Si substrate. The chip substrate was placed on the stage and heated simultaneously for 10 minutes at 200°C and 260°C, respectively, where the glass cover was assigned on the vacuum tip of the Flip Chip Bonder.

Chapter 6



This chapter will give an overview of the necessary tests for validating performance of the micro-thruster model presented in Chapters 3 and 4. Different experimental approaches and tools are recommended to characterize and test micro-thrusters. Therefore, one of the major limitations during experiments is that current equipment at Acre Road facility cannot be used to characterize or evaluate devices at microscale. In other words, particle image velocimetry (PIV) was the best option available because it would have given higher chances of visualizing jet flow emerging from micro-nozzle if current setup is modified by adding larger magnification lens together with appropriate tracer.

At University of Glasgow in Acre Road Facility, a testing rig was built to evaluate subsonic performance of micro-thruster chips. The main objective was to obtain the velocity profile of jet by varying inlet and outlet pressures on chip. For electrostatic mode of operation of micro-thruster chip HVM Technology's model nHV0512N [213] high voltage transformer was chosen. This transformer can produce up to -1.2kV with maximum output current 83 μ A giving 100 mW when supplied with input voltage between 30 mA to 60 mA loaded at 5 VDC. This specification will meet Joule Heating requirement stated in section 4.7 provided pulses below 1×10^{-6} s can be produced by pulse generator. However lack time frame and absence high voltage sources makes it impossible carry out tests on electrostatic modes, limited to perform just in the cold gas mode tests.

It is essential to ensure consistency and correct convergence of simulation results obtained using developed micro-plasma discharge algorithm described in Chapter 3 hence multiple runs were made with different initial conditions until stable solution is reached. Parameters for convergence were based on density of the species, temperature and velocity profiles among others as discussed in

chapter 3. Besides this, model outputs must be checked against analytical solutions or established theoretical predictions where possible because there are certain physical quantities which can only be calculated by means of well known formulas.

One way to verify the micro-thruster model is by Particle Image Velocimetry (PIV) as explained in section 6.1 experimentally. This approach lets us see the jet flow from the micro-nozzle and get velocity profiles at different inlet-outlet pressures. The PIV system needs to be verified with theoretical predictions and simulation results from chapters 3 and 4 based on comparisons between experimental velocity profiles.

Furthermore, specific impulse can be determined as one of the most important performance indicators for thrusters through experimental determination of propellant mass flow rate and exhaust velocity provided this last by the PIV system. These tests will validate the estimation of specific impulse from the model, thereby ensuring efficient operation within expected operation ranges according to section 4.9.

Additionally, it was necessary to perform the testing of micro-thrusters under simulated space conditions inside vacuum chamber. The outcome obtained after carrying out these examinations ought to be compared against predictions made by using given mathematical representation. By doing these extensive tests it was aimed to confirm the validity and accuracy of the micro-thruster model developed in Chapters 3 and 4. This strict process of validation shall make certain that a given model has reliability hence can be used for designing as well optimization micro-thrusters for space applications with confidence. Thus, several challenges appear during the tests of the micro-thruster chip using the PIV system that will be addressed and discussed in this chapter.

6.1. PIV system

Particle image velocimetry (PIV) is a subset of pulse-light velocimetry (PLV), a wider family of velocity measurement techniques. The PIV is comprised of three primary elements: 1) a pulsed laser light sheet, 2) tracer particles, and 3) a camera. Utilizing a laser optical measurement technique generates non-intrusive diagnostics of the instantaneous velocity field within a flow cross-section.

These methods compare the location of each tracer inside an image across time or a series of time-steps to calculate the displacements of tracers in a fluid [214]. PLV and PIV approaches differ based on the tracer's kind, size, and density; the type, duration, and number of light pulses; and the type, frame rate, and number of imaging devices.

Chapter 6. Experimental testing of the micro-thruster chip

Consequently, each technique use the first-order definition to estimate the local velocity vector \vec{u} , which is written as follows:

$$\vec{u}(x, t) \doteq \frac{\Delta x(x, t)}{\Delta t} \quad \text{Eq. 136}$$

If Δx represents the displacement of a tracer at x -position and t time, and Δt is the time between two observed states of that tracer. The pulsed laser light sheet illuminates the tracer particles with each pulse (separated by Δt) while the camera captures images to determine the tracer particles' displacement in the flow.

A customized experimental setup was assembled based on a previously mounted PIV setup by Andreou, T. [215] at Acre Road facilities. As a result, it was modified by including a vacuum chamber, modifying the position of the laser and the laser arm, changing the magnification lens, and adding a pressure regulator and monitoring system for the seeding to control the flow that passes through the microdevice.

Thus, the time-resolved stereoscopic particle image velocimetry system used was given by TSI (Figure 6-1 and Figure 6-2) is made consisting of the following components:

- Photron APX-RS High Speed camera
- Optical Arm
- Magnification lens Nikon 200mm f/4 ED-IF AF Micro-NIKKOR
- TSI 9307-6 Seed Particle Generator
- TSI 610035 Laser Pulse Synchronizer
- Litron LDY301 High repetition rate laser
- Computer
- INSIGHT 4G Software
- μm -scale PIV calibration plates

A description of each component is provided below:

Chapter 6. Experimental testing of the micro-thruster chip

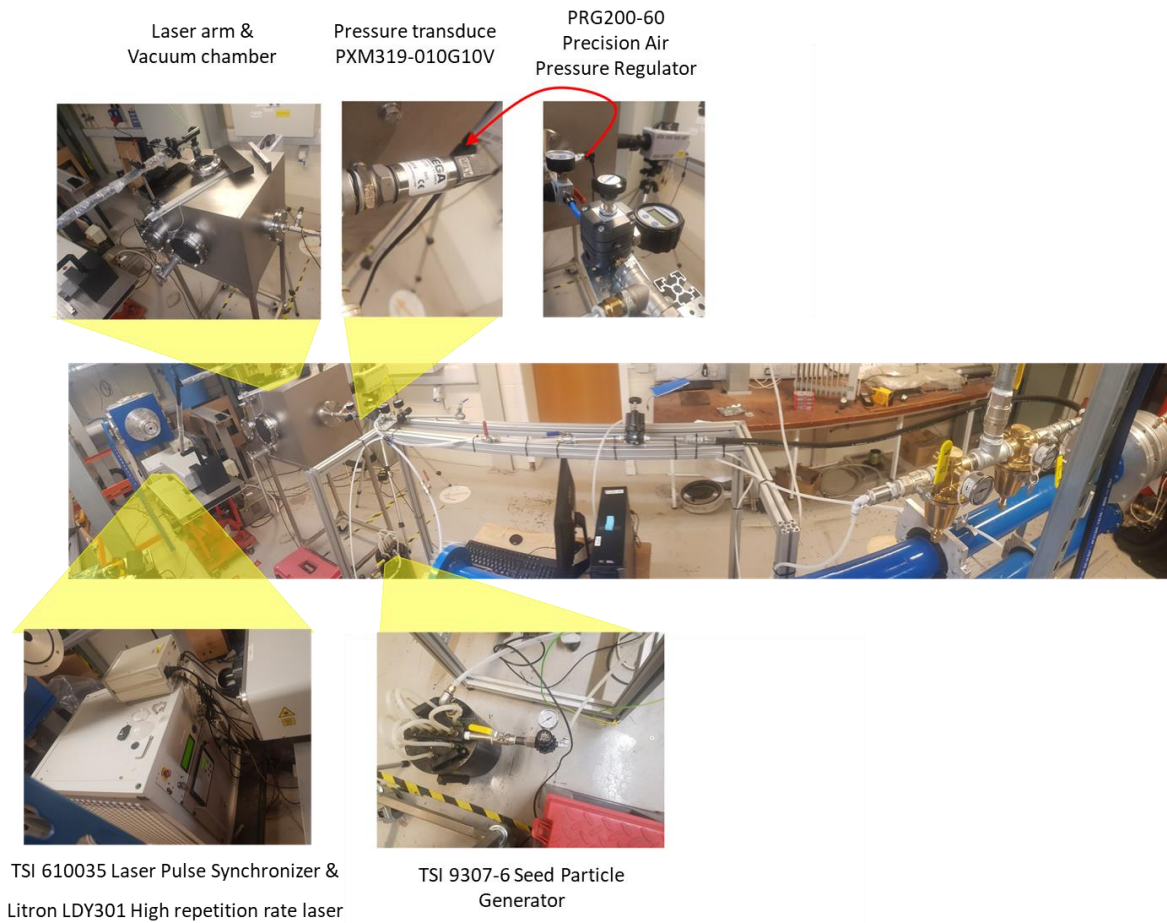


Figure 6-1. Lateral perspective of the experimental PIV setup.

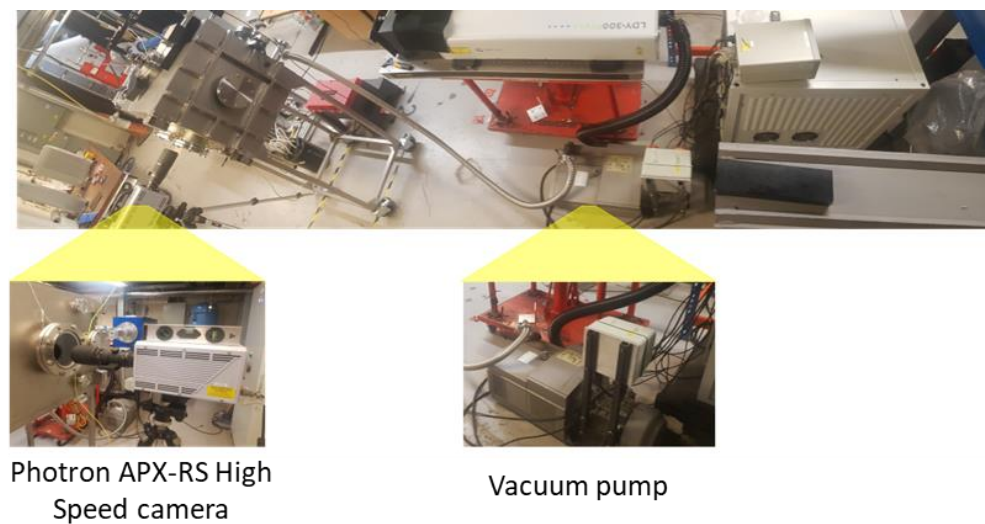


Figure 6-2. Frontal perspective of the experimental PIV setup.

6.2. Hardware

6.2.1. Pneumatic setup

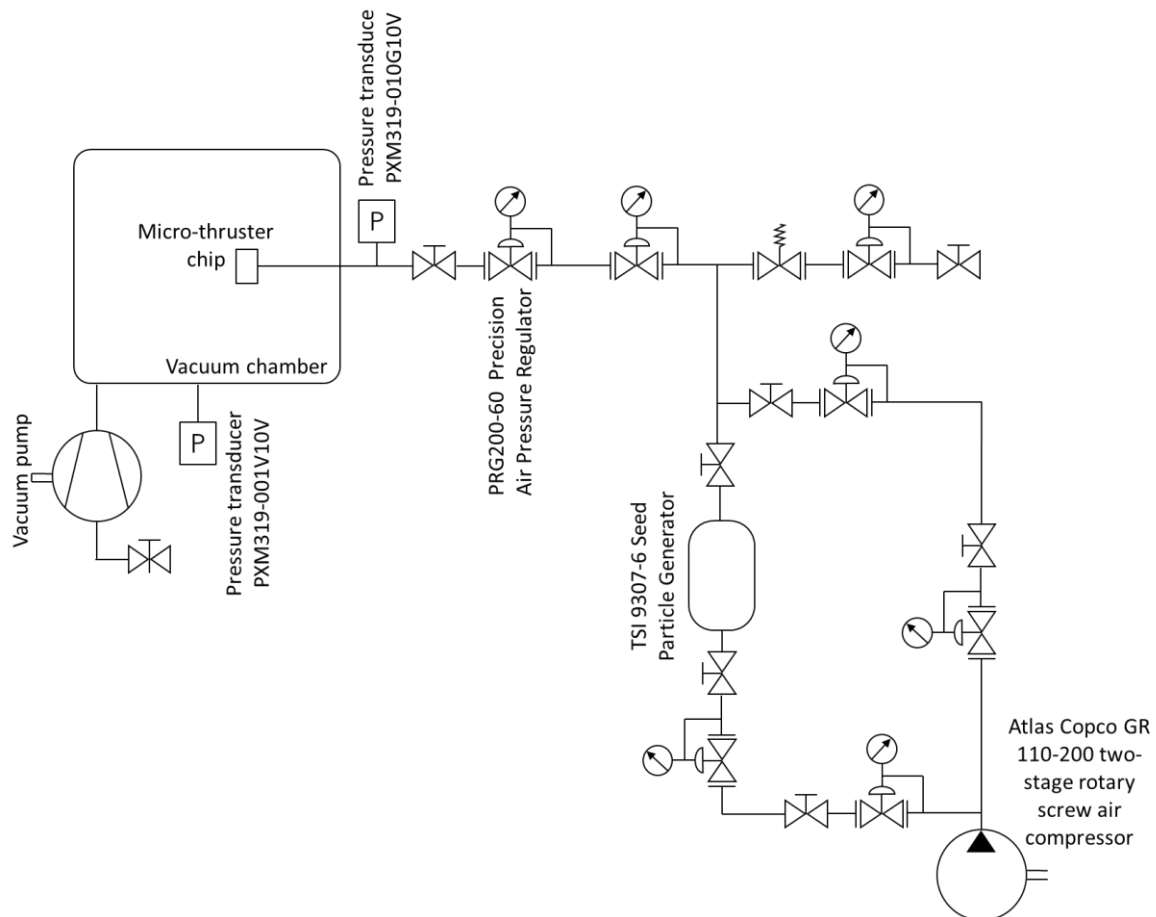


Figure 6-3. Pneumatic schematic of the micro-thruster chip testing PIV experimental setup.

A stainless steel vacuum chamber with 12mm-thick walls, a cross-sectional area of 0.22m^2 , and an internal volume of 0.131m^3 was used at the Acre Road facilities to provide a dark setting for better PIV visualisation, but more importantly, to provide a vacuum environment for experiments and an enclosed area to minimise laser beam reflection outside the chamber. On its apertures, stainless steel flanges ranging in thickness from 12 to 16 millimeters were mounted; 16mm-thick large windows with model ISO160 and 12mm-thick medium flanges without windows with model ISO100.

A flange-mounted pressure transducer - PXM319-001V10V was used to measure the pressure within the vacuum chamber. A TSI 9307-6 Seed Particle Generator coupled to an Atlas Copco GR 110-200 two-stage rotary screw air compressor supplied the micro-thruster with compressed air containing

Chapter 6. Experimental testing of the micro-thruster chip

atomized olive oil particles. The microtubing(30G needle) micro-thrusters were linked to the pneumatic setup through a Male Luer Metal to 1/8-27" Fitting TSD931-54B attached to 1/8" stainless steel pipe that was coupled to the interior face of the drilled ISO160 flange in order to be positioned inside the vacuum chamber.

A 316 stainless steel Tee 1/4" fitting was installed on the exterior of the chamber to link a pressure transduce PXM319-010G10V to monitor the inlet pressure over the micro-thruster chip, as well as to connect a safety shut-off valve to an S PRO Pneumatic Regulator 600 NI/min. Then, a PRG200-60 Precision Air Pressure Regulator and a DPG108-3.0KG digital gauge, both from OMEGA Engineering Inc., are installed to regulate and read the flow pressure that comes straight from a stainless steel Tee 1/4 "connection to the TSI 9307-6 Seed Particle Generator. A Norgren G 1/4 Pneumatic Regulator was installed on the opposite end of the Tee. Initially, the relief valve was intended to prevent condensation of atomized seeding particles due to the small volume and high pressure inside the Tee, necessitating the release of the mixed flow to keep the oil particles atomized.

Atomisation of seeding particles presented a challenge at the beginning, where the TSI 9307-6 atomised mixture becomes condensed by the decrease in volume on the fittings and piping, capturing bigger seeding particles through the camera where the velocity profile can be modified by the increase in density of the air/seeding mixing. Two methods were tried at the beginning shown on Figure 6-4; 1) add a controlled relief valve, being open when the system is turned on to avoid condensation and not over increase the pressure and seeding particle density on the tee junction. Unfortunately, no improvement in the atomisation of the seeding during the ejection from the micro-thruster was presented by keeping open the relief valve. Additionally, keeping the relief valve open can be a risk of the possibility of activating the fire alarms. 2)The second method consists of adding a junction connected before the tee to mix the seeding coming out from the TSI 9307-6 and an air source(compressor) to control the mix proportion of air and seeding. This option caused the decrease in seeding density mixed with the air, making it challenging to visualise particles through the high-speed camera. When the mixing density reached the point able to be visualised by the camera, no improvement in the atomisation was presented.

Therefore, increasing the pressure on the TSI 9307-6 will cause more seeding particles to be ejected from the micro-thruster chip, which will increase the amount of oil spilt and leak from the pressure regulator valves. Consequently, methods 1 and 2 for particle atomisation were discarded due to a lack of improvement in the mixing. No differences were displayed between using the direct connection to the seeding generator, the air compressor, and the relief valve.

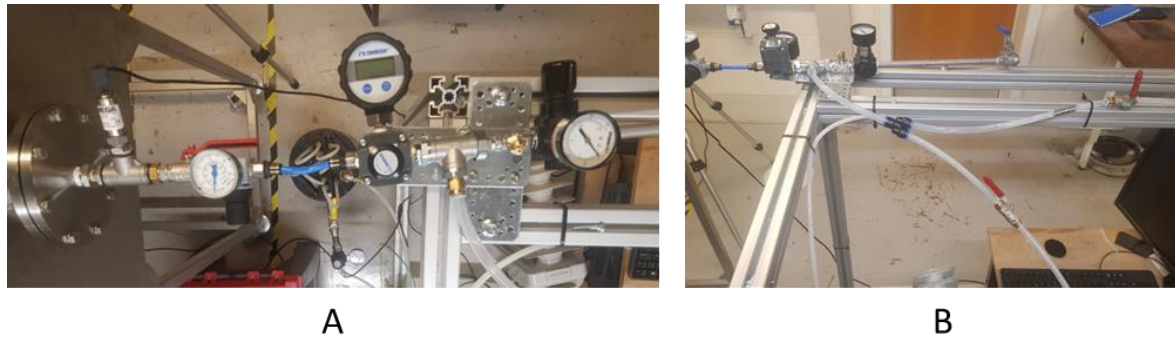


Figure 6-4. Potential setup methods to improve atomisation of particles; A) Method 1-controlled relief valve, B) Method 2-mixing with additional air connection.

6.2.2. Laser

A Litron LDY301 High repetition ND: YLF rate laser with a 527nm wavelength and 20mJ per cavity was utilised as a laser source. An optical arm was placed from Litron's shutter to the chamber's ISO160 window flange to bring the laser beam inside the chamber and produce a light sheet to illuminate the micro-jet. A series of mirrors within the arm directs the laser beam through the end of the pipe, where a diverging lens spreads the beam into a thin sheet.

The interval between laser pulses, also known as the pulse separation time Δt , is a variable that must be modified based on the experimental flow circumstances. The correct value of Δt must be short enough to capture the fastest-moving particles but long enough to ensure that a sufficient number of particles are present within the interrogation window. It varied for each of the examined plane configurations and the employed lenses. Initial estimates of Δt were derived using empirical formulas based on various parameters, including peak velocity and field of view (FoV) size. It is assumed that the particle displacement is a quarter of the targeted interrogation window (section 6.3.1), where Δt is specified as follows:

$$\Delta t = \frac{\Delta_x}{M * U_{peak}} \quad \text{Eq. 137}$$

Where Δ_x is the pixel displacement distance, U_{peak} is the maximum velocity of the particles, and M is the magnification factor in pixels/mm given by:

$$M = \frac{x_{A-B}}{\Delta d} \quad \text{Eq. 138}$$

Being x_{A-B} the number of pixel between point A and B, and Δd the distance between pixels.

In addition, the out-of-plane motion of the particles must be less than one-fourth the thickness of the laser sheet, and these values were modified further throughout the experiment to produce better outcomes.

6.2.3. Tracer

Tracers are one of the primary components of the PIV system, where particle dynamics play a significant role in measuring particle motion to obtain velocity vectors. Tracer selection is crucial for a successful implementation of the PIV system, where specific considerations must be taken into account, such as the non-intrusiveness of the tracer so as not to impact the flow dynamics, where particles accurately follow the flow without interacting with one another.

In order to select an appropriate tracer, it is necessary to measure the flow tracing capability by computing the particle relaxation time τ_p , which is determined by the equation:

$$\tau_p = \frac{d_p^2 \rho_p}{18 \mu_f} \quad \text{Eq. 139}$$

Where d_p is the particle diameter, ρ_p is the particle density, and μ_f is the fluid's viscosity.

Once τ_p is specified, in order to evaluate the tracer's ability to track the flow accurately, the Stokes number St must be calculated by:

$$St = \frac{\tau_p}{\tau_f} \quad \text{Eq. 140}$$

If $St < 1$, indicates that the particles will perfectly follow the flow. Therefore, to obtain the characteristic timescale of the flow, it is described as follows:

$$\tau_f = \frac{d_h}{U_m} \quad \text{Eq. 141}$$

Where U_m is the mean velocity, and d_h is the diameter of the outlet orifice.

Olive oil particles of 0.9 μm – 1 μm diameter with $\rho_p \approx 912 \text{kgm}^{-3}$ at 6-35 $^\circ\text{C}$ were used as tracer particles in the experimental PIV setup for two reasons: the TSI 9307-6 Seed Particle Generator was available at Acre Rd, and the viscosity of the olive oil particles allows them to slide smoothly on the micro-channel walls, reducing the possibility of friction on the surface or becoming stuck, which could cause obstructions during the test. The Stokes number St of olive oil is 1.73×10^{-3} , which is much less than 1, indicating that the atomized oil particles may properly follow the flow at the calculation:

Table 27. Olive oil tracing parameters

d_p	ρ_p	μ_f	τ_p	d_h	U_m	τ_f	St
1.00E-06	912	0.084	6.03E-10	3.09E-05	90	3.43E-07	1.76E-03

6.2.4. Cameras and Lenses

In order to capture the displacement of the tracers on flow, a Photron APX-RS digital high-speed camera placed on a tripod with a maximum resolution of 1024 x 1024 pixels at 3000fps was utilised. A magnification lens was required to catch the micro-jet and determine its velocity profile due to the micrometre scale size of the outputs on the micro-thrusters. The chosen lens was the Nikon 200mm f/4 ED-IF AF Micro-NIKKOR since an increase in the camera's magnification, but at the same time, provides a detrimental effect on the field of view (FoV).

6.2.5. Calibration plate

In order to calibrate the 2D PIV, a calibration plate is necessary. Consequently, the current plate has a dual-sided, dual-plane dimension of 200 mm x 200 mm with a 10 mm space between each calibration point. For the micro-thruster PIV characterization, the distance between the points prevents using the present calibration plate. Therefore, the Nikon 200mm magnification lens was employed, reducing the FoV to a maximum distance of 20mm to catch the tracer exiting the outlet. Hence, the distance points must be much shorter than the FoV to identify the camera's alignment and calibration.

In order to adapt and expand the possibilities of the existing TSI system, 48mm x 30mm x 2mm micro-scale PIV calibration plates and their holders were developed (Figure 6-5). This upgrade was made in conjunction with T. Andreou [215]. The Trotec fast 300 fibre laser cutter was used to manufacture the plates with a 2mm gap between points and a 0.1mm diameter from a 2mm-thick sheet of acrylic.

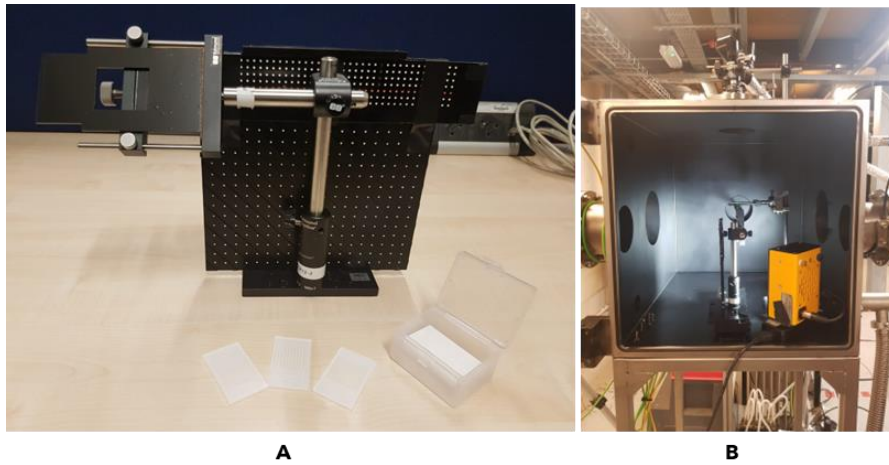


Figure 6-5. Micro-scale PIV calibration instrument; A) Calibration Kit - holder with calibration plates box. B) Calibration system installed inside the vacuum chamber.

For the PIV arrangement, the calibration sheet must be parallel to the laser sheet and perpendicular to the camera lens focus. The camera position was then calibrated using the INSIGHT 4G software by matching the dots on the calibration plate with the X and Y directions of the program's grid (Figure 6-6).

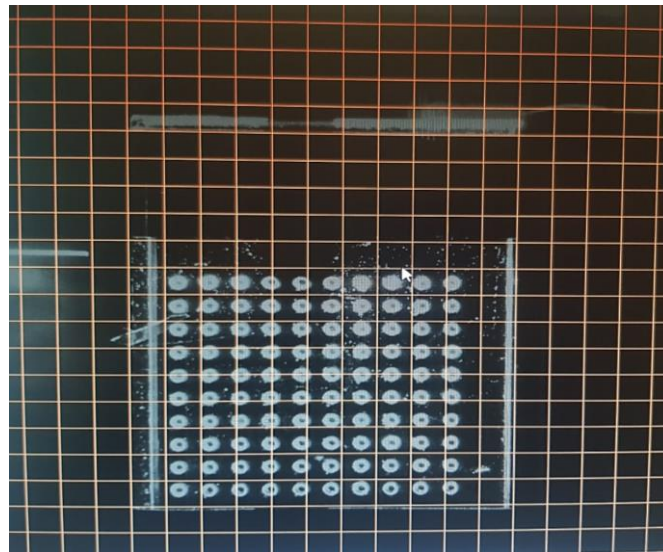


Figure 6-6. Image from the desktop screen of the calibration of the camera on INSIGHT 4G software. The camera focuses on the micro-scale PIV calibration plate; the camera focus will be moved until the virtual grids from the software are aligned with the dots on the calibration plate for a correct alignment.

6.3. Software - measurement settings

6.3.1. Interrogation window

Typically, the following parameters can be adjusted to optimise the measurement: laser pulse interval (dt), image shifting, magnification, light sheet dimensions, seed particle, seed concentration, and interrogation spot size. The last one, the interrogation window, refers to partitioning a picture into pairs of smaller windows. This iterative technique aims to divide the picture into smaller regions to follow the uniform motion of particles throughout the computation of their displacement. In consideration of these criteria, the following rules were developed:

- The size of the interrogation spot must be small enough such that a single vector can represent the flow within the spot.
- Each interrogation area should have more than ten particle image pairs.
- The maximum in-plane movement must be less than a quarter of the size of the interrogation point.
- The minimum in-plane displacement should be twice the diameter of the particle picture.
- The exposure must be sufficient to display the particles.

In order to determine which interrogation window size adheres to the regulations and best characterises the jet, the PIV data result at various interrogation windows were post-processed, as seen in the Figure 6-7:

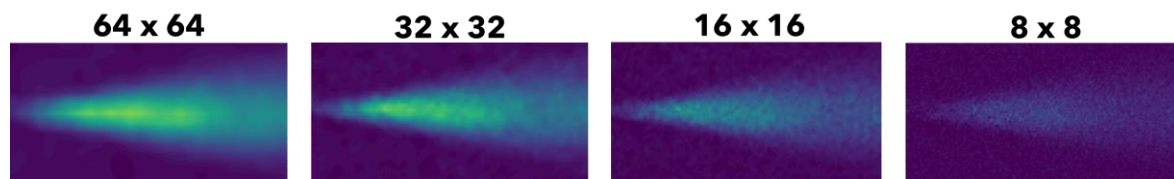


Figure 6-7. Visualisation of the velocity profile of a micro-thruster jet at various interrogation window sizes: 64 x 64, 32 x 32, 16 x 16, and 8 x 8.

The jet was created by averaging 100 continuous PIV captures at 250Hz with an interframe duration of $\Delta t = 6 \mu s$ and input and output pressures of 4 and 0.9 bar, respectively. Thus, post-processed PIV findings reveal a decrease in particle visibility as the interrogation window size increases, where 64 X 64 is too large to capture the particles' motion accurately, resulting in a hazy jet picture. In contrast, by reducing the interrogation window to 8 x 8, it was possible to capture the particles in fine detail, although at the expense of the visibility of the jet's velocity profile due to the reduced particle density

within the window. Therefore, there were two possibilities for selecting the size of the interrogation window: 16×16 or 32×32 . The 16×16 sizes were selected as the optimal option for providing a detailed visualisation of the particle along with sufficient particle density inside a window to reconstruct the velocity profile of the jet.

6.3.2. Inter-frame time Δt

The inter-frame time Δt is the time between captures (frame A and frame B) captured by a high-speed camera; hence, the duration is constrained by the equipment. The present PIV system utilises a Photron APX-RS High-Speed camera, for which the lowest Δt reported by the manufacturer, TSI, is $4 \mu\text{s}$. Infrequently, throughout the experiment, any Δt value less than $6 \mu\text{s}$ caused problems with the capture of frame A, but if it was set to $6 \mu\text{s}$, both frames could be captured. According to Eq. 137, the greater the particle's velocity, the shorter Δt must be to capture the particle motion on frame A and the displacement on frame B before the particle leaves the FoV.

Various Δt were applied to the micro-jet thruster as a test in order to determine the influence on the particle's visualisation. Following, on Figure 6-8 are the results of interframe time settings of 6 , 20 , 40 , and $80 \mu\text{s}$:

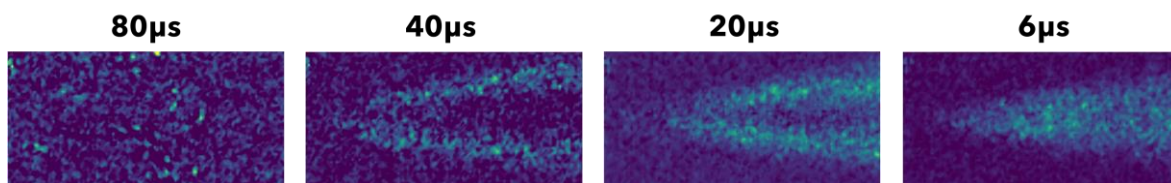


Figure 6-8. Visualisation of the velocity profile of a micro-thruster jet at various inter-frame times Δt .

At greater values of Δt , the captured PIV picture of the jet demonstrates a decomposition, according to the test results. Where increasing the delay between frames prevents the capture of particles with higher velocities, avoiding the capture of the core at $20 \mu\text{s}$ and $40 \mu\text{s}$ because the particles have moved out of the field of view (FoV) by the time frame B is captured—providing only a description of the jet's shear layer. For Δt values greater than $80 \mu\text{s}$, it was not feasible to visualise the jet in which all particles left the FoV before the second capture. This test determined that for the PIV test on a micro-thruster, the lowest possible Δt is required to characterise the microdevice's complete jet.

6.4. PIV experimental results

PIV jet results were obtained using L50E3 geometry (Section 4.8.3) by applying inlet pressures of 2, 4, 6, 8, 10, and 12 bar in vacuum chamber settings of 0.3, 0.5, and 0.7 bar. The velocity profile mapping is displayed in Figure 6-10. In all cases, the shape of the jet is discernible, and the molecular interactions grow more pronounced when the pressure of the surrounding environment decreases due to the jet's expansion and the rise in the density of the particles surrounding it.

This research used a Particle Image Velocimetry (PIV) system which has limitations in determining the velocity of the jet accurately. This is because it cannot capture particles with high accelerations within its narrow field of view (FoV). A Photron APX-RS high-speed camera is employed in this study, but it struggles to handle particles moving beyond its maximum capture velocity.

Particularly, with its narrow FoV of 23.71 mm and the lowest interframe time of 6 μ s, the PIV system can record maximum velocities of 1.966, 1.222, 0.939 and 0.659 m/s at outlet pressures of 0.9, 0.7, 0.5 and 0.3 bar respectively (minimum velocities). These velocities do not represent the entire velocity profile of the jet but rather indicate minimum velocity that can be detected under such conditions by this system.

However, there is a problem since higher accelerating particles escape the FoV before being caught between frames A and B by the camera hence this limitation. In other words while providing some data, it does not measure accurately full velocity profile especially at higher speeds where they leave too fast to be tracked as they fall outside FoV.

6.4.1. The field of view (FoV)

The field of view (FoV) produced by the Nikon 200mm f/4 ED-IF AF Micro-NIKKOR was 23.71 mm x 23.71 mm. Distances on the x and y axes were normalised by the length of the nozzle's exit $D = 302.5\mu\text{m}$. In contrast, the velocity profile was normalised by taking the highest velocity obtained in all cases $v_{max} = 1.966$ m/s, being taken as 2 m/s.

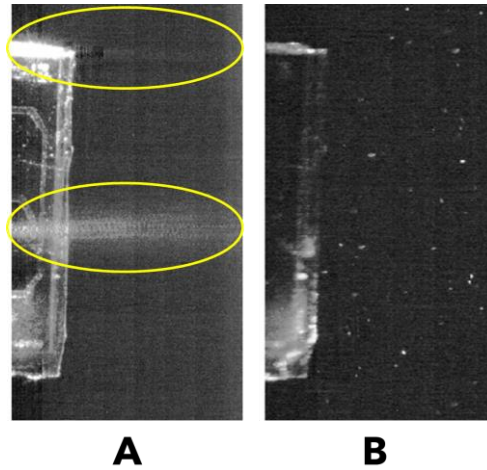


Figure 6-9. Effects of laser sheet proximity to the microdevice on image capture; A) Defects on an image by the appearance of bright spots (circled in yellow) when the laser sheet is 100 μm closer to the device. B) A laser sheet of approximately 302.5 μm yields a high-quality picture.

The jets lengths are displayed up to 19.665 mm from a distance of 790 μm from the nozzle's outlet, given by the separation of the laser sheet from the device in order to avoid laser reflection from the micro-thruster surface, which generates bright regions that prevent the visualisation of the ejected seeding particles (Figure 6-9).

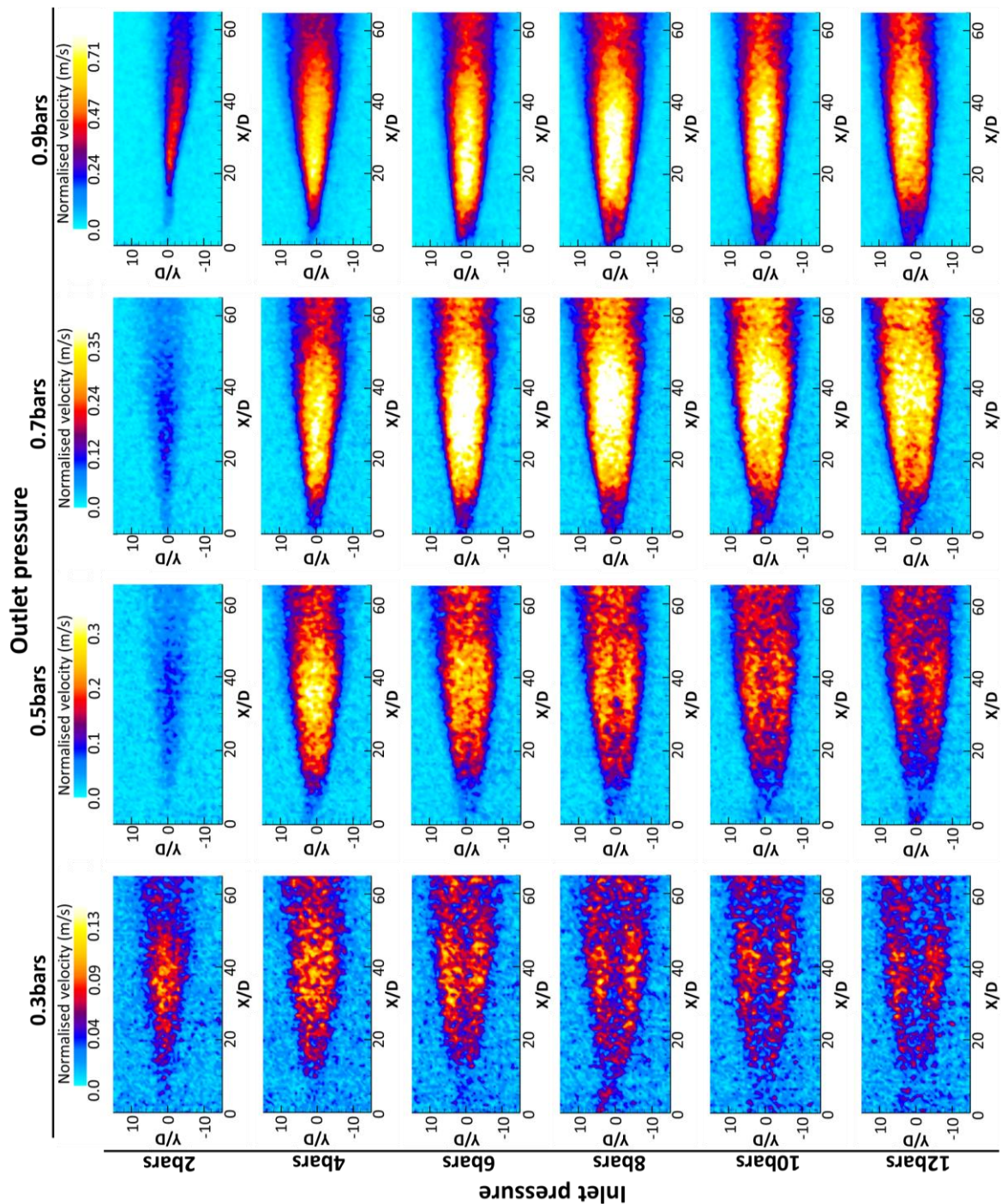


Figure 6-10. PIV results of the velocity profiles of the jet on the L50E3 micro-thruster chip by supplying an inlet pressure of 2, 4, 6, 8, 10, and 12 bar at outlet pressures of 0.3, 0.5, 0.7, and 0.9 bar.

For the L50E3 micro-thruster, the maximum velocities for each case were determined based on the jet results shown in Figure 6-10 (jet results) to identify the differences in velocity behaviour according to the inlet and outlet pressures. Following shown is a diagram of maximum velocities:

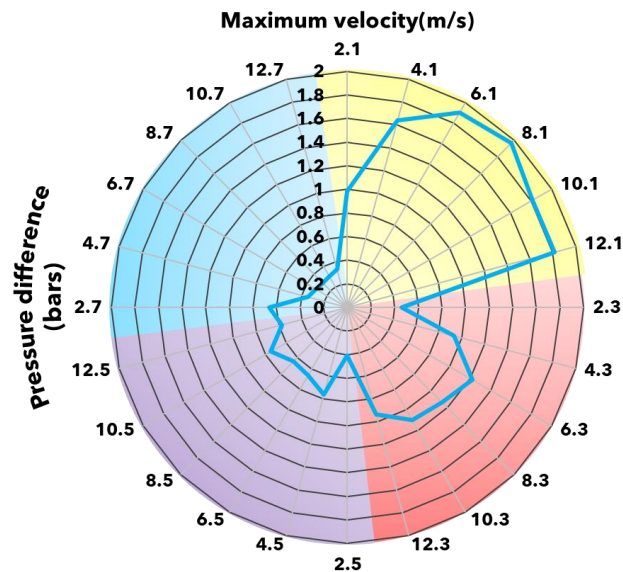


Figure 6-11. Polar diagram illustrating the maximum velocity of a jet with the differential pressure between the intake and outflow.

A polar plot, shown in Figure 6-11, is used to represent the performance of a micro-thruster as cold-gas thruster under different combinations of inlet and outlet pressures. The radial axis represents velocity which ranges from 0 to 2 m/s while the angular axis represents inlet pressure from 2 to 12 bar. Each quadrant is colour coded according to different outlet pressure conditions for easy understanding of how these variables affect its performance.

In Quadrant I (Yellow), the micro-thruster operates at an outlet pressure of 0.3 bar. This creates large gas expansion due to high differential pressure across nozzle especially at high inlet pressures resulting into higher jet velocities. This is best for maximum thrust thus suited for applications needing high propulsive efficiency in vacuum or near-vacuum environments. With increasing values of inlet pressure also increases the value of jet velocity but only till it gets aerodynamically limited.

Quadrant II (Red) has an outlet pressure equalling 0.5 bar, where slight reduction in differential pressure causes reduction in velocity though still causing it to increase because of gas expansion too. This quadrant achieves moderate velocities implying a trade-off between thrust and operational stability; hence if slightly lower thrust is allowed but stable operation desired then this will be the ideal area. The data shows that significant jet velocity remains available therefore indicating good capability by micro-thruster under such operating conditions.

Quadrant III (Purple) represents an outlet pressure equal to 0.7 bar whereby further decrease in differential leads to lesser jet speeds than what was observed within quadrants I & II. This means that potential energy is merely partly converted into kinetic power due to limited gas spreading as seen from performance metrics. Therefore it can find relevance when we require medium levels of

Chapter 6. Experimental testing of the micro-thruster chip

propulsion force with controlled or accurate movements required during operation. Performance suggests that while there are reduced velocities, control and stability are still maintained by thruster.

Quadrant IV (Blue) indicates conditions with outlet pressure being 0.9 bar which is the lowest differential among all other quadrants hence giving rise to very low jet velocity since only a small portion of gas expands. This situation may be used in applications that require fine adjustment and precision where high thrusts are not necessary but control and stability become key factors. The information shows that at such moments when micro thrusters are required to operate under these conditions they achieve lower velocities thereby signifying their involvement in tasks demanding more of precise force than strong push.

Velocities in Figure 6-11 show an increase in velocity when the inlet pressure rises to 8 bar at 0.9bar of outlet pressure, displaying an increase from 0.986 m/s to a maximum velocity of 1.967 m/s. Afterwards, pressure drops to 1.8m/s for 10 and 12 bar of inlet pressure. By decreasing the outlet pressure, PIV results show a decrease in the jet profile, where the velocity tends to increase by supplying a higher inlet pressure. For an outlet pressure of 0.7 bar, the velocity increased from 0.458m/s at 2 bars to 1.222 m/s for 6 bars, then dropped to 1.134, 1.1, and 0.939 m/s for 8, 10, and 12 bars of inlet pressure, respectively. For 0.5 bar outlet pressure, lower velocities values of 0.406 m/s and 0.576 m/s were displayed for 2 and 12 bars. Thus, highest velocities of 0.767 m/s and 0.749 m/s were presented on inlet pressures of 4 and 10 bar. By decreasing the pressure of the chamber to 0.3 bars, the jet velocity profile showed a drop in the values from 0.659 m/s to 0.337 m/s when the inlet pressure increased from 2 bar to 12 bar. Therefore, differential pressures will result into higher velocities of jet as well as thrusts, however this relationship is not linear and it is affected by flow chokes and particle interactions among other things. Such observations are important since they help in creating efficient propulsion systems especially for aerospace applications where accurate manipulation plus highest possible efficiency are very necessary. It is through appreciating what happens at different pressure levels that one can be able to come up with mission specific micro-thrusters which would work effectively under various operational environments while still guaranteeing success and reliability alike.

In general, for all cases in Figure 6-10, it was expected an increase in the jet velocity when the inlet pressure increased, and the outlet pressure decreased according to the exhaust velocity equation:

$$c_e = u_e + \frac{A_e}{\dot{m}}(p_e - p_a) \quad \text{Eq. 142}$$

The PIV data demonstrates this predicted behaviour with an input pressure of 0.9 bar. Contrary to outlet pressures of 0.70 bar, 0.50 bar, and 0.30 bar. The jet velocity decreases due to an increase in inlet pressure and a decrease in outlet pressure. The constraints of the PIV system dictate this behaviour. The current PIV system is appropriate for situations requiring less magnification. In the situations of 0.7, 0.5, and 0.3 bar, if the mixed seeding particles exhaust speed up, they will escape the field of vision without being captured when the magnification increases. The more significant the decrease in outlet pressure, the greater the acceleration of the ejected seeding particles will be, by reducing the probability of interaction, such as collision, with air particles inside the vacuum chamber, where the seeding particles' energy is lost due to the energy transfer. Due to the small length of the FoV of 23.71 mm and approaching the fundamental constraint of the lowest interframe time of 6 μ s from the Photron APX-RS high-speed camera, particles with maximum velocities of 1.966, 1.222, 0.939, and 0.659 m/s at outlet pressures of 0.9, 0.7, 0.5, and 0.3 bar could be captured. Where these results do not represent the entire velocity profile of the jet, the Insight 4G software identifies the motion of a particle and computes its velocity vectors by displaying only particles with enough acceleration that the camera was able to capture, where particles did not leave the field of view before frames A and B was captured.

6.4.2. Challenges in PIV for micro-thruster jet characterisation

The challenges in using PIV for the characterization of the micro-thruster jet can be classified into three main factors, as follows:

1) Density of Flow Measurement: The main challenge faced when applying PIV in determining flow density comes with having an appropriate tracer particle density. Few particles yield insufficient data while many result in overlapping making it difficult to distinguish individual particle motions. Further accuracy may also be affected by variations in the density of particles used for measuring velocity.

2) Determining Flow Coverage: The limitation within this field lies in determining how far does flow extend due to narrow FoV. Any particle that goes beyond this view is not recorded and hence system inability to capture whole flow field. This problem is worse at higher velocities where particles exit visible region very fast thereby giving incomplete information about expansion and behaviour of jets.

3) Constraints between Interframe Times: It is necessary to handle carefully interframe time (Δt) so as to trap particles moving at high speeds. If Δt takes too long, second frame will be taken after fast-moving ones have left FoV hence leading to loss of data. On the other hand, short Δt may fail to give enough displacement needed for accurate measurement of velocity.

PIV cannot determine speed fully because the system fails to capture high-speed particles but it shows how they spread outwards from one point. These limitations could be addressed through various modifications including; increased camera resolution, faster rates of capturing and managing tracer particles better amongst others according to future endeavors made towards advancing PIV technology must overcome these shortcomings in order enhance precision as well coverage during jet flows description.

6.4.3. Jet characterisation

The reason why velocity values of jets are not accurate is because the equipment used to measure these jets at micrometre level has some natural restrictions. These errors are caused by the incapability of the system to capture fast moving particles in a small area it can see. In order to get precise profile of a jet, it is necessary that the camera being utilized should have high speed and be able to achieve shorter inter-frame time ranges.

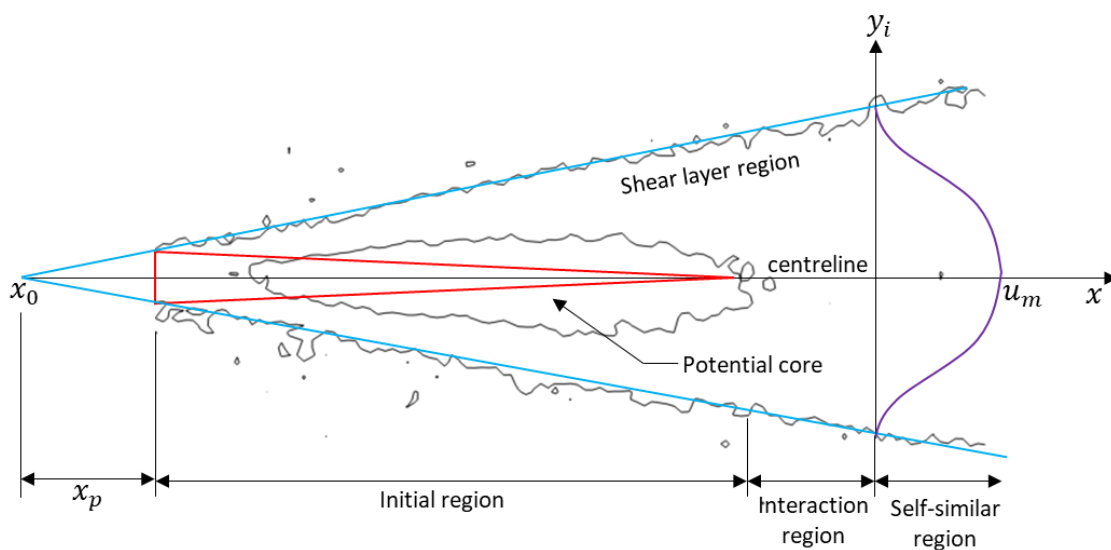


Figure 6-12. Schematic of the structure of the jet flows exhaust from the micro-nozzle thruster's outlet.

Consequently, PIV jet data can provide information regarding the shape and expansion of the jet when the angle can be characterised. Before estimating the angle α , the virtual origin must be calculated. The virtual origin x_0 is the location along the x-axis where the jet appears to begin when the line joining the half-widths is stretched backwards. The jet half-width is defined as the distance between the jet's centreline and the transverse plane at which the jet's mean velocity becomes half of the centreline velocity [216]. Generally, half-width grows linearly with x , excluding regions of axis flipping.

Thus, the distance between the diffuser outlet and the virtual origin is as it is shown in the Figure 6-12, where the angle α is measured with respect to the line connecting the half-width and the x-axis [217].

Thus, the virtual origin x_0 can be obtained from the relation [218]:

$$\frac{u_e}{u_m} = K_u \left(\frac{x - x_0}{D} \right) \quad \text{Eq. 143}$$

Solving for x_0 follows,

$$x_0 = -\frac{u_e D}{u_m K_u} + x \quad \text{Eq. 144}$$

Where u_e is the exit velocity and u_m is the maximum velocity profile, D is the length of the nozzle outlet, x is the position on the x-axis from the centreline, and K_u is the jet spread rate.

The jet spread rate K_u is the slope of the half-width line in the axial direction. In order to calculate K_u , it can be approximated by [219],

$$K_u = \frac{x\sqrt{\pi}}{2y_i} \quad \text{Eq. 145}$$

Being x a position of the jet at x-axis and y_i is the jet half-width being the line in the axial direction from the centerline velocity on the bell-shaped velocity.

i. Jet half-width

In order to obtain the jet half-width y_i from the PIV experimental results, it was extracted the velocity profiles on the y-axis from the jet centreline from the normalised length distance when $\frac{x}{D} = 20, 40,$ and 60, as it is shown in the following Figure 6-13:

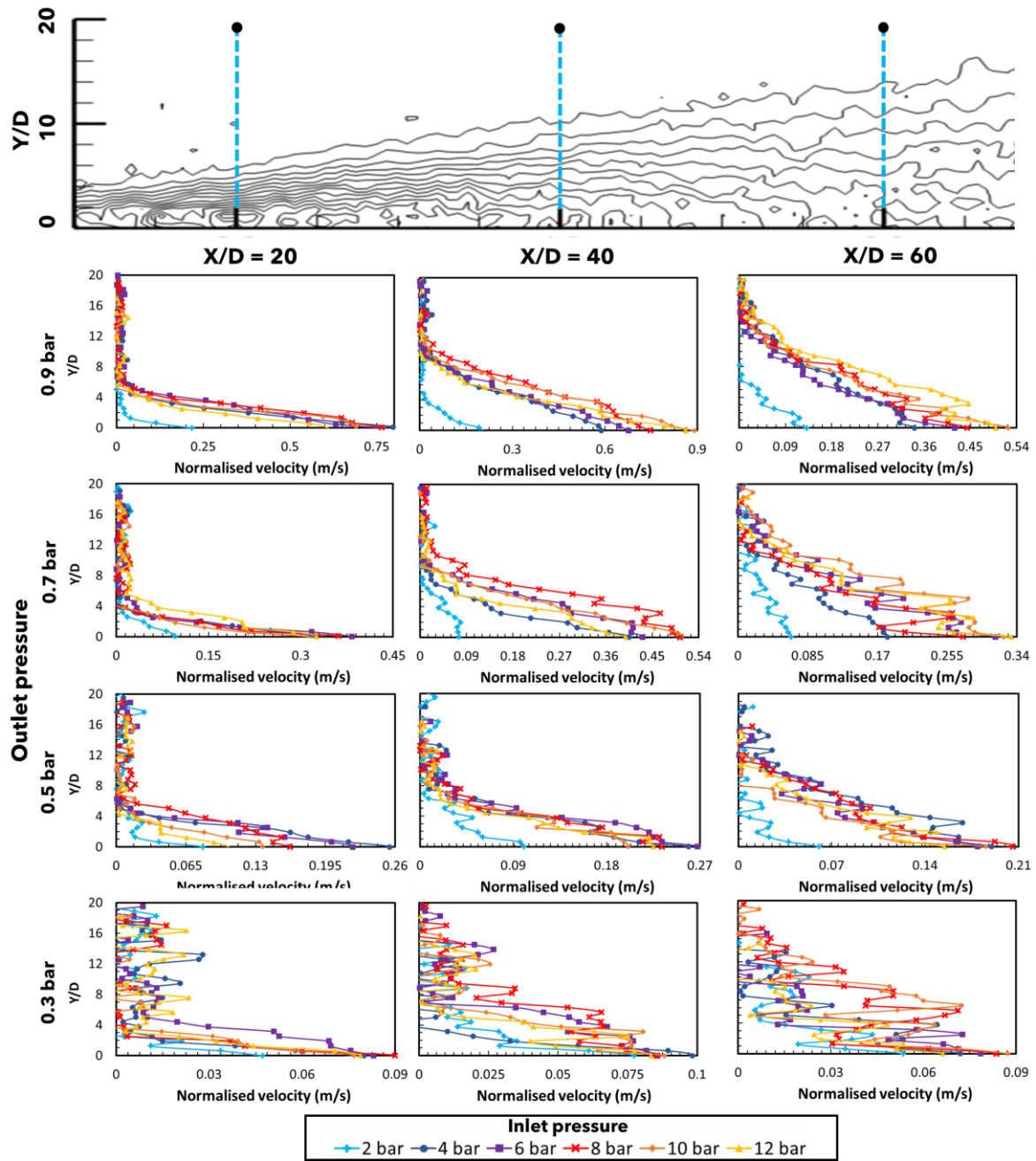


Figure 6-13. Half-width jet velocities from PIV experimental results based on inlet and outlet pressures at $X/D = 20, 40,$ and 60 .

ii. Jet spread rate

Once y_i is obtained, it was proceeded to calculate K_u . Results of jet spread rates according to inlet and outlet pressures and X/D position are following shown on Figure 6-14:

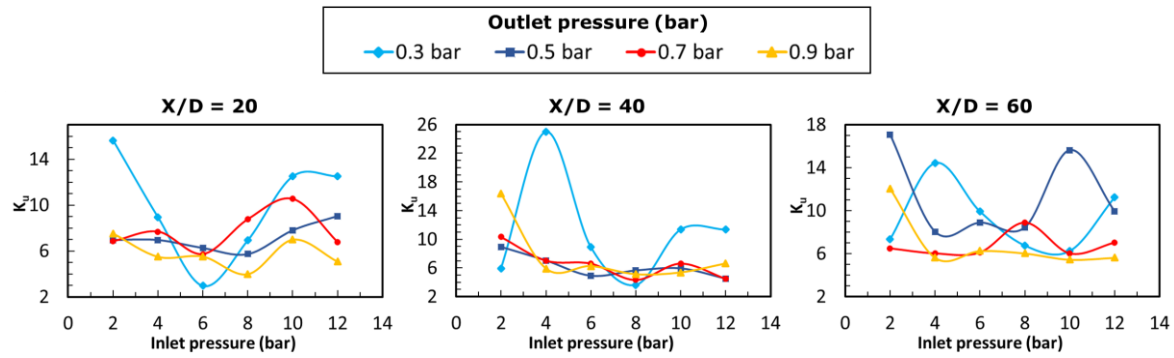


Figure 6-14. Jet spread rate according to inlet and outlet pressures on the L50E3 micro-thruster.

iii. Jet virtual origin

Then, by computing K_u from Eq. 145, the virtual origins x_0 were calculated by using Eq. 144, where the results on Figure 6-15 follow:

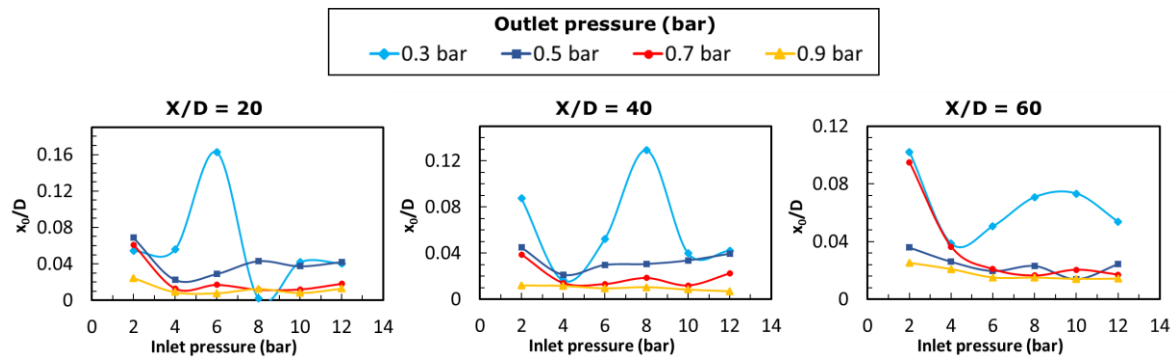


Figure 6-15. Virtual origin values according to inlet and outlet pressures on the L50E3 micro-thruster.

Therefore, an average of the virtual origin x_0 was necessary to calculate a standardised value applicable to all PIV cases of the L50E3 thruster's jet. If x_0 is not standardised, x_0 , it will vary in each case according to Eq. 144, adding complexity to analyse the jet angle without having the same reference position for all cases, where the virtual origin average \bar{x}_0 was equal to $-10.7\mu\text{m}$ or $\bar{x}_0/D = -0.0332$ from the nozzle exit.

It is vital to note that the visualised length of the jet on the PIV result was measured from $790\mu\text{m}$ before the nozzle exit, where the zero point was fixed. Therefore, the virtual origin was placed $-10.7\mu\text{m}$ from the nozzle's outlet. Using the position of the jet's visualisation as the zero position's reference; x_0 is $-800.7\mu\text{m}$ from $X/D = 0$.

Once the standard x_0 was established, the angle of the jet for each case was calculated by tracing a line contouring the jet expansion, as the blue line depicts in the figure (angle jet). The distance between the centreline and the jet expansion contour at $X/D = 60$ was then calculated using the formula Y_α/D , as seen by the red line in Figure 6-16.

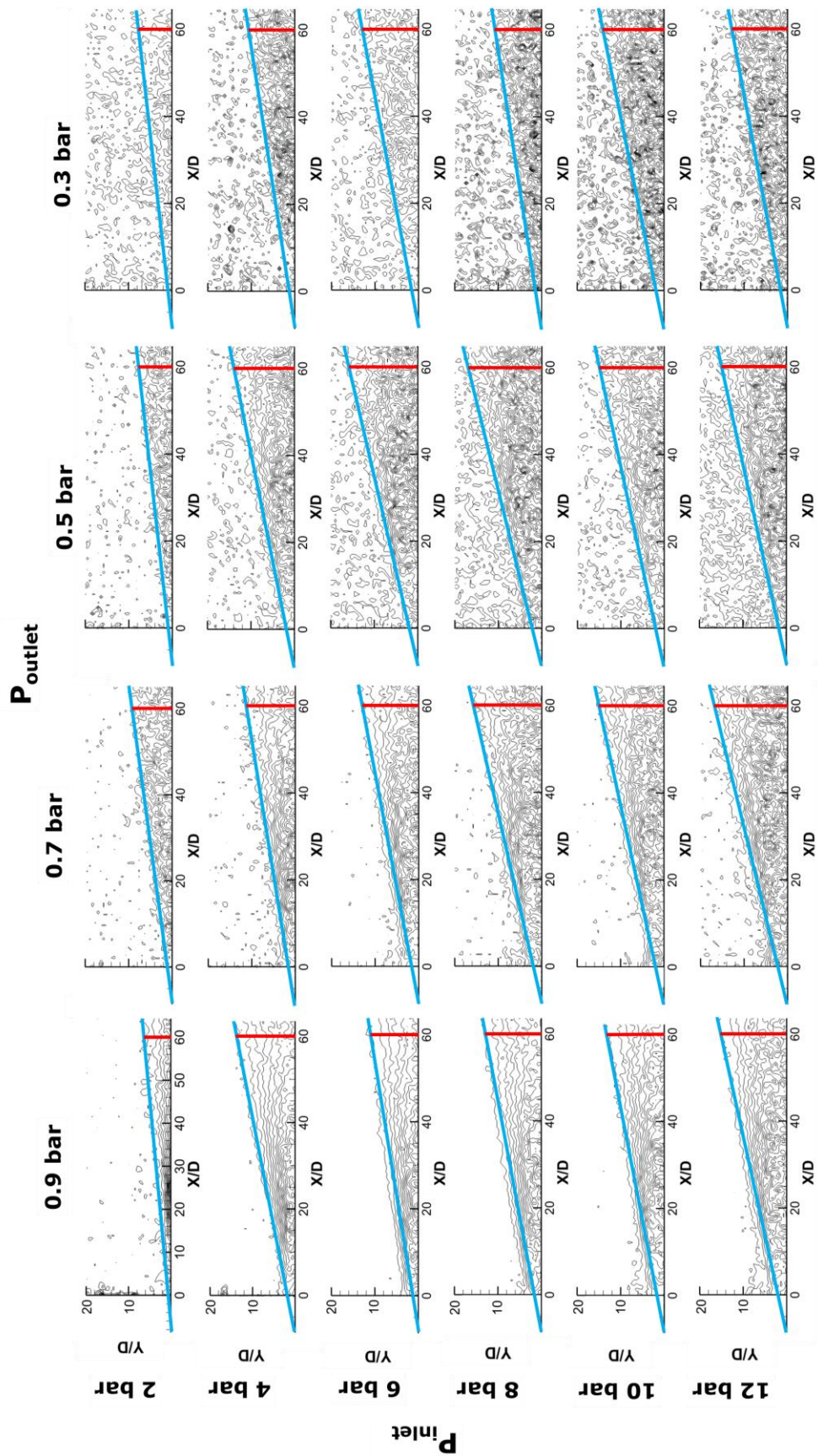


Figure 6-16. Jet contour tracing from the centerline; the blue line delimits the jet shape from the virtual origin, and the red line represents jet width.

iv. Jet angle

Then the normalised distance from x_0 to $X/D = 60$, was defined as $X_\alpha/D = 62.643$. Thus, the angles α were calculated from:

$$\alpha = \tan^{-1} \left(\frac{Y_\alpha/D}{X_\alpha/D} \right) \quad \text{Eq. 146}$$

Results from Eq. 146 of the L50E3 thruster's jet angle are displayed in Figure 6-17 according to the inlet and outlet pressure.

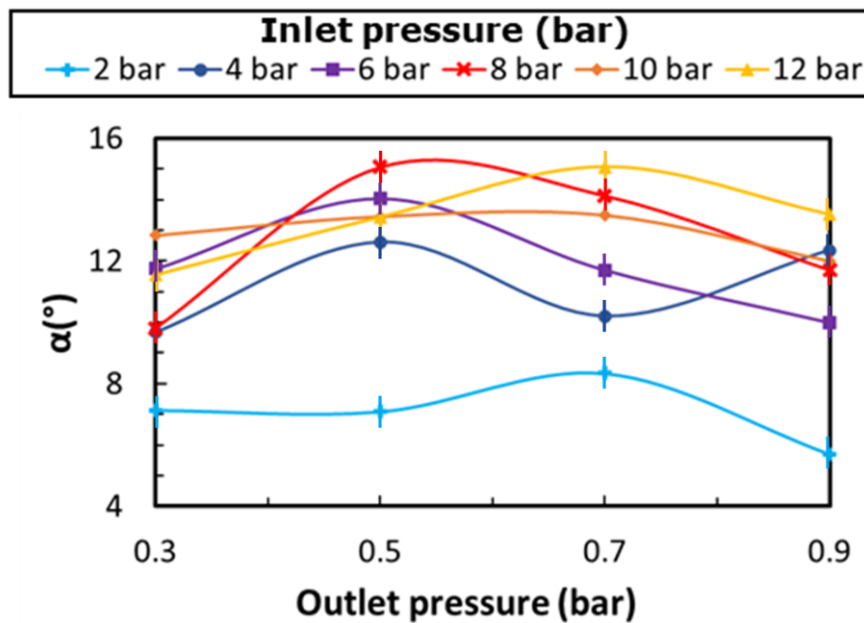


Figure 6-17. Jet angles (angular width) of L50E3 micro-thruster according to inlet and outlet pressures. Vertical lines on each of the points represent the uncertainty of angular width of $\pm 0.43^\circ$.

Figure 6-17 shows different angles in a range between 5.2° to 14.8° with a uncertainty of $\pm 0.43^\circ$ (section 6.4.4), in which angles present a periodic behaviour with the same P_{inlet} but different P_{outlet} . Therefore, the increase of the inlet pressures from 2 bar to 12 bar shows an increase in the angle. Therefore, for 6 bar at 0.3 and 0.5 bar, the angle tends to be higher than 8 and 10 bar pressures, but at P_{outlet} equals 0.5 bar tends to overpass the angle of the 12 bar case, also P_{inlet} with 8 bar presented a maximum angle expansion of 14.8° . Based on the rise in jet rarefaction at lower outlet pressures, an inference may be formed on the source of changes in angles without a consistent trend in P_{outlet} between 0.3 and 0.5 bar. The movement of particles tends to have a higher velocity and a greater degree of trajectory on the x, y, and z axes during expansion. By increasing P_{inlet} , the density of the air mixed with the seeding particles increases the collision interactions between them at lower

P_{outlet} values. A significant proportion of exhaust particles can be ejected on the z-axis, outside the illumination laser sheet range, thereby reducing the jet's expansion width and kinetic energy. Additionally, as it was commented previously, lowering P_{outlet} increases the acceleration of the ejected particles where the lowest interframe time on the camera was not able to capture all the velocity profiles; therefore, some of the information in shape is not fully covered. This assumption becomes clearer when P_{outlet} increases to 0.7 and 0.9 decreasing the degree of rarefaction where the inlet pressures tend to have a wider angle in the same magnitude as the P_{inlet} increases by lowering the acceleration of the particles, being able to capture a complete profile of the jet.

6.4.4. Uncertainty calculation

Downstream location variability, PIV measurement variability and calibration errors are some of the main factors that affects angular width determination in experimental setups. Angular width measured can be greatly impacted by the selection of where to put downstream. Different positions may have different jet expansions and shapes which result into different calculated angular widths hence need for taking measurements at several points downstream for quantification of this effect with their standard deviation giving an idea about uncertainty.

Moreover, PIV system accuracy depends on factors like interrogation window size, inter-frame time, seeding density and calibration accuracy. These parameters if varied can bring about errors during measuring process. For instance; various sizes of interrogation windows will capture diverse flow details thereby causing changes in velocity profiles leading subsequently to calculations of different widths between them. Calibration plate used for aligning camera with laser sheet so as to ensure accurate measurement of velocity fields also introduces some doubts due misalignment or error on it hence affecting outcomes obtained from there upon repeated calibrations while checking consistencies in results will reveal these mistakes. Calibration errors should be minimized by understanding how they occur and reducing such other causes which increase their occurrence frequency during experiments thus making angular width measurements less reliable when conducting scientific investigations.

i. Downstream Location Variability

It was measure the angular width at three different downstream locations ($X/D = 20, 40, 60$).

$$X/D = 20: \alpha_1 = 7.0^\circ$$

$$X/D = 40: \alpha_2 = 7.4^\circ$$

$$X/D = 60: \alpha_3 = 6.8^\circ$$

The angular widths obtained are α_1 , α_2 , and α_3 . The mean angular width ($\bar{\alpha}$) and standard deviation (σ_α) are calculated as:

Mean Angular Width:

$$\bar{\alpha} = \frac{\alpha_1 + \alpha_2 + \alpha_3}{3} = \frac{7.0 + 7.4 + 6.8}{3} = 7.067^\circ \quad \text{Eq. 147}$$

Standard Deviation:

$$\sigma_\alpha = \frac{\sqrt{(\alpha^1 - \bar{\alpha})^2 + (\alpha^2 - \bar{\alpha})^2 + (\alpha^3 - \bar{\alpha})^2}}{2} \approx 0.305^\circ \quad \text{Eq. 148}$$

ii. PIV Measurement Variability

Considering the different interrogation window sizes (16x16 and 32x32) where the visualisation of the jet profile was clear of the micro-thruster. For each size, it was calculated the angular width and determined the variability, as follows:

For 16X16:

$$\alpha_{16,1} = 12.1^\circ$$

$$\alpha_{16,2} = 12.5^\circ$$

$$\alpha_{16,3} = 12.0^\circ$$

For 32X32:

$$\alpha_{32,1} = 11.9^\circ$$

$$\alpha_{32,2} = 12.2^\circ$$

$$\alpha_{32,3} = 12.4^\circ$$

Then, the Mean Angular Width was obtained:

For 16X16:

$$\bar{\alpha}_{16} = \frac{\alpha_{16,1} + \alpha_{16,2} + \alpha_{16,3}}{3} = \frac{12.1 + 12.5 + 12.0}{3} = 12.2^\circ \quad \text{Eq. 149}$$

For 32X32:

$$\bar{\alpha}_{32} = \frac{\alpha_{32,1} + \alpha_{32,2} + \alpha_{32,3}}{3} = \frac{11.9 + 12.2 + 12.4}{3} = 12.167^\circ \quad \text{Eq. 150}$$

Finally, take the square root of the variance to obtain the standard deviation (σ_α) for each window size, it is obtained:

$$\sigma_{\alpha_{16}} = \sqrt{\sigma_{16}^2} = \sqrt{0.07} \approx 0.265^\circ \quad \text{Eq. 151}$$

$$\alpha\sigma_{\alpha_{32}} = \sqrt{\sigma_{32}^2} = \sqrt{0.063333} \approx 0.252^\circ \quad \text{Eq. 152}$$

To get a single value representing the PIV measurement variability, the standard deviations can be averaged from different window sizes:

$$\sigma_{\alpha_{PIV}} = \frac{\sigma_{\alpha_{16}} + \sigma_{\alpha_{32}}}{2} = \frac{0.265 + 0.252}{2} = 0.259^\circ \quad \text{Eq. 153}$$

iii. Calibration Errors

Results of multiple calibrations allows to calculate the mean and standard deviation of angular widths. It was performed several calibrations and the angular width (σ_α) was extract from the five calibration measurements. Thus, the angular width measurements obtained from five calibrations are:

$$\text{Calibration 1: } \alpha_{cal,1} = 12.2^\circ$$

$$\text{Calibration 2: } \alpha_{cal,2} = 12.0^\circ$$

$$\text{Calibration 3: } \alpha_{cal,3} = 12.1^\circ$$

$$\text{Calibration 4: } \alpha_{cal,4} = 12.3^\circ$$

$$\text{Calibration 5: } \alpha_{cal,5} = 11.9^\circ$$

Therefore, calculating the mean ($\overline{\alpha_{cal}}$) of the angular widths from the calibrations, follows:

$$\overline{\alpha_{cal}} = \frac{\alpha_{cal,1} + \alpha_{cal,2} + \alpha_{cal,3} + \alpha_{cal,4} + \alpha_{cal,5}}{5} = 12.1^\circ \quad \text{Eq. 154}$$

Next, the variance (σ_{cal}^2) of the calibration measurements is obtained by:

$$\sigma_{cal}^2 = \frac{(\alpha_{cal,1} - \overline{\alpha_{cal}})^2 + (\alpha_{cal,2} - \overline{\alpha_{cal}})^2 + (\alpha_{cal,3} - \overline{\alpha_{cal}})^2 + (\alpha_{cal,4} - \overline{\alpha_{cal}})^2 + (\alpha_{cal,5} - \overline{\alpha_{cal}})^2}{5 - 1} \quad \text{Eq. 155}$$

Finally, take the square root of the variance to obtain the standard deviation ($\sigma_{\alpha_{cal}}$):

$$\sigma_{\alpha_{cal}} = \sqrt{\sigma_{cal}^2} = \sqrt{0.025} \approx 0.158^\circ \quad \text{Eq. 156}$$

The standard deviation for the calibration errors is approximately 0.158° .

iv. Combined Uncertainty

The combined uncertainty (U) was estimated using the root sum of squares of the individual uncertainties by:

$$U = \sqrt{\sigma_{\alpha}^2 + \sigma_{\alpha_{PIV}}^2 + \sigma_{\alpha_{cal}}^2} \quad \text{Eq. 157}$$

Where the standard deviations were already calculated for:

$$\sigma_{\alpha} = 0.305^\circ$$

$$\sigma_{\alpha_{PIV}} = 0.259^\circ$$

$$\sigma_{\alpha_{cal}} = 0.158^\circ$$

The combined uncertainty are:

$$U = \sqrt{0.305^2 + 0.259^2 + 0.158^2} = \sqrt{0.18507} \approx 0.43^\circ \quad \text{Eq. 158}$$

The approximate uncertainty of determination of angular width is $\pm 0.43^\circ$ which represents variability due to downstream location, PIV measurement conditions and calibration errors. This review is useful in establishing how dependable these measurements are as well as their precision shown by Figure 6-14 through Figure 6-16.

General accuracy in measuring can be seen and enhanced for future experiments if we evaluate this sources of uncertainties collectively systematically.

6.4.5. Thrust and Specific Impulse calculation challenges and future improvements

The PIV system could not accurately measure thrust and specific impulse due to its inability to capture high-speed particles and provide full velocity profile of the jet. The narrow field of view and the fact that particles moved too quickly for the equipment to trap them meant that some data was missing; as a result, these important performance measures could not be reliably determined. Moreover, since the setup did not allow for recording such things as how far the jet spread out or what happened when

it came into contact with other substances in its environment, there was no way to match experimental findings against theoretical predictions very accurately.

PIV system needs several improvements for optimization. These changes include using high-speed cameras with lower inter-frame rate which take images at shorter than $6 \mu s$, increasing power output from lasers used so that particles are illuminated better during tests and implementing advanced algorithms capable of tracking more than one particle at once among others; all these would enhance accuracy as well as completeness in measurement of velocities recorded by this device. Also extending width seen through lenses should cover entire flow area while adjusting density of tracer particles employed may offer wider scope for gathering information about different regions within flows themselves thus yielding richer datasets necessary for analysis purposes. With such enhancements made, it will be possible to make precise estimations on thrust and specific impulse thereby allowing detailed comparison between experimental results obtained in testing setups vis-a-vis those predicted numerically through simulations; further investigations might use these stronger points associated with improved PIV technique for validating or calibrating the micro-plasma used in modelling micro-thruster systems, in section 4.8.3, hence achieving higher levels of accuracy during design stages.

6.5. Summary

The factors influencing jet spread include inlet pressure, nozzle geometry, temperature, outlet pressure, half-width, and virtual origin. For the micro-thruster chip, increasing the inlet pressure raises the jet spread velocity by boosting the differential pressure at the divergent nozzle, as indicated by Eq. 142. Consequently, if the outlet pressure trends toward higher vacuum environments, the velocity will also increase due to the reduced interaction where expelled particles lose energy through collisions with gas particles in the external environment.

The development and fabrication of a micro-scale PIV calibration plate and its holder for camera alignment enhanced the TSI PIV system capability to characterize micro-scale flow, but it was insufficient for characterizing the jet of the L50E3 micro-thruster. The L50E3 micro-thruster's velocity profile cannot be accurately characterized due to the PIV system's limitations. The testing achieved a field of view (FoV) of 23.71 mm x 23.71 mm using a Nikon 200mm magnification lens. Thus, the narrow length of the camera's FoV approaches the practical limits of the camera's lowest inter-frame time of $6 \mu s$. Contrary to Eq. 137, when the micro-thruster operated at inlet pressures of 2, 4, 6, 8, 10, and 12 bar, it captured particles with maximum velocities of 1,966, 1,222, 1,039, and 0.659 m/s at 0.9, 0.7, 0.5, and 0.3 bar, respectively. The Insight 4G software identifies particle motion and determines its

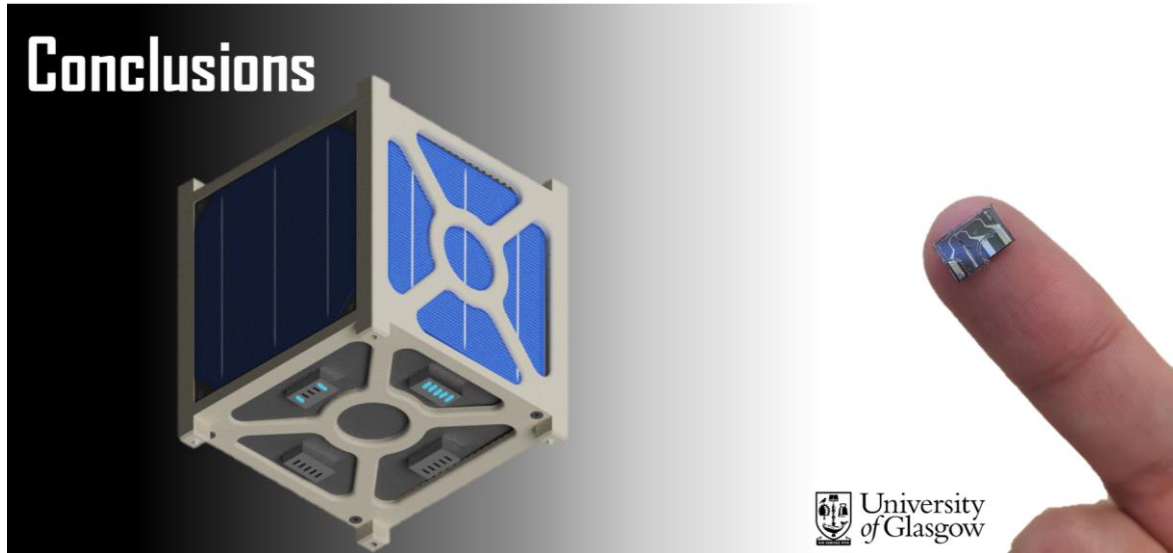
Chapter 6. Experimental testing of the micro-thruster chip

velocity vector, but PIV experimental results do not represent the entire velocity profile of the jet; they only display particles that remained within the FoV long enough to be captured in frames A and B.

An alternative solution was to lower the pressure below 2 bars; however, the visibility of the jet would be greatly reduced because the flow would lack sufficient air/oil density to visualize the micro-jet. The 20 mJ illumination provided by the Litron LDY301 High repetition rate laser is insufficient to visualize the reduced air-seeding particle concentrations. To decrease the inlet pressure and test lower thrust ranges, it is recommended to employ a different laser source with higher energy to increase particle illumination.

Characterizing the jet flow on a micrometre scale required adapting a PIV system, a significant challenge heavily dependent on the performance of individual components. It was possible to observe the jet's virtual origin and spread angle.

Chapter 7



The basic idea behind this project is to develop a novel plasma-based micro-thruster chip that can be used in nano-satellites and pico-satellites. This work takes many steps towards advancing micro propulsion technology which meets the needs of small spacecraft missions. Various sections in this thesis reflect different stages followed during research work. In these chapter, it is presented what was achieved at every stage thereby giving an integrated view about findings obtained and future improvements for micro-thruster chip.

7.1. Chapter 2: Literature survey achievements

- Summary of Recent Developments – highlighted recent developments in micro-propulsion providing context for innovations presented within this thesis
- Identification of Research Gaps – identified gaps in current researches as well as potential areas that may be explored further thus setting stage towards contributions made by this particular work.

7.2. Chapter 3: Micro-plasma discharge algorithm development achievements

- Development of Micro-Plasma Discharge Algorithm (MPDA) – created an algorithm based on Direct Simulation Monte Carlo (DSMC) method which is used for simulating DC micro-plasma impacts on flow.
- Validation of Algorithm – validated the algorithm for micro-plasma discharge through multiple configurations and conditions to ensure its reliability.
- Application of Fowler-Nordheim Equation: utilized Fowler-Nordheim equation to calculate ionic current density without increasing computational power during simulations.
- Integration of MPDA on dsmcFOAM+ Solver – integrated micro-plasma discharge algorithm with dsmcFOAM+ solver making it possible do full scale simulation of micro-plasmas effects on flow.
- Simulation of Different Electrode Configurations: demonstrated capability of MPDA to simulate various electrode configuration and their effect on discharge characteristics.

7.3. Chapter 4: Designing the micro-thruster chip achievements

- Hybrid Micro-Thruster Design – developed a design that combines cold gas and electrostatic plasma thrusters on a chip size.
- Optimization of Electrode Configuration and Geometry – defined where electrodes should be allocated and their shape to maximize thrust while minimizing overheating.
- Detailed Design Process – documented complete detail design process for micro-thruster chip including theoretical considerations.
- Theoretical Operational Micro-thruster Value Ranges – calculated operational value ranges for Joule Heating, electrical current, and voltage to ensure effective plasma generation.
- Handleable Chip Design – ensured the chip's dimensions and structure allow an easy handling and integration with existing electrical connectors.

7.4. Chapter 5: Nanofabrication of the micro-thruster chip achievements

- Detailed Nanofabrication Process Development – detailed process of nanofabrication has been developed that involves photolithography, wet etching, dry etching, metal deposition and bonding.
- Conformal Metal Deposition Innovative Procedure – utilized SPR220-7 positive photoresist and physical vapor deposition (PVD) for conformal deposition of gold in micro-trenches.

- Glass Cover Fabrication Method Development – developed a fabrication and bonding method for glass covers on the micro-thruster chip using Trotec Speedy 300 laser engraver and Cyclotene 3022-57 adhesive.
- Multiple Chip Designs Production – fabricated of 63 different micro-thruster chips designs on a single silicon wafer showing the scalability and versatile of the nanofabrication procedure.

7.1. Chapter 6: Experimental testing of the micro-thruster chip achievements

- Addressing Challenges in PIV Testing – identified and proposed possible solutions to challenges such as the higher interframe rate, the limited field of view and the insufficient particle illumination, improving the capability to visualise on the velocity jet profile.

7.2. Future work

- Large-scale tests using various propellants such as Xe, Ar, Kr are required to obtain a more comprehensive understanding of thrust and specific impulse I_{sp} concerning different gases and their contribution to thrust by varying ionisation rates and breakdown voltages of gases using an expanded variety of electrical power source options (I-V).
- Optimization of the nozzle's geometry is required by adding curvature to the sharp shapes. To minimise the drag on flow and pressure drop, enabling an increase in thrust inside the micro-device as long as the aspect ratio between the width of the microchannel and the etched depth doesn't overpass the 60:1 for the Bosch Deep Silicone Etching process [192].
- Spray coating application during the microfabrication phase to optimise the coating of the resist mask for conformal deposition, reducing the resist thickness and, by extension, the exposure and development times required for photolithography.
- Find and implement an adhesive agent to replace Cyclotene 3022-57 (BCB) for long-term attachment of stainless steel to silicon, preferably one that maintains the same properties as low dielectric constant and low dielectric loss materials, including resistance to moisture absorption and outgassing, a low curing temperature, and good planarization.
- Run simulation cases for the jet's velocity profile based on the same boundary conditions as the experimental tests covering the FoV of 23.71 x 23.71 mm with a Nikon 200mm magnification lens.
- Re-execute the experimental test on micro-thrusters using a high-speed camera with a reduced inter-frame rate ($\ll 6 \mu\text{s}$) in conjunction with a higher laser power over 20mJ or a micro-PIV system to capture particles with greater velocities and produce precise experimental data.

Chapter 7. Conclusions

- It is necessary to conduct a high voltage test on the micro-thruster to determine the plasma's capabilities and performance at varying currents, voltages, and DC pulses and their influence on thrust. To establish the performance of the micro-thruster chip in LEO and space, further tests like EMI/EMC testing, thermal testing, and mechanical testing must be performed.

Bibliography

- [1] J. H. Schilling, R. A. Spores and G. G. Spanjers, "Micropropulsion Options for the TechSat 21Space-Based Radar Flight," in *Micropropulsion for small spacecraft*, Progress in Astronautics and Aeronautics Vol 187, 2000, pp. 3-23.
- [2] M. M. Micci and A. D. Ketsdever, *Micropropulsion for small spacecraft*, United States: American Institute of Aeronautics and Astronautics, Inc., 2000.
- [3] J. Bouwmeester and J. Guo, "Survey of worldwide pico-and nanosatellite missions, distributions and subsystem technology," *Acta Astronautica*, vol. 67(8), pp. 854-862, 2010.
- [4] S. C. Kim, "Calculations of low-Reynolds-number resistojet nozzles.," *Journal of Spacecraft and Rockets*, vol. 31(2), pp. 259-264, 1994.
- [5] A. D. Greig, "Pocket Rocket: An electrothermal plasma micro-thruster," *The Australian National University*, pp. 1-122, 2015.
- [6] I. Levchenko, K. Bazaka, Y. Ding, Y. Raitses, S. Mazouffre, T. Henning, P. Klar, S. Shinohara, J. Schein, L. Garrigues and M. Kim, "Space micropropulsion systems for Cubesats and small satellites: From proximate targets to furthestmost frontiers," *Applied Physics Reviews*, vol. 5, no. 1, p. 011104, 2018.
- [7] Z. Behtash, Hossein, K. Kontis and S. Roy, "Flow control at subsonic speeds using serpentine plasma actuators," *45th AIAA plasma dynamics and lasers conference, Atlanta*, no. GA, 2014.
- [8] M. M. Wojewodka, C. White, T. Ukai, A. Russell and K. Kontis, "Pressure dependency on a nanosecond pulsed dielectric barrier discharge plasma actuator," *Physics of Plasmas*, vol. 26(6), p. 063512, 2019.
- [9] T. Ukai, A. Russell, H. Zare-Behtash and K. Konstantinos, "Temporal variation of the spatial density distribution above a nanosecond pulsed dielectric barrier discharge plasma actuator in quiescent air," *Physics of Fluids*, vol. 30(11), p. 116106, 2018.
- [10] R. Ruisi, H. Zare-Behtash, K. Kontis and R. Erfani, "Active flow control over a backward-facing step using plasma actuation," *Acta Astronautica*, vol. 126, pp. 354-363, 2016.
- [11] D. B. Go and D. A. Pohlman, "A mathematical model of the modified Paschen's curve for breakdown in microscale gaps," *Journal of Applied physics*, vol. 107(10), p. 103303, 2010.
- [12] C. J. Capon, M. Brown, C. White, T. Scanlon and R. R. Boyce, "pdFOAM: A PIC-DSMC code for near-Earth plasma-body interactions," *Computers & Fluids*, vol. 149, pp. 160-171, 2017.
- [13] M. Auweter-Kurtz, M. Fertig, D. Petkow, T. Stindl, M. Quandt, C. D. Munz, P. Adamis, M. Resch, S. Roller, D. D'Andrea and R. Schneider, "Development of a hybrid PIC/DSMC code," *29th international electric propulsion conference*, pp. 1-15, 2005.

-
- [14] W. Reschke, T. Binder, J. Kleinert, A. Mirza, P. Nizenkov, M. Pfeiffer, S. Fasoulas, S. Copplestone, P. Ortwein and C. D. Munz, "Recent developments of DSMC within the reactive plasma flow solver PICLas," *AIP Conference Proceedings*, vol. 1786(1), p. 130003, 2016.
- [15] L. Brieda, J. Pierru, R. Kafafy and J. Wang, "Development of the DRACO code for modeling electric propulsion plume interactions," *40th AIAA/ASME/SAE/ASEE Joint Propulsion Conference and Exhibit*, p. 3633, 2004.
- [16] W. Baumjohann and A. Rudolf, *Basic space plasma physics*, London: Imperial College Press, 2012.
- [17] V. Nehra, "Study of design criteria of a non-thermal plasma based VUV/UV source," *Doctoral thesis, Faculty of Engineering and Technology, Maharshi Dayanand University*, no. <http://shodhganga.inflibnet.ac.in/handle/10603/113674>, p. Chapter 2, 2008.
- [18] S. Pavón, "Interaction between a surface dielectric barrier discharge and transonic airflows," No. *THESIS. EPFL*, 2008.
- [19] M. Radmilovi, B. Radjenovic, S. Bojarov, M. Klas and S. Matejcik, "The Breakdown Mechanisms In Electrical Discharges: The Role Of The Field Emission Effect In Direct Current Discharges In Micro gaps," *Acta Physica Slovaca*, vol. 63(3), pp. 105 - 205, 2013.
- [20] G. Meng and Y. Cheng, "Electrical Breakdown Behaviors in Microgaps," *Electrostatic Discharge-From Electrical breakdown in Micro-gaps to Nano-generators*, vol. IntechOpen, 2019.
- [21] A. Semnani, A. Venkatraman, A. Alexeenko and D. Peroulis, "Pre-breakdown evaluation of gas discharge mechanisms in microgaps," *American Institute of Physics*, vol. 102(17), p. <https://doi.org/10.1063/1.4803179>, 2013.
- [22] D. B. Go and A. Venkatraman, "Microscale gas breakdown: ion-enhanced field emission and the modified Paschen's curve," *Journal of Physics D: Applied Physics* 47(50), p. 503001, 2014.
- [23] P. Soucek, "Elementary collision and transport," 13 October 2010. [Online]. Available: http://physics.muni.cz/~dorian/Soucek_Srazky_v_plazmatu.pdf.
- [24] C. Scharlemann, M. Tajmar, I. Vasiljevich, N. Buldrini, D. Krejci and B. Seifert, "Propulsion for nanosatellites," *In 32nd International Electric Propulsion Conference, Wiesbaden, Germany*, vol. 171, pp. IEPC-2011, 2011.
- [25] Y. Takao, T. Takahashi, K. Eriguchi and K. Ono, "Microplasma thruster for ultra-small satellites: Plasma chemical and aerodynamical aspects.," *Pure and Applied Chemistry*, vol. 80(9), pp. 2013-2023, 2008.
- [26] S. Mazouffre, "Electric propulsion for satellites and spacecraft: established technologies and novel approaches," *Plasma Sources Science and Technology*, vol. 25(3), p. 033002, 2016.
- [27] C. Charles, A. Bish, R. W. Boswell, J. Dedrick, A. Greig, R. Hawkins and T. S. Ho, "A short review of experimental and computational diagnostics for radiofrequency plasma micro-thrusters," *Plasma Chemistry and Plasma Processing*, vol. 36(1), pp. 29-44, 2016.

-
- [28] T. Takahashi, Y. Takao, Y. Eriguchi and K. Ono, "Numerical and experimental study of microwave-excited microplasma and micronozzle flow for a microplasma thruster," *Physics of plasmas*, vol. 16(8), p. 083505, 2009.
- [29] V. N. Blinov, I. S. Vavilov, V. V. Fedynin, V. V. Shalay, P. S. Yachmenev and V. I. Ruban, "Experimental investigations of nitrogen arcjet thruster with control unit for small spacecrafts," *Journal of Physics: Conference Series*, vol. 1210(1), p. 012019, 2019.
- [30] D. O'Reilly, G. Herdrich and D. F. Kavanagh, "Electric propulsion methods for small satellites: A review," *Aerospace*, vol. 8(1), p. 22, 2021.
- [31] I. S. Vavilov, V. V. Fedynin, P. S. Yachmenev, K. I. Zharikov, A. I. Lukyanchik and P. V. Stepen, "Review of electric thrusters with low consumption power for corrective propulsion system of small space vehicles," *Journal of Physics: Conference Series*, vol. 1546(1), p. 012071, 2020.
- [32] S. H. Yan, T. O. Yinggang, W. E. Fuzhi, Y. A. Zhaopu and H. U. Dawei, "Influences of characteristic parameters on starting-up process of an arcjet thruster," *Chinese Journal of Aeronautics*, vol. 33(12), pp. 3011-3017, 2020.
- [33] T. Haag and F. Curran, "High-power hydrogen arcjet performance," *27th Joint Propulsion Conference*, 1991.
- [34] H. Horisawa, T. Noda, K. Onodera and I. Kimura, "Micro-arcjet: microfabrication with UV lasers and thrust characteristics," *29th International Electric Propulsion Conference Paper*, pp. IEPC-2005-123, 2005.
- [35] K. Zhang, S. K. Chou and S. S. Ang, "MEMS-based solid propellant microthruster design, simulation, fabrication, and testing," *Journal of microelectromechanical systems*, vol. 13(2), pp. 165-175, 2004.
- [36] B. Liu, X. Li, J. Yang and G. Gao, "Recent advances in MEMS-based microthrusters," *Micromachines*, vol. 10(12), p. 818, 2019.
- [37] A. Chaalane, R. Chemam, M. Houabes, R. Yahiaoui, A. Metatla, B. Ouari, N. Ouari, D. Metatla, D. Mahi, A. Dkhissi and D. Esteve, "A MEMS-based solid propellant microthruster array for space and military applications," *Journal of Physics: Conference Series*, vol. 600(1), p. 012137, 2015.
- [38] M. H. Wu and R. A. Yetter, "A novel electrolytic ignition monopropellant microthruster based on low temperature co-fired ceramic tape technology," *Lab on a Chip*, vol. 9(7), pp. 910-916, 2009.
- [39] A. Cervone, B. Zandbergen, D. C. Guerrieri, M. D. De Athayde Costa e Silva, I. Krusharev and H. van Zeijl, "Green micro-resistojet research at Delft University of Technology:," *CEAS Space Journal*, vol. 9(1), pp. 111-125, 2017.
- [40] W. J. Guman, "Solid propellant pulsed plasma propulsion system design," *Journal of spacecraft and rockets*, vol. 13(1), pp. 51-53, 1976.

-
- [41] Applied Ion Systems, "AIS-gPPT3-1C Single-Channel Gridded Pulsed Plasma Thruster," 2022. [Online]. Available: <https://appliedionsystems.com/portfolio/ais-gppt3-1c-single-channel-gridded-pulsed-plasma-thruster/>. [Accessed 12 April 2022].
- [42] A. Kakami, H. Koizumi, K. Komurasaki and Y. Arakawa, "Design and performance of liquid propellant pulsed plasma thruster.," *Vacuum*, Vols. 73(3-4), pp. 419-425, 2004.
- [43] G. I. Taylor, "Disintegration of water drops in an electric field.," *Mathematical and Physical Sciences*, vol. 280(1382), pp. 383-397, 1964.
- [44] G. Lenguito, J. F. De La Mora and A. Gomez, "Scaling up the power of an electrospray microthruster," *Journal of Micromechanics and Microengineering*, vol. 24(5), p. 055003, 2014.
- [45] H. Huh and R. E. Wirz, "Numerical simulation of electrospray thruster extraction," *Proceedings of the 36th International Electric Propulsion Conference*, pp. 15-20, 2019.
- [46] F. Martel, L. Perna and P. Lozano, "Miniature ion electrospray thrusters and performance test on cubesats," *26th Annual AIAA/USU Conference on Small Satellites*, pp. SSC12-VI-5, 2012.
- [47] R. V. Akhmetzhanov, A. V. Bogatyri, D. A. Kashirin, V. A. Obukhov, G. A. Popov, V. V. Svitina and S. A. Khartov, "Low-Power Ion Thrusters. State of Development at Research Institute of Applied Mechanics and Electrodynamics, MAI.," *IOP Conference Series: Materials Science and Engineering*, vol. 927(1), p. 012075, 2020.
- [48] R. Shastry, R. E. Thomas, G. C. Soulas, M. C. Gonzalez, M. J. Patterson and C. M. Tolbert, "NASA's Evolutionary Xenon Thruster-Commercial (NEXT-C)," *Double Asteroid Redirection Test (DART) Mission*, 2021.
- [49] M. Bekemans, F. Bronchart, T. Scalais and A. Franke, "Configurable high voltage power supply for full electric propulsion spacecraft," *2019 European Space Power Conference (ESPC)*, vol. IEEE, pp. 1-5, 2019.
- [50] J. J. Bontempo, A. N. Brigeman, H. B. Fain, M. C. Gonzalez, L. R. Pinero, A. G. Birchenough, M. V. Aulizio, J. Fisher and B. Ferraiuolo, "The NEXT-C Power Processing Unit: Lessons Learned from the Design, Build, and Test of the NEXT-C PPU for APL's DART Mission," *AIAA Propulsion and Energy 2020 Forum*, p. 3641, 2020.
- [51] Y. Jinghua, J. I. A. Shaoxia, Z. Zhang, X. Zhang, J. I. N. Ting, L. I. Long, C. Yong and C. Jian, "Performance of a 4 cm iodine-fueled radio frequency ion thruster," *Plasma Science and Technology*, vol. 22(9), p. 094006, 2020.
- [52] R. G. Jahn and E. Y. Choueiri, "Encyclopedia of physical science and technology," *Academic Press*, vol. 3, pp. 125-141, 2002.
- [53] C. Rossi, "Micropropulsion for Space—A Survey of MEMS-based Micro Thrusters and their Solid Propellant Technology.," *Sensors update*, vol. 10(1), pp. 257-292, 2002.
- [54] ExoTerra, "Electric propulsion systems," ExoTerra Resource, 2022. [Online]. Available: <https://exoterracorp.com/products/electric-propulsion-systems/>. [Accessed 19 April 2022].

-
- [55] D. M. Goebel, I. Katz and I. G. Mikellides, *Fundamentals of electric propulsion*, John Wiley & Sons, 2023.
- [56] G. P. Sutton and O. Biblarz, *Rocket propulsion elements*, John Wiley & Sons, 2011.
- [57] "About Electric Propulsion," Space Propulsion Laboratory - Massachusetts Institute of Technology, [Online]. Available: <https://spacepropulsion.mit.edu/about-electric-propulsion>.
- [58] M. J. Turner, *Rocket and spacecraft propulsion: principles, practice and new developments*, Springer Science & Business Media, 2008.
- [59] M. Leomanni, A. Garulli and A. Giannitrapani, "Propulsion Options for Very Low Earth Orbit Microsatellites," *Dipartimento di Ingegneria dell'Informazione e Scienze Matematiche Universit`a di Siena*, 2016.
- [60] P. Sharpley, "Noble Gases," University of Illinois, 2011. [Online]. Available: <http://butane.chem.uiuc.edu/pshapley/GenChem1/L6/1.html>.
- [61] H. H. Gatzert, V. Saile and J. Leuthold, *Micro and Nano Fabrication*, Springer-Verlag Berlin Heidelberg. DOI 10.1007/978-3-662-44395-8, 2015.
- [62] J. Watson, National Physical Laboratory (NPL), 2017. [Online]. Available: http://www.kayelaby.npl.co.uk/general_physics/2_2/2_2_4.html.
- [63] P. G. Crawford, "Zelite membranes for the separation of krypton and xenon from spent nuclear fuel reprocessing," *Georgia Institute of Technology: School of Chemical and Biomolecular Engineering*, p. xvi, 2013.
- [64] M. Gad-el-Hak, "The fluid mechanics of microdevices—the Freeman scholar lecture," *Journal of Fluids Engineering*, vol. 121(1), p. 5–33, 1999.
- [65] C. White, M. K. Borg, T. J. Scanlon and J. M. Reese, "A DSMC investigation of gas flows in micro-channels with bends," *Computers & Fluids*, vol. 71, pp. 261-271, 2013.
- [66] G. Karniadakis, A. Beskok and N. Aluru, in *Microflows and Nanoflows: Fundamentals and Simulation*, New York, Springer, 2005.
- [67] B. Wahlberg, G. Harmanvir, J. R. Jessie and M. Michel, "Ex vivo biomechanical characterization of syringe-needle ejections for intracerebral cell delivery.," *Scientific Reports (Nature Publisher Group)*, vol. 8, pp. 1-17, 2018.
- [68] B. Wie, V. Lappas and J. Gil-Fernández, "Attitude and orbit control systems," *The International Handbook of Space Technology*, no. Springer, Berlin, Heidelberg, pp. 323-369, 2014.
- [69] T. Zhuang, A. Shashurin, T. Denz, M. Keidar, P. Vail and A. Pancotti, "Performance characteristics of micro-cathode arc thruster.," *Journal of Propulsion and Power*, vol. 30(1), pp. 29-34, 2014.

-
- [70] D. Krejci, A. Reissner, T. Schönherr, B. Seifert, Z. Saleem and R. Alejos, "Recent flight data from IFM Nano Thrusters in a low earth orbit," *Proceedings of the 36th International Electric Propulsion Conference*, no. Vienna, Austria, pp. 5-20, 2019.
- [71] N. R. Demmons, Z. D. Wood, A. Margousian, J. Knott and T. Fedkiw, "Electrospray Attitude Control System Flight Preparation," *AIAA SCITECH 2022 Forum*, p. p. 0039, 2022.
- [72] A. Ebrahimi and E. Roohi, "DSMC investigation of rarefied gas flow through diverging micro- and nanochannels," *Microfluidics and Nanofluidics*, vol. 21(2), pp. 1-12, 2017.
- [73] C. White, M. K. Borg, T. J. Scanlon, S. M. Longshaw, B. John, D. R. Emerson and J. M. Reese, "dsmcFoam+: An OpenFOAM based direct simulation Monte Carlo solver," *Computer Physics Communications*, vol. 224, pp. 22-43, 2018.
- [74] G. Lapenta, "DEMOCRITUS: An adaptive particle in cell (PIC) code for object-plasma interactions," *Journal of Computational Physics*, vol. 230(12), pp. 4679-4695, 2011.
- [75] J. Forest, A. Hilgers, B. Thiebault, L. Eliasson, J.-J. Berthelier and H. De Feraudy, "An open-source spacecraft plasma interaction simulation code PicUp3D: tests and validations," *IEEE transactions on plasma science*, vol. 34(5), pp. 2103-2113, 2006.
- [76] G. L. Delzanno, E. Camporeale, D. J. Moulton, J. E. Borovsky, E. A. MacDonald and M. F. Thomsen, "CPIC: a curvilinear particle-in-cell code for plasma-material interaction studies," *IEEE Transactions on Plasma Science*, vol. 41(12), pp. 3577-3587, 2013.
- [77] J. F. Padilla, "Comparison of DAC and MONACO DSMC codes with flat plate simulation," Vols. NASA/TM-2010-216835, 2010.
- [78] S. J. Plimpton and M. A. Gallis, "SPARTA direct simulation Monte Carlo (DSMC) simulator," Sandia National Laboratories, USA, 2015. [Online]. Available: <http://sparta.sandia.gov>.
- [79] H. G. Weller, G. Tabor, H. Jasak and C. Fureby, "A tensorial approach to computational continuum mechanics using object-oriented techniques," *Computers in physics*, vol. 12(6), pp. 620-631, 1998.
- [80] A. Hassanvand, M. B. Gerdroodbary, R. Moradi and Y. Amini, "Application of Knudsen thermal force for detection of inert gases," *Results in Physics*, vol. 9, pp. 351-358, 2018.
- [81] G. A. Bird, "Approach to translational equilibrium in a rigid sphere gas," *The Physics of Fluids*, vol. 6(10), pp. 1518-1519, 1963.
- [82] J. C. Chen and A. S. Kim, "Brownian dynamics, molecular dynamics, and Monte Carlo modeling of colloidal systems," *Advances in colloid and interface science*, Vols. 112.1-3, pp. 159-173, 2004.
- [83] M. Ripoll, K. Mussawisade, R. G. Winkler and G. Gompper, "Dynamic regimes of fluids simulated by multiparticle-collision dynamics," *Physical Review*, vol. E 72.1, p. 016701, 2005.
- [84] J. J. Burby and T. J. Klotz, "Slow manifold reduction for plasma science," *Communications in Nonlinear Science and Numerical Simulation*, vol. 89, p. 105289, 2020.

-
- [85] K. Wiesenmann, "A short introduction to plasma physics," *arXiv preprint arXiv*, p. 1404.0509, 2014.
- [86] G. A. Bird, *Molecular Gas Dynamics and the Direct Simulation of Gas Flows*, New York: Oxford Science Publications, Oxford University Press Inc, 1994.
- [87] J. C. Maxwell, "On stresses in rarefied gases arising from inequalities of temperature," *Philosophical Transactions of the Royal Society Part 1*, p. 170:231–256, 1879.
- [88] M. S. Ivanov and S. V. Rogasinsky, "Analysis of numerical techniques of the direct simulation Monte Carlo method in the rarefied gas dynamics," *Russian Journal of Numerical*, pp. 453-466, 1988.
- [89] N. G. Hadjiconstantinou, A. L. Garcia, M. Z. Bazant and G. He, "Statistical error in particle simulations of hydrodynamic phenomena.," *Journal of Computational Physics*, vol. 187(1), p. 274–297, 2003.
- [90] C. White, "Benchmarking, Development and Applications of an Open Source DSMC Solver," *University of Strathclyde - Department of Mechanical & Aerospace Engineering*, 2013.
- [91] M. Gallis, J. Torczynski, D. Rader and G. Bird, "Accuracy and convergence of a new DSMC algorithm," *40th Thermophysics Conference*, p. 3913, 2008.
- [92] D. E. R. Espinoza, V. Casseau, T. J. Scanlon and R. E. Brown, "An open-source hybrid CFD-DSMC solver for high speed flows," *AIP Conference Proceedings*, vol. 1786(1), no. AIP Publishing LLC, p. 050007, 2016.
- [93] C. Mata, E. Longmire, D. McKenna, K. Glass and A. Hubel, "Cell motion and recovery in a two-stream microfluidic device," *Microfluidics and nanofluidics*, vol. 8(4), pp. 457-465, 2010.
- [94] M. Mobli, "Thermal Analysis of High Pressure Micro Plasma Discharge," *University of South Carolina (Thesis)*, p. 40, 2014.
- [95] S. Park, W. Choe, S. Y. Moon and S. J. Yoo, "Electron characterization in weakly ionized collisional plasmas: from principles to techniques," *Advances in Physics: X*, vol. 4(1), p. 1526114, 2019.
- [96] R. W. Chabay and B. A. Sherwood, "Chapter 17: Electric Potential," in *Matter and interactions*, North Carolina, John Wiley & Sons, 2015, p. 664.
- [97] R. G. Jahn, *Physics of electric propulsion*, Courier Corporation, 2006.
- [98] A. N. Kontaratos, "On the functional dependence of Townsend's first ionization coefficient," *Applied Scientific Research, Section A*, vol. 12(1), pp. 27-32, 1965.
- [99] Š. Matejčík, R. Branislav, K. Matej and R.-R. Marija, "Field emission driven direct current argon discharges and electrical breakdown mechanism across micron scale gaps," *The European Physical Journal D*, vol. 69(11), p. 251, 2015.

-
- [100] R. A. Wijisman, "Breakdown probability of a low pressure gas discharge," *Physical Review*, vol. 75(5), p. 833, 1949.
- [101] J. M. Meek and J. D. Craggs, *Electrical Breakdown Of Gases*, Oxford At The Clarendon Press, 1953.
- [102] T. Yoshinaga and A. Haruaki, "Effects of secondary electron emission coefficients on Townsend's second ionization coefficient in argon dielectric barrier discharges," *IEEJ Transactions on Electrical and Electronic Engineering*, vol. 9(5), pp. 459-464, 2014.
- [103] W. S. Boyle and P. Kisliuk, "Departure from Paschen's law of breakdown in gases," *Physical Review*, vol. 97(2), p. 255, 1955.
- [104] C. H. Moore, M. M. Hopkins, P. S. Crozier, J. J. Boerner, L. C. Musson, R. W. Hooper and M. T. Bettencourt, "1D PIC-DSMC simulations of breakdown in microscale gaps," *In AIP Conference Proceedings*, vol. 1501(1), no. American Institute of Physics, pp. 629-636, 2012.
- [105] A. Venkatraman and A. A. Alexeenko, "Scaling law for direct current field emission-driven microscale gas breakdown," *Physics of plasmas*, vol. 9(12), p. 123515, 2012.
- [106] C. H. Miller, "Values of Fowler-Nordheim field emission functions: $v(y)$, $t(y)$, and $s(y)$," *Journal of the Franklin Institute*, vol. 282(6), pp. 382-388, 1966.
- [107] A. P. Godse and U. A. Bakshi, *Electronic Devices*, Technical Publications, 2009.
- [108] M. A. Lieberman and A. J. Lichtenberg, "Principles of plasma discharges and materials processing," *MRS Bulletin*, vol. 30.12, pp. 899-901, 1994.
- [109] M. A. Lieberman, "A mini-course on the principles of plasma discharges," University of California, Berkeley, [Online]. Available: <https://people.eecs.berkeley.edu/~lieber/LiebBadHonnef12Sep06.pdf>. [Accessed 06 June 2024].
- [110] C. F. Francis, *Introduction to plasma physics and controlled fusion* (Third ed.), Champ: Springer, 2015, pp. 211-215.
- [111] M. Moisan and P. Jacques, "Physics of collisional plasmas: introduction to high-frequency discharges," in *Appendix I: Some Properties of the Maxwell-Boltzman (M-B) Velocity Distribution*, Springer Science & Business Media, 2012, pp. 387-394.
- [112] D. M. Katz, "Physics for Scientists and Engineers: Foundations and Connections," in *Chapter 20. Kinetic Theory of Gases*, Nelson Education, 2015, p. 606.
- [113] G. J. Kim, F. Iza and K. L. Jae, "Electron and ion kinetics in a micro hollow cathode discharge," *Journal of physics D: applied physics*, vol. 39(20), p. 4386, 2006.
- [114] W. Su, S. Lindsay, H. Liu and L. Wu, "Comparative study of the discrete velocity and lattice Boltzmann methods for rarefied gas flows through irregular channels," *Physical Review E*, vol. 96(2), p. 023309, 2017.

-
- [115] J. J. Szabo, "Fully kinetic numerical modeling of a plasma thruster," *Doctoral dissertation, Massachusetts Institute of Technology*, 2001.
- [116] T. D. Arber, K. Bennett, C. S. Brady, A. Lawrence-Douglas, M. G. Ramsay, N. J. Sircombe, P. Gillies, R. G. Evans, H. Schmitz, A. R. Bell and C. P. Ridgers, "Contemporary particle-in-cell approach to laser-plasma modelling," *Plasma Physics and Controlled Fusion*, vol. 57(11), p. 113001, 2015.
- [117] J. P. Verboncoeur, "Particle simulation of plasmas: review and advances," *Plasma Physics and Controlled Fusion*, vol. 47(5A), p. A231, 2005.
- [118] M. Wang, M. Macrossan and Z. Li, "Relaxation time simulation method with internal energy exchange for perfect gas flow at near-continuum conditions," *Communications in Nonlinear Science and Numerical Simulation*, vol. 12.7, pp. 1277-1282, 2007.
- [119] Y. Fu, P. Zhang and J. P. Verboncoeur, "Paschen's curve in microgaps with an electrode surface protrusion," *Applied Physics Letters*, vol. 113(5), p. 054102, 2018.
- [120] H. B. Michaelson, "The work function of the elements and its periodicity," *Journal of applied physics*, vol. 48(11), pp. 4729-4733, 1977.
- [121] A. Rokhlenko, "Strong field electron emission and the Fowler–Nordheim–Schottky theory," *Journal of Physics A: Mathematical and Theoretical*, vol. 44(5), p. 055302, 2011.
- [122] Y. Chen, "Electrical breakdown of Gases in subatmospheric pressure," *Auburn University*, 2016.
- [123] Y. Fu, J. Krek, P. Zhang and J. P. Verboncoeur, "Evaluating microgap breakdown mode transition with electric field non-uniformity," *Plasma Sources Science and Technology*, vol. 27(9), p. 095014, 2018.
- [124] M. J. Kushner, "Modeling of microdischarge devices: Pyramidal structures," *Journal of applied physics*, vol. 95(3), pp. 846-859, 2004.
- [125] L. Lin and Q. Wang, "Microplasma: a new generation of technology for functional nanomaterial synthesis," *Plasma Chemistry and Plasma Processing*, vol. 35(6), pp. 925-962, 2015.
- [126] P. Kurunczi, H. Shah and K. Becker, "Hydrogen Lyman-and Lyman-emissions from high-pressure microhollow cathode discharges in Ne-H₂ mixtures," *Journal of Physics B: Atomic, Molecular and Optical Physics*, vol. 32(22), p. L651, 1999.
- [127] P. Kurunczi, J. Lopez, H. Shah and K. Becker, "Excimer formation in high-pressure microhollow cathode discharge plasmas in helium initiated by low-energy electron collisions," *International Journal of Mass Spectrometry*, Vols. 205(1-3), pp. 277-283, 2001.
- [128] K. Van Laer and A. Bogaerts, "Influence of gap size and dielectric constant of the packing material on the plasma behaviour in a packed bed DBD reactor: a fluid modelling study," *Plasma Processes and Polymers*, Vols. 14(4-5), p. 1600129, 2017.

-
- [129] W. J. Bell, "Proposed model of thermionically assisted breakdown and implementation on electrostatic thrusters.," *Naval Postgraduate School Monterey C.A.*, 1991.
- [130] I. Guskov, S. Lebedev and V. G. Rodionova, "Electrical breakdown through a gap in glass in an atmosphere of cesium vapor(Electric breakdown dependence on cesium vapor pressure, cathode temperature and slit size of two glass cylinders).," *Soviet Physics-Technical Physics*, vol. 10, p. 123, 1965.
- [131] J. Choi, F. Iza, J. K. Lee and C. M. Ryu, "Electron and ion kinetics in a DC microplasma at atmospheric pressure," *IEEE transactions on plasma science*, vol. 35(5), pp. 1274-1278, 2007.
- [132] G. J. Kim, F. Iza and J. K. Lee, "Field emission and lifetime of microcavity plasma," *Physics of Plasmas*, vol. 16(1), p. 013502, 2009.
- [133] D. Levko and L. L. Raja, "Breakdown of atmospheric pressure microgaps at high excitation frequencies," *Journal of Applied Physics*, vol. 117(17), p. 173303, 2015.
- [134] A. Alamatsaz, "Computational Kinetic Study of Low-Temperature Argon Microdischarges," *Doctoral dissertation, UC Merced*, 2018.
- [135] Y. P. Raizer and J. E. Allen, *Gas discharge physics*, Berlin: Springer, 1997.
- [136] K. H. Becker, K. H. Schoenbach and J. G. Eden, "Microplasmas and applications," *Journal of Physics D: Applied Physics*, vol. 39.3, p. R55, 2006.
- [137] A. Schutze, J. Y. Jeong, S. E. Babayan, J. Park, G. S. Selwyn and R. F. Hicks, "The atmospheric-pressure plasma jet: a review and comparison to other plasma sources," *IEEE transactions on plasma science*, vol. 26(6), pp. 1685-1694, 1998.
- [138] K. Burm, "Calculation of the Townsend discharge coefficients and the Paschen curve coefficients," *Contributions to Plasma Physics*, vol. 47(3), pp. 177-182, 2007.
- [139] Y. Fu, J. Krek, P. Zhang and J. P. Verboncoeur, "Evaluating microgap breakdown mode transition with electric field non-uniformity," *Plasma Sources Science and Technology*, vol. 27(9), p. 095014, 2018.
- [140] R. Massarczyk, P. Chu, C. Dugger, S. R. Elliott, K. Rielage and X. Wenqin, "Paschen's law studies in cold gases," *Journal of Instrumentation*, vol. 12.06, p. P06019, 2017.
- [141] A. Peschot, C. Poulain, N. Bonifaci and O. Lesaint, "Electrical breakdown voltage in micro- and submicrometer contact gaps (100nm-10µm) in air and nitrogen," *2015 IEEE 61st Holm Conference on Electrical Contacts (Holm)*, vol. IEEE, pp. 280-286, 2015.
- [142] S. Ishigami, K. Kawamata and S. Minegishi, "Measurement and Consideration of the Breakdown Voltage in a Micro Gap ESD," *Faculty of Engineering, Tohoku Gakuin University, Japan*, 2017.
- [143] ECE - University of Rochester, "Electrical breakdown limits for MEMS," *ECE234/434 Handout*.

-
- [144] A. M. Loveless, G. Meng, Q. Ying, F. Wu, K. Wang, Y. Cheng and A. L. Garner, "The transition to Paschen's law for microscale gas breakdown at subatmospheric pressure," *Scientific reports*, vol. 9(1), pp. 1-7, 2019.
- [145] Solar Atmosphere, "Understanding Vacuum and Vacuum Measurement," *Vacuum Furnance Reference Series*, vol. 9, pp. 1-9, 2016.
- [146] B. Helmut, *Liquid Ring Vacuum Pumps, Compressors and Systems: Conventional and Hermetic Design.*, WILEY-VCH Verlag GmbH & Co ISBN: 3-527-31249-8, 2005.
- [147] M. Schmid, "«Vapor Pressure Calculator,» TU Wien-Institut für Angewandte Physik , 17 December 2018. [En línea]. Available: https://www.iap.tuwien.ac.at/www/surface/vapor_pressure.," TU Wien-Institut für Angewandte Physik, 2019. [Online]. Available: https://www.iap.tuwien.ac.at/www/surface/vapor_pressure.. [Accessed 10 February 2022].
- [148] L. D. GmbH, "Converting electrical energy into heat energy – measuring with the joule and wattmeter," *LD Physics Leaflets*, vol. P2.3.4.2, pp. 1-4.
- [149] M. I. o. T. (MIT), "Introduction to Engineering Heat Transfer," 2002. [Online]. Available: https://ocw.mit.edu/courses/aeronautics-and-astronautics/16-050-thermal-energy-fall-2002/lecture-notes/10_part3.pdf. [Accessed 12 December 2018].
- [150] F. P. Incropera, D. P. Dewitt, T. L. Bergman and A. S. Lavine, *Fundamentals of Heat and Mass Transfer* (sixth edition), United States of America: John Wiley & Sons, Inc., 2006.
- [151] S. B. Bopche and S. Arunkumar, "Determination of view factors by contour integral technique," *Annals of Nuclear Energy*, Vols. 36.11-12, pp. 1681-1688, 2009.
- [152] M. K. Gupta, K. J. Bumtariya, H. A. Shukla, P. Patel and Z. Khan, "Methods for Evaluation of Radiation View Factor: A Review," *Materials Today: Proceedings*, vol. 4(2), pp. 1236-1243, 2017.
- [153] D. S. Ghosh, "Basics of Ultrathin Metal Films and Their Use as Transparent Electrodes," in *Ultrathin Metal Transparent Electrodes for the Optoelectronics Industry*, Switzerland, Springer International Publishing, 2013.
- [154] G. Chen, P. Hui, K. Pita, P. Hing and L. Kong, "Conductivity drop and crystallites redistribution in gold film," *Applied Physics A*, 2005.
- [155] P. Warriar and A. Teja, "Effect of particle size on the thermal conductivity of nanofluids containing metallic nanoparticles," *Nanoscale research letters*, vol. 6(1), pp. 1-6, 2011.
- [156] D. Thuau, I. Koymen and R. Cheung, "A microstructure for thermal conductivity measurement of conductive thin films," *Microelectronic engineering*, vol. 88(8), pp. 2408-2412, 2011.
- [157] K. Tokunaga, N. Yoshida, Y. Kubota, N. Noda, Y. Imamura, T. Oku, A. Kurumada, T. Sogabe, T. Kato and L. Plöchl, "High heat flux test of actively cooled tungsten-coated carbon divertor mock-ups," *Fusion engineering and design*, vol. 49, pp. 371-376, 2000.

-
- [158] Z. Cheng, L. Liu, S. Xu, M. Lu and X. Wang, "Temperature dependence of electrical and thermal conduction in single silver nanowire," *Scientific reports*, vol. 5(1), pp. 1-12, 2015.
- [159] S. Acharya, "Single-Phase Convective Heat Transfer: Basic Equations and Solutions," in *Handbook of Thermal Science and Engineering*, Cham, Springer, 2018, pp. 363-390.
- [160] NIST, "Nitrogen," NIST Chemistry WebBook, SRD 69, 2023. [Online]. Available: <https://webbook.nist.gov/cgi/cbook.cgi?ID=C7727379&Mask=1#Thermo-Fluid>.
- [161] G. Sidebotham, "Nusselt number correlations," *Heat Transfer Modeling: An Inductive Approach*, pp. 351-375, 2015.
- [162] S. Kandlikar, S. Garimella, D. Li, S. Colin and M. R. King, "Heat transfer and fluid flow in minichannels and microchannels.," *elsevier*, 2005.
- [163] H. Okada, M. Baba, M. Furukawa, K. Yamane, H. Sekiguchi and A. Wakahara, "Formation of SiO₂ film by chemical vapor deposition enhanced by atomic species extracted from a surface-wave generated plasma," *AIP Conference Proceedings*, vol. 1807(1), p. 020006, 2017.
- [164] N. Hegedüs, K. Balázs and C. Balázs, "Silicon nitride and hydrogenated silicon nitride thin films: A review of fabrication methods and applications.," *Materials*, vol. 14(19), p. 5658, 2021.
- [165] D. Qin, X. Younan and G. M. Whitesides, "Soft lithography for micro- and nanoscale," *Nature protocols*, vol. 5(3), p. 491, 2010.
- [166] J. Grant, "Introduction to electron beam," *ENG5174: Nanofabrication (2016-17) - University of Glasgow*, 2016.
- [167] D. Qin, Y. Xia, J. A. Rogers, R. J. Jackman, X. M. Zhao and G. M. Whitesides, "Microfabrication, Microstructures and Microsystem," *Department of Chemistry and Chemical Biology, Harvard University, Cambridge, MA 0213*.
- [168] "How to choose the right photomask to fabricate your Su-8 microfluidic mold?," Elveflow, an Elveflow brand, 2021. [Online]. Available: <https://www.elveflow.com/microfluidic-reviews/soft-lithography-microfabrication/su-8-photolithography-photomask/>.
- [169] G. J. Zinsmeister, "Quartz-The Ultimate Mask Material For Optical Lithography?," *Submicron Lithography I*, vol. 333, pp. 40-47, 1982.
- [170] Y. Zhang, "Photolithography and Optical Inspection," *ENG5174: Nanofabrication (2016-17) - University of Glasgow*, 28 September 2016.
- [171] H. J. Levinson, *Principles of Lithography*, Washington, USA: SPIE Press, 2005.
- [172] M. J. Madou, *Fundamentals of Microfabrication: The Science of Miniaturization*. Second Edition., vol. Secon, United States: CRC Press, 2002.
- [173] "MEGAPOSIT™ SPR™220 series photoresists," *Rohm and Haas Electronic Materials*, vol. Rev. 1, p. ME04N097, 2004.

-
- [174] J. M. Quero, F. Perdignes and C. Aracil, "Smart Sensors and MemS," in *Microfabrication technologies used for creating smart devices for industrial applications*, Woodhead Publishing, 2018, pp. 291-311.
- [175] M. M. Morshed and S. M. Daniels, "Effect of Positive Photoresist on Silicon Etching by Reactive Ion Etching Process.," *IEEE Transactions on Plasma Science*, vol. 38(6), pp. 1512-1516, 2010.
- [176] C. Farmer, "JWNC Wiki: MA6 & MA8 output power (measured power under different modes/filters)," [Online]. Available: https://glamy.sharepoint.com/:x:/g/personal/corrie_farmer_glasgow_ac_uk/Ed3nr6c_AmtFs-yONq39uKYBzV9_uMGORuVSvo-KryPdSQ?e=eaGESa. [Accessed 9 November 2021].
- [177] T. A. Brunner and C. A. Fonseca, "Optimum tone for various feature types: positive versus negative," *Advances in Resist Technology and Processing XVIII*, vol. 4345, pp. 30-37, 2001.
- [178] R. Hogg and P. Dobson, "Optical Lithography & Lab Session Process Flow," *ENG5055: Micro- and Nanotechnology - University of Glasgow*, 2015.
- [179] M. D. Levenson, N. S. Viswanathan and R. A. Simpson, "Improving resolution in photolithography with a phase-shifting mask," *IEEE Transactions on electron devices*, vol. 29.12, pp. 1828-1836, 1982.
- [180] D. W. Schubert, "Spin coating as a method for polymer molecular weight determination," *Polymer Bulletin*, vol. 38(2), pp. 177-184, 1997.
- [181] "RCD8 Coater & Developer," SÜSS MicroTec SE, 2021. [Online]. Available: <https://www.suss.com/en/products-solutions/coater-developer/rcd8>. [Accessed 12 November 2021].
- [182] MicroChemical, "Spin-Coating," [Online]. Available: https://www.microchemicals.com/technical_information/spin_coating_photoresist.pdf. [Accessed 11 November 2021].
- [183] MicroChemicals, "SOFTBAKE," [Online]. Available: https://www.microchemicals.com/technical_information/softbake_photoresist.pdf.
- [184] E. Kukharenka and M. Kraft, "Realization of electroplating molds with thick positive SPR 220-7 photoresist," *Journal of Materials Science: Materials in Electronics*, vol. 14(5), pp. 319-322, 2003.
- [185] Z. Cui, *Nanofabrication: Principles, Capabilities and Limits*, Switzerland: Springer Nature, 2017.
- [186] M. E. Van Valkenburg, *Reference Data for Engineers: Radio, Electronics, Computers and Communications - 9th Edition.*, United States: Newnes, 2002.
- [187] N. P. Avinash, V. J. Logeeswaran and M. Saif Islam, "Wet and Dry Etching," *University of California, Davis. California*.

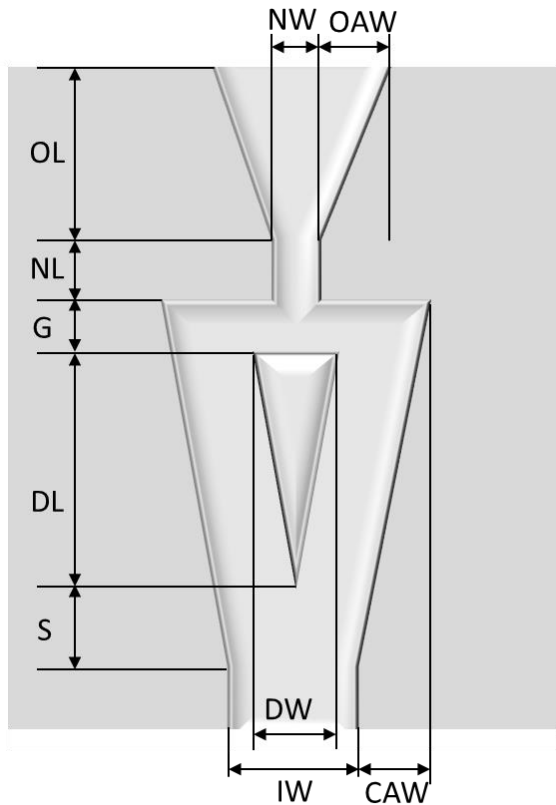
-
- [188] "Chapter 9 Etch," National Taipei University of Technology, 2006. [Online]. Available: http://www.me.ntut.edu.tw/introduction/teacher/lu/IC%20fabrication_GA/IC_ch09.pdf.
- [189] Y. Tang, A. Sandoughsaz, K. J. Owen and K. Najafi, "Ultra deep reactive ion etching of high aspect-ratio and thick silicon using a ramped-parameter process," *Journal of Microelectromechanical Systems*, vol. 27(4), pp. 686-697, 2018.
- [190] J. C. Wirth and J. J. Shepard, "ICP RIE - Birck Nanotechnology Center Wiki," 6 March 2020. [Online]. Available: <https://wiki.itap.purdue.edu/display/BNCWiki/ICP+RIE>. [Accessed 13 December 2021].
- [191] James Watt Nanofabrication Centre, "Estrelas TWE 100µm comparison," 202. [Online]. Available: https://glamy.sharepoint.com/:p:/g/personal/corrie_farmer_glasgow_ac_uk/EVNjT8VCx4lBt4pjwHWuj7sBxTYMeYiwNFrmuFcDLoZzWw?e=8mA6u6. [Accessed 6 January 2022].
- [192] "Oxford Instruments - Plasma Technology," 2021. [Online]. Available: www.oxford-instruments.com/products/etching-deposition-and-growth/processes/etching-processes/silicon. [Accessed 29 November 2021].
- [193] M. A. Blauw, T. Zijlstra and E. W. J. M. van der Drift, "Balancing the etching and passivation in time-multiplexed deep dry etching of silicon," *ournal of Vacuum Science & Technology B: Microelectronics and Nanometer Structures Processing, Measurement, and Phenomena*, vol. 19(6), pp. 2930-2934, 2001.
- [194] B. Chang, "Technology Development of 3D Silicon Plasma Etching Processes for Novel Devices," *Technical University of Denmark*, 2018.
- [195] SantoLubes LLC, "SANTOVAC® FLUIDS," 2021. [Online]. Available: <https://www.santolubes.com/products/santovac/>. [Accessed 2021 December 2021].
- [196] V. Teixeira, J. Carneiro, P. Carvalho, E. Silva, S. Azevedo and C. Batista, "High barrier plastics using nanoscale inorganic films," in *Multifunctional and nanoreinforced polymers for food packaging*, Woodhead Publishing, 2011, pp. 285-315.
- [197] M. R. Amirzada, A. Tatzel, V. Viereck and H. Hillmer, "Surface roughness analysis of SiO₂ for PECVD, PVD and IBD on different substrates," *Applied Nanoscience*, vol. 6(2), pp. 215-222, 2016.
- [198] Y. T. Kim, D. S. Kim and D. H. Yoon, "PECVD SiO₂ and SiON films dependant on the rf bias power for low-loss silica waveguide," *Thin Solid Films*, Vols. 475(1-2), pp. 271-274, 2005.
- [199] James Watt Nanofabrication Centre, "Deposition," 16 June 2021. [Online]. Available: <http://jwnc.eng.gla.ac.uk/index.php?module=process&cmd=wiki>. [Accessed 26 December 2021].
- [200] Plassys Electron Beam Evaporation System, "Universtiy of Pittsburgh: Gertrude E. & John M. Petersen Institute of Nanoscience and Engineering," 201. [Online]. Available: <http://www.nano.pitt.edu/node/468>. [Accessed 26 December 2021].

-
- [201] "Plassys," Manufacturer of equipment for thin film deposition and etching, 2018. [Online]. Available: <https://plassys.com/sputtering-systems-hv-uhv/>. [Accessed 26 December 2021].
- [202] Y. Lin, *Advanced nano deposition methods*, John Wiley & Sons, 2016.
- [203] J. Sarkar, "Chapter 2: Sputtering and Thin Film Deposition," in *Sputtering Materials for VLSI and Thin Film Devices*, William Andrew, 2010, pp. 93-170.
- [204] V. Cremers, P. L. Riikka and J. Dendooven, "Conformality in atomic layer deposition: Current status overview of analysis and modelling," *Applied Physics Reviews*, vol. 6(2), p. 021302, 2019.
- [205] D. P. Pulsifer, A. Lakhtakia and R. J. Martín-Palma, "Improved conformal coatings by oblique-angle deposition for bioreplication.," *Applied Physics Letters*, vol. 95(19), p. 193701, 2009.
- [206] Z. Wang, P. R. West, X. Meng, N. Kinsey, V. M. Shalaev and A. Boltasseva, "Angled physical vapor deposition techniques for non-conformal thin films and three-dimensional structures," *MRS Communications*, vol. 6(1), pp. 17-22, 2016.
- [207] T. C. Tisone and J. Drobek, "Diffusion in thin film Ti–Au, Ti–Pd, and Ti–Pt couples," *Journal of Vacuum Science and Technology*, vol. 9(1), pp. 271-275, 1972.
- [208] M. Todeschini, A. Bastos da Silva Fanta, F. Jensen, J. B. Wagner and A. Han, "Influence of Ti and Cr adhesion layers on ultrathin Au films." *ACS applied materials & interfaces*, *ACS applied materials & interfaces*, vol. 9(42), pp. pp.37374-37385, 2017.
- [209] T. Betancourt and L. Brannon-Peppas, "Micro-and nanofabrication methods in nanotechnological medical and pharmaceutical devices.," *International journal of nanomedicine* , vol. 1(4), p. 483, 2006.
- [210] H. S. Kim, R. H. Blick, D. M. Kim and C. B. Eom, "Bonding silicon-on-insulator to glass wafers for integrated bio-electronic circuits," *Applied Physics Letters*, vol. 85(12), pp. 2370-2372, 2004.
- [211] P. Merz, H. J. Quenzer, H. Bernt, B. Wanger and M. Zoberbier, "A novel micromachining technology for structuring borosilicate glass substrates," *TRANSDUCERS'03. 12th International Conference on Solid-State Sensors, Actuators and Microsystems. Digest of Technical Papers (Cat. No. 03TH8664)*, vol. Vol. 1, pp. 258-261, 2003.
- [212] "Cyclotene Series," A-Gas Electronic Materials, 2022. [Online]. Available: <https://www.agasem.com/suppliers/dupont-formerly-dow/semiconductor-manufacturing/bcb-products/>. [Accessed 18 february 2022].
- [213] "nHV Series," HVM Technology, [Online]. Available: <https://www.hvmtech.com/nhv-series>.
- [214] R. J. Adrian, "Particle-imaging techniques for experimental fluid mechanics," *Annual review of fluid mechanics*, vol. 23(1), pp. 261-304, 1991.
- [215] T. S. Andreou, "Investigation of flow phenomena occurring in axial swirlers and their design optimisation," *Doctoral dissertation, University of Glasgow*, 2022.

-
- [216] A. Maddox and E. Gutmark, "Experimental study of a lenticular jet," *Experiments in fluids*, vol. 61(4), pp. 1-16, 2020.
- [217] A. T. Kirkpatrick and A. E. Kenyon, "Flow characteristics of three-dimensional wall jets," *Transactions-american society of heating refrigerating and air conditioning engineers*, vol. 104, pp. 1755-1762, 1998.
- [218] A. Kelsey, R. Bettis and G. Tickle, "Modelling of angled jet impingement on large flat surfaces," *Institution of Chemical Engineers Symposium-Hazards XVIII*, 2004.
- [219] C. C. Chrisman, "Evaluation of the Free Jet Spreading Rate Parameter for Axi-symmetric Flow of Air at Mach Number Three," *Doctoral dissertation, Oklahoma State University*, 1962.
- [220] E. H. Hall, "On a new action of the magnet on electric currents," *American Journal of Mathematics*, vol. 2(3), pp. 287-292, 1879.
- [221] M. F. Closs, "Numerical Modelling and Optimisation of Radio-Frequency Ion Thrusters," *Herbert Utz Verlag*, vol. 37, 2002.

Appendices

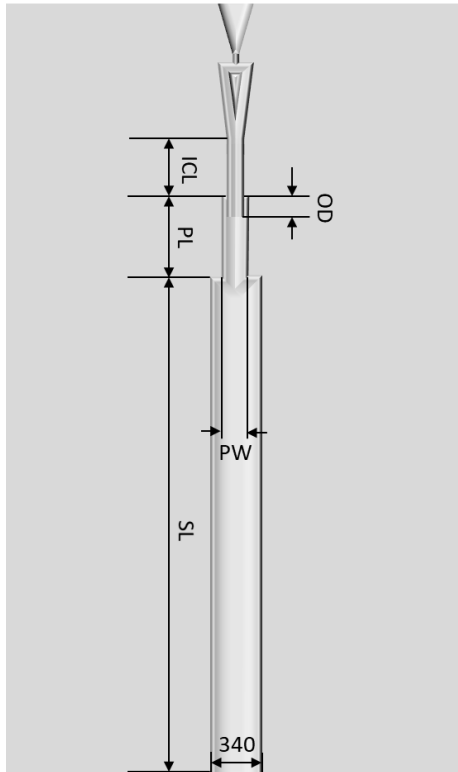
A. Geometrical dimensions of the micro-thruster chip



- OL – Outlet length
- NL – Neck length
- G - Gap
- DL – Divider length
- S – Separation
- OAW – Outlet's Angle screen width
- NW – Neck width
- DW –Divider's width
- CAW – Channel's Angle screen width
- IW – Inlet width

	XS	S	M	L
NW	10	20	50	70
OAW	4	7	18	37
OL	10	20	50	100
NL	10	20	50	100
G	5	10	10	10
	10	20	20	20
	20	50	50	50
	30	75	75	75
	50	100	100	100
DL	90	180	300	400
S	10	20	50	100
DW	31	64	105	142
IW	40	60	100	200
CAW	27	53	63	101

Appendices



SL – Supply Channel Length

PL – Plenum Length

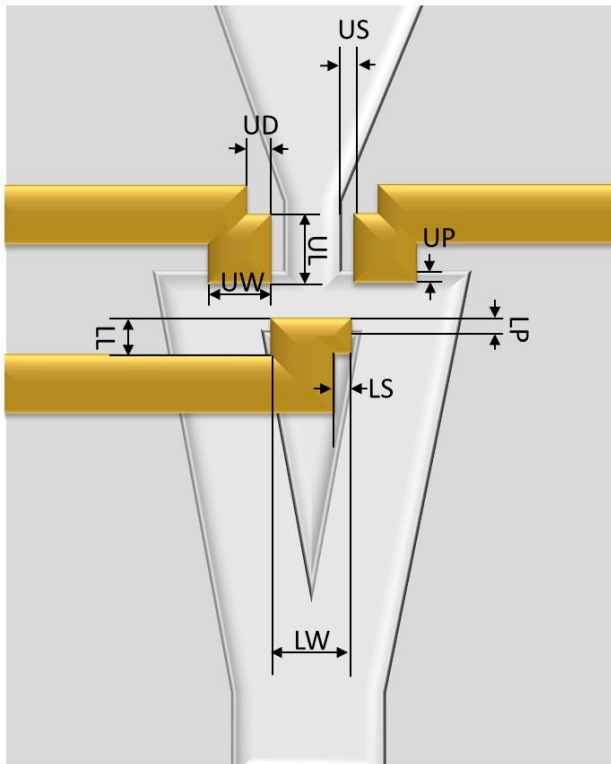
ICL – Inlet Channel Length

PW – Plenum Width

OD – Overlapped Distance

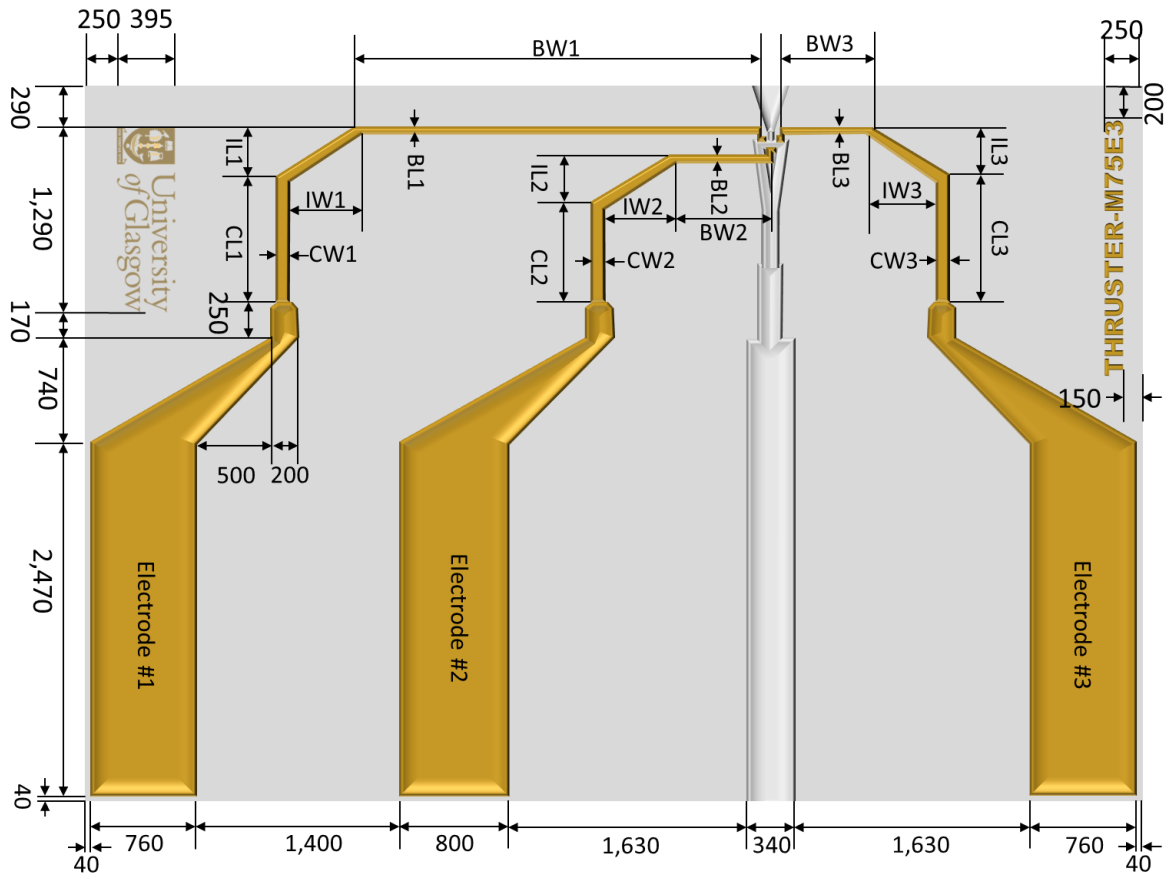
		ICL	OD	PL	SL	PW
L	100	250	40	500	3250	266
	75	272	40	500	3250	266
	50	297	40	500	3250	266
	20	327	40	500	3250	266
	10	337	40	500	3250	266
M	100	417	40	500	3250	166
	75	442	40	500	3250	166
	50	468	40	500	3250	166
	20	497	40	500	3250	166
	10	507	40	500	3250	166
S	100	610	40	500	3250	126
	75	635	40	500	3250	126
	50	660	40	500	3250	126
	20	690	40	500	3250	126
	10	700	40	500	3250	126
XS	50	770	40	500	3250	126
	30	790	40	500	3250	126
	20	800	40	500	3250	126
	10	810	40	500	3250	126
	5	815	40	500	3250	126

Appendices



UW – Upper Electrode Width
 UL – Upper Electrode Length
 US – Upper Separation
 UP – Upper Protruding Surface
 UD – Upper displacement
 LW – Lower Electrode Width
 LL – Lower Electrode Length
 LS – Lower Separation
 LP – Upper Protruding Surface

GAP	SIZE	UW	UL	US	UP	UD	LW	LL	LS	LP
100 μ m	S	25	25	15	10	10	38	26	10	10
	M	55	50	15	20	23	70	43	13	20
	L	75	90	15	20	30	96	48	20	20
75 μ m	S	25	25	15	10	10	38	26	10	10
	M	55	50	15	20	23	70	43	13	20
	L	75	90	15	20	30	96	48	20	20
50 μ m	XS	16	23	10	6	6	16	16	4	6
	S	25	25	15	10	10	38	26	10	10
	M	55	50	15	20	23	70	43	13	20
	L	75	90	15	20	30	96	48	20	20
20 μ m	XS	16	23	10	6	6	16	16	4	6
	S	25	23	15	8	10	38	24	10	8
	M	55	40	15	8	23	70	33	13	8
	L	75	90	15	8	30	96	37	20	8
10 μ m	XS	16	21	10	4	4	16	14	4	6
	S	23	25	15	4	10	38	23	10	4
	M	55	36	15	4	23	70	30	13	4
	L	75	90	15	4	30	96	34	20	4
30 μ m	XS	16	23	10	6	6	16	16	4	6
5 μ m	XS	23	19	3	2	7	16	13	4	2



	XS	S	M	L
CL1	860	873	867	867
IL1	343	333	339	339
BL1	15	25	55	75
CW1	25	45	100	140
IW1	527	527	500	480
BW1	2842	2838	2834	2844
CL2	810	737	713	689
IL2	327	327	327	327
BL2	15	25	55	75
CW2	25	45	100	140
IW2	537	527	500	500
BW2	655	659	672	659
CL3	863	873	873	873
IL3	343	333	333	334
BL3	15	25	55	75
CW3	25	45	100	140

Appendices

IW3	537	527	500	480
BW3	642	613	640	644

CL1 routing connector length

IL1 routing inclination length

BL1 Routing base length

CW1 routing connector width

IW1 routing inclination width

BW1 routing base width

Appendices

B. Micro-thruster performance as a cold gas thruster based on dsmcFoam+.

#	Separation	Angle	Inlet width	Length	Outlet length	Gap distance	Outlet angle (θ)	Outlet length (OL)	P (Pa)	Thrust (nN)
1	5	60	100	0	20	50	0	0	30000	203
2	20	60	100	250	20	50	0	0	30000	232
3	40	60	100	250	20	50	0	0	30000	315
4	50	60	100	250	20	50	0	0	30000	215
5	60	60	100	250	20	50	0	0	30000	291
6	80	60	100	250	20	50	0	0	30000	226
7	100	60	100	250	20	50	0	0	30000	239
8	100	20	100	250	20	50	0	0	30000	222
9	100	30	100	250	20	50	0	0	30000	296
10	100	40	100	250	20	50	0	0	30000	193
11	100	50	100	250	20	50	0	0	30000	422
12	100	60	100	250	20	50	0	0	30000	306
13	100	70	100	250	20	50	0	0	30000	198
14	100	80	100	250	20	50	0	0	30000	225
15	100	50	150	250	20	50	0	0	30000	259
16	100	50	300	250	20	50	0	0	30000	253
17	100	50	510	250	20	50	0	0	30000	190
18	100	50	840	250	20	50	0	0	30000	277
19	100	50	150	200	20	50	0	0	30000	306
20	100	50	150	250	20	50	0	0	30000	259
21	100	50	150	300	20	50	0	0	30000	227
22	100	50	150	400	20	50	0	0	30000	103
23	100	50	150	500	20	50	0	0	30000	87
24	100	50	150	300	20	50	0	0	30000	227
25	100	50	150	300	50	50	0	0	30000	227
26	100	50	150	300	60	50	0	0	30000	227
27	100	50	150	300	80	50	0	0	30000	227
28	100	50	150	300	100	50	0	0	30000	227
29	100	50	150	300	50	5	0	0	30000	10
30	100	50	150	300	50	50	0	0	30000	504
31	100	50	150	300	50	100	0	0	30000	113
32	5	60	100	250	20	50	0	0	1000	3
33	20	60	100	250	20	50	0	0	1000	3
34	40	60	100	250	20	50	0	0	1000	4
35	50	60	100	250	20	50	0	0	1000	4
36	60	60	100	250	20	50	0	0	1000	4
37	80	60	100	250	20	50	0	0	1000	4
38	100	60	100	250	20	50	0	0	1000	4
39	100	20	100	250	20	50	0	0	1000	3
40	100	30	100	250	20	50	0	0	1000	4

Appendices

41	100	40	100	250	20	50	0	0	1000	4
42	100	50	100	250	20	50	0	0	1000	4
43	100	60	100	250	20	50	0	0	1000	4
44	100	70	100	250	20	50	0	0	1000	4
45	100	80	100	250	20	50	0	0	1000	4
46	100	50	150	250	20	50	0	0	1000	4
47	100	50	300	250	20	50	0	0	1000	4
48	100	50	510	250	20	50	0	0	1000	4
49	100	50	840	250	20	50	0	0	1000	4
50	100	50	150	200	20	50	0	0	1000	4
51	100	50	150	250	20	50	0	0	1000	4
52	100	50	150	300	20	50	0	0	1000	4
53	100	50	150	400	20	50	0	0	1000	3
54	100	50	150	500	20	50	0	0	1000	3
55	100	50	150	300	20	50	0	0	1000	4
56	100	50	150	300	40	50	0	0	1000	3
57	100	50	150	300	50	50	0	0	1000	3
58	100	50	150	300	60	50	0	0	1000	3
59	100	50	150	300	80	50	0	0	1000	2
60	100	50	150	300	100	50	0	0	1000	2
62	100	50	150	300	50	20	0	0	1000	2
63	100	50	150	300	50	40	0	0	1000	3
64	100	50	150	300	50	50	0	0	1000	3
65	100	50	150	300	50	60	0	0	1000	3
66	100	50	150	300	50	80	0	0	1000	3
67	100	50	150	300	50	100	0	0	1000	3
68	100	50	100	300	20	50	20	50	1000	5
69	100	50	100	300	20	50	30	50	1000	4
70	100	50	100	300	20	50	40	50	1000	3
71	100	50	100	300	20	50	50	50	1000	3
72	100	50	100	300	20	50	60	50	1000	3
73	100	50	100	300	20	50	70	50	1000	3
74	100	50	100	300	20	50	20	50	30000	246
75	100	50	100	300	20	50	30	50	30000	346
76	100	50	100	300	20	50	40	50	30000	185
77	100	50	100	300	20	50	50	50	30000	286
78	100	50	100	300	20	50	60	50	30000	482
82	100	50	150	300	20	50	80	50	1000	3
83	100	50	150	300	20	50	80	50	1000	3
84	100	50	150	300	20	50	80	100	1000	3
85	100	50	150	300	20	50	80	200	1000	3
86	100	50	150	300	20	50	80	300	1000	2

Appendices

C. Performance of plasma thrust based on dsmcFoam+.

#	d (μm)	I (μA)	V	P (Kpa)	Thrust (nN)
1	10	1000	200	10	37
2	10	1000	400	10	22
3	10	1000	800	10	23
4	10	1000	1200	10	539
5	10	1000	200	50	234
6	10	1000	400	50	211
7	10	1000	800	50	34
8	10	1000	1200	50	144
9	10	1000	200	100	499
10	10	1000	400	100	472
11	10	1000	800	100	42
12	10	1000	1200	100	141
13	10	100	200	10	37
14	10	100	400	10	36
15	10	100	800	10	7
16	10	100	1200	10	15
17	10	100	200	50	235
18	10	100	400	50	233
19	10	100	800	50	161
20	10	100	1200	50	20
21	10	100	200	100	498
22	10	100	400	100	499
23	10	100	800	100	445
24	10	100	1200	100	131
25	10	10	200	10	37
26	10	10	400	10	37
27	10	10	800	10	35
28	10	10	1200	10	11
29	10	10	200	50	233
30	10	10	400	50	233
31	10	10	800	50	233
32	10	10	1200	50	226
33	10	10	200	100	498
34	10	10	400	100	497
35	10	10	800	100	498
36	10	10	1200	100	494
37	10	1	200	10	37
38	10	1	400	10	37
39	10	1	800	10	37
40	10	1	1200	10	36
41	10	1	200	50	234

Appendices

42	10	1	400	50	234
43	10	1	800	50	233
44	10	1	1200	50	234
45	10	1	200	100	499
46	10	1	400	100	498
47	10	1	800	100	497
48	10	1	1200	100	463
49	50	1000	200	10	110
50	50	1000	400	10	425
51	50	1000	800	10	6
52	50	1000	1200	10	237
53	50	1000	200	50	555
54	50	1000	400	50	953
55	50	1000	800	50	1587
56	50	1000	1200	50	29
57	50	1000	200	100	1082
58	50	1000	400	100	1504
59	50	1000	800	100	1773
60	50	1000	1200	100	2820
61	50	100	200	10	111
62	50	100	400	10	117
63	50	100	800	10	510
64	50	100	1200	10	1058
65	50	100	200	50	557
66	50	100	400	50	552
67	50	100	800	50	910
68	50	100	1200	50	1459
69	50	100	200	100	1109
70	50	100	400	100	1099
71	50	100	800	100	1352
72	50	100	1200	100	5191
73	50	10	200	10	111
74	50	10	400	10	110
75	50	10	800	10	118
76	50	10	1200	10	222
77	50	10	200	50	549
78	50	10	400	50	547
79	50	10	800	50	551
80	50	10	1200	50	558
81	50	10	200	100	1095
82	50	10	400	100	1093
83	50	10	800	100	1094
84	50	10	1200	100	1100
85	50	1	200	10	113
86	50	1	400	10	110
87	50	1	800	10	111

Appendices

88	50	1	1200	10	109
89	50	1	200	50	548
90	50	1	400	50	558
91	50	1	800	50	549
92	50	1	1200	50	549
93	50	1	200	100	1112
94	50	1	400	100	1094
95	50	1	800	100	1096
96	50	1	1200	100	1095
97	100	1000	200	10	121
98	100	1000	400	10	170
99	100	1000	800	10	2076
100	100	1000	1200	10	682
101	100	1000	200	50	594
102	100	1000	400	50	650
103	100	1000	800	50	3271
104	100	1000	1200	50	2577
105	100	1000	200	100	1185
106	100	1000	400	100	1230
107	100	1000	800	100	5506
108	100	1000	1200	100	6788
109	100	100	200	10	122
110	100	100	400	10	122
111	100	100	800	10	282
112	100	100	1200	10	879
113	100	100	200	50	604
114	100	100	400	50	620
115	100	100	800	50	599
116	100	100	1200	50	1166
117	100	100	200	100	1183
118	100	100	400	100	1186
119	100	100	800	100	1229
120	100	100	1200	100	5411
121	100	10	200	10	123
122	100	10	400	10	121
123	100	10	800	10	121
124	100	10	1200	10	134
125	100	10	200	50	602
126	100	10	400	50	595
127	100	10	800	50	594
128	100	10	1200	50	602
129	100	10	200	100	1181
130	100	10	400	100	1188
131	100	10	800	100	1180
132	100	10	1200	100	1187
133	100	1	200	10	121

Appendices

134	100	1	400	10	122
135	100	1	800	10	123
136	100	1	1200	10	122
137	100	1	200	50	593
138	100	1	400	50	603
139	100	1	800	50	592
140	100	1	1200	50	600
141	100	1	200	100	1182
142	100	1	400	100	1184
143	100	1	800	100	1185
144	100	1	1200	100	1182

D. Traveller procedure for the nanofabrication of the plasma-based micro-thruster chip

STAGE 1 MICROTUBBING CHANNEL PATTERN ETCHING

1. **Cleans** on dipper, clean wafer 3 mins ultrasonic acetone, isopropanol, methanol, DI rinse, N2 dry.
2. **Dehydration bake** 2mins 120°C hotplate.
3. **Spin**: SPR220-7.0 on RCD8 automated spinner.
*60s@70rpm@400 rpm/s (spread)
*30s@1200rpm@1200 rpm/s (final thickness)
*2s@0rpm@1200 rpm/s (slow to stop)
4. **Softbake** on hotplate 90s@118 °C setpoint.
5. **Maskplate clean**: 5" mask compatible glass cleaning tanks: soak in acetone glass tank 5 min, rinse in DI glass tank 3 mins, N2 blow dry.
6. **Exposure**: MA6 standard broadband hard contact. Good alignment using wafer edges and flat. Expose 33 sec using cleaned mask.
7. **Develop**: prepare three dog bowls. Two containing 300 ml fresh MF-CD-26 each, and one with DI. STATIC develop 2 mins in 1st bowl + static develop 1min in 2nd bowl, 5mins DI rinse, N2 dry.
8. **Descum** plasmafab 2 mins 100 W
9. **Dry etching**: Bosch process in Estrelas for a 320 µm-depth etch .
*Recipe: 00_BSH_J05_IC_fpl_25-99-_TWE_R08T7_DbE2b_LF60W, with Cycle[152, 153, 154, 154] for [stage1, Stage2, stage3, stage4] . Timings on each stage[5.25, 5.45, 5.65, 5.85]secs for a total process time of 56.53 min.
10. **Cleans** on dipper, clean wafer 3 mins ultrasonic acetone, isopropanol, methanol, DI rinse, N2 dry.

Appendices

STAGE 2 MICRONOZZLE PATTERN ETCHING

11. **Dehydration bake** 2 mins 120 °C hotplate.
12. **Spin:** SPR220-7.0 on RCD8 automated spinner.
 - *60s@70rpm@400 rpm/s (spread)
 - *30s@1200rpm@1200 rpm/s (final thickness)
 - *2s@0rpm@1200 rpm/s (slow to stop)
13. **Softbake** on hotplate 90s@118 °C setpoint.
14. **Maskplate clean:** 5" mask compatible glass cleaning tanks: soak in acetone glass tank 5 min, rinse in DI glass tank 3 mins, N2 blow dry.
15. **Exposure:** MA6 standard broadband hard contact. Good alignment using wafer edges and flat. Expose 33 sec using cleaned mask.
16. **Develop:** prepare three dog bowls. Two containing 300 ml fresh MF-CD-26 each, and one with DI. STATIC develop 2 mins in 1st bowl + static develop 1 min in 2nd bowl, 5 mins DI rinse, N2 dry.
17. **Descum** plasmafab 2 mins 100 W
18. **Dry etching:** Silicon mixed etching process in Estrelas for a 100 µm-depth etch .
 - *Preconditioning time: 10 minutes
 - *Recipe: 000 MIX J05 Ic fpH RYT1 HF Test for 64.31 minutes (etching rate 1.55µm/min)
19. **Cleans** on dipper, clean wafer 3mins ultrasonic acetone, isopropanol, methanol, DI rinse, N2 dry.

STAGE 3 ELECTRODE PATTERN ETCHING

20. **Dehydration bake** 2 mins 120 °C hotplate.
21. **Spin:** SPR220-7.0 on RCD8 automated spinner.
 - *60s@70rpm@400 rpm/s (spread)

Appendices

- *30s@1200rpm@1200 rpm/s (final thickness)
- *2s@0rpm@1200 rpm/s (slow to stop)
- 22. **Softbake** on hotplate 90s@118 °C setpoint.
- 23. **Maskplate clean:** 5" mask compatible glass cleaning tanks: soak in acetone glass tank 5min, rinse in DI glass tank 3 mins, N2 blow dry.
- 24. **Exposure:** MA6 standard broadband hard contact. Good alignment using wafer edges and flat. Expose 33 sec using cleaned mask.
- 25. **Develop:** prepare three dog bowls. Two containing 300 ml fresh MF-CD-26 each, and one with DI. STATIC develop 2 mins in 1st bowl + static develop 1 min in 2nd bowl, 5 mins DI rinse, N2 dry.
- 26. **Descum** plasmafab 2 mins 100 W
- 27. **Dry etching:** Silicon mixed etching process in Estrelas for a 510 nm-depth etch .
 - *Preconditioning time: 10 minutes
 - *Recipe: 000 MIX J05 Ic fpH RYT1 HF Test for 20 secs (etching rate: 1.55 µm/min)
- 28. **Cleans** on dipper, clean wafer 3mins ultrasonic acetone, isopropanol, methanol, DI rinse, N2 dry.
- 29. **Deposition** on PECVD SPTS Delta for 5 µm-thin SiO₂ layer@300 °C/high rate/standard.
 - *Recipe: Jash_HiRateOx_300C_5um.devModRpe
- 30. **Cleans** on dipper, clean wafer 3 mins ultrasonic acetone, isopropanol, methanol, DI rinse, N2 dry.

STAGE 4 ELECTRODES METALLISATION

- 31. **Dehydration bake** 2 mins 120 °C hotplate.
- 32. **Spin:** SPR220-7.0 on RCD8 automated spinner. (first layer)
 - *60s@70rpm@400 rpm/s (spread)

Appendices

- *30s@800rpm@800 rpm/s (final thickness)
- *2s@0rpm@1200 rpm/s (slow to stop)
- 33. **Softbake** on hotplate 90s@118 °C setpoint.
- 34. **Spin**: SPR220-7.0 on RCD8 automated spinner. (second layer)
 - *60s@70rpm@400 rpm/s (spread)
 - *30s@450rpm@450 rpm/s (final thickness)
 - *2s@0rpm@1200 rpm/s (slow to stop)
- 35. **Softbake** on hotplate 90s@80 °C setpoint.
- 36. **Softbake** inside oven 20min@90 °C setpoint, followed by 20min@120 °C.
- 37. **Maskplate clean**: 5" mask compatible glass cleaning tanks: soak in acetone glass tank 5 min, rinse in DI glass tank 3 mins, N2 blow dry.

-----From this point the steps are repeated 11 times in the following sequence-----
- 38. **Exposure**: MA6 standard broadband hard contact. Good alignment using wafer edges and flat. Expose 33 sec using cleaned mask.
- 39. **Develop**: prepare three dog bowls. Two containing 300 ml fresh MF-CD-26 each, and one with DI. STATIC develop 2 mins in 1st bowl + static develop 1min in 2nd bowl, 5 mins DI rinse, N2 dry.
-----End of the repetitive cycle-----
- 40. **Descum** plasmafab 2 mins 100W
- 41. **Metallisation**: on Plassys IV, deposition of Ti (30nm-thick)/Au (500nm-thick) with 30° tilt + rotational process.
- 42. **Lift off**: On dipper, wafer placed with acetone and left in a warm bath for a minimum of 1 hour.
Used of plastic pipette to remove the leftover metallic pieces.
- 43. **Clean** on dipper 3 mins DI rinse and N2 dry.

Appendices

44. **Cleaving:** scribe straight lines with a diamond tip pen around the microdevice on wafer's surface. Add pressure on correct points to cleave.

STAGE 5 GLASS COVER

45. **Laser etching:** on Trotec speedy 300 place a 18 mm x 18 mm x 0.17 mm borosilicate glass slides at 40 W, 15 m/s speed and 10,000 PPI/Hz with 10 passes on cutting mode.
46. **Cleaving:** hold with tweezers the glass slide, pulling the segment of the glass pattern at the same direction of the laser etch until it break off.

STAGE 6 BONDING

47. **Pouring:** on both extreme sides(right & left sides) of the glass cover pour around 1/4 of a BCB pippete drop with a stick.
48. **Bonding:** on Flip Chip Bonder place the chip substrate on vacuum tip and the glass cover on the stage, *Simultaneously heating by 200°C(tip) and 260 °C(stage) for 10 minutes at 10 N.
49. **Pouring** a BCB drop with a pippete on aperture between the micropiping channel inlet and the needle. Afterwards, place the needle with chip on vertically standing inside a peaker.
50. **Curing** on oven for 20min@260 °C.

E. jet half width velocities results from PIV experimental results

X/D	Inlet P	Outlet P	Y/Dmax	Y/D0.5	V0.5(Y/D)	V _{max_norm}	K2	C _{2u}
20	2	0.3	2.519	1.13355	0.034	0.047	15.64	-20.00
40	4	0.3	3.148	1.4166	0.033	0.098	25.02	-40.00
20	12	0.3	3.149	1.41705	0.032	0.079	12.51	-20.00

Appendices

20	10	0.3	3.149	1.41705	0.039	0.077	12.51	-20.00
20	10	0.7	3.737	1.68165	0.070	0.318	10.54	-19.99
20	12	0.5	4.358	1.9611	0.041	0.105	9.04	-20.00
20	4	0.3	4.409	1.98405	0.012	0.080	8.93	-20.00
20	8	0.7	4.49	2.0205	0.075	0.392	8.77	-19.99
40	2	0.9	4.801	2.16045	0.081	0.206	16.41	-40.00
20	10	0.5	5.046	2.2707	0.052	0.137	7.81	-19.99
20	4	0.7	5.126	2.3067	0.061	0.402	7.68	-19.99
20	2	0.9	5.23	2.3535	0.021	0.218	7.53	-20.00
20	10	0.9	5.626	2.5317	0.176	0.694	7.00	-19.97
20	2	0.5	5.66	2.547	0.019	0.084	6.96	-20.00
20	4	0.5	5.667	2.55015	0.074	0.255	6.95	-19.99
20	8	0.3	5.668	2.5506	0.003	2.834	6.95	-20.00
20	2	0.7	5.756	2.5902	0.018	0.096	6.84	-20.00
20	12	0.7	5.825	2.62125	0.123	0.326	6.76	-19.98
20	6	0.5	6.297	2.83365	0.113	0.220	6.26	-19.98
20	8	0.5	6.876	3.0942	0.083	0.162	5.73	-19.99
20	6	0.7	6.88	3.096	0.033	0.413	5.72	-19.99
60	2	0.5	6.927	3.11715	0.024	0.065	17.06	-60.00
40	12	0.3	6.927	3.11715	0.041	0.083	11.37	-40.00
40	10	0.3	6.927	3.11715	0.051	0.088	11.37	-40.00
20	6	0.9	7.126	3.2067	0.257	0.912	5.53	-19.95
20	4	0.9	7.151	3.21795	0.092	0.797	5.51	-19.98
60	10	0.5	7.564	3.4038	0.065	0.186	15.62	-60.00
40	2	0.7	7.626	3.4317	0.054	0.100	10.33	-39.99
20	12	0.9	7.756	3.4902	0.054	0.610	5.08	-19.99
60	4	0.3	8.186	3.6837	0.039	0.072	14.43	-60.00
40	6	0.3	8.816	3.9672	0.057	0.086	8.94	-39.99
40	2	0.5	8.817	3.96765	0.051	0.100	8.93	-39.99
60	2	0.9	8.817	4.4085	0.053	0.131	12.06	-60.00
20	8	0.9	8.886	4.443	0.097	0.798	3.99	-19.98
60	12	0.3	9.453	4.7265	0.004	0.066	11.25	-60.00
40	4	0.5	10.075	5.0375	0.057	0.269	7.04	-39.99
40	4	0.7	10.083	5.0415	0.070	0.405	7.03	-39.99
60	12	0.5	10.705	5.3525	0.061	0.165	9.93	-59.99
40	12	0.9	10.705	5.3525	0.210	0.863	6.62	-39.97
60	6	0.3	10.712	5.356	0.022	0.080	9.93	-60.00
40	10	0.7	10.713	5.3565	0.169	0.509	6.62	-39.97
40	6	0.7	10.713	5.3565	0.186	0.462	6.62	-39.97
40	6	0.9	11.335	5.6675	0.235	0.677	6.25	-39.96
20	6	0.3	11.96	5.98	0.012	0.083	2.96	-20.00
40	2	0.3	11.964	5.982	0.015	0.077	5.93	-40.00
40	10	0.5	11.964	5.982	0.027	0.201	5.93	-40.00
40	4	0.9	11.964	5.982	0.152	0.588	5.93	-39.97
60	6	0.5	11.971	5.9855	0.046	0.231	8.88	-59.99
60	8	0.7	11.973	5.9865	0.088	0.274	8.88	-59.99

Appendices

40	8	0.5	12.594	6.297	0.049	0.233	5.63	-39.99
60	8	0.5	12.594	6.297	0.076	0.206	8.44	-59.99
60	4	0.5	13.223	6.6115	0.069	0.192	8.04	-59.99
40	10	0.9	13.224	6.612	0.235	0.890	5.36	-39.96
40	8	0.9	13.853	6.9265	0.291	0.748	5.12	-39.94
60	2	0.3	14.483	7.2415	0.014	0.053	7.34	-60.00
40	6	0.5	14.483	7.2415	0.034	0.276	4.90	-39.99
60	12	0.7	15.113	7.5565	0.125	0.333	7.04	-59.98
40	12	0.5	15.742	7.871	0.010	0.225	4.50	-40.00
60	8	0.3	15.742	7.871	0.050	0.084	6.76	-59.99
40	12	0.7	15.75	7.875	0.044	0.398	4.50	-39.99
60	2	0.7	16.372	8.186	0.026	0.065	6.50	-60.00
40	8	0.7	16.38	8.19	0.076	0.503	4.33	-39.98
60	10	0.3	17.002	8.501	0.049	0.087	6.25	-59.99
60	6	0.9	17.002	8.501	0.089	0.426	6.25	-59.99
60	6	0.7	17.3728	8.6864	0.084	0.314	6.12	-59.99
60	8	0.9	17.631	8.8155	0.114	0.444	6.03	-59.98
60	10	0.7	17.631	8.8155	0.137	0.324	6.03	-59.98
60	4	0.7	17.632	8.816	0.044	0.182	6.03	-59.99
60	4	0.9	18.89	9.445	0.099	0.341	5.63	-59.98
60	12	0.9	18.891	9.4455	0.146	0.500	5.63	-59.97
60	10	0.9	19.52	9.76	0.093	0.523	5.45	-59.98
40	8	0.3	19.521	9.7605	0.012	0.085	3.63	-40.00